



This work is protected by copyright and other intellectual property rights and duplication or sale of all or part is not permitted, except that material may be duplicated by you for research, private study, criticism/review or educational purposes. Electronic or print copies are for your own personal, non-commercial use and shall not be passed to any other individual. No quotation may be published without proper acknowledgement. For any other use, or to quote extensively from the work, permission must be obtained from the copyright holder/s.



The investigation of surface chemical and nanotopographical cues to engineer biointerfaces

Folashade Kuforiji

School of Postgraduate Medicine

Institute for Science and Technology in Medicine

Keele University

Thesis submitted to the Keele University for the degree of

Doctor of Philosophy

2014

SUBMISSION OF THESIS FOR A RESEARCH DEGREE

Part I. DECLARATION by the candidate for a research degree. To be bound in the thesis
Degree for which thesis being submitted Doctor of Philosophy

Title of thesis The investigation of surface chemical and nanotopographical cues to engineer biointerfaces

This thesis contains confidential information and is subject to the protocol set down for the submission and examination of such a thesis.

Date of submission Original registration date 10-10-2010

(Date of submission must comply with Regulation 2D)

Name of candidate Miss Folashade Kuforiji

Research Institute ISTM Name of Lead Supervisor Dr Paul Roach

I certify that:

- (a) The thesis being submitted for examination is my own account of my own research
- (b) My research has been conducted ethically. Where relevant a letter from the approving body confirming that ethical approval has been given has been bound in the thesis as an Annex
- (c) The data and results presented are the genuine data and results actually obtained by me during the conduct of the research
- (d) Where I have drawn on the work, ideas and results of others this has been appropriately acknowledged in the thesis
- (e) Where any collaboration has taken place with one or more other researchers, I have included within an 'Acknowledgments' section in the thesis a clear statement of their contributions, in line with the relevant statement in the Code of Practice (see Note overleaf).
- (f) The greater portion of the work described in the thesis has been undertaken subsequent to my registration for the higher degree for which I am submitting for examination
- (g) Where part of the work described in the thesis has previously been incorporated in another thesis submitted by me for a higher degree (if any), this has been identified and acknowledged in the thesis
- (h) The thesis submitted is within the required word limit as specified in the Regulations

Total words in submitted thesis (including text and footnotes, but excluding references and appendices) 49,097 words

Signature of candidate Date 31/07/2014

Note

Extract from Code of Practice: If the research degree is set within a broader programme of work involving a group of investigators – particularly if this programme of work predates the candidate's registration – the candidate should provide an explicit statement (in an 'Acknowledgments' section) of the respective roles of the candidate and these other individuals in relevant aspects of the work reported in the thesis. For example, it should make clear, where relevant, the candidate's role in designing the study, developing data collection instruments, collecting primary data, analysing such data, and formulating conclusions from the analysis. Others involved in these aspects of the research should be named, and their contributions relative to that of the candidate should be specified (this does not apply to the ordinary supervision, only if the supervisor or supervisory team has had greater than usual involvement).

Abstract

This thesis is focused on understanding the fundamental physical interaction occurring, when a material interacts with a biological fluid containing protein molecules and cells. The interaction of proteins with defined surface chemistry and nanotopography is of major interest in the field of biomaterials. Despite the degree of research undertaken to study this interface, there is still a lack of understanding of how the protein layer evolves with respect to surface parameters, and further how cells condition the surface. By understanding these processes, advanced biomaterial coatings may be developed that allow control over specific cell responses to direct healing processes.

Colourimetric and fluorometric assays were carried out to assess protein-surface affinity and amount of protein adsorption. Infrared spectroscopy was used to quantify protein conformational changes incurred upon adsorption on defined nanoscale surfaces presenting a range of chemical functional groups. Model experiments were performed using bovine albumin and fibrinogen adsorbing onto surfaces presenting defined surface chemistry: OH, COOH, NH₂, and CH₃. Surface curvature on the nanoscale was used to model topography on the same length scale as protein molecules. Silica colloidal dispersions were prepared in batches, 11-215 nm diameters allowing chemical modification whilst keeping nanotopography constant.

3T3 fibroblasts were cultured over a library of surfaces presenting a spectrum of batches chemical functionality and nanostructure. Changes in cell attachment, morphology, migration and proliferation were examined. Media was removed at two different time points of 30 minutes and 24 hours, and examined to identify changes in fibroblast secreted proteins. Liquid chromatography was used to separate the cell culture media after incubation with cells over various chemically functionalised surfaces. Electrospray ionisation (ESI) and matrix

assisted laser desorption (MALDI) mass spectrometry were used to identify changes in media with respect to the varying surfaces used and over time.

The studies presented in this thesis give a better understanding of the interaction between silica nanoparticles and protein molecules, including conformational changes that occur when protein adsorbs on the nanoparticle; the effect of surface nanotopography and defined chemistry on protein adsorption is examined with respect to both chemical functionality and nanotopography. Clear differences were observed in the amount of protein adsorbed and its structural presentation when bound. The strength of the interaction, described through isotherm fitting, gave insight into the mechanism of competitive protein binding. Surface curvature on the nanoscale was also found to act synergistically with surface chemistry to dictate the dynamic accumulation of protein at the surface interface. In the later chapter discussion is given in terms of cell-surface interaction. Experimental evidence is shown for different mass spectroscopic analysis of reduced complexity media following initial cell-surface interaction and that after 24 hours. From this it is postulated that cell secretions are effected through interaction with the surface, with these changes being significant even after 30 minutes of cell culture with the defined surfaces. These changes are specific to the presented surface as they do not alter with respect to longer culture periods, but media are clearly different collected from cells cultured on different surfaces.

This research will help solve challenges facing materials science, understand biological responses to surroundings and help in the development and advance of medical devices, drug delivery, therapeutics and diagnostics.

Contents

Chapter No.		Page No
	Abstract	iii
	List of Figures	ix
	List of Tables	xii
	List of Abbreviations	xiii
	Publications and Presentations	xv
	Acknowledgement	xvi
 Chapter One	 Introduction	
1.1	Tissue Engineering	2
1.2	Biomaterials	5
1.2.1	Biomaterial Interface	7
1.3	Surface Chemistry	10
1.4	Protein Adsorption Control	12
1.4.1	The Vroman Effect	13
1.4.2	Protein Adsorption on Nanoparticle	14
1.4.3	Protein Corona	15
1.5	Infrared Spectroscopy	17
1.5.1	Fourier Transform Infrared for Protein Surface Analysis	17
1.6	Stem Cells	18
1.7	Cell Adhesion	20
1.8	Secreted Proteins	22
1.9	Analysis of Biological-Surface Interactions	26
1.9.1	Biological Mass Spectrometry	26
1.9.1.1	Electrospray Ionization	27
1.9.1.2	Matrix Assisted Laser Desorption Ionization	28
1.9.2	Multivariate Analysis	30
1.9.3	Statistical Analysis	30
1.10	Aims and Objectives	32
1.11	References	34
 Chapter Two	 Materials and Methods	
2.1	Self Assembled Monolayer (SAM) Formation using Silane	47
2.2	Preparation of Silica Spheres	51
2.2.1	Preparation of Functionalised Silica Spheres	52
2.2.2	Piranha Etching	53
2.3	Contact Angle Measurements	55
2.4	Fourier Transform Infrared Spectroscopy (FTIR)	57
2.4.1	Diffuse Reflectance Infrared Fourier Transform Spectroscopy (DRIFTS)	59
2.4.2	X-ray Photoelectron Spectroscopy	60
2.5	Scanning Electron Microscopy	61
2.6	Dynamic Light Scattering /Zeta Sizing	63
2.7	Proteins Studied	64
2.7.1	Bovine Serum Albumin	64
2.7.2	Fibrinogen	65
2.8	Protein Assays	66

2.8.1	Bicinchoninic Acid Assay Protein Quantification	66
2.8.2	Fluorescence Assay for Competitive Protein Quantification	67
2.9	Ultraviolet-Visible (UV-Vis) Spectroscopy	67
2.10	Protein Adsorption	69
2.10.1	Secondary Protein Structure	70
2.10.2	Smoothing of Infrared and Mass Spectrometry Dataset	74
2.11	Cell Culture	75
2.11.1	Thawing of Mouse Embryonic Stem Cells	76
2.11.2	Cell Passage	76
2.11.3	Cell visibility	77
2.11.4	Cell Staining	77
2.11.4.1	Cell Fixing	77
2.11.4.2	Primary Antibody Staining	78
2.11.4.3	Secondary Antibody Fixing	78
2.11.4.4	Image Capture for Fluorescence	78
2.11.4.5	Statistical Analysis	78
2.12	Secreted Protein	79
2.12.1	Acetonitrile Precipitation	79
2.12.2	Ziptip	79
2.13	Mass spectrometry	80
2.13.1	Liquid Chromatography Mass Spectrometry	80
2.13.2	Matrix Assisted Laser Desorption Ionisation	81
2.14	Statistical Analysis	82
2.14.1	Principal Component Analysis	82
2.15	Summary of Secretome Experiment	83
2.16	References	84
Chapter Three	Protein Adsorption from Single Protein Solutions	
3.1	Introduction	89
3.2	Materials and Method	92
3.2.1	Preparation of Silica Spheres	92
3.2.2	Preparation of Functionalised Silica Spheres	92
3.2.3	Protein Adsorption from Single Protein Solution	92
3.2.4	Bicinchoninic acid Assay (BCA) Protein Quantification	93
3.2.5	Adsorption Isotherm	93
3.2.6	Statistical Analysis	94
3.2.7	Summary	95
3.3	Results	96
3.3.1	Surface Characterisation	96
3.3.2	Functionalised Silica Particles Characterisation	97
3.3.3	Infrared Vibration features and chemical functions	98
3.3.4	x-ray Photoelectron Spectroscopy	100
3.3.5	Protein Serial Dilution	101
3.3.6	Bicinchoninic Acid Assay	102
3.3.7	Adsorption Isotherms	102
3.3.7.1	Bovine Serum Albumin-Surface Chemistry	103
3.3.7.2	Bovine Serum Albumin-Particle Size	105
3.3.7.3	Fibrinogen-Surface Chemistry	107
3.3.7.4	Fibrinogen- Particle Size	109
3.3.8	Affinity Constant and Saturation Amount	111

3.3.9	Amide I Band Position to Secondary Structure	116
3.4	Discussion	125
3.5	Conclusion	135
3.6	References	137
Chapter Four	Competitive Binding of Proteins	
4.1	Introduction	144
4.2	Materials and Methods	146
4.2.1	Protein Solutions	146
4.2.1.1	Human Serum Albumin	146
4.2.1.2	Fibrinogen	146
4.2.2	Protein Adsorption from Multiple Protein Solutions	146
4.2.3	Infrared Spectroscopy	147
4.2.4	Adsorption of Proteins to Nanoparticles	147
4.2.5	Summary	148
4.3	Results and Discussion	149
4.3.1	Calibration plot of HSA and Fg	149
4.3.2	Adsorption of Proteins to Nanoparticles	151
4.3.3	Competitive Adsorptions of Proteins	152
4.3.3.1	Effect of Surface Chemistry on HSA Adsorption	152
4.3.3.2	Effect of Surface Chemistry on Fg Adsorption	154
4.3.3.3	Effect of Surface Curvature on HSA Adsorption	156
4.3.3.4	Effect of Surface Curvature on Fg Adsorption	158
4.3.3.5	Ratio of Surface Chemistry on HSA/Fg Adsorption	160
4.3.3.6	Ratio of Surface Curvature on HSA/Fg Adsorption	162
4.3.4	Fitting of Amide I	164
4.3.5	PCA Analysis	172
4.3.5.1	Loading Plots	173
4.3.5.2	Score Plots	174
4.4	Discussion	181
4.5	Conclusions	190
4.6	References	192
Chapter Five	Investigation of Cell Secretome in Response to Surface Cues	
5.1	Introduction	197
5.2	Materials and Methods	200
5.2.1	Preparation of Self Assembled Monolayer (SAM) using Silanes	200
5.2.2	Characterisation of SAM	200
5.2.2.1	Water Contact Angle (WCA) Measurements	200
5.2.2.2	Fourier Transform Infrared Spectroscopy –Attenuated total reflectance	201
5.2.3	Cell Culture	201
5.2.3.1	Cell Passage	202
5.2.4	Cell Culture and Different Media Composition	202
5.2.4.1	Cell Culture in Serum free medium	204
5.2.4.2	Cell culture in Serum free medium with SAMs Chemistries	204
5.2.5	Acetonitrile Precipitation	205
5.2.6	Ziptip	206
5.2.6.1	Ziptip Procedure	206
5.2.7	Mass Spectrometry	206
5.2.7.1	Liquid Chromatography –Electrospray Ionisation (LC-ESI)	206

5.2.7.2	Matrix Assisted Laser Desorption Ionisation (MALDI)	207
5.2.8	Summary	208
5.3	Results	209
5.4	Discussion	222
5.5	Conclusions	240
5.6	References	242
 Chapter Six	 General Discussion, Future Work and Conclusion	
6.1	Discussion	
6.2	Future Work	
6.3	References	
	Appendix	

List of Figures

Figure	Title	Page No.
Figure 1.1	Tissue engineering process and its component	3
Figure 1.2	Examples of biomaterials and its applications	6
Figure 1.3	The time-scale required for material-host tissue interactions	7
Figure 1.4	Schematic of self assembled monolayer formation	11
Figure 1.5	Schematic representation of soft and hard protein corona	16
Figure 1.6	Classification of fibroblast cell	19
Figure 1.7	Cell secretome in response to local environmental cues	23
Figure 1.8	An increasing number of publications on the term Secretome	23
Figure 1.9	Illustration of secretome analysis	26
Figure 1.10	Schematic of the basic components of a mass spectrometer	27
Figure 1.11	Schematic representation of electrospray ionization	28
Figure 1.12	Schematic of the matrix assisted laser desorption ionization technique	29
Figure 1.13	Principal component analysis showing scores and loadings	31
Figure 2.1	Process of preparing the carboxylic acid functionalised SAMs	49
Figure 2.2	Preparation of silica nanoparticle	52
Figure 2.3	SEM image of closed packed amine-modified silica nanoparticle	54
Figure 2.4	Young equation showing the relationship between three interfacial tension	55
Figure 2.5	Schematic of contact angle measurement	56
Figure 2.6	Schematic of an attenuated total reflectance crystals	58
Figure 2.7	Principle of Diffuse Reflectance Infrared Fourier Transform Spectroscopy	59
Figure 2.8	Component of x-ray Photoelectron Spectroscopy System	61
Figure 2.9	Structure of scanning electron microscope	62
Figure 2.10	Three dimensional structure of bovine serum albumin	65
Figure 2.11	Structure of Fibrinogen molecule	65
Figure 2.12	Standard curve of BSA and Fg at 562 nm	67
Figure 2.13	Comparison of Infrared Spectrum	71
Figure 2.14	Omnic macro-basic intuitive graphical interface	72
Figure 2.15	Computer simulation to calculate secondary protein structure	73
Figure 2.16	Scheme for smoothing infrared and mass spectrometry dataset	74
Figure 2.17	Phase contrast of 3T3 fibroblast cell	75
Figure 2.18	Schematic of method used for secreted Fibroblast	81
Figure 2.19	The different stages of secretome analysis using mass spectrometry	83
Figure 3.1	A detailed description of experiment	95
Figure 3.2	DLS size distribution data and silica sphere diameters	96
Figure 3.3	WCA of hydrophobic and hydrophilic silica nanoparticle	97
Figure 3.4	ATR-IR spectrum of functionalised silica spheres	99
Figure 3.5	XPS spectra of functionalised silica spheres	100
Figure 3.6	Serial dilution of BSA and Fg concentration with less error	101
Figure 3.7	Adsorption isotherm of BSA on surface chemistry	103
Figure 3.8	Adsorption isotherm of BSA on surface curvature	105
Figure 3.9	Adsorption isotherm of Fg on surface chemistry	107
Figure 3.10	Adsorption isotherm of Fg on surface curvature	109
Figure 3.11	Curve fitting of BSA on 64 nm	111
Figure 3.12	Summary of measured affinity constant for BSA and Fg	112

Figure 3.13	Summary of measured saturation amount for BSA and Fg	114
Figure 3.14	FTIR analysis on Amide I band	116
Figure 3.15	Conformation assessment of BSA on methyl-surface	117
Figure 3.16	Conformation assessment of BSA on hydroxyl surface	119
Figure 3.17	Conformation assessment of Fg on methyl-surface	121
Figure 3.18	Conformation assessment of Fg on hydroxyl surface	123
Figure 3.19	Effect of surface chemistry on Fg adsorption at highest concentration	125
Figure 3.20	Effect of surface chemistry on BSA adsorption at highest concentration	126
Figure 3.21	Schematic representation of BSA and Fg adsorbing on silica nanoparticle	127
Figure 3.22	Protein adsorption on methyl and hydroxyl surface	128
Figure 3.23	BSA adsorption on amine and hydroxyl surface	129
Figure 3.24	Saturation amount of Fg on methyl and hydroxyl surface	130
Figure 3.25	Saturation of Fg adsorption on methyl surface	131
Figure 3.26	Percentage of secondary structure of Fg on methyl and hydroxyl surface	132
Figure 3.27	Percentage of secondary structure of BSA on amine and methyl surface	133
Figure 3.28	BSA & Fg concentration on secondary structure on methyl surface	134
Figure 4.1	Schematic layout plan of the experiment	148
Figure 4.2	Calibration of HSA vs Fluorescence units	149
Figure 4.3	Calibration of Fg vs Fluorescence units	150
Figure 4.4	Functionalised hydroxyl (OH) silica nanoparticle of 64 nm	151
Figure 4.5	Variation of HSA adsorption and timepoints on different functionalised silica surface	152
Figure 4.6	Fg adsorption at different timepoints on functionalised silica particle,	154
Figure 4.7	HSA adsorption on surface curvature at different timepoints	156
figure 4.8	Fg adsorption on surface curvature at different timepoints	158
Figure 4.9	Ratio of HSA/ Fg (19:1) adsorption on surface curvature at different timepoints	160
Figure 4.10	Ratio of HSA/ Fg (19:1) adsorption on surface chemistry at different timepoints	162
Figure 4.11	Percentage of secondary structure of HSA/Fg at 10 minutes	164
Figure 4.12	Percentage of secondary structure of HSA/Fg at 30 minutes	166
Figure 4.13	Percentage of secondary structure of HSA/Fg at 60 minutes	168
Figure 4.14	Percentage of secondary structure of HSA/Fg at 90 minutes	169
Figure 4.15	Percentage of secondary structure of HSA/Fg at 120 minutes	170
Figure 4.16	Percentage of secondary structure of HSA/Fg at 180 minutes	171
Figure 4.17	Eigenvalues of principal component	172
Figure 4.18	Amide I loading plot of PC1 and PC2	173
Figure 4.19	Score Plot of hydroxyl (OH) at 10-180 minutes	174
Figure 4.20	Score Plot of methyl (CH ₃) at 10-180 minutes	175
Figure 4.21	PC1 and PC2 score plots of amide I of 11 nm at different timepoints	177
Figure 4.22	PC1 and PC2 score plots of amide I of 215 nm at different timepoints	179
Figure 4.23	HSA adsorption on carboxylic and methyl surface	182
Figure 4.24	Fg adsorption on carboxylic and methyl surface	183
Figure 4.25	Percentage of secondary structure on CH ₃ and COOH on 11 and 215 nm	184
Figure 4.26	PC 1 and PC2 show the variability in amide I on COOH and CH ₃ surface	186
Figure 4.27	HSA adsorption on 11 and 215 nm	187
Figure 4.28	Fg adsorption on 11 and 215 nm The percentage of secondary structure on methyl and carboxylic surface	188

Figure 4.29	Effect of surface chemistry on HSA/Fg (19:1) adsorption	188
Figure 5.1	Challenges of secretome analysis	198
Figure 5.2	Water contact angle measurement	200
Figure 5.3	Schematic of experiment layout for cell protein secretion	204
Figure 5.4	Protein precipitation using acetonitrile	205
Figure 5.5	Schematic of method used in secretome experiment using MS	208
Figure 5.6	Schematic illustration of the procedure used for fibroblast secreted proteins	208
Figure 5.7	Images of water droplets on defined SAM	209
Figure 5.8	FTIR spectra of various SAM surfaces	210
Figure 5.9	Phase contrast optical microscopy of 3T3 fibroblast cultured in test medias	211
Figure 5.10	Illustration of how cell numbers were calculated using ImageJ	212
Figure 5.11	Illustration of how cell adhered were calculated using ImageJ	213
Figure 5.12	Data representation of 3T3 fibroblast with different media complexity	214
Figure 5.13	Data representation of 3T3 fibroblast with Glutamine	215
Figure 5.14	Data representation of 3T3 fibroblast without Glutamine	215
Figure 5.15	Data representation of adhered 3T3 fibroblast with different media complexity	216
Figure 5.16	Area of cells on different media complexity	217
Figure 5.17	Adhered of 3T3 fibroblast with SAMs chemistries	218
Figure 5.18	Spreading of 3T3 fibroblast with SAMs chemistries	218
Figure 5.19	Schematic illustration of mass spectrometry analysis	219
Figure 5.20	Liquid chromatography and mass spectrum of a sample	220
Figure 5.21	Illustrate the MALDI-Tof-Tof experimental setup label	221
Figure 5.22	Wettability and polarity of surface functional groups	222
Figure 5.23	Infrared spectra of SAM modified surfaces	223
Figure 5.24	Cell numbers cultured in varying test medias over 48 hours	225
Figure 5.25	Eigen values of each principle component analysed for the LC-ESI dataset	228
Figure 5.26	Clustering of PC1 vs PC2 mass spec data from cell secretome analysis	229
Figure 5.27	PC1 and PC2 loadings associated with (a) PC1 and (b) PC2 due to secretome variance with respect to surface chemistry	231
Figure 5.28	Effect of incubation time on cell secretion variance	233
Figure 5.29	Eigen values of each principle component analysed for the MALDI-Tof-Tof data set	234
Figure 5.30	Clustering of PC1 vs PC2, PC3 vs PC4 mass spectrometry data from cell secretome analysis	235
Figure 5.31	Effect of incubation time on cell secretion variance	236
Figure 5.32	PC1 and PC2 loadings plot for the first two PCs	237
Figure 6.1	Overlaid image of Fibroblast cells seeded on functionalised silica NP	

List of Tables

Table	Title	Page No
Table 1.1	Economic cost of major illness in the USA	4
Table 2.1	SAMs chemistries, label and formula	48
Table 2.2	Names, models and chemical structure of chemistries	50
Table 2.3	Reaction condition for sphere preparation	52
Table 3.1	Calculation of Protein Concentration of BSA and Fg	101
Table 5.1	Different media composition	203
Table 5.2	Different measurement of water contact angle measurement	210
Table 5.3	Surface Functionality using Infrared Spectroscopy	223
Table 5.4	Species found in PC1 for ESI -MS	232
Table 5.5	Species found in PC2 for ESI -MS	232
Table 5.6	Loading values in PC1 using MALDI-MS	238
Table 5.7	Loading values of PC 2 using MALDI -MS	238

List of Abbreviations

ACN	Acetonitrile
APTES	3- Aminopropyltriethoxysilane $\text{Si}(\text{OC}_2\text{H}_5)_3(\text{CH}_2)_3\text{NH}_2$
APS	Adult Stem Cells
ATR	Attenuated Total Reflectance
BMSCs	Bone Marrow Stromal Stem Cells
BSA	Bovine Serum Albumin
CI	Chemical Ionisation
Da	Dalton
DAPI	4'-Diamidino-2-Phenylindole
DLS	Dynamic Light Scattering
DMEM	Dulbecco Medium
DMSO	Dimethylsulfoxide
DE	Digest Electrophoresis
DTGS	Deuterated triglycinesulfate
DRIFTS	Diffuse reflectance infrared fourier transform spectroscopy
ECM	Extracellular matrix
EI	Electron Impact
ESB	European Society of Biomaterials
ESCs	Embryonic Stem Cells
ESI	Electrospray Ionization
FCS	Fetal Calf Serum
Fg	Fibrinogen
FGM	Fibroblast Growth Medium
FN	Fibronectin
FTIR	Fourier Transform Infrared Spectroscopy
HESC	Human Embryonic Stem Cell
HPLC	High Pressure Liquid Chromatography
HSCs	Hematopoietic Stem Cells
IPSc	Induced Pluripotent Stem Cells
IR	Infrared Spectroscopy
KCl	Potassium Chloride
KH₂PO₄	Potassium Dihydrogen Phosphate

LV	Liquid Vapour
LC	Liquid Chromatography
MALDI	Matrix Assisted Laser Desorption Ionization
Mins	Minutes
MS	Mass Spectrometry
MS/MS	Tandem Mass Spectrometry
MSCs	Mesenchymal Stem Cells
MTEOS	Methyltriethoxysilane $\text{Si}(\text{OC}_2\text{H}_5)_3\text{CH}_3$
M/Z	Mass-to-charge-ratio
MVA	Multivariate Analysis
NaCl	Sodium Chloride
Na₂HPO₄	Sodium Pyrophosphate
NP	Nanoparticle
PBS	Phosphate Buffered Saline
PCA	Principal Component Analysis
PGA	Polyglycolic Acid
PLA	Polylactic Acid
PLS	Partial Least Squares
PMMA	Poly(methylmethacrylate)
RGD	Arginine-Glycine-Aspartic
SAM	Self Assembled Monolayers
SEM	Scanning Electron Microscope
SL	Solid Liquid
SV	Solid Vapour
TEOS	Tetraethoxysilane $\text{Si}(\text{OCH}_2\text{CH}_3)_4$
TESPSA	3-triethoxysilylpropyl succinic anhydride $\text{Si}(\text{OC}_{13}\text{H}_{24}\text{O}_6)$
TFA	Trifluoroacetic Acid
USA	United State of America
UV-Vis	Ultraviolet Visible Spectroscopy
WCA	Water Contact Angle
XPS	X-ray Photoelectron Spectroscopy
γ	Surface Energy
ZnSe	Zinc Selenide

Publications and Presentations

Research Publications

Khot G, Kuforiji F, Rupert W and Roach P. Dynamic Assessment of Fibrinogen Adsorption and Secondary Structure Perturbation, Conference Papers in Science, (2014) Article ID 601546

Kuforiji F, Roach P. Cellular Response on Functionalised surface in Young Scientist Forum (YSF) Newsletter 3, Page 8, (2012)

Kuforiji F, Review article in Preparation (2014), in preparation for Soft matter (*Invited review*)

Kuforiji F, Roach P. Protein Adsorption from Single Protein Solutions (*In Preparation*)

Kuforiji F, Roach P. Competitive Binding of HSA and Fg on functionalised Silica Nanoparticle (*In Preparation*)

Kuforiji F, Roach P. Investigation of Cell Secretome in Response to Surface Cues (*In Preparation*)

Published Poster Presentations

Kuforiji F, Roach P. Engineered Nanosurface to Dictate Surface Functionality. Biological Surfaces and Interfaces Conference, Spain (July, 2013)

Kuforiji F, Roach P. Engineered Nanosurface to Dictate Surface Functionality. UKSB conference, Birmingham University (June, 2013)

Kuforiji F, Roach P. Fibroblast Response to Surface Chemical and Nanotopographical Cues. UKSB Conference, Nottingham University (June, 2012)

Kuforiji F, El-haj A, Roach P. Directing Biological Response Through Material Properties. TERMIS World Congress, Grenada (September, 2011)

Conference Oral Presentations

Kuforiji F, Roach P, El-Haj A, Fibroblast Response to Surface Chemical and Nanotopographical Cues. Regenerative Medicine DTC Joint Conference, Nottingham University (April, 2012)

Acknowledgements

I will like to appreciate God Almighty for giving me the grace and the strength to embark on this journey. You are my source of joy and motivation not to give up.

I would like to express my deepest appreciation to my supervisor, Dr Paul Roach and co supervisor Prof Alicia El Haj for their guidance and support have made this thesis a very fulfilling experience. I appreciate Dr Rosemary Fricker for her suggestions and support she gave me during my PhD study especially during the group meetings.

I would like to thank Dr Heidi Fuller, Dr Sarah Hart and Dr Elzbieta Piatkowska for performing mass spectrometry analysis on my samples. Special thank you to Dr Neil Tedding for allowing me to use the speed dryer, Dr Clare Hoskins for using Malvern Zeta nanosizer and National EPSRC XPS User's Service (NEXUS) at Newcastle University, an EPSRC Mid-Range Facility for using the x-ray photoelectron spectra (XPS)

My special thanks to all the people at Guy Hilton research centre. I can't start listing all their names but I appreciate all your help, moral advice, guidance and assistance throughout my stay at the research centre.

I would like to extend my gratitude to my funding bodies, Engineering and Physical Science Research Council (EPSRC) for their financial assistance.

I would like to express my most sincere gratitude to my parent Mr & Mrs Kuforiji, brother Femi Kuforiji, sisters, Fisayo and Ibukunolu Kuforiji without their moral support, this thesis would not have been possible. Their advice and encouragement are what allowed me to carry this project so far. A Special thank you to Temitayo Borisade, Simisola Onalaja and Olusile Akinremi .Thank you to Pastor Marcus and Norah Chilaka and all the member of RCCG Living Water Parish (Stoke) your help and advice has not gone unnoticed.

Most importantly, I would like to thank my husband, Dare Dandare, for giving me the encouragement and strength needed to achieve my goals. Your support means the world to me.

CHAPTER 1

Introduction

1.1 Tissue Engineering

Tissue engineering is an emerging multidisciplinary field involving biology, medicine and engineering that aims to improve the quality of life of people by the development and manipulation of laboratory grown molecules, cells, tissues and organs to replace, maintain and support the function of defective or injured body parts.¹ Tissue engineering focuses on understanding how tissue formation and regeneration function, with the aim to induce new functional tissues.

Varying approaches are being investigated to provide alternative therapies (i.e. for people with organ failure) that will reduce pain and be cost effective. For example, in orthopaedic field, there are several limitations in the use of autologous or allogenic graft for surgeries. Examples of the challenges are the time required to harvest autologous graft, lack of donor tissues in autologous and risk of disease in allogenic grafts, which can lead to morbidity. However, tissue engineering offers to overcome the challenge by replacing and restoring tissues and organs through the delivery of stem cells and bioactive molecules onto specific biomaterials and in three dimensional structures² as shown in Figure 1.1.

Bone defect repair using tissue engineering approach is believed to be the best approach because the patient's own tissue can be used by the time the regeneration is complete.^{3,4}

Tissue engineering have been used in drug therapy, wound repair and creating an artificial component of the system to repair or replace organ failure. According to the global market, the estimated value in tissue engineering is expected to be approximately \$27 billion by 2018.⁵ In USA, a huge amount of money of approximately \$80 billion is spent annually to restore, maintain and improve tissue function while more than \$400 billion dollars is lost in repairing tissue or organ failure,⁶ Table 1.1

Cells, biomaterial scaffolds and growth stimulating signals are the key factors to engineered tissues. The aim of tissue engineering is shown in Figure 1.1: (1) isolate specific cells through a biopsy from patients, (2)- (3) grow the cells on 3D scaffolds under controlled culture conditions, (4) deliver the construct to the desired site in the patient's body and (5) direct new tissue formation into the scaffold that can be degraded over time.¹

Biomaterial scaffold is very important in tissue engineering due to its function, making sure the organisation, differentiation of cells in tissue engineered constructs and physical supports for the cells such as the chemical and biological cues needed in forming functional tissues.⁷ Tissue Engineering has been used to engineering 3D constructs to prescribing biochemical and physical cues to direct biological responses.⁸

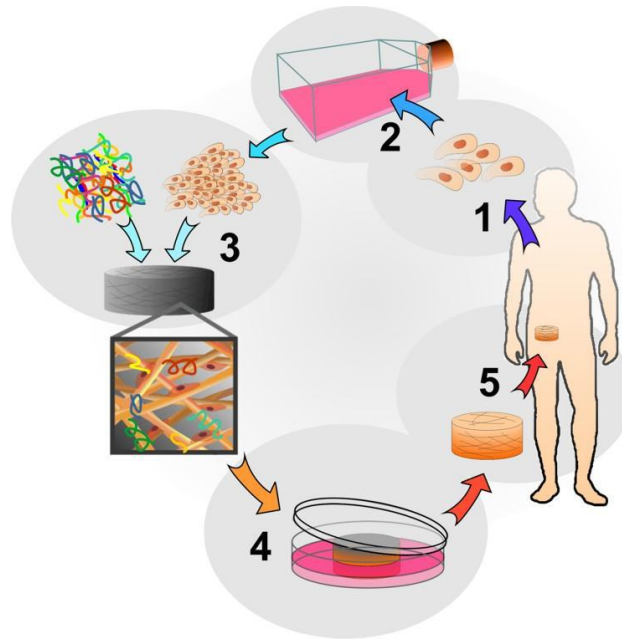


Figure 1.1 Tissue engineering process and its components.⁸

Tissue engineering is currently emerging as an important field globally based on the published reviews coupled with the success stories such as cartilage repair and skin replacement.^{9, 10} Successful regeneration of tissues or organs requires consideration of several critical elements including biomaterial scaffolds that serve as mechanical support for the cell

growth, the cells that can differentiate into specific cell types and growth factors that can modulate cellular activities. Despite extensive carried out in tissue engineering; there are several challenges that need to be resolved such as the lack of biomaterials with desired mechanical, chemical and biological properties.

Biomaterials have been researched upon and shown to consist of a potential cell carrier substance for cartilage repair. Cartilage is a very good example leading into nano-architecture of their environment. Cartilage injuries affect several millions of people and it is very difficult to repair. Alternative treatment of cartilage, make use of stem cells which have being shown to help in repairing cartilage injuries.¹¹ The choice of biomaterial is critical to the success of tissue engineering approaches in cartilage repair. A variety of biomaterials, naturally occurring, synthetic, biodegradable and non-biodegradable, have been introduced as potential cell-carrier substances for cartilage repair.¹² Collagen based biomaterials^{13,14} in the form of gels¹⁵ and synthetic polymer¹⁶-based biomaterials have been studied for cartilage repair.

Table 1.1 Economic cost of major illness in the USA in 2003¹⁷

Conditions	Total Cost (US/\$ billions)
Heart failure	404.4
Diabetes, insulin dependent	55
Stroke	33.7
Parkinson's disease	71
Spinal cord Injury	40.3

1.2 Biomaterials

Biomaterials are predominantly used in medical applications for drug delivery, device based therapies and tissue engineering as shown in Figure 1.2. The application of biomaterials in tissue engineering has increased rapidly from merely interacting with biological systems to influencing biological processes. According to the European society of Biomaterials (ESB), the current definition of biomaterial is defined as “*material intended to interface with biological systems to repair, replace or augment tissue or organ back to normal function*”.¹⁸ It has been estimated that at least 20 million people in the United States have undergone implantation of an exogenous material or device.¹⁹ The medical and surgical cost of treating device failure or implant-associated infection is estimated at US\$50,000 per patient,²⁰ which is very expensive and a successful outcome is not guaranteed. The impact of advanced engineering of biomaterials intended for long term implantation is vast, with attention over the past decade turning more and more towards optimised design of biomaterial surfaces.

Over the past decades, synthetic and natural derived polymers have been studied for improvement. Biomaterials have played an essential role in the treatment of disease and the improvement of health care. An advance in biomaterials has led to the use of biological scaffolds (decellularised donor tissues) with an autologous stem cell to replace lung airway.²¹ Recently, successful human embryonic stem cells trials have helped reverse patients’ disease (blindness); retinal cells derived from embryonic stem cells were delivered into the eyes of two patients suffering from progressive blindness, and the results help the patients regain their sight and vision after the treatment.²² Also, autologous stem cells have been used to replace the windpipe of a woman which was the world’s first recipient of reconstructed windpipe tissue, although it was successful, the success is likely due to the tissue being a natural construct, the ability to harvest such materials (i.e. from cadaver) is

very limited. Therefore there is a need to better engineer biomaterials.²³ Despite the huge success of biomaterial applications, biomaterial scientists remain faced with several challenges, such as the design and engineering of materials that have optimal properties to integrate into biological tissues and perform their intended purpose. These requirements have altered over the past decades as our understanding has evolved. Understanding how *current* biomaterials can be optimised to be more compatible with an implant site has been a focus of interest over the past decade.

When biomaterials are implanted into the body, it comes in contact with the body or body fluids, interfacial phenomena occur such as protein adsorption, control essential parameters for biocompatibility of the material. The term '*biocompatibility*' is widely used but has also evolved to fit several purposes related to the exact requirements. It reflects the nature and degree of interaction between a biomaterial and its host tissue, and is one of the critical concerns in biomaterials research.²⁴ Biocompatibility can be defined as the ability of a material to perform with an appropriate host response in a specific application,²⁵ being dependent upon the site of implantation, function and size of the implant, and the duration of implantation.^{26,27}

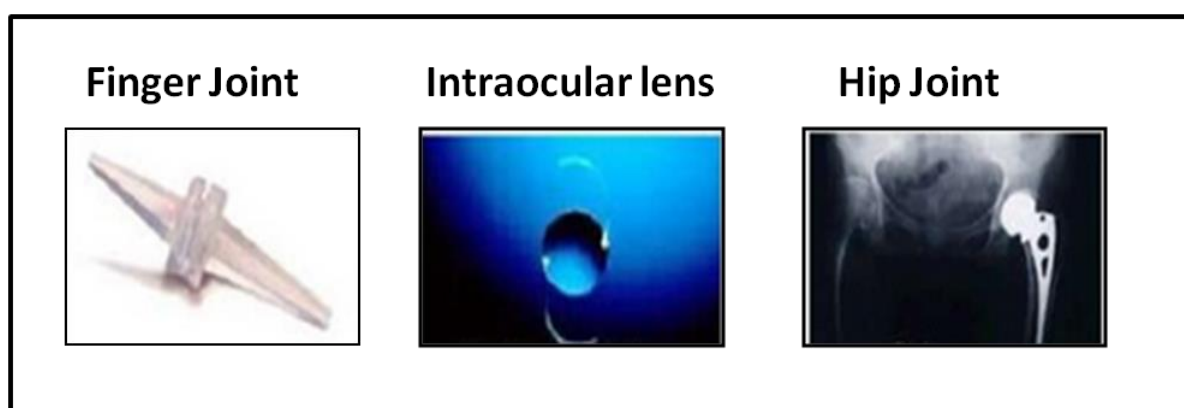


Figure 1.2 Example of Biomaterials and its applications, edited and adapted ²⁸

1.2.1 Biomaterial Interface

On presentation of a material to a biological fluid a water shell immediately interacts with the surface, transporting ions which may accumulate adjacent to the surface. Materials possessing a distinct positive or negative surface charge at physiological pH would necessarily be surrounded by a layer of hydrated ions forming an electric double layer. Being present in lesser abundance compared to ionic salts protein molecules eventually reach the material's surface via diffusion. These will then interact with the ions and eventually reach the surface of the material.

In a dynamic process being initiated milliseconds after initial contact between the material and the fluid, although possibly not reaching equilibrium for many minutes, the surface becomes conditioned by a protein layer. After implantation, synthetic materials undergo dynamic adsorption of proteins and other bio-molecules which induce inflammatory cell responses.

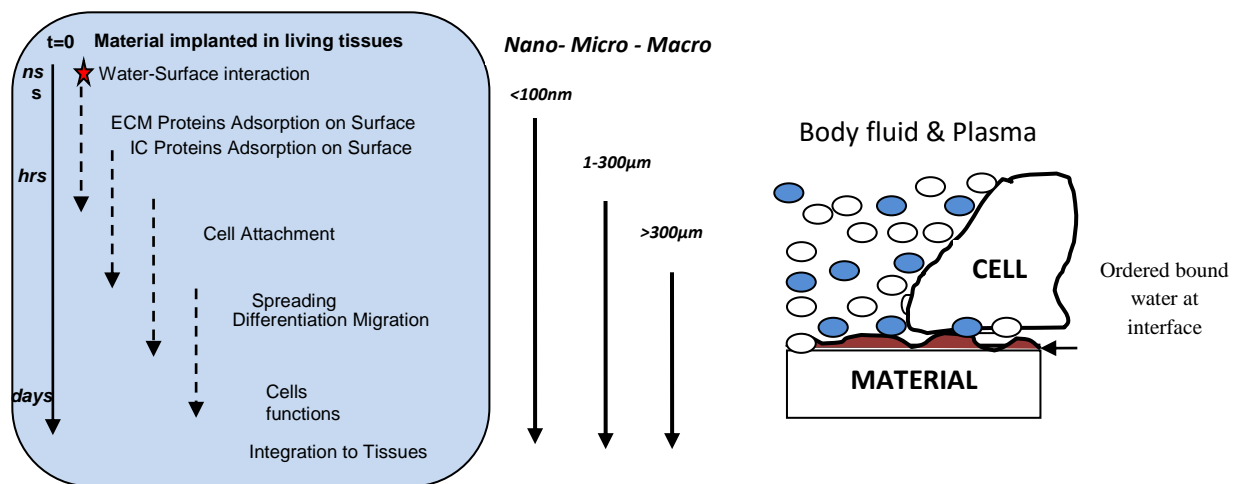


Figure 1.3 (a) Time-scale required for material implanted in living tissues²⁹ (b) material-host tissue interactions.

The time-scale required for material-host tissue interactions to become established is shown in Figure 1.3. The initial response to a material surface being placed in a biological milieu is for water molecules to reach the surface and create a water shell around the material on a nanosecond timescale which is denoted with a red star shape (★). At the second stage, the material becomes covered in an adsorbed layer of proteins initially present in the extra cellular matrix, from seconds to hours. The cell surface interaction occurs between cell and surface-bound protein, which starts from hours up to days. The last stage is the continuing development of the early implant stages which can take place from days up to decades (i.e. total hip replacement). The modification of an interface between the surface of biomaterials and the biological environment is significant for modern tissue and cell engineering methods. Surface engineering is used to present desired surface cues, such that the outmost edges of a material that first come into contact with biological fluids and attaching tissues govern initial interactions. These cues have largely been centred on surface chemistry, topography and stiffness, although electrical activity has also been shown to affect some cell types.³⁰

Surface chemistry and topography are the two most important factors that influence biological reactions.³¹ There are an umbrella of terms that can be used to characterise differences in surface chemistry, example is the functional group normally given as the head-group of molecules tethered in some way to the surface. The head group may be classified in terms of surface charge, surface wettability or surface energy. This group may be attributed as a method of characterisation, which accounts for the polarity of the presented chemistry. For example, Webb *et al*; observed significantly higher fibroblast cell attachment and spreading on hydrophilic model silane surface compare to hydrophobic surface.³² Surface chemical composition such as wettability, charge and energy have been shown to affect protein adsorption.³³⁻³⁵

Topographic cues can also be categorised in numerous ways, and as such there are many discrepancy. Feature heights and widths are commonly referenced in terms of their ability to guide cell responses, although aspect ratio (height /width) has also been shown to be a useful measure.³⁶ Micro-sized grooves are well known to be large enough for cells to perceive them, with ‘*contact guidance*,’ a term coined by Dunn *et al*; in 1982 to describe how cells interact with surface feature edges, found to guide cells when feature height is above ~0.5 microns.^{37,38} Nano-curvature, being on the same length scale as protein molecules, is now widely accepted to be crucial in determining how protein molecules accumulate on surfaces.³⁹ Protein-surface interactions are governed by their ability to adsorb and rearrange once attached to a surface, with feature shape and size, as well as protein molecule shape and size being shown to determine binding strength and conformation.⁴⁰ Most studies conducted examining protein-surface interaction have been carried out on single protein systems, or with very few proteins adsorbing in competition. This has largely been due to the technical difficulties in obtaining useful information when dealing with more ‘real-life’ complex solutions of multiple proteins competing for adsorption sites.

We are now at a stage where we understand that the composition of this adsorbed protein layer is key in terms of subsequent cell responses and understand that nanoscale features and their chemistry can dictate the final composition of the adsorbed layer, although we are now beginning to understand the intricacies of what protein molecules may be presented in the locality of the surface, obviously impacting greatly on adsorbed composition. Cells perceive and strive to moderate their environment to support their own requirements. Secretary molecules act as communication signals between cells and aid the build-up of the extracellular matrix (ECM) necessary for cell attachment to surfaces and the development of bulk tissues. The nature of these secretary molecules is becoming of interest due to our better understanding of this interface and the technical ability to measure such a dynamic and

complex system. Through investigation of this mechanism we may be able to design advanced materials, having the ability to fine tune the development and function of regenerated tissues.

1.3 Surface Chemistry

A large number of review articles have been published to demonstrate the importance of surface chemistry with respect to biocompatibility.^{41,42} Material surfaces can be modified by using different methods such as the application of surface chemical gradients, self-assembled films, polymer brushes, molecular grafting, addition of surface active bulk additives and surface chemical reactions.⁴³ Chemical surface modification of biomaterials has been achieved using different techniques and methods. The most common method is self-assembled monolayers (SAMs) Figure 3, which involve the process of coating the surface to form highly ordered structures on specific substrates. The application of SAMs has increased rapidly since its introduction by Whitesides *et al.*⁴⁴ Several self-assembly systems have been researched upon, such as thiols on gold⁴⁵⁻⁴⁹ and alkylsilanes⁵⁰⁻⁵⁴ on silicon. SAMs provide a well-defined surface chemistry and have been applied to model biomaterial surfaces.⁵⁵⁻⁵⁷ Self assembly of silane molecules have been widely studied due to the ability to form chemically and physically stable covalently attached monolayers on surfaces such as glass.⁵⁸

SAMs are easy to construct and manipulate. For example; changing one atom of the terminal group can alter the properties of the surface such as wettability and cellular adhesion/proliferation. Studies have shown that initial cell adhesion to SAMs was greatly affected by their surface functional groups and displacement of adsorbed serum proteins with cell adhesive proteins playing an important role in cell adhesion.⁵⁹ The functionalization of surfaces provides the opportunity to tailor the surface properties such as wettability, topography, as the terminal groups allows the tuning of these properties.⁶⁰ SAMs consist of

three parts as shown in Figure 1.4, the head group, the alkyl chain and the terminal end group. The head group is responsible for the anchoring of the molecule onto the substrate, i. e. triethoxysilane, while the alkyl chain provides the stability of the monolayer, due to van der Waals and hydrophobic interactions which influence the ordering of the SAMs; finally the terminal end group introduces chemical functionality into the monolayer systems.^{61, 62}

SAMs have gained much attention since they allow the investigation of fundamental physical properties of interfacial chemistry, solvent molecule interaction and self organization.^{63, 64} Numerous studies have been performed using SAM to present a range of functional groups such as alkyl, thiols, carboxylic acids and with each, a much more clear understanding is laid over molecular surface interaction and the role of different molecules in surface chemistry. For example, researchers have investigated the interaction of protein molecules with SAMs, examining how specific surface characteristics are important and how they affect adsorption kinetics, adsorbed concentrations and biological activity of the protein layer.^{65,66}

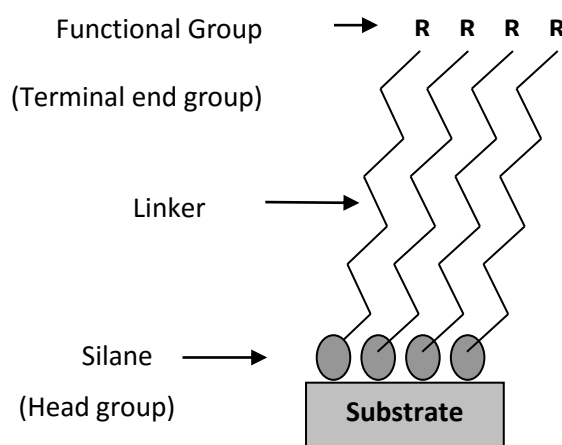


Figure 1.4 Schematic of Self assembled monolayers

1.4 Protein Adsorption Control

Protein adsorption on surfaces is the first step in biological processes and plays a vital role in the integration of implants in the living tissue. Protein adsorption is important in pharmaceutical science, biotechnology, material science and biomedical applications which has led to an increase in the number of published articles/review.⁶⁷⁻⁶⁹ For example, protein adsorption can lead to fouling processes and degrading the analytical performance of medical devices.⁷⁰ The interaction between surface properties and cell response is not well understood. Protein produced by the cell, pre-adsorbed proteins and surface properties have been linked in determining the strength and type of adhesion.

Initial protein adsorption occurs within milliseconds, although is a highly dynamic processes wherein protein molecules may bind, rearrange and detach, thus affording a protein conditioned surface which may later mediate further interaction.⁷¹⁻⁷⁵ As a protein molecule diffuses near to a surface, interaction is governed by the surface chemical groups of the material and of the outer shell of the protein molecule. Pockets of localised charge (and/or polarisable groups) presented on the protein molecule, along with the strength of inner bonding holding the secondary structure in place, will dictate initial adsorption orientation and conformation. Depending on the size of the protein molecule there may be many areas on the surface having similar characteristics, and therefore adsorption is more likely to result in many randomly oriented molecules

Generally the plethora of proteins present in a mixed biological fluid, such as serum, will comprise 30-40 thousand proteins each having specific affinity towards a surface, dependent upon the interaction of their outer shell and the surface. As protein adsorption is largely a dynamic process, with adsorption-desorption occurring until an equilibrium surface concentration is reached, the composition of a protein layer from a mixed protein solution (i.e. serum) evolves dramatically over time. Those proteins with higher affinity for the

surface will reside for longer, eventually being replaced by molecules with even higher surface affinity. Leo Vroman was the first to highlight this effect whilst examining the surface concentration of fibrinogen.⁷⁶

1.4.1 The Vroman Effect

There is competition between different proteins on surfaces when proteins adsorbed on nano-surfaces and this phenomena is known as the Vroman effect.⁷⁷ Leo Vroman described adsorption of fibrinogen preferentially to tantalum and silicon surface from blood plasma samples.⁷⁷ “In a given solution of protein sample, proteins with low molecular weight arrives at surface first and are displaced by relatively higher molecular weight proteins which arrive later,” which is known as the Vroman effect.⁷⁸ The surface concentration of fibrinogen was found to reach a maximum at an intermediate contact time, indicating that fibrinogen is replaced over time by one or more families of different proteins.⁷⁹ The phenomenon is applicable to many other proteins and is not specific to fibrinogen only,^{80,81} highlighting that plasma proteins compete for the occupation of a surface resulting in competitive adsorption.

The Vroman effect is influenced by different factors such as the temperature, the surface charge, wettability of the surface, plasma dilution and surface chemistry.⁸² Research reveals that fibrinogen adsorbs relatively rapidly to hydrophilic glass surfaces, displacing earlier bound more mobile proteins from the surface.⁸³ Species arriving at the surface are largely limited by diffusion, with smaller molecules diffusing more rapidly. After some time fibrinogen itself is then displaced by larger, usually less abundant but more adhesive proteins such as high molecular weight fibrinogen.^{84,85} Due to the dynamics of this process, and dependent upon the complexity of the protein mixture and concentration, the protein layer may evolve to mediate or hinder cell attachment.⁸⁶ Clearly the ability to define the adsorbed

protein layer composition allows the surface engineer to design specific requirements of materials through the careful consideration of material surface properties.

Different theories have been applied to understand the kinetics of protein adsorption on a biomaterial surface. One of the most important models to understanding the kinetics of protein adsorption is the random sequential adsorption (RSA) model. In this theory, proteins are assumed to be rigid particles that interact only through excluded volume interactions and particles do not overlap on each other.⁸⁷ The particles are assumed to irreversibly adsorb on the surface and thus they do not have translational degrees of freedom.^{88,89} Further contributions to this model came from Van Tassel *et al*, who extended the model to include conformational changes, desorption and adsorption kinetics for mixtures of protein sample.^{90,91} Different models have been proposed by different research groups; however none of the models explains how a single molecular approach can be applied for a variety of protein experimental systems.

1.4.2 Protein adsorption on Nanoparticles

Nanoparticles are known to bind with protein layer and thus forming a coating known as protein corona which plays a vital role in determining the fate of nano-materials inside the body.^{92,93} Lundqvist *et al*; demonstrated that 15 nm diameter silica nanoparticles cause approximately 6 fold higher change in secondary structure than 6 nm particles.⁹⁴ Vertegel *et al*; illustrate that 4 nm diameter silica adsorbed more lysozyme compared to 20 nm and 100 nm silica.⁹⁵ The wettability of the surface has also been shown to promote protein adsorption, Belfort *et al*; reveals that non-polar surfaces destabilize protein adsorption causing conformational changes and strong protein surface interaction.⁹⁶

Albumin and fibrinogen have being shown to undergo greater conformational disordering, by adsorbing onto hydrophobic rather than hydrophilic surfaces using silica particles according to Roach *et al.*⁹⁷ Gessner *et al.*,⁹⁸ used polymethyl-methacrylate (PMMA) to illustrate that decreasing surface hydrophobicity leads quantitatively to decreasing amounts of adsorbed proteins and qualitatively to changes in the obtained protein adsorption patterns. However, the study also clearly demonstrated that not only surface hydrophobicity, but also the functional groups present affect the protein adsorption. Bovine serum albumin (BSA) undergoes conformational changes and denaturation, especially at a hydrophobic interface, eventually leading to irreversible adsorption.⁹⁹

Protein corona binding induces a new local properties onto nano-materials when inserted, to produce a new nano-materials properties that attracts cells as they see the adsorb protein layer.¹⁰⁰ Biological activity determines physiological responses of cell to nano-materials which includes agglomeration, cellular uptake of nano-materials by cell, circulation lifetime, transport and toxicity.¹⁰⁰

1.4.3 Protein Corona

The major classes of molecules taking part in protein corona are blood plasma proteins and minor traces of lipids. The adsorption of these molecule is governed by protein-protein interaction, protein-nanoparticle interaction and binding affinity of proteins to nanoparticles. Protein molecules bind to nano-materials based on their affinity. The affinity towards nano-materials can be either hard or soft. Hard corona proteins are tightly bound to surface and they do not readily de-adsorb from the surface. On the other hand proteins having lower affinity towards surface will bind loosely the surface and thus the protein shows “*soft*” corona. The soft corona can detach from the surface easily. Protein corona can be expressed in terms of time whereby hard corona binds to nano-materials for much longer time while soft corona binds for a lesser time as shown in Figure 1.5

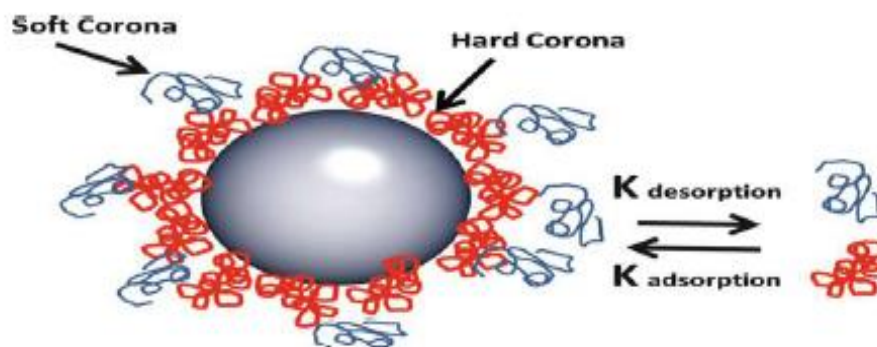


Figure 1.5 Schematic representation of soft and hard protein corona. Red colour represents “hard” corona and blue represent “soft” corona binding proteins.¹⁰¹

Chatelier *et al*, proposed a hypothesis of interaction between proteins with nanoparticles where hard corona proteins interact directly with nano-materials while soft corona proteins interact with hard corona proteins via protein-protein interactions.¹⁰² Studies performed on human adult haemoglobin report minor changes in conformational activity with bare cadmium sulfide (CdS) nanoparticles, where the sulphur atom of cystine residues is the main driver for attachment of haemoglobin and through this interaction 10% reduction in alpha-helix structure is observed.¹⁰³

A valuable tool used for detecting protein surface coating is mass spectrometry (MS). MS is used in industrial and academic purpose for measuring the molecular mass of a sample. The use of MS and bioinformatics techniques reveals a comprehensive detail of cell-surface interactions and interaction of proteins with nanoparticle coating. Kim *et al*, use mass spectrometry in understanding the isolation of cell-surface proteins using silica beads coating.¹⁰⁴

Protein-surface interaction is complex and more research is required to understand complicated features such as protein attachment on different synthetic materials. Different

synthetic materials can be surface tailored with different properties to promote cell development and hence it is important to understand the properties of materials at molecular levels. This thesis will explain the general mechanistic rules of protein adsorption phenomena and how the adsorption influence protein's biological function. Protein adsorption mechanism have been studied and reviewed extensively, but the mechanism still remains unclear. Examples of topics that need further investigation under protein-surface interaction are competitive adsorption of single and multiple proteins, protein adsorption on surface and specific kinetic behaviour of adsorption processes.

1.5 Infrared Spectroscopy

1.5.1 Fourier Transform Infrared (FTIR) for Protein Surface Analysis

FTIR spectroscopy is a measurement of wavelength and intensity of absorption of radiation by a sample. The technique for measuring protein adsorption to surfaces is the use of radiolabelled proteins,¹⁰⁵ which are sensitive but cannot provide quantitative information about protein adsorbed to surfaces. FTIR is used in obtaining information regarding protein adsorption to surfaces.¹⁰⁶ FTIR provide infrared spectra of proteins either in solutions or on surfaces. Infrared spectra can be obtained from small amount of protein samples. Infrared spectroscopy is also used for protein secondary structure analysis. Structural information such as the shape and position of the bands can be used in determining protein conformational changes.

1.6 Stem Cells

Stem cells are undifferentiated cells capable of self-regeneration/ renewal and can differentiate into various cell types.¹⁰⁷ The ability of stem cells to differentiate into specialized cell types make them unique. Stem cells are able to differentiate into all of the 210 tissues types in the body¹⁰⁸ and can be categorized based on their differentiated cell types; *totipotent cells* are produced by the fusion of egg and sperms; *oligopotent cells* can differentiate into only a few cells such as lymphoid or myeloid stem cells; *unipotent cells* can make only one cell type; *multipotent cells* can differentiate into a number of closely related family of cells like mesenchymal stem cells; *pluripotent cells* that can differentiate into numerous cells types.¹⁰⁹

Embryonic stem cells (ESCs) are pluripotent cells. They are derived in the inner cell mass of blastocyst.¹¹⁰ ESCs can differentiate into the three germ layers; mesoderm, endoderm and ectoderm. Embryonic stem cell are unique because they can be maintained and expanded as pure populations of undifferentiated cells for a long period of time, and secondly their pluripotent potential gives them the capacity to generate every cell type in the body.¹¹¹

Adult stem cells (ASCs) are also known as somatic stem cells, meaning ‘cells of the body’. Somatic cells are undifferentiated cells found in tissues or organs that can renew by themselves. Research on adult stem cells shows that bone marrow consists of two types of stem cells namely hematopoietic stem cells (HSCs,) which form all blood cells in the body, can also generate non-hematopoietic cells;¹¹² and bone marrow stromal stem cells (mesenchymal stem cells (MSC). Bone marrow stromal stem cells (BMSCs) make up a small proportion of the stromal cell population in the bone marrow and can generate bone, cartilage, fat, cells that support the formation of blood, and fibrous connective tissue.¹¹³ Bone marrow derived mesenchymal stem cells can differentiate into osteoblasts, adipocytes and

chondrocytes. Stem cells isolated from ASCs are more ethically acceptable while ESCs are severely limited by unresolved ethical issues.

Fibroblast synthesizes ECM, secreting elastin and collagen amongst other proteins. Collagen which is a structure framework for animal tissues and has an important role in wound healing processes.¹¹⁴ The suffix "*blast*" is used in cellular biology to denote a stem cell or a cell in an activated state of metabolism. Fibroblast belongs to the connective tissue family. Fibroblast cell culture systems are optimised to synthesise the ECM and collagen, the structural framework for animal tissues that play a critical role in healing. Fibroblasts also convert to bone cells and into fibroblast cells as shown in Figure 1.6.¹¹⁵

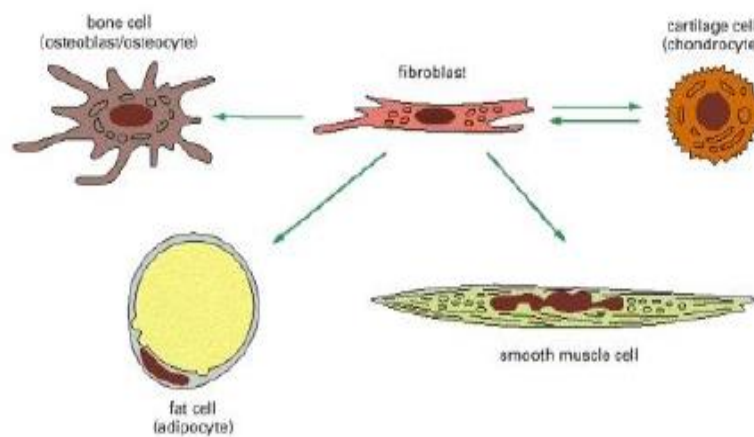


Figure 1.6 Classification of fibroblast cell¹¹⁵

Fibroblasts are important in the wound healing process; when a wound occurs in the body, fibroblasts migrate towards the wound site and deposit large amounts of collagen and ECM thus leading to repair of wounds.¹¹⁵ This makes fibroblast first choice in studying wound healing models. Bucala *et al*, led to discovery of fibrocytes which have beings shown to be similar to fibroblast cells.¹¹⁶

Fibroblasts main function is maintaining structural integrity of the connective tissues by continuous secretion of ECM. The composition of ECM determines the fate of connective tissues and hence differentiation of fibroblast is dependent on ECM.¹¹⁶ Fibroblasts from

different body sites show different characteristics, shown by Castor *et al*, who studied different metabolic differences of mesothelial fibroblast, fibroblast of skin, articular tissues and periosteum.¹¹⁷ Fibroblasts have been demonstrated to be sensitive to a pitted topography with regards to the diameter of the pits which influences the motility and proliferation.¹¹⁸

1.7 Cell Adhesion

Cell-material interaction is a vital topic which has been investigated since the early 1990's where different methods are applied to understand how cells interact with surfaces at different scales (micro or nano). A large number of articles have been published on cell-surface interaction over the past two decades but there is still lack of understanding of the mechanism involved in cell response to the surface. It is widely understood that cells interact with surfaces via pre-adhered protein molecules, although many groups have only investigated the relationship between surface parameters and cell responses. Cell adhesion to biomaterials is affected by their surface properties such as wettability, surface charge, topography (roughness) and chemical functionalities. The choice of cell type on surface properties is important since different cell types may respond in differing ways to surface properties.

Cells bind to the ECM and continue their biological activity such as formation of tissue, migration, signalling, proliferation, etc. The process of cell adhesion is a complex process and different factors are associated with binding cells to surfaces. Factors such as surface energy, binding receptors, availability of cell adhesion molecules are simultaneously required for cell adhesion. Cell adhesion is governed by a specific process involving the recognition of specific membrane binding sites. These binding sites are recognized by adhesive matrix proteins, present on the cell surface, which mediate the binding of cells when adsorbed to the surface.¹¹⁹

Studies related to cell adhesion are fundamentally important to tissue engineers, to understand the molecular mechanisms that govern the process of cell adhesion and the binding of normal cells to substrates. Carnegie *et al*, proposed cell adhesion is governed by a family of specific adhesion proteins (laminin, fibronectin, vitrogen and some collagen) which have a specific binding site containing RGD (arginine-glycine-aspartic) amino acid sequence.¹²⁰ RGD binds to integrin receptors and the essential motif for cell adhesion and was first identified in fibronectin (FN) receptors.¹²¹ The RGD motif plays a crucial role in cell adhesion, cell recognition, delivering drugs at target specific sites in tumor therapy and tissue engineering by recombinant methods.¹²² RGD recognition is widely exploited by pathogen such as viruses and bacteria for gaining entry into host cells by binding to a specific integrin which leads to endocytosis.^{123,124}

Curtis *et al*; proposed that cell adhesion to topography can be defined by a change in cytoskeleton network on 60 nm silica nanoparticles. These changes are stretching of cytoskeleton activity and activation of cell receptors present on the surface.¹²⁵ Cell responses can differ with a change in surface landscape. It is well documented by various research groups that cellular response to nanoscale topographies is more delicate and not strong.¹²⁶ On a nano-topographic surface, cells response depend on protein for its signalling, functions and growth. This process takes more time which can be observed and hence it is easy to understand cell responses to nano-topographic surfaces. Studies on nano-topographic surfaces can offer insight on cell surface binding because changes in the order of sizes of surface and cell and cell-surface interactions can be controlled by controlling various degree of roughness.¹²⁷ This thesis will investigate the effect of cell response on different nanotopography and surface chemistry at different time points to give a better understanding of protein surface interaction.

1.8 Secreted Proteins

The latest novel methodologies in understanding the molecular mechanisms related to the functions of cells can be approached using proteomic and secretome analysis.¹²⁸ Proteomics is defined as the study and function of protein while ‘proteome’ (proteins expressed by a genome) derived by Wilkins *et al*; is defined as the total set of proteins expressed in a cell, tissue or organism.¹²⁹

Proteomic analysis is used to understand how cells proliferate or differentiate into specific lineages. The selection of culture additives conditions is an important factor when culturing cells. Cells require numerous factors in order to sustain their development and growth. *In vivo* these factors are available in the biological fluids surrounding cells, whilst in culture conditions they are commonly added in the form of foetal calf serum. Within serum there are roughly 30-40k of signalling molecules, many of which have characteristics that are little understood. For this reason the common stance for cell culture is to use serum supplemented media (diluted to 5-10%) although some cell types have been shown to be better sustained in media which has been pre-conditioned by cells previously grown in it. During culture cells secrete many factors in order to communicate and mediate their surroundings, and so it is not unexpected that such *conditioned media* presents a better environment compared to that of standard culture media. For example, a study was carried out on self renewal and differentiation of human embryonic stem cells (hESC) on conditioned and unconditioned matrigelTM using mass spectrometry. MatrigelTM is a gelatinous mixture that is secreted by Engelbreth-Holm-Swarm mouse sarcoma cells. Results reveal 80 extracellular proteins in matrix conditioned by hESC.¹³⁰

In an attempt to better understand which factors are important for specific cell types, researchers are turning towards proteome and secretome analysis

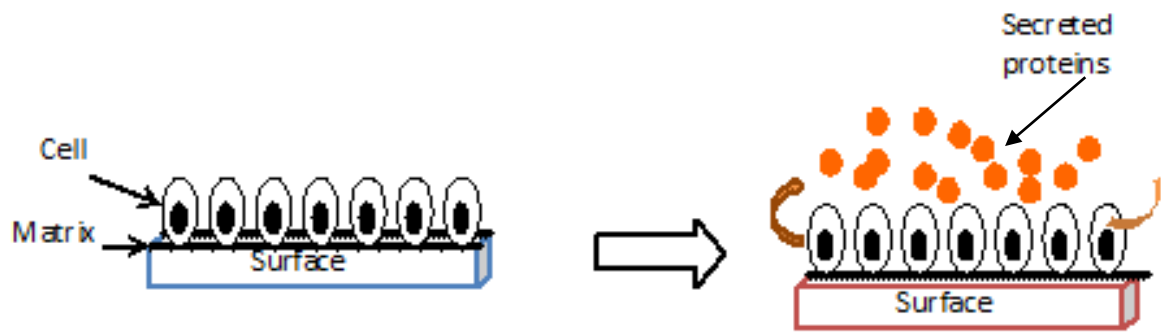


Figure 1.7 Cell secretome in response to local environmental cues

Secreted proteins comprise vital molecules which are encoded by approximately 10% of the human genome¹³¹, Figure 1.7. The secreted molecules mediate intercellular interactions and help in maintenance of homeostasis at the level of organs and systems in the body.¹³² There have been an increasing number of articles published that contains the word “secretome” in their title or abstract according to the Pubmed database since 2000 when Tjalsam *et al* coined this term¹³³ Figure 1.8.

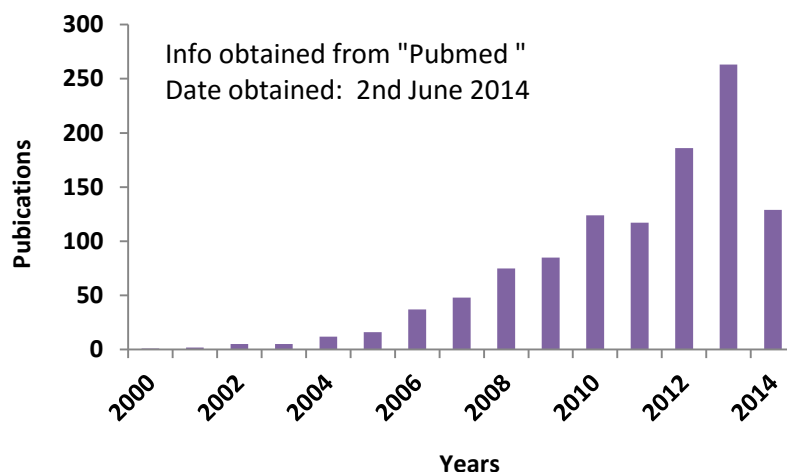


Figure 1.8 An increasing number of publications including the term “Secretome”

Recent advances in secretome studies utilises various cancer cells to discover new biomarkers that be used in cancer diagnostics.¹³⁴⁻¹³⁶ For example, the glioblastoma cell line

from brain tumours in adults has been investigated and the results identify 148 non-redundant proteins using liquid chromatography tandem mass spectrometry (LC-MS/MS).¹³⁷ Stem cells have been used in secretome research to understand cell response, discover potential drug and find therapeutic targets. Few authors (~8) have investigated the secretome of mesenchymal stem cells using different proteomic technologies and techniques to analyse their data.¹³⁸⁻¹⁴⁰ The main reason to investigate stem cell secreted proteins is because the cell culture will closely resemble and mimic the *in vivo* conditions which are more suitable to study and understand how secreted factors affects cell proliferation and differentiation.¹⁴¹ The challenges facing “secretome analysis” are the following: cell culture media, concentration, protein analysis and identification, data interpretations and verification of results. There have been an increasing number of studies over the last decade focusing on secretome characterization from a wide range of biological samples from microorganisms to human embryos and cell lines.^{138, 141}

While investigating secreted molecules from cells the media has to be comparatively less complex in order to observe less abundant species. Cells can be incubated in serum free media for 18 - 48 hrs in order to detect low abundance proteins,¹³⁸ although it is important to investigate the effect of this serum starvation on cell growth before conducting secretome experiments. Wu *et al*,¹⁴² demonstrated that it is possible to adapt the cells by slowly decreasing serum concentration in the culture media. The duration of culture intervals is another important factor that needs to be optimised, and depends on the cell types. The leakage of intracellular proteins from dead cells or cells undergoing apoptosis should be avoided.¹⁴³

Zyonic *et al*, compared the secretome obtained from four primary adipose derived stem cell cultures, in uninduced or adipogenic –induced conditioned media, using 2D gel electrophoresis and MS/MS.¹⁴⁴ Other studies by Lim *et al*¹⁴⁵ and Prowse *et al*¹⁴⁶ examined

conditioned media from mouse embryonic fibroblast feeder layers and human neonatal foreskin cell line. Both reported the identification of several proteins involved in cell growth, differentiation, extracellular matrix formation, and many intracellular proteins were also identified. Chen *et al* demonstrated that growth medium conditioned by murine bone marrow-derived MSC (mesenchymal stem cells) contained high levels of cytokines and was enough to stimulate macrophages.¹⁴⁷ Kim *et al*, reported growth medium conditioned by adipose-derived MSCs contained several collagens, fibronectin and growth factors.¹⁴⁸ All these results demonstrate how secretome studies will be beneficial in identification of biomarkers involved in cell proliferation, differentiation, growth and death. Of particular interest is the control of cells through the use of specific molecules, e.g. directed differentiation.

Many researchers have used different techniques for culturing (and washing) cells from standard cell culture media containing serum, to serum-free media, in order to remove highly abundant serum proteins. The majority of articles published to date have used serum free media or phosphate buffered saline (PBS) to wash their cells, but the incubation times reported differ from one to the next. Higa *et al* washed cells with PBS twice before incubation for 16 hrs with serum-free media (DMEM),¹⁴⁹ whilst Srisomasp *et al* washed cells twice with serum-free media before incubation in serum-free medium for 24 hrs.¹⁵⁰ Lack of standardised procedures may give rise to variations in results due to prolonged cell starvation. Although there are risks involved in washing cells too harshly this process is required in order to remove any contaminants from the previous media. The incubation time should also be considered because it could affect the profile of the secreted proteins. The process of secretome analysis is illustrated in Figure 1.9.

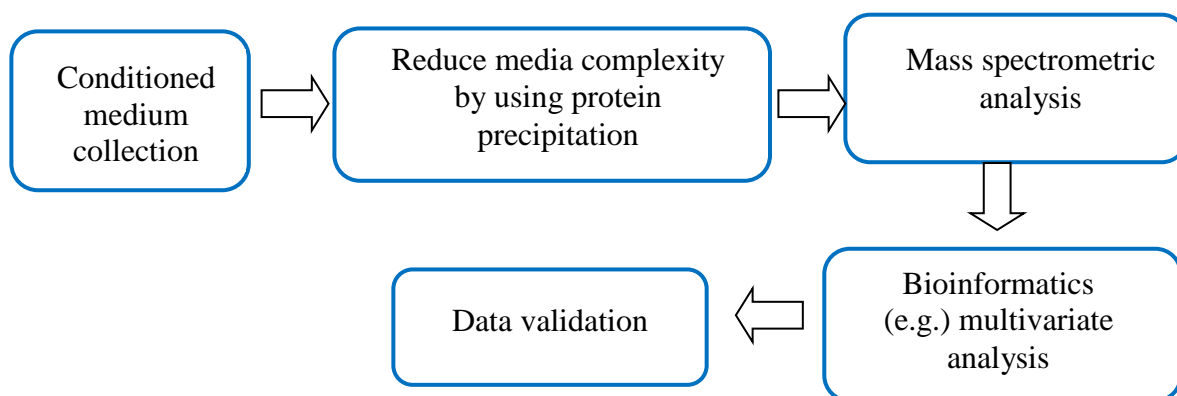


Figure 1.9 Illustration of Secretome analysis

1.9 Analysis of Biological-Surface Interactions

1.9.1 Biological Mass Spectrometry

Mass spectrometry (MS) is used for measuring the compositional molecular mass of a sample.¹⁵¹ Biologists, geologists, physicists and astronomers make use of mass spectrometry to provided information on various sample types/ uses: food contaminations, drug testing and establishing the elemental composition of materials.¹⁵²

A mass spectrometer is a molecular mass-sensitive analytical device which is used to detect charged analytes based on their mass-to-charge (m/z) ratio. The analyte is first ionized from the solid or liquid phase into the gas phase and imparts a positive or negative charge, allowing them to be manipulated using electric or electromagnetic fields. The ions are separated based on their m/z ratio using a mass filter. Common mass filters include ion traps, quadrupoles and time-of-flight. These filters operate on the common principle that an ion will travel through an electromagnetic field following a path dependent upon its m/z ratio; manipulation of that field enables the filtering of particular ions, such that only ions of a specific m/z will pass to the detector.¹⁵³ The biological applications of mass spectrometry

include screening of newborns for metabolic disorders,¹⁵⁴ comparing protein expression levels between cells grown in different media¹⁵⁵ and studying how pharmaceutical drugs are metabolized in- vivo and in-vitro.¹⁵⁶

All mass spectrometers contain at least three major components: an ion source, a mass analyzer, and an ion collection/detection system. The instrument must also be connected to a computer system to process and record the data and a vacuum pump to control the pressure within the mass spectrometer (see Figure 1.10)

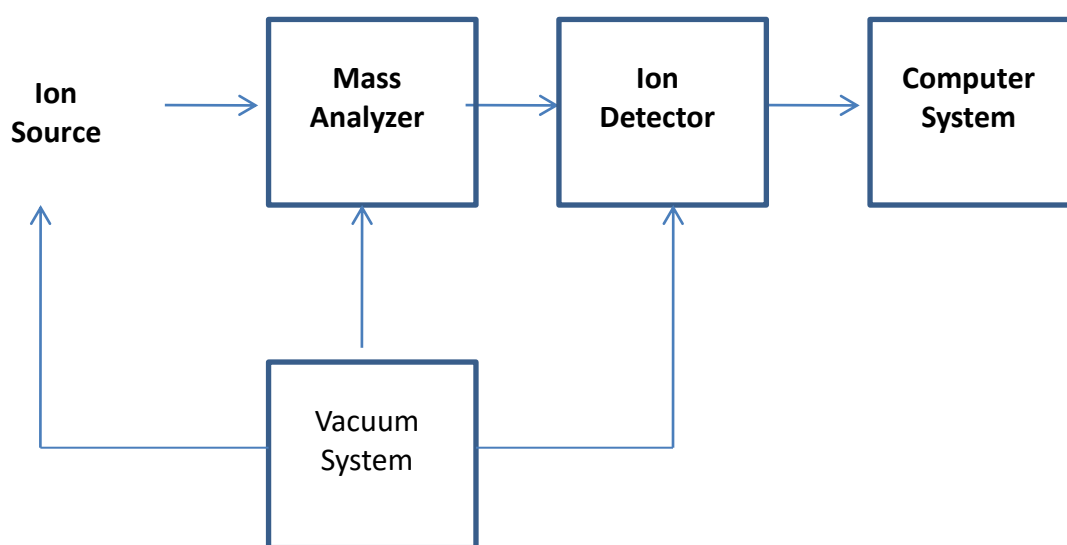


Figure 1.10 Schematic of the basic components of a mass spectrometer

1.9.1.1 Electrospray Ionisation

The first stage of mass spectrometric analysis is ionization. One of the most popular and powerful ionization methods for analysis of biomolecules is electrospray ionization (ESI). The ability to ionize larger molecules using ESI was established by Fenn and Co workers in 1988.¹⁵⁷ The process involves the application of a high voltage to a liquid sample flowing through a stainless steel needle.¹⁵⁸ The sample is ionized when the inlet stream (liquid phase) is emitted from a capillary that has a voltage applied to it. The voltage

produces charged molecules in the sample, which form droplets as they exit the needle in a cone formation. The advantages of ESI are that it is easily interfaced and compatible with liquid chromatography; ionization often results in multiply charged ions and because mass spectrometers measure the mass-to-charge ratio (m/z), having multiple charges increases the range of masses that can be analyzed,¹⁵⁸ Figure 1.11.

Nanospray ionisation is the latest development of ESI, which is used on low amounts and dilute concentration. Peaks generated from nanoscale liquid chromatography typically have higher analyte concentrations compared to microscale liquid chromatography, resulting in greater sensitivity when coupled with nanospray-ESI mass spectrometry.¹⁵⁸ Nanospray uses a small diameter needle to which the high voltage is applied. The major disadvantage of nanospray-ESI is poorer robustness due to the small needle size, which can easily become clogged with particulates, destabilizing the spray.

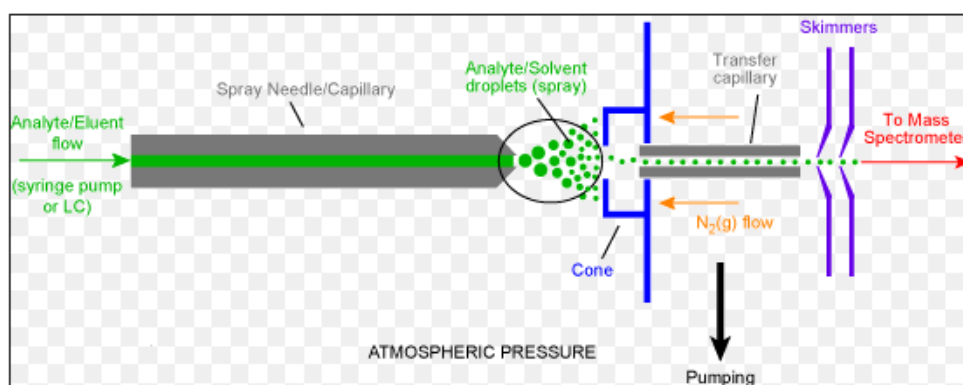


Figure 1.11 Schematic representation of electrospray ionization¹⁵⁸

1.9.1.2 Matrix Assisted Laser Desorption Ionization (MALDI)

MALDI is an ionization technique which is suitable for protein and peptide analysis. MALDI uses pulsed light from a laser source to transfer analytes from a solid surface to the gas phase. Ions generated during this process are transferred from the source into the mass spectrometer under high vacuum. Samples are first mixed with an acidic matrix solution, and

deposited in small droplets onto a metal surface where the spot dries; forming a crystalline structure on the surface of the plate ¹⁵⁹ A pulsed nitrogen laser is directed at various regions of the sample spots on the plate. The energy from the laser excites the matrix molecules, causing a transfer of charge to the analyte and desorption from the plate surface, Figure 1.12.

MALDI typically generates singly charged ions for proteins and peptides, simplifying spectral interpretation compared to ESI. Advantages of MALDI are high sensitivity, high tolerance of salts and impurities, and the ability to analyze an entire plate (up to 384 samples on one plate) in a high-throughput manner using newer instruments with automated data acquisition software.

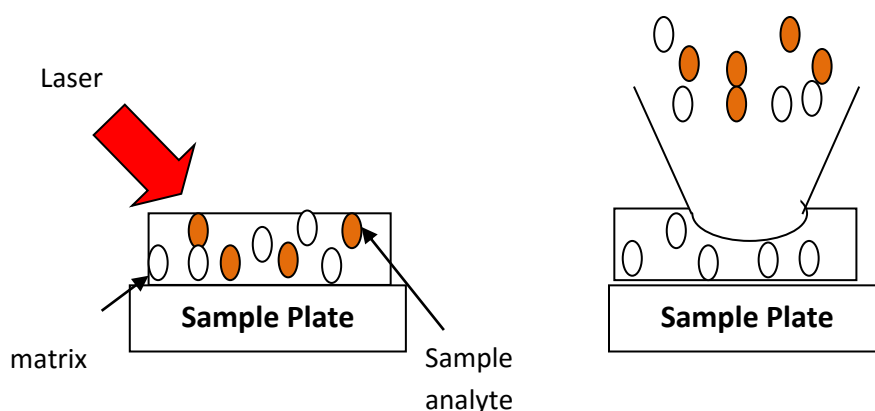


Figure 1.12 Schematic of the matrix assisted laser desorption ionization technique

The introduction of tandem MS instrumentation is the MALDI TOF/TOF, ¹⁶⁰ Two TOF analyzers are separated by a pressurized collision cell, which fragments the precursor ion and then reaccelerates the product ions before they enter the second TOF analyzer. This instrument benefits from both the high mass accuracy associated with TOF mass analyzers and the ability to do collision-induced dissociation.

1.9.2 Multivariate Analysis

Experimental data can only be meaningful by revealing the important information in the data. The introduction of chemometric has provided a useful resource for data analysis. Chemometrics is the application of statistical and mathematical methods to reveal the important information within complex datasets. Chemometric analysis provides vital information from experimental data and the use of multivariate data analysis.

Multivariate analysis (MVA) is the statistical study of the dependence between different variables. MVA reduces the complexity of MS spectra data sets and can be used to interpret slight variance between datasets.. MVA can be used discriminate between samples with respect to single or many multiple differences. In terms of MS data thousands of peaks across the mass range may vary, either singularly if one component changes in quantity from one sample to another, or multiply if this component fragments and interacts to give rise to other spectral components. For example, a cellular signal may give rise to a cascade of events wherein multiple markers are excreted by cells. The advantages of multivariate analysis for these types of data mining are as follows: the extraction of important features is fast and efficient; uses all the information available and is statistically valid. The disadvantages are that the process can be difficult to understand and the method does not aid in data interpretation.¹⁶¹

1.9.3 Statistical Analysis

There are different techniques which have been used to analyse and interpret mass spectrometric data such as principal component analysis (PCA), multivariate curve resolution (MCR), partial least squares (PLS) and mixture models. PCA is a technique used to reduce the dimensionality of dataset consisting of a large number of interrelated variables while retaining as much as possible of the variation present in the dataset.¹⁶²

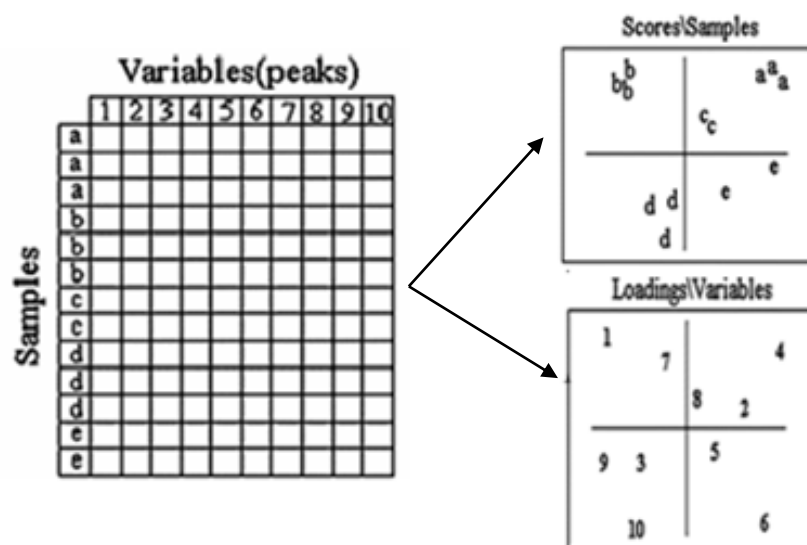


Figure 1.13 Principal component analysis showing scores and loadings.¹⁶⁴

The data shown in Figure 1.13 is placed in an $n \times m$ matrix containing n samples (i.e. spectra) and m variables (peak intensities). The inputs for each cell in the data matrix are the peak areas (or intensities) for a given peak from a given spectrum. The matrix may be pre-processed before the PCA is carried out, which may consist of normalizing the peak intensities. PCA consists of the singular value decomposition of the variance-covariance matrix, yielding the characteristic vectors (eigenvectors) and characteristic roots (eigenvalues) of the variance-covariance matrix.^{163,164} From the example given in Figure 1.13, It can be seen that variables 1 and 7 are positively correlated with samples *b* as seen by their location on the loading plots and score plots. More detailed information on PCA can be found in a review written by Wold¹⁶⁵ and Jackson^{166,167}. The advantages of PCA is to reduce the size of a dataset by making use of all the information available and simplifies chemical interpretation by identifying peaks which likely arise from the same chemical species.

1.10 Aims and Objectives

The aim of this study was to gain an in-depth understanding of cell-material interactions at the protein level, using adsorption assays, conformational assessment and proteomics to interrogate secreted proteins and understand how both the material surface and the cell mediate protein layer composition. Protein adsorption onto model hydrophobic (CH_3) and hydrophilic (OH) surfaces was performed to understand the differing interactions between the two proteins, bovine serum albumin (BSA) and fibrinogen (Fg), and the surface chemistries. Comparison of BSA and Fg, having different size, shapes and dimensions has allowed insight into the importance of surface chemistry with regard to protein size and shape.

Structural differences between proteins adsorbed onto differing surface chemistries have been investigated to understand the impact of surface chemistry on surface-bound protein conformation. Infrared spectroscopy was used for the investigation of the secondary structure of surface-bound proteins. Furthermore topographical effects have been investigated, with and without the effects of surface chemistry. Nano-sized substrates were used to present varying degrees of surface curvature as a model for surface topography. Silica spheres were produced and chemically modified to again compare hydrophilic and hydrophobic surface chemistry effects on protein adsorption. A fluorometric assay was also used to quantitatively assess the amount of protein adsorbed onto surfaces of differing chemistry. UV-Vis spectrometry and fluorometry were used to assess protein surface affinity and the amount of protein adsorbed at surface saturation levels. A comparison of protein adsorption characteristics onto super-hydrophobic and super-hydrophilic surfaces were also examined using this fluorometric assay.

The overall aim of this study was to deepen our understanding of protein and cell biological responses to surface cues at the nano-level, specifically focusing on the impact of

surface chemistry and nanotopography at different nanoscale diameter to understand surface protein interaction at nano-level. The following objectives were studied;

- 1) **Chapter 3** Investigate protein adsorption from single protein solutions (albumin and Fibrinogen) on functionalised silica nanoparticle of 11-215 nm diameters to assess the effect of surface chemistry, nano-curvature at different protein concentrations and conformational changes
- 2) **Chapter 4** Investigate competitive binding of proteins (albumin and fibrinogen) on functionalised silica nanoparticles of 11-215 nm diameters to assess conformational changes based on protein ratio, surface chemistries and size of nanoparticle.
- 3) **Chapters 3 and 4** Identify the conformational changes that take place in single and competitive protein solution.
- 4) **Chapter 5** Establish a methodology for the analysis of cell secretome with respect to surface interaction.
- 5) **Chapter 5** Investigate secretome of fibroblast cell in response to surface physicochemical cues using mass spectrometry.

1.11 References

1. Langer, R. & Vacanti, J. Tissue engineering. *Science*, 260, 920–926 (1993).
2. Langer, R. Selected Advances in Drug Delivery and Tissue Engineering, *J Control Release*, (1999): 62: 7–11.
3. Laurencin, C. T., Ambrosio, A. M., Borden, M. D. & Cooper, J. A. Tissue engineering: orthopedic applications. *Annu. Rev. Biomed. Eng.* 1, 19–46 (1999).
4. Laurencin, C., Khan, Y. & El-Amin, S. F. Bone graft substitutes. *Expert Rev. Med. Devices* 3, 49–57 (2006).
5. Market research website, <http://www.marketresearch.com/Industry-Experts-v3766/Tissue-Engineering-Combination-Cells-Global-680971>; accessed on the 3rd March (2015)
6. Pittsburgh Tissue Engineering initiatives, <http://www.ptei.org/interior.php?pageID=95>, Accessed on the 20th May (2014)
7. Langer, R. & Tirrell, D. A. Designing materials for biology and medicine. *Nature* 428, 487–92 (2004).
8. Fedorovich, N. E. *et al.* Hydrogels as extracellular matrices for skeletal tissue engineering: state-of-the-art and novel application in organ printing. *Tissue Eng.* 13, 1905–25 (2007).
9. Salgado, A. J., Coutinho, O. P. & Reis, R. L. Bone tissue engineering: state of the art and future trends. *Macromol. Biosci.* 4, 743–65 (2004).
10. Karageorgiou, V. & Kaplan, D. Porosity of 3D biomaterial scaffolds and osteogenesis. *Biomaterials* 26, 5474–91 (2005).
11. Anderson, J. A. *et al.* Stem Cell Therapies for Knee Cartilage Repair: The Current Status of Preclinical and Clinical Studies. *Am. J. Sports Med.*, (2014), 42(9):2253–61
12. Grande, D. A., Halberstadt, C., Naughton, G., Schwartz, R. & Manji, R. Evaluation of matrix scaffolds for tissue engineering of articular cartilage grafts. *J. Biomed. Mater. Res.* 34, 211–20 (1997).
13. Speer, D. P., Chvapil, M., Volz, R. G. & Holmes, M. D. Enhancement of healing in osteochondral defects by collagen sponge implants. *Clin. Orthop. Relat. Res.* 326–35 (1979).
14. Nehrer, S. *et al.* Canine chondrocytes seeded in type I and type II collagen implants investigated in vitro. *J. Biomed. Mater. Res.* 38, 95–104 (1997).
15. Kang R, Marui T, Nita I, Georgescu HI, Suh J-K, Robbins RD, Evans CH. Ex vivo gene transfer to chondrocytes in full-thickness articular cartilage defects a feasibility study. *O A Cartilage* 1997; 5:139, 43

16. Kim, W. S. *et al.* Cartilage engineered in predetermined shapes employing cell transplantation on synthetic biodegradable polymers. *Plast. Reconstr. Surg.* 94, 233–7; discussion 238–40 (1994).
17. Niklason, Laura E. Langer, Robert. Prospects for organ and tissue replacement. *JAMA* 285 (2001): 573–576
18. O'Brien, F. J. Biomaterials & scaffolds for tissue engineering. *Mater. Today* 14, 88–95 (2011).
19. Marwick C. Implant Recommendations. *JAMA* (2000): 283:869.
20. Darouiche RO, Treatment of infections associated with surgical implants *N Engl J Med* (2004); 350 :1422-9
21. Macchiarini, P. *et al.* Clinical transplantation of a tissue-engineered airway. *Lancet* 372, 2023–30 (2008)
22. New study reports on early success in a human embryonic stem cell trial to treat blindness [Online] (updated 24th January 2012) [Accessed 18 March 2014], Available at <http://healthland.time.com/2012/01/24/early-success-in-a-human-embryonic-stem-cell-trial-to-treat-blindness/#ixzz26o1cQqKS>.
23. New scientist website [online] (updated 11 April 2011) Available at <http://www.newscientist.com/article/dn16072-woman-receives-windpipe-built-from-her-stem-cells.html> [Accessed 02 April 2014].
24. Mikos, A., McIntire, L., Anderson, J. & Babensee, J. Host response to tissue engineered devices. *Adv. Drug Deliv. Rev.* 33, 111–139 (1998).
25. Schoen FJ, Anderson JM. Host response to biomaterials and their evaluation. In: Ratner BD, Schoen FJ, Lemons JE, editors. *Biomaterials science: an introduction to materials in medicine*, 2nd. San Diego: *Elsevier*; (2004). pp. 293–296
26. Anderson, J. M. & Miller, K. M. Biomaterial biocompatibility and the macrophage. *Biomaterials* 5, 5–10 (1984).
27. Niinomi, M. Biologically and Mechanically Biocompatible Titanium Alloys. *Mater. Trans.* 49, 2170–2178 (2008).
28. Ratner BD, Castner DG. Biomedical surface science: Foundations to Frontiers, *Surface Science* 500, 28–60, (2002).
29. Roach, P., Eglin, D., Rohde, K. & Perry, C. C. Modern biomaterials: a review - bulk properties and implications of surface modifications. *J. Mater. Sci. Mater. Med.* 18, 1263–77 (2007).

30. Yang, Jie An; Lohse, Samuel E; Murphy, Catherine J, Tuning cellular response to nanoparticles via surface chemistry and aggregation *Small*; (8) p. 1642-51 (2014)
31. C. Galli, M.C. Coen, R. Hauert, V.L. Katanaev, *et al. Colloid Surf. B*, 26 (2002), pp. 255–267
32. Webb K, Hlady V, Tresco PA. The relative importance of surface wettability and charged functional groups on NIH 3T3 fibroblast attachment, spreading, and cytoskeletal organization. *J Biomed Mater Res* (1998);41:422–430.
33. Sigal, GB, Mrksich, G.M. Whitesides J. Am. Chem. Soc., 120 (1998), pp. 3464–3473
34. Kidoaki S, T. Matsuda *Langmuir*, 15 (1999), pp. 7639–7646
35. McClary KB, T. Ugarova, D.W. Grainger J. Biomed. Mater. Res., 50 (2000), pp. 428–439
36. Curtis ASG and Clark P, The effects of topographic and mechanical properties of material on cell behaviour. *Crit. Rev. Biocompat.* 5, 343–362, 1997
37. Roach, P., Eglin, D., Rohde, K. & Perry, C. C. Modern biomaterials: a review - bulk properties and implications of surface modifications. *J. Mater. Sci. Mater. Med.* 18, 1263–77 (2007).
38. Darouiche RO, Treatment of infections associated with surgical implants *N Engl J Med* (2004); 350 :1422-9
39. Roach, P., Farrar, D. & Perry, C. C. Surface tailoring for controlled protein adsorption: effect of topography at the nanometer scale and chemistry. *J. Am. Chem. Soc.* 128, 3939–45 (2006).
40. Jansen, E. J. P. *et al.* Hydrophobicity as a design criterion for polymer scaffolds in bone tissue engineering. *Biomaterials* 26, 4423–31 (2005).
41. Mrksich, M. What can surface chemistry do for cell biology? *Curr. Opin. Chem. Biol.* 6, 794–7 (2002).
42. Miller, J. D., Yalamanchili, M. R. & Kellar, J. J. Surface charge of alkali halide particles as determined by laser-Doppler electrophoresis. *Langmuir* 8, 1464–1469 (1992).
43. Murphy, W. L., Mercurius, K. O., Koide, S. & Mrksich, M. Substrates for Cell Adhesion Prepared via Active Site-Directed Immobilization of a Protein Domain. *Langmuir* 20, 1026–1030 (2004).
44. Whiteside, S. P., Lynam, D. R., Miller, J. D. & Reynolds, S. K. Validation of the UPPS Impulsive Behaviour Scale : a Four-factor Model of Impulsivity. 574, 559–574 (2005).
45. Nuzzo, R. G. & Allara, D. L. Adsorption of bifunctional organic disulfides on gold surfaces. *J. Am. Chem. Soc.* 105, 4481–4483 (1983).

46. Porter MD, T. B. Bright, D. L. Allara, C. E. D. Chidsey, *J. Am. Chem. Soc.* (1987), *109*, 3559–3568.
47. Creager SE, G. K. Rowe, *Anal. Chim. Acta* (1991), *246*, 233–239
48. Ulman, A. Formation and Structure of Self-Assembled Monolayers. *Chem. Rev.* *96*, 1533–1554 (1996).
49. Netzer, L. & Sagiv, J. A new approach to construction of artificial monolayer assemblies. *J. Am. Chem. Soc.* *105*, 674–676 (1983).
50. Wasserman, SR, M Y.-T. Tao, G. M. Whitesides, *Langmuir* 1989, *5*, 1074–1087
51. Maoz R, J. Sagiv, *J. Colloid Interface Sci.* 1984, *100*, 465–496.
52. Gun J, R. Iscovici, J. Sagiv, *J. Colloid Interface Sci.* 1984, *101*, 201–213.
53. Gun, J, Sagiv, J, *J. Colloid Interface Sci.* (1986), *112*, 457–472
54. Keselowsky, B. G., Collard, D. M. & García, A. J. Integrin binding specificity regulates biomaterial surface chemistry effects on cell differentiation. *Proc. Natl. Acad. Sci. U. S. A.* *102*, 5953–7 (2005).
55. Toworfe, G. K. *et al.* Effect of functional end groups of silane self-assembled monolayer surfaces on apatite formation, fibronectin adsorption and osteoblast cell function. *J. Tissue Eng. Regen. Med.* *3*, 26–36 (2009).
56. Liu, D. F. *et al.* Periodic ZnO nanorod arrays defined by polystyrene microsphere self-assembled monolayers. *Nano Lett.* *6*, 2375–8 (2006).
57. Mrksich, M, Whitesides, GM *Trends Biotechnol.* (1995), *13*, 228–235.
58. Kapur, R, K. A. Giuliano, *et al.* Streamlining the drug discovery process by integrating miniaturization, high throughput screening, high content screening, and automation on the cell chip TM System. *Biomedical micro devices*, (1999), *2*:99-109.
59. Smith RK, P. A. Lewis, P. S. Weiss, *Prog. Surf. Sci.* (2004), *75*, 1–68.
60. Chaki NK, Vijayamohanan K, *Biosens. Bioelectron.* 2002, *17*, 1–12. A. N. Parikh, D. L. Allara, I. B. Azouz, F. Rondelez, *J. Phys. Chem.* (1994), *98*, 7577–7590.
61. Aswal DK, Lenfant S, D. Guerin, J. V. Yakhmi, D. Vuillaume, *Anal. Chim. Acta* (2006), *568*, 84–108.
62. Bigelow, WC.; Pickett, D.L.; Zisman, W.A; *J. Colloid. Sci.* (1946), *1*, 513-538.
63. Ulmana A; Formation and Structure of Self-Assembled Monolayers, *Chem. Rev.* (1996), *96*, 1533-1554
64. Lundqvist, M., *et al.* Nanoparticle Size and Surface Properties Determine the Protein Corona with Possible Implications for Biological Impacts. *Proc; Natl, Science* *105*, 38, (2008)

65. Mrksich M, Whitesides GM. Using self-assembled monolayers to understand the interactions of man-made surfaces with proteins and cells. *Annu Rev, Biophys Biomol Struct* 1996; 25:55-78.
66. Bain CD, Troughton EB, Tao YT, Evall J, Whitesides GM, Nuzzo RG. Formation of monolayer films by the spontaneous assembly of organic thiols from solution onto gold. *J Am Chem Soc* (1989); 111:321-35.
67. Lundqvist, M., et al. The Evolution of the Protein Corona Around Nanoparticles: A Test Study. *ACS Nano* 59, (2011): 7503-9.
68. Tarrant, R. D. R., et al. Host Cell Protein Adsorption Characteristics during Protein a Chromatography. *Biotechnology progress* 28.4 (2012): 1037-44.
69. Dell'Orco, D., et al. Modeling the Time Evolution of the Nanoparticle-Protein Corona in a Body Fluid. *PLoS ONE* 5.6 (2010).
70. Elofsson U, Paulsson M and Amebrant T; Adsorption of B lactoglobulin A and B : Effects of Ionic strength and Phosphate Ions . *Colloids and Surfaces B: Biointerfaces*. 1997, 8:p163-169
71. Kasemo, B., and J. Gold. Implant Surfaces and Interface Processes. *Advances in Dental Research* 13 (1999): 8-20.
72. Geiger, B., et al. Transmembrane Extracellular Matrix-Cytoskeleton Crosstalk. *Nature Reviews Molecular Cell Biology* 2.11 (2001): 793-805
73. Lundqvist, M., et al. Nanoparticle Size and Surface Properties Determine the Protein Corona with Possible Implications for Biological Impacts. *Proc; Natl, Science* 105.38 (2008): 14265-70.
74. Lundqvist, M., et al. The Evolution of the Protein Corona Around Nanoparticles: A Test Study. *ACS Nano* 5.9 (2011): 7503-9.
75. Lundqvist, M., et al. Nanoparticle Size and Surface Properties Determine the Protein Corona with Possible Implications for Biological Impacts. *Proc; Natl, Science* 105.38 (2008): 14265-70.
76. Vroman L, Adams AL, Fischer GC, Munoz PC. Interaction of high molecular weight kininogen, factor XII and fibrinogen in plasma at interfaces. *Blood* (1980); 55: 156-159
77. Vroman L, *Nature*, (1962), 196, 476-477.
78. Ortega-Vinuesa JL and R. Hidalgo-Alvarez, *Biotechnology and Bioengineering*, (1995), 47, 633-639.
79. Holmberg M and X. Hou, Competitive Protein Adsorption - Multilayer Adsorption and Surface Induced Protein Aggregation, *Langmuir*, (2009), 26, 938-942.

80. Jackson DR, S. Omanovic and S. G. Roscoe, *Langmuir*,(2000), 16, 5449–5457
81. Vroman L and A.L. Adams. Identification of rapid changes at plasma solid interfaces. *Journal of Biomedical Materials Research*, 3(1):43,67, (1969).
82. Kasemo, B., and J. Gold. Implant Surfaces and Interface Processes. *Advances in Dental Research* 13 (1999): 8-20.
83. Geiger, B., *et al.* Transmembrane Extracellular Matrix-Cytoskeleton Crosstalk. *Nature Reviews Molecular Cell Biology* 2.11 (2001): 793-805
84. Vroman L, *Nature*, 1962, 196, 476–477.
85. Ortega-Vinuesa JL and R. Hidalgo-Álvarez, *Biotechnology and Bioengineering*, (1995), 47, 633–639
86. Holmberg M and Hou X, Holmberg M and X. Hou, Competitive Protein Adsorption - Multilayer Adsorption and Surface Induced Protein Aggregation, *Langmuir*, (2009), 26, 938–942
87. Feder, J and I. Giaever (1980) Adsorption of ferritin. *J. Colloid Interface Sci*; 78:144–154.
88. Derand H, Malmsten M. Protein Interfacial Behavior in Microfabricated Analysis Systems and Microarrays. In: Malmsten M, editor. *Biopolymers at Interfaces*.: Marcel Dekker; (1998). pp. 393–413.
89. Schaaf, P., and J. Talbot. (1989). Surface exclusion effects in adsorption processes. *J. Chem. Phys.* 91:4401–4409.
90. Van Tassel, P. R., L. Guemouri, J. J. Ramsden, G. Tarjus, P. Viot, and J. Talbot. (1998). A particle level model of irreversible protein adsorption with a postadsorption transition. *J. Colloid Interface Sci.* 207:317–323.
91. Iordanskii, A. L., V. S. Markin, L. P. Razumovskii, R. Y. Kosenko, N. A., Tarasova, and G. E. Zaikov. .Diffusion model of protein adsorption and effect of protein layer composition on water permeability for ultra filtration membranes. *Desalination*. 104: (1996).113–118
92. Derand H, Malmsten M. Protein Interfacial Behavior in Microfabricated Analysis Systems and Microarrays. In: Malmsten M, editor. *Biopolymers at Interfaces*. Marcel Dekker; (1998). pp. 393–413
93. Iordanskii, A. L., V. S. Markin, L. P. Razumovskii, R. Y. Kosenko, N. A., Tarasova, and G. E. Zaikov..Diffusion model of protein adsorption and effect of protein layer composition on water permeability for ultra filtration membranes. *Desalination*. 104: (1996)113–118.
94. Lundqvist, M., *et al*; Protein Adsorption onto Silica Nanoparticles: Conformational Changes Depend on the Particles' Curvature and the Protein Stability (2004)

95. Vertegel A; Silica Nanoparticle Size Influences the Structure and Enzymatic Activity of Adsorbed Lysozyme, *Langmuir*, (2004), 20 (16), pp 6800–6807
96. Anand G, Sharma S, Dutta AK, Kumar SK, Belfort G. Conformational transitions of adsorbed proteins on surfaces of varying polarity, *Langmuir* (2010);26:10803
97. Roach P, Farrar D, Perry CC, Surface Tailoring for Controlled Protein Adsorption: Effect of Topography at the Nanometer Scale and Chemistry, *Journal of the American Chemical Society* 2006 128(12), 3939-3945
98. Gessner A., *et al*, Nanoparticles with Decreasing Surface Hydrophobicities: Influence on Plasma Protein Adsorption. *International Journal of Pharmaceutics*, vol. 196, no. 2, (2000). pp. 245-249
99. Green R, M. Davies, C. Roberts and S. Tendler, *Biomaterials*, (1999), 20, 385—391
100. Iordanskii, A L., V. S. Markin, L. P. Razumovskii, R. Y. Kosenko, N. A., Tarasova, and G. E. Zaikov. Diffusion model of protein adsorption and effect of protein layer composition on water permeability for ultra filtration membranes. *Desalination*. (1996) 104:113–118
101. Frochot C., Stasio B.D., Vanderesse R., Belguy M.-J., Dodeller M., Guillemin F., Viriot M-L, Barberi-Heyob M. Interest of RGD-containing linear or cyclic peptide targeted tetraphenylchlorin as novel photosensitizers for selective photodynamic activity. *Bioorg. Chem.* (2007);35:205–220.
102. Chatelier, RC. and A. P. Minton. Adsorption of globular proteins on locally planar surfaces: models for the effect of excluded surface area and aggregation of adsorbed protein on adsorption equilibria. *Biophys. J.* (1996).71:2367–2374
103. Cedervall T, I. Lynch, S. Lindman, T. Berggard, E. Thulin, H. Nilsson, K. A. Dawson and S. Linse, *Proceedings of the National Academy of Sciences*, (2007), 104, 2050–2055.
104. Kim, Y. *et al*. Use of colloidal silica-beads for the isolation of cell-surface proteins for mass spectrometry-based proteomics. *Methods Mol. Biol.* 748, 227–41 (2011).
105. Bale MD, Mosher DF, Wolfarht L, Sutton RC. Competitive adsorption of fibronectin, fibrinogen, immunoglobulin, albumin and bulk plasma proteins on polystyrene latex. *J Colloid Interface Sci* (1988);125:516.
106. Feng L, Andrade JD. Surface atomic and domain-structures of biomedical carbons observed by scanning tunneling microscopy (STM). *J Biomed Mater Res* (1993);27(2):177
107. Chamberlain, G., Fox, J., Ashton, B. & Middleton, J. Concise review: mesenchymal stem cells: their phenotype, differentiation capacity, immunological features, and potential for homing. *Stem Cells* 25, 2739–49 (2007).

108. Shambloott, MJ., Edwards, B.E. & Gearhart, J.D., Pluripotent Stem Cells in Principles of Tissue Engineering, eds. Robert P. Lanza, Robert Langer & Joseph Vacanti, *Academic Press*, San Diego, (2000) pp. 369-381.
109. Hubner, K *et al* .Derivation of oocytes from mouse embryonic stem cells. *Science* 300, 1251-1256 (2003)
110. Gordon Keller. Embryonic stem cell differentiation: emergence of a new era in biology and medicine.
111. Puri, M.C. & Nagy, A. Concise review: Embryonic stem cells versus induced pluripotent stem cells: the game is on. *Stem Cells* 30, 10-4 (2012).
112. Lee PH, Park HJ, Bone marrow derived mesenchymal stem cell therapy as a candidate disease-modifying strategy in Parkinsons disease and multiple system *atrophy.j CLIN Neurol* (2009);5:1-10
113. Stem cell information website (2006), <http://stemcells.nih.gov/info/basics/basics4.asp>
114. Green AM, Jansen JA, van der Waerden JPCM, von Recum AF. Fibroblast response to microtextured silicone surfaces: texture orientation into or out of the surface. *J Biomed Mater Res* (1994);28:647-53.
115. Fibroblast and their transformation Textbook, Fibroblasts and Their Transformations: The Connective-Tissue Cell Family. (2002)
116. Bucala R., Spiegel L.A., Chesney J., Hogan M. and Cerami A. Circulating fibrocytes define a new leukocyte subpopulation that mediates tissue repair. *Mol. Med.* (1994) 1: 71–81.
117. Castor CW, Prince RK, Dorstewitz EL Characteristics of human “fibroblasts” cultivated in vitro from different anatomical sites. *Lab Invest* (1962)11:703–713.
118. Berry et al; The influence of microscale topography on fibroblast attachment and motility; *Biomaterials*, (2004);25(26):5781-8.
119. Webb HK, V. Boshkovikj, C.J. Fluke, V.K. Truong, J. Hasan, V.A. Baulin, R. Lapovok, Y. Estrin, R.J. Crawford, E.P. Ivanova; Bacterial attachment on sub-nanometrically smooth titanium substrata: *Vol. 29, Iss. 2*, (2013).
120. Carnegie JA, Cabaca O. Extracellular matrix composition and resilience: two parameters that influences the in vitro migration and morphology of rat inner cell mass-derived cells. *BiolReprod* (1993): 48: 287-299.
121. Pierschbacher MD., Ruoslahti E. Cell attachment activity of fibronectin can be duplicated by small synthetic fragments of the molecule. *Nature*.(1984);309:30–33.

122. Fen Wang, Yuanyuan Li, Yingqiang Shen, Anming Wang, Shuling Wang, and Tian Xie; The Functions and Applications of RGD in Tumor Therapy and Tissue Engineering; *Int J Mol Sci.* (2013); 14(7): 13447–13462.
123. Bergelson, J.M., Shepley, M.P., Chan, B.M., Hemler, M.E., Finberg, R.W., (1992). Identification of the integrin VLA-2 as a receptor for echovirus *Science* 255, 1718–1720.
124. Bergelson, J.M., Shepley, M.P. *et al.* Identification of the integrin VLA-2 as a receptor for echovirus *Science* ; (1992); 255, 1718–1720.
125. Adam Curtis and Chris Wilkinson: Topographic control of cells; *Biomaterials* 18 (1997) 1573-1583.
126. Bettinger CJ, R. Langer and J.T. Borenstein; Engineering substrate Micro- and nanotopography to control cell function; (2009); 48 (30): 5406-5415.
127. Dalby MJ, Riehle MO, Johnstone H, et al ; In vitro reaction of endothelial cells to polymer de mixed nanotopography. *Biomaterials* (2002); (14)2945-54
128. Roubelakis MG, Trohatou O, Anagnou NP; Amniotic fluid and amniotic membrane stem cells: marker discovery, *Stem cells Int.*, (2012) , p. 107836
129. Wilkins, M. R. *et al.* Progress with proteome projects: why all proteins expressed by a genome should be identified and how to do it. *Biotechnol. Genet. Eng. Rev.* 13, 19–50 (1996).
130. Hughes, Christopher, Mass Spectrometry-Based Proteomics Analysis of the Matrix Microenvironment in Pluripotent Stem Cell Culture; (2012)
131. Pavlou P, Diamandis EP, The cancer cell secretome: a good source for discovering biomarkers? *J. Proteomics* 73 (2010) 1896–1906
132. Skalnikova, H; Motlik, J; Gadher, Suresh Jivan; Kovarova, Hana Mapping of the secretome of primary isolates of mammalian cells, stem cells and derived cell lines, *Proteomics*, (2011), 11, 4, 691-708,
133. Tjalsma, A. Bolhuis, J.D. Jongbloed, S. Bron and J.M. van Dijk, Signal peptide-dependent protein transport in *Bacillus subtilis*: a genome-based survey of the secretome, *Microbiol Mol Biol Rev* 64 (2000), pp. 515–547
134. Pavlou, MP., Diamandis, E.P., The cancer cell secretome: a good source for discovering biomarkers? *J. Proteomics* (2010), 73, 1896–1906.
135. Xue, H., Lu, B., Lai, M., The cancer secretome: a reservoir of biomarkers. *J. Transl. Med.* (2008), 6, 52.
136. Maurya P., Meleady, P., Dowling, P., Clynes, M., Proteomic approaches for serum biomarker discovery in cancer. *Anticancer Res.* (2007), 27, 1247–1255.

137. Polisetty, Ravindra V.; Gupta, Manoj Kumar; Nair, Sudha C.; *et al.* Glioblastoma cell secretome: analysis of three glioblastoma cell lines reveal 148 non-redundant proteins *Journal of Proteomics*; (2011);74(10):1918-25
138. Sze, S. K., de Kleijn, D. P., Lai, R. C., Khia Way Tan, E. *et al.*, Elucidating the secretion proteome of human embryonic stem cell-derived mesenchymal stem cells. *Mol. Cell. Proteomics* (2007), 6, 1680–1689.
139. Sarojini, H., Estrada, R., Lu, H., Dekova, S. *et al.*, PEDF from mouse mesenchymal stem cell secretome attracts fibroblasts. *J. Cell. Biochem.* (2008), 104, 1793–1802.
140. Estrada, R., Li, N., Sarojini, H., An, J. *et al.*, Secretome from mesenchymal stem cells induces angiogenesis via Cyr61. *J. Cell. Physiol.* (2009), 219, 563–571.
141. Chris P, Kulasingam V, Chris R. Smith, Karen Reckamp, Goodglick L, and Eleftherios P.; Identification of five candidate lung cancer biomarkers by proteomics analysis of conditioned media of four lung cancer Cell Lines *Mol Cell Proteomics* (2009), 8: 2746-2758.
142. Hsin-Yi Wu, Ying-Hwa Chang, Yu-Chen Chang, Pao-Chi Liao. Proteomics analysis of nasopharyngeal carcinoma cell secretome using a hollow fiber culture system and Mass Spectrometry. *Journal of Proteome Research* (2009), 8 (1), 380-389
143. Skalnikova, H, *et al.* Mapping of the secretome of primary isolates of mammalian cells, stem cells and derived cell lines, *Proteomics*, (2011), 11, 4, 691-708.
144. Zvonic S, Lefevre M, Kilroy G *et al.* Secretome of primary cultures of human adipose-derived stem cells: Modulation of serpins by adipogenesis. *Mol Cell Proteomics* (2007);6: 18–28.
145. Lim JW, Bodnar A. Proteome analysis of conditioned medium from mouse embryonic fibroblast feeder layers which support the growth of human embryonic stem cells. *Proteomics* (2002);2:1187–1203.
146. Prowse AB, McQuade LR, Bryant KJ *et al.* A proteome analysis of conditioned media from human neonatal fibroblasts used in the maintenance of human embryonic stem cells. *Proteomics* (2005); 5: 978–989
147. Chen L, Tredget EE, P.Y.G. Wu and Y. Wu, Paracrine factors of mesenchymal stem cells recruit macrophages and endothelial lineage cells and enhance wound healing, *PLoS one* 3 (2008), pp.1886.
148. Kim WS, B.S. Park, J.H. Sung, J.M. Yang, S.B. Park, S.J. Kwak and J.S. Park, Wound healing effect of adipose-derived stem cells: a critical role of secretory factors on human dermal fibroblasts, *J. Dermatol. Sci.* 48 (2007), pp. 15

149. Higa, L. M., Caruso, M. B., Canellas, F., Soares, M. R. et al., Secretome of HepG2 cells infected with dengue virus: implications for pathogenesis. *Biochim.Biophys.Acta* (2008),1784, 1607–1616.
150. Srisomsap, C., Sawangareetrakul, P., Subhasitanont, P., Chokchaichamnankit, D. et al., Proteomic studies of cholangiocarcinoma and hepatocellular carcinoma cell secretomes. *J. Biomed. Biotechnol.*, (2010), 437143
151. Jackson JE, 1991. A user guide to principal components. *Wiley New York*
152. Fred W McLafferty FT: Interpretation of mass Spectra, 4 edn: *University Science Books*; (1993)
- 153 .Chace DH, T. A. Kalas, E. W. Naylor; The application of tandem mass spectrometry to neonatal screening for inherited disorders of intermediary metabolism, *Annu. Rev. Genomics Hum. Genet.* 3, 17–45, (2002)
- 154.Gygi SP, B. Rist, T. J. Griffin, J. Eng, R. Aebersold; Proteome analysis of low-abundance proteins using multidimensional chromatography and isotope-coded affinity tags, *J. Proteome Res.* 1, 47–54. (2002)
155. Mano M, Goto J Biomedical and biological mass spectrometry, *Anal. Sci*; (2003) 19, 3–14
156. Fenn JB, M. Mann, C. K. Meng, S. F. Wong, C. M. Whitehouse; Electrospray ionization for mass spectrometry of large biomolecules, *Science* 246, 64–71, (1989)
157. James P, ed. (2001) *Proteome Research: Mass Spectrometry*, Springer-Verlag, Germany
158. University of Britol, School of Chemistry website, accessed on the 7th June 2014 .
<http://www.bris.ac.uk/nerclsmf/techniques/hplcms.html>
159. Nissom PM, Sanny A, Kok YJ, Hiang YT, Chuah SH, Shing TK, Lee YY, Wong KT, Hu WS, Sim MY et al: Transcriptome and proteome profiling to understanding the biology of high productivity CHO cells. *Molecular biotechnology* (2006), 34(2):125-140
160. Medzihradszky KF, J. M. Campbell, M. A. Baldwin, A. M. Falick, P. Juhasz, M. L. Vestal, A. L. Burlingame The characteristics of peptide collision-induced dissociation using a high-performance MALDI-TOF-TOF tandem mass spectrometer, *Anal. Chem*; (2000). 72, 552–558.
161. Jackson JE, (1991).A user guide to principal components. *Wiley New York*
162. Belu A, Castner DJ, David G, Time of flight secondary ion mass spectrometry techniques and applications for the characterization of biomaterial surfaces. *Biomaterials*, (2003), 24, 21, 3635-3653

163. Wagner MS, Graham DJ, Ratner BD *et al.* Maximizing information obtained from secondary ion mass spectra of organic thin films using multivariate analysis. *Surf Sci* (2004); 570:78-97.
164. Graham DJ *et al.*, Information from complexity: Challenges of TOF-SIMS data interpretation, *Applied Surf. Science*, 6860–6868, (2006)
165. Wold S, K. Esbensen, P. Geladi, *Chemom. Intell. Lab. Syst.* 2 (1987) 37–52.
166. Jackson, JE; Principal Components and Factor Analysis: part 1 – principal analysis; *J. Qual. Technol.* 12 (1980) 201–213.
167. Jackson, JE A Users's guide to principal components, *John Wiley & Sons Inc.*, New York, (2004)

CHAPTER 2

Materials and Methods

2.1 Self-Assembled Monolayer Formation using Silanes

Self assembled monolayers (SAMs) can be defined as ordered molecular assemblies formed spontaneously by the adsorption of a molecule with a specific affinity to a substrate.¹ SAMs have been widely used in a multitude of applications such as nanotechnology, analytical chemistry and biotechnology^{2,3} due to their unique properties such as low cost, speed and ease of preparation, and high quality of order that can be obtained in terms of functionalities and structural properties. SAMs have been used to fabricate biologically functional materials for the fundamental study of the biointerfaces and interfacial phenomena. SAMs have been used to tailor surface chemistry.⁴⁻⁷ The most frequent studied SAMs are thiols on gold and silane-based monolayers.⁸

Silanization of surfaces was first established by Malmqvist *et al.*⁹ Silane terminated monolayers show a higher physical and chemical stability with highly ordered and well-packed monolayers being obtained. Silanes are used for SAMs due to covalent siloxane bonds between the molecules and hydroxyl-terminated substrates compared to pseudo – covalent surface – Au bonds of thiols. Silane can hydrolyze to form covalent bonds Si-O substrate on OH groups or in the presence of water.¹⁰

Materials: 3-Aminopropyltriethoxysilane (APTES) and tetraethoxysilane (TEOS) were obtained from Struktol, methyltriethoxysilane (MTEOS) from Acros Organics, succinic anhydride from Aldrich chemical Co., toluene 99.5% (500 ml) from Fisher Scientific and circular coverslips (12 mm diameter) were obtained from Thermo scientific. All chemicals were used as received.

Circular coverslips and bottles were rinsed in toluene solution and air dried before use. Coverslips were handled with forceps to prevent contaminants on the surface. Chemically defined surfaces were prepared using silane-based monolayers: tetraethoxysilane (TEOS) to give hydroxyl (OH), chlorotrimethylsilane (MTEOS) to give methyl (CH₃) and

3-aminopropyltriethoxysilane (APTES) to give terminal (NH₂) at the surface. Circular coverslips were incubated in 5 mL toluene solution with 50 µL of silane: APTES, MTEOS and TEOS. Bottles were sealed with parafilm and left for 24 hours at room temperature. After 24 hours, the coverslips were removed and rinsed with toluene, air dried and placed in a clean container. For OH surfaces, coverslips were further acid washed in 0.1 M HCl in distilled water (dH₂O) for 1 min. The substrates were stored for less than 3 days before analysis and before use. Surfaces were characterised using contact angle measurement and infrared spectroscopy which are in good agreement with those reported by other researchers.¹¹⁻¹³ Table 2.1 and 2.2 shows the functional monolayer used.

Table 2.1 Self assembled monolayers (SAMs) Chemistries and Formula			
Labels	Name	Formula	Functional groups
APTES	3-Aminopropyltriethoxysilane	H ₂ N(CH ₂) ₃ Si(OC ₂ H ₅) ₃	NH ₂
TEOS	Tetraethoxyorthosilane	Si(OC ₂ H ₅) ₄	OH
MTEOS	Methyltriethoxysilane	CH ₃ Si(OCH ₃) ₃	CH ₃
TESPSA	3-Triethoxysilylpropyl succinic anhydride	(C ₂ H ₅ O)Si(CH ₂) ₃ C ₄ H ₄ O ₃	COOH

TESPSA coated surfaces were prepared as shown in Figure 2.1. Firstly, 50 µL of APTES was pipetted into a clean glass bottle, coverslips were added, and the bottle was sealed with parafilm and left for 24 hours at room temperature. Coverslips were removed rinsed in toluene and air dried. This gave rise to the amine functional monolayer which is further reacted with succinic anhydride to form a COOH terminal group. The coverslips were then placed in 0.1 M succinic anhydride (Aldrich chemical Co.) in toluene (~5 mL). The bottle was sealed with parafilm and left for further 24 hours. Coverslips were removed, rinsed with toluene, air dried and placed in a clean container for further analysis. The method for

preparing carboxylic acid functionalized SAMs is summarized in Figure 2.1 The silanization process was performed at room temperature.

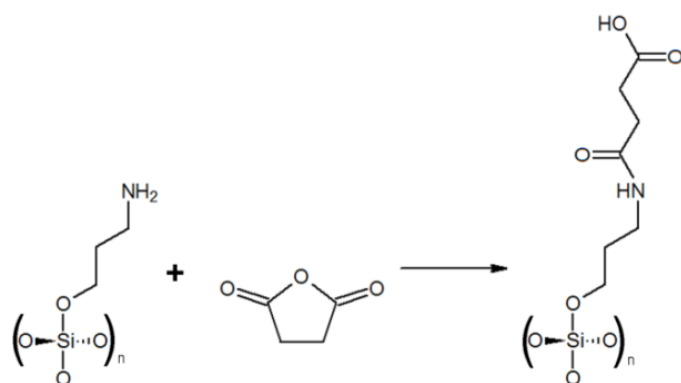
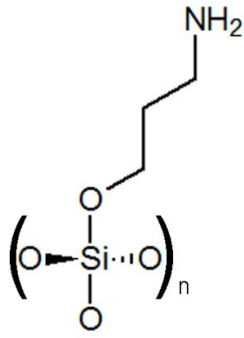
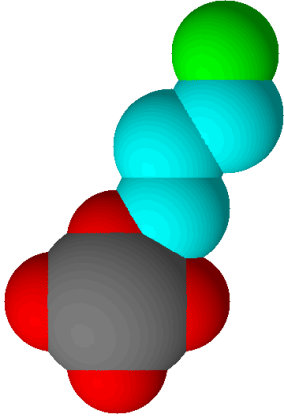
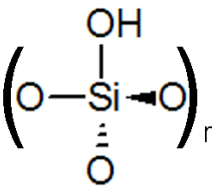
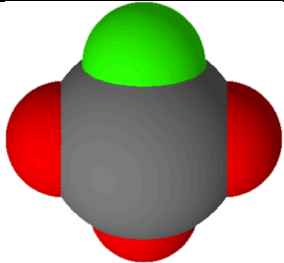
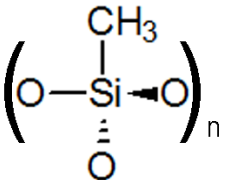
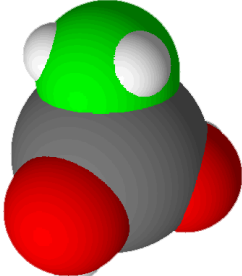
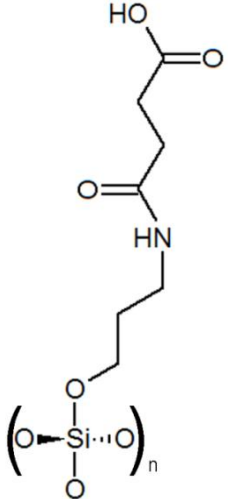
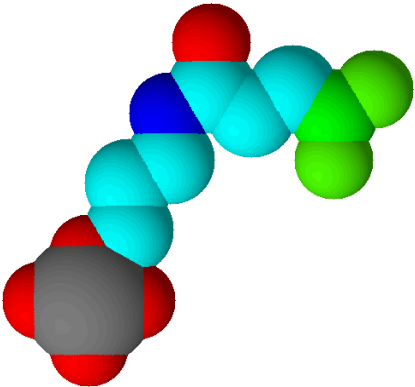


Figure 2.1: Process of preparing the carboxylic acid functionalized SAMs

Table 2.2 Chemical Structure of Chemistries		
Name/ Functional group	Chemical Structure	Models 3D space-filing representation
3-Aminopropyl - silane		
Hydroxyl - silane		
Methyl - silane		
1,4-carboxy-4-aminobutyl-N-3-aminopropyl - silane		

2.2 Preparation of Silica Spheres

The Stöber process¹⁴ was used to prepare mono-disperse silica spheres of varying sizes. The preparation of mono-disperse silica particles was carried out by the hydrolysis and condensation of TEOS in a mixture of water and ammonia which is used as a catalyst. The Stöber process is the most effective and simplest way to prepare a mono-disperse spherical particles of controlled size. Monodisperse colloidal silica particles with uniform size, shape and composition have wide applications in industries such as catalyst, ceramic and pharmacy.

Materials: Tetraethyl orthosilicate (TEOS) purchased from (Sigma Aldrich), Ethanol (Fisher), water bath, distilled water, thermometer and hot plates. All chemicals used as received without further purification.

Batches of silica spheres were prepared by the addition of ammonia to ethanol solutions of tetraethoxysilane (Aldrich) to make a total volume of 100 mL, specific sphere sizes and preparation conditions are given in Table 2.3. The following procedure was followed: (Solution A), 21.6 cm³ of diluted ammonia and water with 80.0 cm³ of ethanol (Solution B) 22.3 cm³ of TEOS diluted with 76.6 cm³ of ethanol. Solution A was slowly mixed with solution B over 2-3 minutes as shown in Figure 2.2. Each solution was heated to 50°C and mixed with stirring for 80 minutes on hot plates, then allowed to mature for 1 day at room temperature and isolated by centrifugation and washing with ethanol thrice, sonicated and centrifuge several times. Dynamic light scattering (DLS) was used to measure particle size distribution of each sample prepared. After DLS, the remaining samples were centrifuged (Beckman model J2-21) overnight at 15,000 rpm, the liquid supernatants was removed while precipitates were speed dried for 12-18 hours.

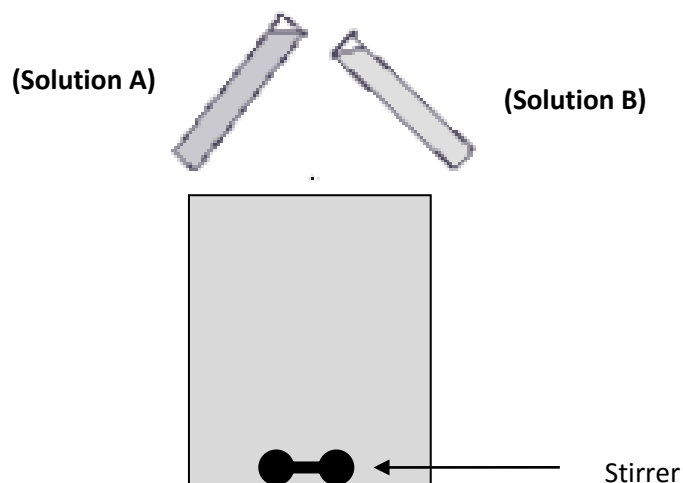


Figure 2.2 Preparation of monodispersed silica nanoparticles (a) ammonia was diluted with water (b) TEOS diluted with ethanol. Both (a) and (b) were heated to 50°C in a water bath.

Table 2.3 Reaction conditions for Silica sphere preparation			
Sphere radius/nm	TEOS/M	Vol. 35% ammonia solution/cm³	Vol. diluted with water/cm³
11 ± 0.13	0.20	2.0	100
64 ± 1.76	0.60	6.0	100
105 ± 1.36	1.00	10.0	100
215 ± 2.88	3.00	30.0	100

Error shown are standard deviation, where n =3

2.2.1 Preparation of Functionalised Silica Spheres

Chemically defined silica particles were prepared using silane (SAMs) as described in section 2.1.1; Dried silica spheres, 3 g were sonicated in toluene (20 mL) for 10 mins to disperse. Silane chemistries, shown in table 2.2 were added dropwise on the silica spheres and left at room temperature for 24 hours. The liquid supernatant was emptied into a clean bottle, toluene (20 mL) was added, centrifuged for 4 hours at 15,000 rpm and again the liquid

supernatant removed. The cycle was repeated thrice. Silica spheres were freeze dried using a 50 mL bottle (Nalgene).

Methyl terminated spheres were produced by silylating hydroxyl-terminated particles with a vast excess of chlorotrimethylsilane (98% Aldrich) in toluene (Fisher), stirring overnight and washing in toluene. Amine terminated spheres were produced by silylating hydroxyl-terminated particles with a vast excess of 3-aminopropyltriethoxysilane (Thermofisher) in toluene (Fisher) stirring overnight and washing in toluene.

Carboxylic acid terminated spheres were produced by silylating hydroxyl-terminated particles with a vast excess of 3-aminopropyltriethoxysilane (Thermo Fisher) in toluene (Fisher) stirring overnight and washing in toluene; then freeze dried. Further, 0.1 M succinic anhydride (Aldrich chemical Co.) in toluene was added to the particles and left overnight to be washed in toluene. The surface chemistry of the silica particles as prepared was analysed by infrared spectroscopy using a NicoletThermo iS50 FTIR spectrometer fitted with a GoldenGate attenuated total reflection (ATR) accessory (Thermo Nicolet). Spectra were recorded at 4 cm^{-1} resolution, averaging 265 scans. Surface wettability was characterised by measuring equilibrium water contact angles using a home built instrument.

Close Packed Assembly of Silica Nanoparticles

2.2.2 Piranha Etching

Close packed assemblies of silica nanoparticles were achieved on 18 x 18 coverslip (Fisher). Coverslips were first cleaned with piranha solution for cleaning glass surface. Piranha etching is a solution of conc. sulphuric acid (H_2SO_4) and 30% w/v hydrogen Peroxide (H_2O_2 , Fischer). Three parts of acid was taken in a cleaned beaker and one part of peroxide was added to the acid from the side of the beaker and mixed gently using a glass rod. Cover slips were added one by one to the piranha solution and a gentle swirl was given.

The solution was left for 30 min and coverslips were transferred to a clean beaker via forceps for washing. Cover slips were washed 4 times with distilled water; after washing, cover slips were stored submerged in distilled water in a new beaker and dried under nitrogen before use.

Close packed silica nanoparticle arrays as shown in Figure 2.3, were prepared by the air-water interface packing method. Silica nanoparticles (powder form) were sonicated in toluene (99% Sigma Aldrich) at a concentration of 0.5 g silica to 5 mL toluene. The silica dispersion was sonicated for 2 hours and centrifuged at 800 rpm for 5 min to allow any particle clusters/aggregates to settle. A volume of 50 μ L of supernatant liquid were pipetted onto a clean coverslip and viewed using light microscopy to check for any remaining aggregates. Repeated sonication and centrifuging was carried out until no aggregate was observed. A large glass Petri plate filled with distilled water was taken and a cover slip (18 x 18 mm (Fisher)) was suspended on the edge in such a way that it interfaced with air and water. A volume of 60 μ L of silica dispersion was pipetted onto the coverslip which served as a connection medium at the air-water interface. A thin layer of silica nanoparticles was formed on top of the distilled water. Samples were collected on 18 x 18 mm coverslips, by scooping with the help of forceps. Samples were allowed to dry at 25°C overnight. Closed-packed silica nanoparticles were analysed using scanning electron microscopy (SEM), at an acceleration voltage of 15 kv, using a benchtop Hitachi 3000 SEM

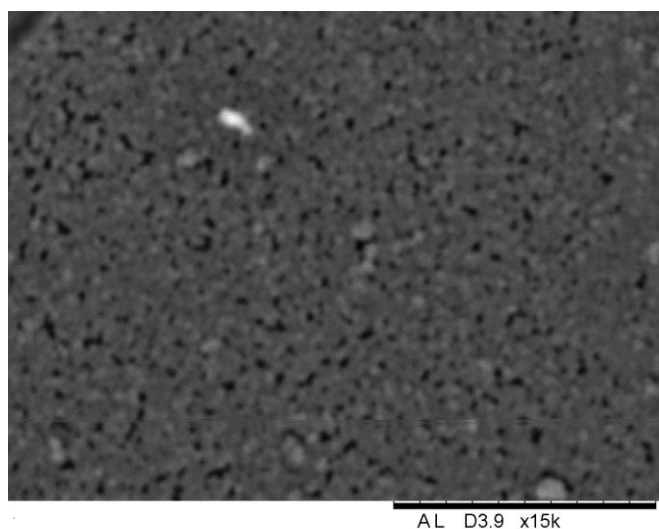


Figure 2.3 SEM image of closed packed amine -modified silica nanoparticle. Scale bar of 5 μ m

Surface/ Materials Characterisation

2.3 Contact Angle Measurements

Contact angle measurements reveals microscopic characteristics of a material such as surface roughness, surface energies of the material and surface coating. Static water contact angle measurement is the most preferable method used to measure a material's degree of wettability because it is quick, economical and a relatively simple technique.¹⁵ Wettability is a property of surfaces that controls many phenomena such as the biological response to materials.¹⁶ Wetting is described as the contact angle between a liquid and a solid is zero or so close to zero that the liquid spreads easily over the solid surface. On the other hand, non-wetting can be described when the liquid tends to ball-up and run off the surface easily. The size of the water contact angle is attributed to either a hydrophilic surfaces (surfaces with polar groups such as alcohol (OH) or hydrophobic surfaces non-surfaces such as methyl (CH₃).¹⁷ As shown in Figure 2.4, drop of liquid on a flat surface will modify its shape under the pressure of the different surface and interfacial tensions until it reaches an equilibrium as described by the Young equation (equation 2.1).

$$\frac{\gamma_{SV} - \gamma_{SL}}{\gamma_{LV}} = \cos\theta_T \quad \text{Equation (2.1)}$$

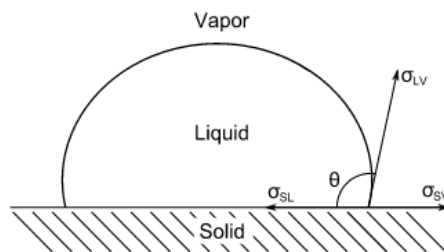


Figure 2.4 Young equations showing the relationship between three interfacial tensions.

‘ γ ’ is the surface energy and the three interfaces are ‘SV’ the solid vapour interface, ‘SL’ the solid liquid interface, ‘ θ ’ the contact angle and ‘LV’ the liquid vapour interface. Depending on the three interfaces, the liquid may spread or remain spherical when in contact with a flat surface. A high water contact angle of $> 90^\circ$ means the surface is hydrophobic while a small water contact angle of $< 90^\circ$ where water will spread on the surface indicates a hydrophilic surface. Wenzel established a theoretical model describing the effect of surface roughness on liquid contact angle.¹⁸ The surface roughness is defined as ‘ r ’ which is defined as the ratio between the actual surface area and geometric projected surface area. The young equation is then modified to form equation 2.2;

$$\frac{r(\gamma_{SV} - \gamma_{SL})}{\gamma_{LV}} = \cos\theta \quad \text{Equation (2.2)}$$

Contact angle data can be obtained with low price instruments and with simple techniques. Water contact angle measurements on SAMs were conducted at room temperature using the sessile drop method. The angle between the baseline of the drop and the tangent at the drop boundary is measured, Figure 2.4. The experimental setup for contact angle is shown in Figure 2.6

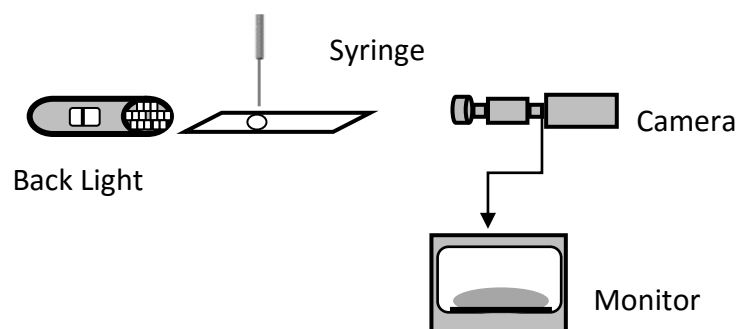


Figure 2.5 Schematic of contact angle measurement

The wettability of surfaces prepared in this study was characterised by taking images of 5 μ L distilled water droplet equilibrium contact angles. A home built system was used consisting of a sample holder, long working distance microscope and image analysis system. The wettability of the silica spheres were measured using dried functionalised silica spheres. The dried samples (0.05 g) were placed on a flat cover slip. Droplets were applied to the surface by a microsyringe with a hydrophobised needle and images were taken immediately to eliminate drying effects. The angles were measured using the ImageJ plugin, and any given contact angle reported in this thesis is an average of at least 3 drops. The mean value of the measurements was calculated.

2.4 Fourier Transform Infrared Spectroscopy (FTIR)

Infrared spectroscopy can be used to investigate molecular vibrations and to identify compounds. IR is used to obtain information on the presence of functional groups in a molecule by identifying characteristics peaks corresponding to the stretching of chemical bonds or bending /deformation. The advantage of FTIR is that the signal level at the detector is higher and automatically improves the signal-to-noise ratio at any point in the spectrum. The single reflection attenuated total reflectance (ATR) technique is a widely used FTIR sampling tool to identify chemical compounds because it gives rapid analysis of samples, improves sample-to-sample reproducibility, and is also non-destructive.¹⁹ FTIR-ATR has become a standard technique in polymer research for investigation of the chemical composition and structure of surfaces because it produces excellent data quality coupled with high reproducibility.

Attenuated total reflectance (ATR) has been widely used to study protein adsorptions to biomaterial surfaces. The Thermo Nicolet iS50-FTIR spectrometer (Thermo Scientific) was used for obtaining all the infrared spectra of samples, fitted with a broad range DTGS

(deuterated triglycinesulfate) detector which provides high signal to noise infrared spectroscopy from 4000 cm^{-1} to 100 cm^{-1} controlled via Thermo Scientific OMNIC software.

Silica spheres were incubated in protein solutions (BSA and Fg) to allow proteins to adsorb on the substrate surface. The spheres were removed by centrifugation, sample allowed to dry and analysed immediately. Protein bound to the surface of silica spheres was analysed using a Single bounce diamond ATR accessory equipped with a DLaTGS-detector. Background spectra of protein-free buffer were recorded averaging 265 scans immediately before sample spectra were taken. Spectra were recorded between 4000 and 400 cm^{-1} at an optical resolution 4 cm^{-1} .

ATR crystal is also known as *internal reflection element* (IRE). The most common ATR crystals used is Zinc Selenide (ZnSe), Diamond and Germanium. Zinc selenide is relatively low cost and can be used for analysing liquids, gels and non-abrasive pastes but it scratches easily. Diamond is used for ATR crystals due to its properties of durability.

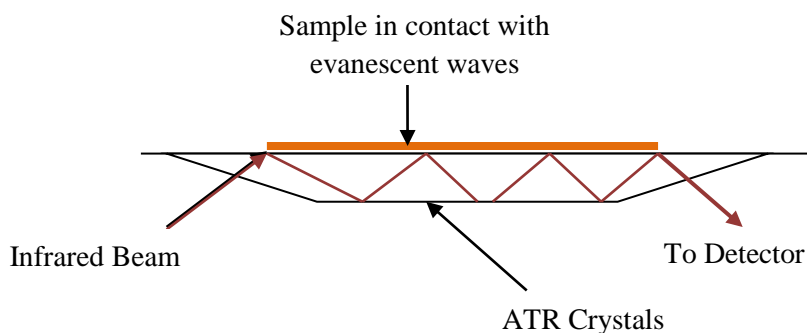


Figure 2.6 Schematic of an attenuated total reflectance crystal.

ATR works by directing the IR beam into a crystal of relatively higher refractive index. The infrared beam reflects from the internal surface of the crystal and creates an evanescent wave; Figure 2.6. The depth of penetration (d_p) is defined as the distance at which the evanescent waves drop. The depth of penetration can be calculated using equation 2.3;

where ‘ λ ’, is the wavelength of the light, θ is the angle of incidence of the IR beam relative to a perpendicular from the surface of the crystal. n_1 is the refractive index of the ATR crystals (IRE) and n_2 refractive index of external medium.

$$d_p = \frac{\lambda}{2\pi\sqrt{n_1^2 \sin^2 \theta - n_2^2}} \quad \text{Equation (2.3)}$$

2.4.1 Diffuse Reflectance Infrared Fourier Transform Spectroscopy (DRIFTs)

Diffuse reflectance infrared Fourier transform spectroscopy (DRIFTs) is a technique used for measurement of powders and rough surfaces, by collecting and analysing scattered infrared energy as seen in Figure 2.7. The advantage of DRIFT is the ability to analyse samples with minimum preparation. DRIFTs analysis of powders or foam is carried out by focusing infrared light onto the sample and the scattered light is collected and is transmitted to the infrared detector.

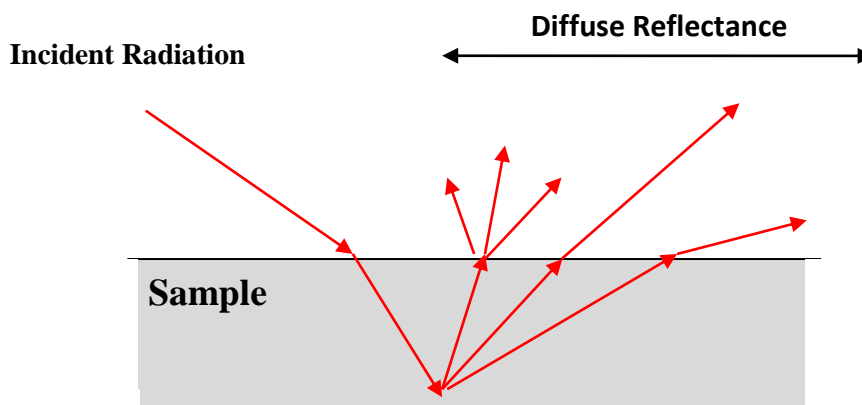


Figure 2.7 Principle of Diffuse Reflectance Infrared Fourier Transform Spectroscopy

The theory of diffuse reflective from powdered samples has been developed by Kubelka and Munk, equation 2.4.

$$f(R) = \frac{(1-R)}{2R} = \frac{k}{s} \quad \text{Equation (2.4)}$$

The theory provides a relationship between reflectance and concentration where R is the absolute reflectance of the layers, s is the scattering coefficient, k is the molar absorption coefficient.²⁰ The measurement of DRIFTS was performed with Alpha's FT-IR spectrometer (Bruker Optic, Germany), equipped with a KBr beamsplitter and DLaTGS detector. The diffuse reflectance sampling accessory including of a macro sample cup (10 mm diameter, 2.3 mm deep). The system was operated using OPUS® version 6.5 software. All the reflection spectra were recorded at 100 scans in 4000–600 cm⁻¹ range with a resolution of 4 cm⁻¹ at a room temperature (25°C).

2.4.2 x-ray Photoelectron Spectroscopy (XPS)

XPS is one of the techniques used for surface analysis and it is widely used in industrial applications for polymer surface modification. It is not complicated and rather easy to use. The sample is irradiated with mono-energetic x-rays causing photoelectrons to be emitted from the sample surface. An electron energy analyzer is used to establish the binding energy of the photoelectrons, which can be used to determine chemical state of an element in a sample as shown in Figure 2.8.

The XPS analysis was performed using the Theta Probe instrument equipped with a monochromated AlK α source (Thermo Scientific) in NEXUS. A pass energy of 200 eV and a step size of 1.0 eV was employed for all survey spectra while a pass energy of 40 eV and a step size of 0.1 eV was used for high resolution spectra of the elements of interest. A flood gun was used for charge compensation. This was carried out using the UK National XPS

facility at Newcastle University; NEXUS Samples were under the guidance of Prof P Cumpson.

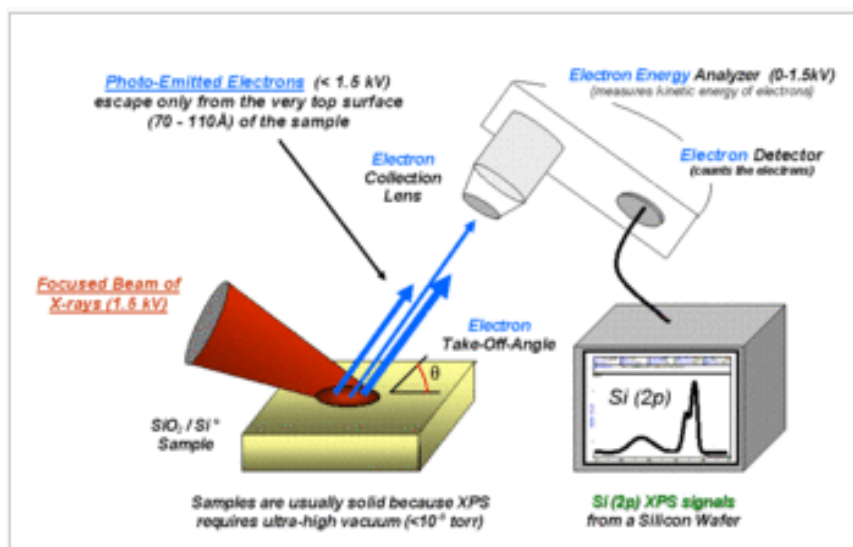


Figure 2.8 Component of XPS system ²¹

2.5 Scanning Electron Microscopy (SEM)

A scanning electron microscope uses a focused beam of high-energy electrons to generate a variety of signals at the surface of solid specimens. When a sample is bombarded with electrons, it emits secondary electrons and x-rays. The intensity of the secondary electrons is detected to generate a high resolution surface image. SEM is one of the more widely available tools in surface analysis and it is often used to measure surface topography.²²

High resolution (1.5 nm) field emission is controlled by the electron beam diameter, the Hitachi S4500, offering incredibly high magnification, high resolution imaging as well as more standard low magnification, high depth-of-field imaging. SEM can produce very high-resolution images of a sample surface, revealing details at less than 1 to 5 nm in size, due to its narrow electron beam. SEM micrographs have a large depth of field yielding a characteristic three-dimensional appearance useful for understanding the surface structure of

a sample. Therefore, resolution, magnification and depth of field are important elements of SEM. A beam of electrons is passed on the sample at the top of the microscope by an electron gun; as shown in Figure 2.9. The electron beam follows a vertical path through the microscope. The beam passes through electromagnetic fields and lenses, which focus the beam down towards the sample. Electrons (Auger, secondary and primary) and x-rays are ejected from the sample when the beam hits the sample. Data were collected over a selected area of the surface of the sample, and images are generated in two monitor that displays spatial variations. Areas ranging from approximately 1 nm to 5 nm in width can be imaged in a scanning mode using conventional SEM techniques (magnification ranging from 20X to approximately 30,000X, spatial resolution of 50 to 100 nm).

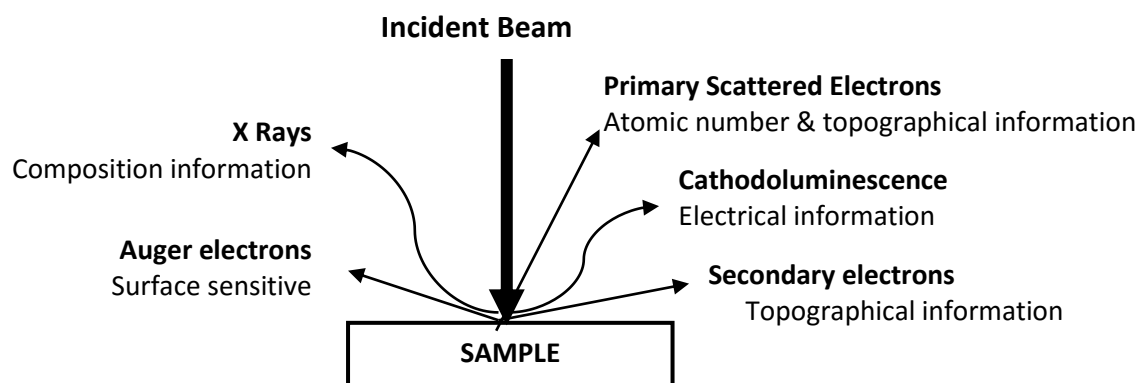


Figure 2.9 Structure of Scanning Electron Microscope

2.6 Dynamic Light Scattering (DLS)

DLS is also known as photon correlation spectroscopy (PCS). It is a powerful light scattering technique for studying the properties of suspensions and solutions of colloids and biological solutions that is non-invasive and non-destructive. DLS has been designed for the rapid measurement of particle size and size distribution. It can be used to determine the radius of small particles in Brownian motion in a solution whereby small particles move faster than large particles; the intensity of the scattered light gives greater variation in small particle compare to large particles. Silica nanoparticle size distribution was determined using Malvern Zetasizer Nano- ZS. The instrument is reliable and accurate in measuring particles size. It can measure the particles of size in the range 0.6 nm-6µm. The principle that governs the measurement of particle size is described by Gregory (2006).²³

Water molecules are in continuous thermal motion due to the kinetic energy, which results in constant collisions with particle suspended in water. The kinetic energy is passed onto the particles and it results in Brownian motion.

At a given time, t, the particle will move a certain distance, x, from its starting point which is expressed in equation 2.5

$$x = \sqrt{Dt} \quad \text{Equation (2.5)}$$

Where D is the diffusion coefficient of the particle, t is the time

The Diffusion coefficient of a particle is described by the Stokes-Einstein equation shown below;

$$D_h = \frac{K_B T}{3\pi\eta d_t} \quad \text{Equation (2.6)}$$

Where 'k_B' is the Boltzmann constant, 'T' is the absolute temperature, 'η' is dynamic viscosity, 'd_t' is the translational diffusion coefficient and 'D_h' is the diameter.

Silica Particles were analysed using a Malvern Instruments, Zetasizer Nano-ZS. The instrument can measure the particles size of ranging from 0.3 nm to 10 μm . The instrument was used in the automeasure mode at 90°, the pinhole size being varied within limits conducive to an acceptable scattering intensity. A volume of 50 μL of silica particle in buffer-free solution sonicated for 30 mins and was measured at room temperature.

2.7 Proteins Studied

2.7.1 Bovine Serum Albumin

Bovine serum albumin is used for conjugation in antibody production and has an important role in storage and transport of energy.^{24,25} Having a molecular weight of 66 kDa with a plasma concentration of approximately 50 mg mL^{-1} , an isoelectric point of 4.8. BSA is the most abundant protein in blood plasma and plays a vital role in the disposition and transportation of various molecules. BSA is single polypeptide chain which is made up of 583 amino acids, shown in Figure 2.10. The estimated structure of alpha helices is 54-68% while beta sheet constitute of 16-18%. BSA was as a model protein due to its solubility, stability and similarity to human serum albumin (HSA).²⁶ BSA and HSA display approximately 76% sequence homology; with 3D structure which is similar to HSA.^{27, 28}

Materials: BSA was purchased from Sigma Aldrich and used without further purification. BSA solution was prepared by dissolving BSA (0.005 g) in phosphate buffer solution (5 mL) at a concentration of 1 mg/mL , and then stored in the refrigerator at 4°C .

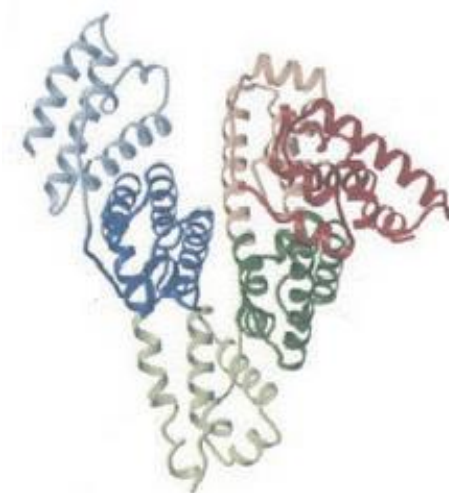


Figure 2.10 Three-dimensional structure of BSA²⁷

2.7.2 Fibrinogen

Fibrinogen is a protein produced by the liver; which is present in the human blood plasma at a concentration of 2.5 mg/mL. Fibrinogen is vital for wound healing, inflammation and other biological functions. Fibrinogen triggers foreign body reactions following an implantation of prosthesis.²⁹ Fibrinogen is an elongated molecule with approximate molecular dimensions of $9 \times 47.5 \times 6$ nm and molecular weight of 350 kDa.³⁰ Fibrinogen was diluted with phosphate buffer solution at different concentration Fibrinogen is a large, complex, fibrous glycoprotein with three pairs of peptide chains, A α , B β , and γ , as shown in Figure 2.11.

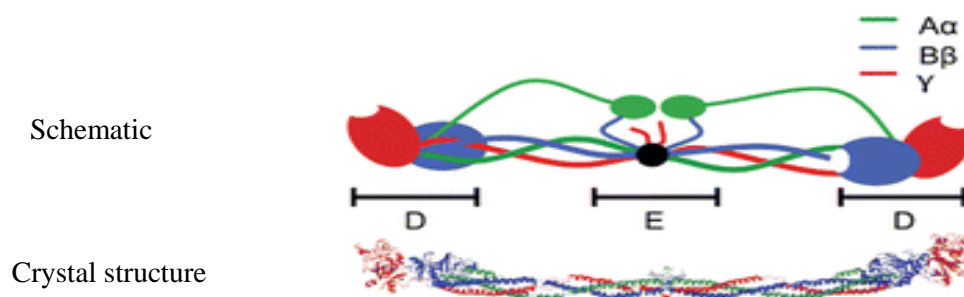


Figure 2.11 Structure of Fibrinogen molecule with colour scheme (bottom) and schematic (Top). A α – chain green, B β -chain in blue, γ -chain in red, fragment D and E.³¹

2.8 Protein Assays

2.8.1 Bicinchoninic acid Assay (BCA) Protein Quantification

BCA (also known as sodium salt) reacts with protein to reduce copper ion Cu^{2+} to cuprous ion Cu^+ under alkaline condition to produce a purple end product with maximum absorbance at 562 nm. The BCA assay has advantages over other protein quantification kits because it is a more sensitive, faster assay with less variation between different proteins. Studies have shown the effectiveness of the assay based on temperature³², elimination of foreign substances³³ and high sensitivity³⁴. The staining method requires calibration which involves preparation of a standard curve using a serial dilution series (0.1-1.0 mg/mL) of a known protein sample concentration, i.e. see BSA and Fg standard curves in Figure 2.12.

Chemically modified silica particles were measured into an eppendorf tube, 1 mL buffer was added to each eppendorf tube, sonicated for 2-3 hours until it turns to milky a solution. A volume of 50 μL of silica solution were pipetted into 96 well plates containing BSA and Fg solutions in the range of 8-900 $\mu\text{g mL}^{-1}$ were placed in an eppendorf tube; 250 μL of working reagents (BCA assay) was added to the sample in 96 well plate, the well plate was mixed on a plate shaker for 30 seconds and incubated for 30 min at 37°C. After incubation, the plate was cooled to room temperature and the absorbance was measured at 562 nm using a UV-VIS spectrophotometer.

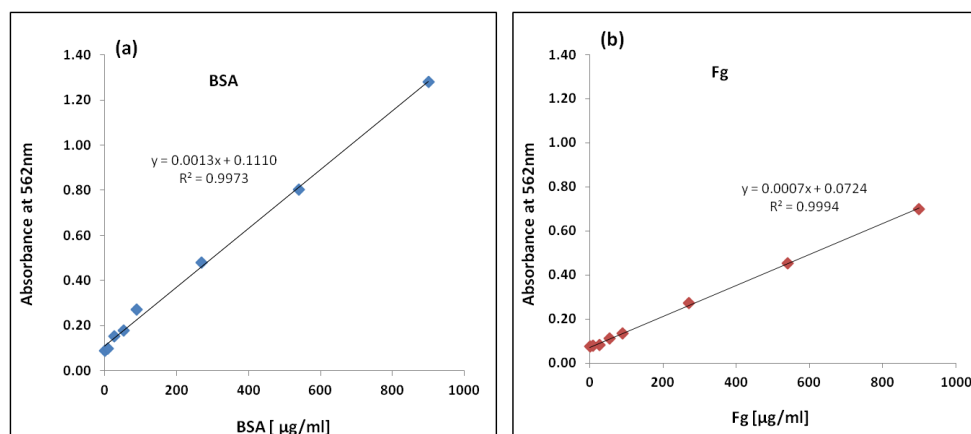


Figure 2.12 Standard curves of (a) bovine serum albumin and (b) fibrinogen at 562 nm

The standard curve shows an increase in absorbance as shown in Figure 2.12 (a) and (b). As the protein concentration increases for both proteins (BSA and Fg), the absorbance increases. The correlation coefficient, R^2 value for BSA is approximately 0.998 while Fg is 0.999. Both values show the line fits the data very well.

2.8.2 Fluorescence Assay for Competitive Protein Quantification

Solutions of HSA and Fg were prepared at concentrations of 15 $\mu\text{g/mL}$ and 0.8 $\mu\text{g/mL}$ respectively in PBS. 8.87 μL of Fg and 249.6 μL of HSA were diluted each into separate vials of 415 μL of PBS, before combining these together. 500 μL of the functionalised silica particles (made at a calculated concentration to present 1 m^2mL^{-1}) were added to 160 μL of the mixed protein solution and vortexed stirred. After each time point samples were centrifuged and 50 μL supernatant was pipetted into a fluorescence microplate, being read on a Biotek Synergy 2 Multimode Reader at an excitation of 485 nm/emission 540 nm (HSA) and excitation of 528 nm/emission 590 nm (Fg). Amplification of the signal was optimised via the electrical gain function on the plate reader. This was carried out for each batch sample set, with calibration curves being taken to assess sensitivity levels and linearity. Samples were freeze dried and stored at -20°C).

Protein Analysis

2.9 Ultraviolet-Visible (UV-Vis) Spectroscopy

UV-Vis spectroscopy is the measurement of light absorption at different wavelengths when it passes through a sample. The ability of a molecule to absorb ultraviolet and visible light is associated with the transitions between electronic energy levels. The absorption of ultraviolet light corresponds to the excitation of outer electrons in the molecules.

Most absorption spectroscopy of organic compounds is based on transitions of n or π electrons to the π^* orbitals. The absorption peaks for transitions fall in the region of the

spectrum (200-700 nm). Transitions occurring above 200 nm involve the excitation of electrons from n and π orbitals.

The Beer-Lambert Law is used to determine the concentration of sample by measuring the absorbance at various wavelengths. The Beer-Lambert law state that the proportion of light absorbed is independent of the incident intensity, being proportional to the number of absorbing molecules, given by;

$$A = \log_{10} \left(\frac{I_o}{I} \right) \quad \text{Equation (2.7)}$$

Beer – Lambert Law is the relationship between absorbance and concentration.

$$\text{Since } A = \epsilon c l$$

$$\text{Therefore,} \quad \log_{10} \left(\frac{I_o}{I} \right) = \epsilon c l \quad \text{Equation (2.8)}$$

where ' I ' and ' I_o ' are the intensities of the transmitted and incident beams respectively, ' ϵ ' is the molar extinction coefficient or molar absorptivity constant, ' c ' is the concentration of adsorbing species and ' l ' is the length of solution the light passes through and ' A ' is the absorbance.^{35,36}

Protein (BSA and Fg) serial dilutions were performed as follows; the experiments were conducted at room temperature and ambient pressure. Silica spheres were sonicated in PBS to form homogenous dispersions prior to the addition of proteins for a certain period of time. With continuous stirring, the silica suspension was added to each protein solution to give a substrate surface area per solutions of 1 m²/ml. Solutions were stirred for one hour and left for a further 2 hours to minimise shearing effects that might occur due to stirring. Solutions were centrifuged after two hours to induce sedimentation of the silica. Blank experiments with protein only were carried out to rule out the possibility of protein sedimentation.

The residual protein concentration in solution was determined using Synergy 2 Multi-mode microplate reader (Biotek) UV Vis spectrometer using 96 well plates, measuring absorbance at 562 nm. Calibration was carried out using a series of protein solutions of known concentration. The experiment was performed in triplicate and results were analysed using Microsoft Excel.

2.10 Protein Adsorption

Protein Adsorption on solid surface is a complex phenomenon and is a process that is required in several applications such as food industries, nanotechnology and biomaterial. The Langmuir isotherm model^{37, 38} describes the dependence of the surface coverage of an adsorbent and is given by the equation's 2.9- 2.11

$$\frac{Q}{Q_m} = \frac{K_d C}{1 + K_d C} \quad \text{Equation (2.9)}$$

The Langmuir model describes the relationship between the adsorbate surface concentration ' Q ' and the concentration in the phase adjacent to the surface ' C ', ' Q_m ' is the maximum adsorbate binding capacity and ' K_d ' is a binding affinity constant. Some of the assumptions of this model are not necessarily true for protein adsorption. According to the Langmuir isotherm, the adsorption of molecule ' A ' onto the surface sites ' S ', an equilibrium constant ' k ' governs the chemical reaction for adsorption, which is represented as $A + S \rightleftharpoons AS$; The equilibrium constant for this reaction is given by

$$k = \frac{[AS]}{[A][S]} \quad \text{Equation (2.10)}$$

[A] is the concentration of A while [S] and [AS] are the two dimensional concentrations, expressed in units as mol/cm². [AS] is also proportional to the surface coverage, θ , surface with unattached site (not adsorbed) is represented as (1- θ). Therefore from equation 2.10,

$$k = \frac{\theta}{[A](1-\theta)} \quad \text{Equation (2.11)}$$

[A] expressed as C, while $\theta = \frac{Q}{Q_m}$; which gives the equation 2.9

The main assumptions for this model are that, the surface has a specific number of sites where solute molecules can be adsorbed and the surface is completely homogeneous. There are other models such as Freundlich isotherms.³⁹ The Langmuir isotherm is preferable used due to its simplicity and correlates well with experimental data as shown in experimental sections in chapter three and four.

2.10.1 Secondary Protein Structure

Understanding the biological function of an adsorbed protein molecule requires some control of the direction of the protein at the interface. Several experimental studies on protein adsorption found some conformational changes in protein molecules that occur upon adsorption,^{53, 54} Structural changes in protein are vital for many biological functions. FT-IR was used to analyze the secondary protein structure (Amide I or II) as shown in Figure 2.13. The secondary structure of BSA and Fg varies such as the secondary structure is composed of 10% turn, 67% helix and 23% extended chain.⁵⁵⁻⁵⁷ The percentage of secondary protein structure result in chapter 3 were calculated. The β -sheet structure were further split into two, regular and distorted. Fraction of α -helix, β sheet, β pleated and random

coil were generated using Thermofisher software (macrobasics) and homebuilt programming language shown in Figure 2.14 (a) to (f).

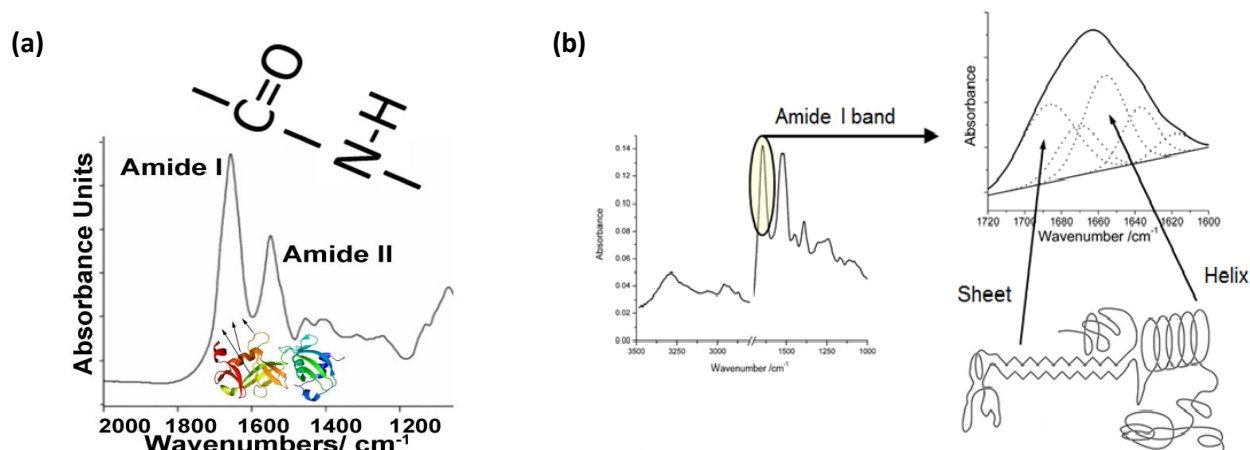


Figure 2.13 (a) Comparison of the infrared spectrum, identifying the peaks for Amide I band (1700 -1600 cm⁻¹) which is due to C=O stretch vibration & Amide II band (1500-1600 cm⁻¹). Amide I is the most sensitive spectral region (b) Spectra obtained from ATR-FTIR with a focus on the amide band I using Origin software to determine the secondary structure either α helix, β sheet, β turn or random.

Curve fitting was performed in the region of 1600-1700 cm^{-1} . The data were smoothed to cancel the absorption of residual vaporized water. Computer simulation was used to determine protein secondary structure percentage from sample protein spectra which is illustrated below; Figure 2.14 (a) to (f). The values obtained are represented as percentages of the amide I band adsorption.

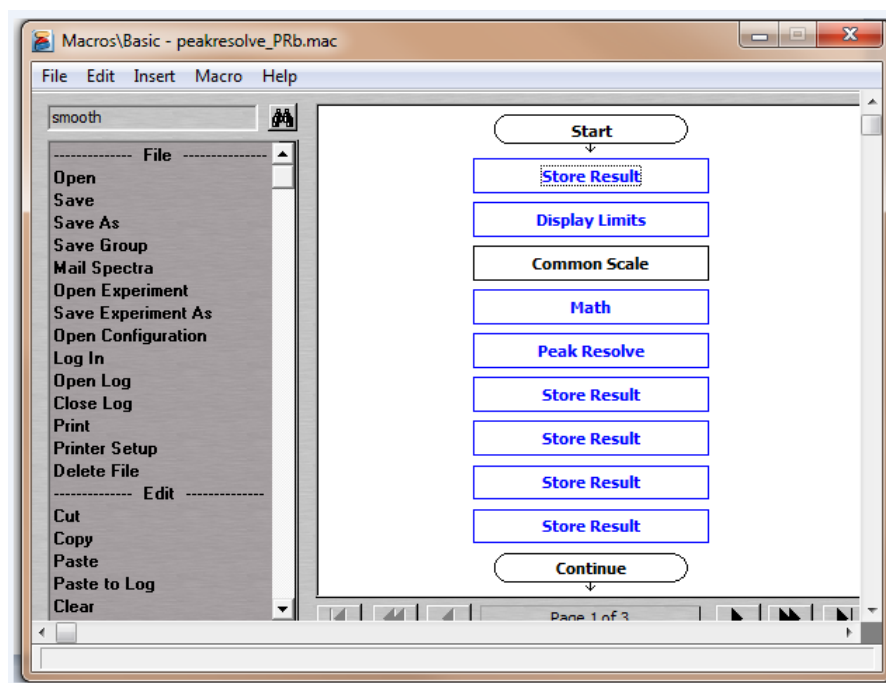


Figure 2.14 OMNIC Macros-Basic intuitive graphical interface used for IR Spectra dataset.

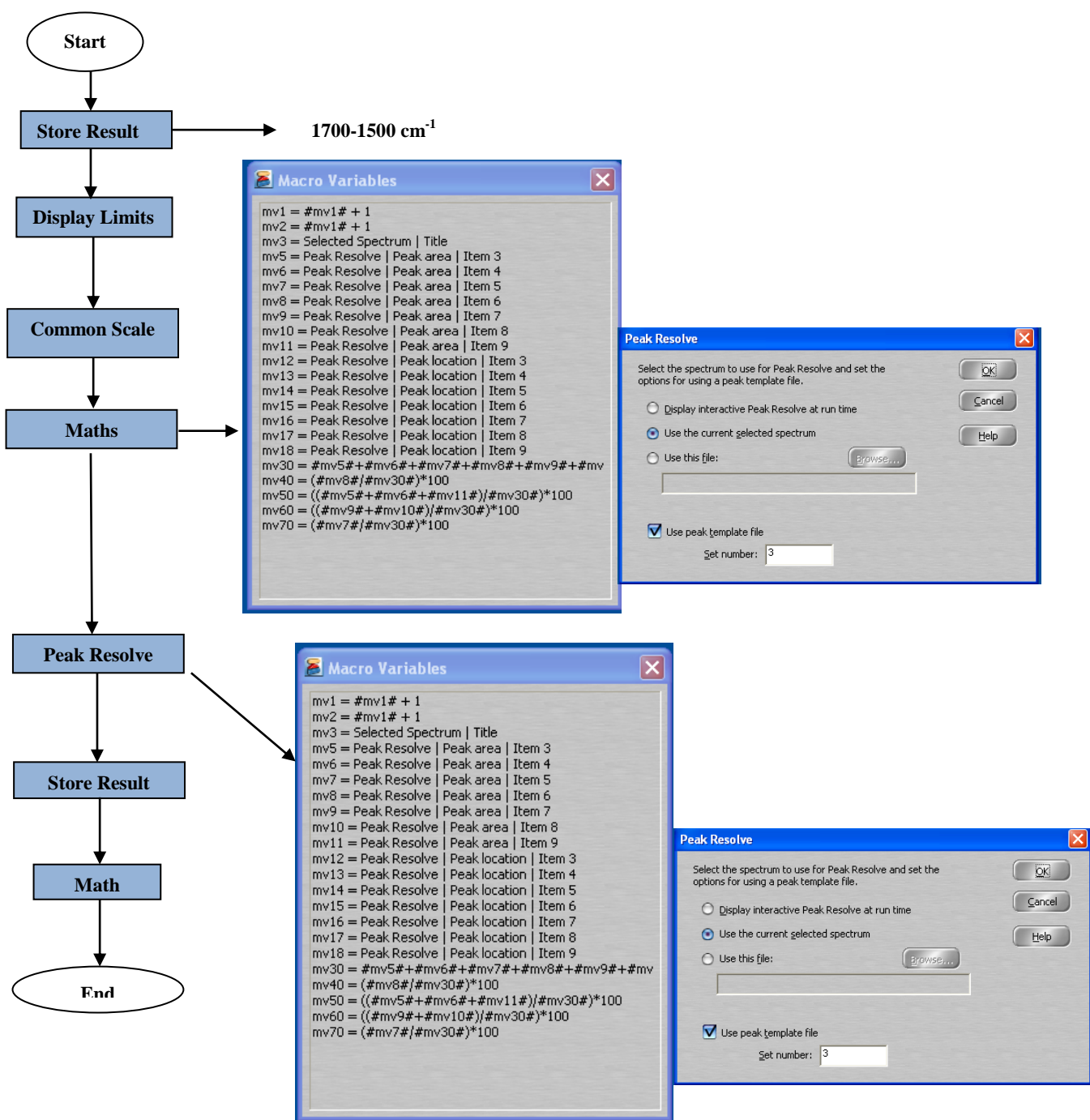


Figure 2.15 A schematic process of Macros-Basic used to determine the structure of secondary protein structure using IR spectra dataset

2.10.2 Smoothing of Infrared and Mass Spectrometry Dataset

The secondary structure of protein were analysed via the FTIR (ATR) .The baseline of amide I region was adjusted from 1600 to 1700 cm^{-1} and smoothed using Omnic software smooth function at 9 point which will not distort the peak location or height and to remove the noise. The amide I band was fitted with multiple component bands having a linear baseline 1720 – 1580 cm^{-1} .Data were first smoothed using 9 points Gaussian peak analysis of the amide I band was performed using PCA analysis. A small script was prepared in Omnic macro basic following the protocol outlined in Figure 2.16 for amide I fitting.

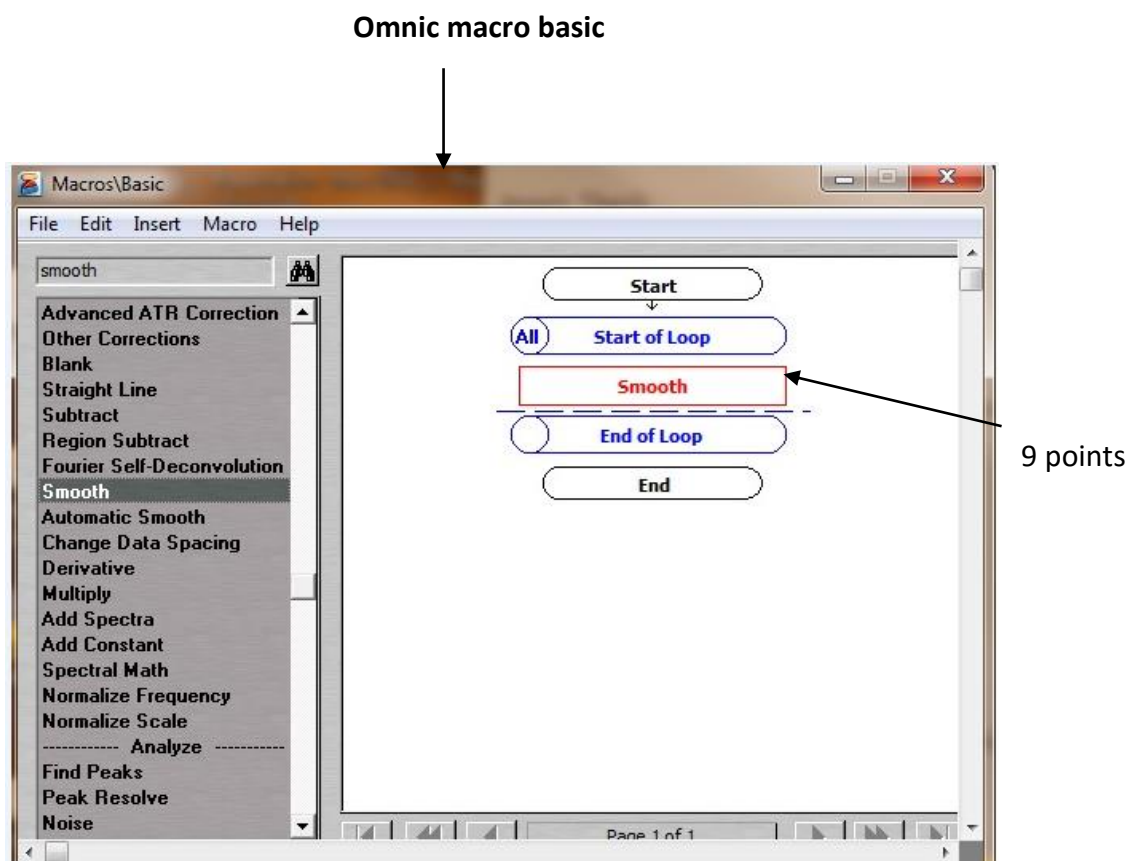


Figure 2.16 Scheme for smoothing IR and MS Dataset

2.11 Cell Culture

All work using cell cultures was performed in a class 2 laminar flow cabinet using aseptic technique. The cabinet was sterilized by UV light prior to use and all equipment was cleaned using 70% ethanol prior to use. 3T3 mouse embryonic fibroblasts were used for this study, preserved in liquid nitrogen until required. 3T3 was first discovered and cultured by George Todaro and Howard Green in 1962.⁴⁰ 3T3 refers to 3 day transfer and inoculum at 3×10^5 cells as shown in Figure 2.17. The cells can be stored in liquid nitrogen. Freezing media is made up of 95% Fetal calf serum (FCS) and 5% dimethyl sulfoxide (DMSO). The cells were removed from liquid nitrogen and maintained in complete medium; Dulbecco's modified eagles medium, DMEM (Biosera), supplemented with 10% Fetal calf serum, (FCS), 2% L-glutamine and 1% penicillin/streptomycin were warmed in the 37°C water bath before being passaged.

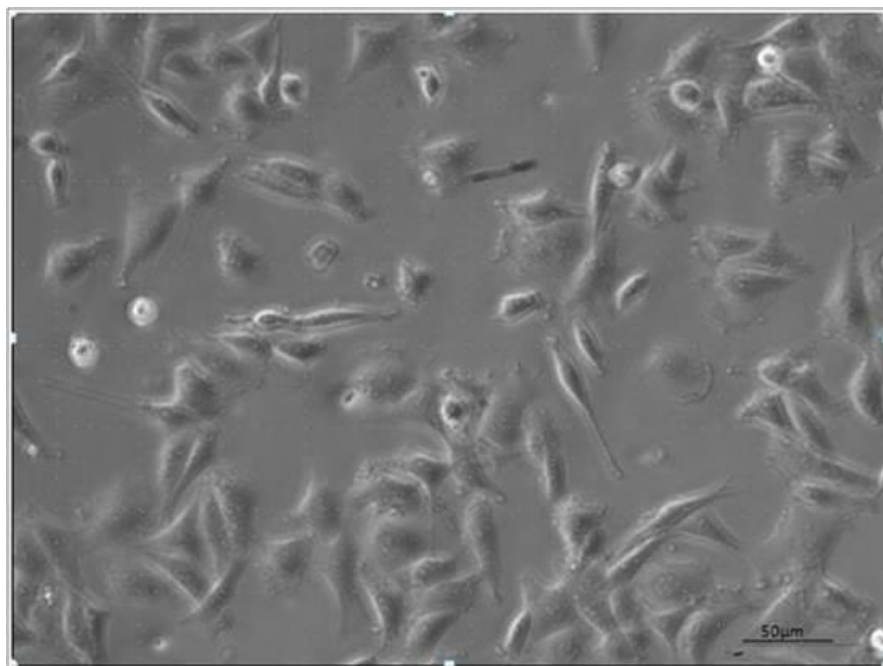


Figure 2.17 Phase contrast of 3T3 fibroblast cells were cultured in complete medium consisting of Dulbecco's Modified Eagle Medium (DMEM) supplemented with 10% fetal calf serum, 2% L-glutamine, and 1% penicillin/streptomycin, x20 magnification.

2.11.1 Thawing of 3T3 Fibroblast cells

Fibroblast cell used was less than three passaged. The frozen vial was thawed by immersing the bottom half of the cryovial in a 37°C water bath and swirling the tube around. A volume of 10 ml of pre-warmed culture media was transferred to a 30 mL centrifuge tube. Less than one ml of the medium from the centrifuge tube was transferred to the half thawed cryotube to thaw the remainder quickly and then the cell suspension was transferred into the 30 mL centrifuge tube. The suspensions were centrifuged at 1200 rpm for 3 minutes and the supernatant was discarded. The cell pellets were re-suspended in 10 mL of fresh warm media and gently mixed and plated in 0.1% gelatin-coated T25 flask and incubated at 37°C and 5% CO₂ until confluent.

2.11.2 Cell Passaging

3T3 Fibroblast cells were passaged when they became ~80% confluent. Culture media (Fibroblast growth medium (FGM) was prepared by adding Dulbecco's Modified Eagle medium (DMEM), 1% Penicillin, Streptomycin extract and Fetal calf serum (FCS) were warmed at 37°C in water bath before starting to passage. The confluent culture flask was taken out of the incubator and examined under a phase contrast microscope. The medium was aspirated and cells were washed 2 times with 10 mL of PBS. A volume of 1 mL of trypsin in PBS was added and incubated for 5 minute to detach cells from tissue culture flask. During this step the tissue culture flask with trypsin was incubated under standard tissue culture conditions. Following incubation for detachment of cells from the surface, the solution was transferred to a centrifuge tube and centrifuged at 12 rpm for 10 mins. Cells being heavier settled at the bottom and the supernatant was discarded and replaced by 10 mL of FGM medium for washing. Cells re-suspension was done in 1mL of fresh FGM medium and gently mixed for cell viability. Cell viability and cell count was determined using trypan blue assay.

Cell suspension was loaded into a haemocytometer (5 μ L of cell suspension and 45 μ L of Trypan blue) and the cell count was done using a haemocytometer and the total numbers of cells in the flask were calculated. A sample of 1×10^6 cells were seeded in a T25 culture flask with 10 mL fibroblast growth media (FGM) which was incubated at 37°C and 5% CO₂.

2.11.3 Cell visibility

Trypan blue 0.5% solution (LM-T1708- Biosera) is used in cell culture and for cell counting. Trypan blue is an azo dye, derived from toluidine. It is used to distinguish between viable cells and non-viable cells. Non-viable cells are blue in colour while viable cells are not coloured because trypan blue is not absorbed into viable cells due to intact cell membranes. Trypan blue is a 0.5% solution of trypan blue in dulbecco's phosphate buffered saline.⁵²

2.11.4 Cell Staining

Cell staining was done for actin, cytoskeleton and focal adhesion using Millipore staining kit (FAK 100). Cells when reached ~50-60% of confluent stage were used for staining actin, cytoskeleton structure.

2.11.4.1. Cell Fixing

Cells were fixed by using methanol as a fixative agent where methanol arrests the cell growth and helps in fixing the cell. Nutrient media from the samples was discarded by using a glass dropper/ pipette and dropped in a beaker containing methanol (care should be taken that media is discarded properly). Samples were given a wash with 1ml of 0.2 M PBS pH 7.4 for each well followed by 0.5 mL of methanol for 5 mins. A white colour turbid solution was observed as a resulting of protein precipitation in the well, this solution was discarded and 1ml of PBS was added to each well and left for overnight incubation in fridge at 4°C with PBS buffer.

2.11.4.2 Primary Anti Body Staining

- Samples were over night with primary antibody.
- Cells were permeabilized with 0.1% Triton X-100 in PBS for 1 hour and incubated in fridge 4°C, following washing once in PBS.
- Primary antibody (anti- vinculin was mixed with 5% goat serum (Sigma Aldrich). 1mL of goat serum was diluted with PBS and anti-vinculin was diluted to a working conc. of 1:200. The antibody was incubated with the sample overnight.

2.11.4.3 Secondary Anti Body Fixing

- Samples were removed from fridge following overnight incubation and washed with PBS.
- Secondary anti body (1% goat serum mixed with FITC) was added to samples and incubate for 2 hours at room temperature in dark conditions. For double labelling TRITC-conjugated Phalloidin (1:500) can be incubated simultaneously with the secondary antibody for 30-60 minutes at room temperature. The wells were washed with PBS.
- Samples were incubated with DAPI stain (in dark room) for 15 min in dark room and followed by washing 1 time with PBS. The samples were mounted inverted onto clean glass microscopic slides and visualized using fluorescence microscope.

2.11.4.4 Image Capture for Fluorescence

Image capture for fluorescence was performed Nikon Fluorescence microscope with 20X objective. Samples were observed under 3 different channels DAPI, FITC and TRITC and image acquisition was done

2.11.4.5 Statistical analysis

The statistical analysis used in cell culture are as follows; Images were obtained using light microscopy Olympus software (Olympus, Germany), and analysis was performed using ImageJ 1.45 software. Other analysis was performed using Microsoft Excel and Origin 9.0.

All reported values of standard deviation are carried out using the Microsoft Excel function STDEV, which uses the n-1 function to report standard deviation.

2.12 Secreted Protein (Secretome)

2.12.1 Acetonitrile Precipitation- Secretome Experiment

Acetonitrile (ACN) precipitation is a method used to reduce high, large abundant proteins and is widely used in bioanalytical laboratories for small molecule analysis.⁴⁰ All samples contained large amounts of BSA in comparison to the cell secreted proteins, so an ACN crash was used to remove the large protein. ACN is used to remove serum, denature large proteins and allow the small, low abundance proteins to bind because they have more chance to interact with ACN. A volume of 400 μL acetonitrile was added into each of the sample volumes as shown in Figure 2.17. After Speed Vac concentrating the solution, a white solid remained at the bottom of the 0.5 mL eppendorf tube. A volume of 50 μL of 0.1% trifluoroacetic acid (TFA) in distilled water was added and Ziptip technique was carried out.

2.12.2 Ziptip -Secretome Experiment

Ziptips are a commercial product used for purifying and concentrating femtomoles to picomoles of proteins or peptide samples for analysis. Each Ziptip is a 10 μL pipette tip with a 0.6 or 0.2 μL chromatography media fixed at its end. The sample is aspirated through the tip, with the species of interest binding to the packing. This allows washing, de-salting and prior to the sample being dispensed, giving rise also to a more concentrated sample.⁴¹

Ziptip C₄ (Millipore) was attached to a 20 μL Gilson pipette and set to dispense 10 μL aliquots. The following procedure was carried out for sample analysis.

1. Equilibrate

- The tip was wetted with 2 cycles of 50% acetonitrile/ water, ensuring that air bubbles were not introduced into the Ziptip. The tip was then equilibrated ready for sample binding with 5 cycles of 0.1% TFA in H₂O.

2. Bind & Wash

- Peptides were then bound to the tip (acidifies to 0.1% TFA) with 10 cycles of sample solution. The sample volume should be less than 100 µL. The salts that bound to the tips were washed off with 2 cycles of 0.1% TFA in water and dispense to waste.

3. Elute

- 4 µL of 80% acetonitrile/water + 0.1% TFA were dispensed into a 500 µL eppendorf tube using a Gilson pipette tip. The cycle solvents were done at least 3 times without introducing air into the sample. The sample is sent for MS analysis (acknowledgement to Dr Sarah Hart, Keele University).

2.13. Mass Spectrometry

2.13.1 Liquid chromatography mass spectrometry (LC-MS)

Secreted protein samples were analysed by using liquid chromatography and electrospray ionisation mass spectroscopy (LC-ESI-MS). The instrument is an LTQ Velos (Thermo Fisher Scientific, Hemel Hempstead, Herts), coupled to a Dionex Ultimate3000 split flow system with Famous autosampler (Dionex Corporation, Crawley, Surrey). The gradient was a 35min linear ramp from 2%-60% B (MeCN: 0.1% formic acid), with solvent A being 2% MeCN: 0.1% FA. the column was a 75 µm i.d. 15cm PepMap with 5µm beads, 200 Å pore size (Dionex), and the trap column was the same packing material in a 2 mm guard. All solvents were from Fisher, and LC-MS grade formic acid was from Sigma. Samples (5 µL loading vol.) were loaded from zero dead-volume vials (Waters, Elstree, Herts) in buffer A. Columns were washed in 90% B for 5 min and re-equilibrated in 2% B for 15 min prior to the

next injection. The MS program ran from 300 or 400 m/z up to 2000 m/z in survey (MS) mode only. Figure 2.18 shows the method used for secretome experiment.

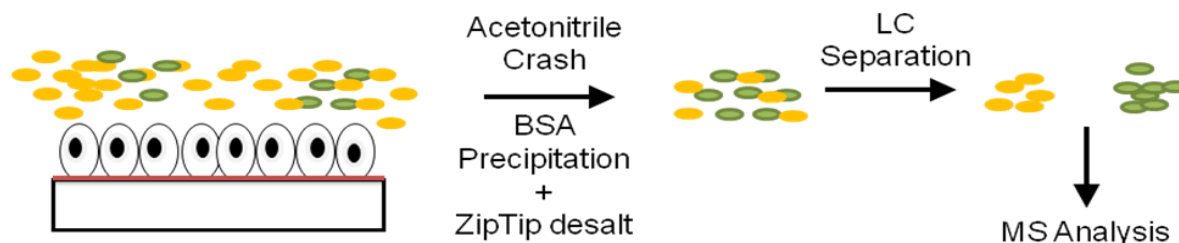


Figure 2.18 Schematic of method used for secreted fibroblast

2.13.2 Matrix Assisted Laser Desorption Ionization (MALDI-MS)

Secreted protein samples were subject to the acetonitrile precipitation process while C₄ ziptip (C₄) was used to clean up proteins was mixed in a 1:1 ratio (v/v) with α -cyano-4-hydroxycinnamic acid (CHCA, 10 mg/mL in 0.1% TFA, 80% acetonitrile) on a stainless steel MALDI target plate, and analysed by a MALDI time-of-flight (TOF/TOF) instrument (MALDI 4800, AB Sciex, Warrington, Cheshire). MS data were acquired in a positive reflector mode in the mass range of 700-3,600 m/z , 800-1,000 laser shots were accumulated during survey scan acquisition. Close external calibration was performed using Calmix 5, a mixture of 5 protein standards (Bradykinin, Angiotensin, P14R, and ACTH fragment 18-39, Glufibrinopeptide). All spectra were externally calibrated using calibration spots. All chemicals were obtained from Sigma-Aldrich (Poole, Dorset).

2.14 Statistical Analysis

Multivariate data analysis is used to reduce a large number of variables to a smaller number of factors by multivariate statistical methods. Multivariate analysis comprises a collection of methods that can be used to analysis datasets with more than one variable. Multivariate analysis is used by researchers to obtain to process information in a meaningful way.⁴⁷ Multivariate statistical techniques have been applied to quantitative evaluation of biological and environmental sample such as the identification of source of chemical pollutants⁴⁸, quality of some food products⁴⁹ and evaluation of methods.⁵⁰ Examples of multivariate statistical methods are principal component analysis, factor analysis and linear analysis.

2.14.1 Principal Component Analysis

Principal component analysis (PCA) is a clustering method for identifying and expressing patterns in high dimension data. PCA creates “new” dimension of the data and evaluates a reduced number of independent factors or principal components.⁵¹ PCA is an efficient tools used to estimate effectiveness of different samples; i.e. mass spectrometry datasets. Data in the form of mass spectra were acquired using a software called Xcalibur and processed by a statistical software programme (Matlab, Eigenvector). The aim of PCA is to find a few components of factors that explain the major variations within the data matrix. Mean centering was carried out so that each variable is centred by the subtraction of its mean value across all the samples, in MS, it is the same as subtracting the mean spectrum of the data set from each sample.⁵¹ All spectra analyses were performed in Matlab 7.2 environment (The Mathworks Inc.) employing the Eigenvector toolbox 5.0.3 (Eigenvector Research, Wenatchee, WA).

2.15 Summary of Secretome Experiment

The experimental setup of secretome experiment is shown in Figure 2.19

Secretome Analysis via Mass Spectrometry

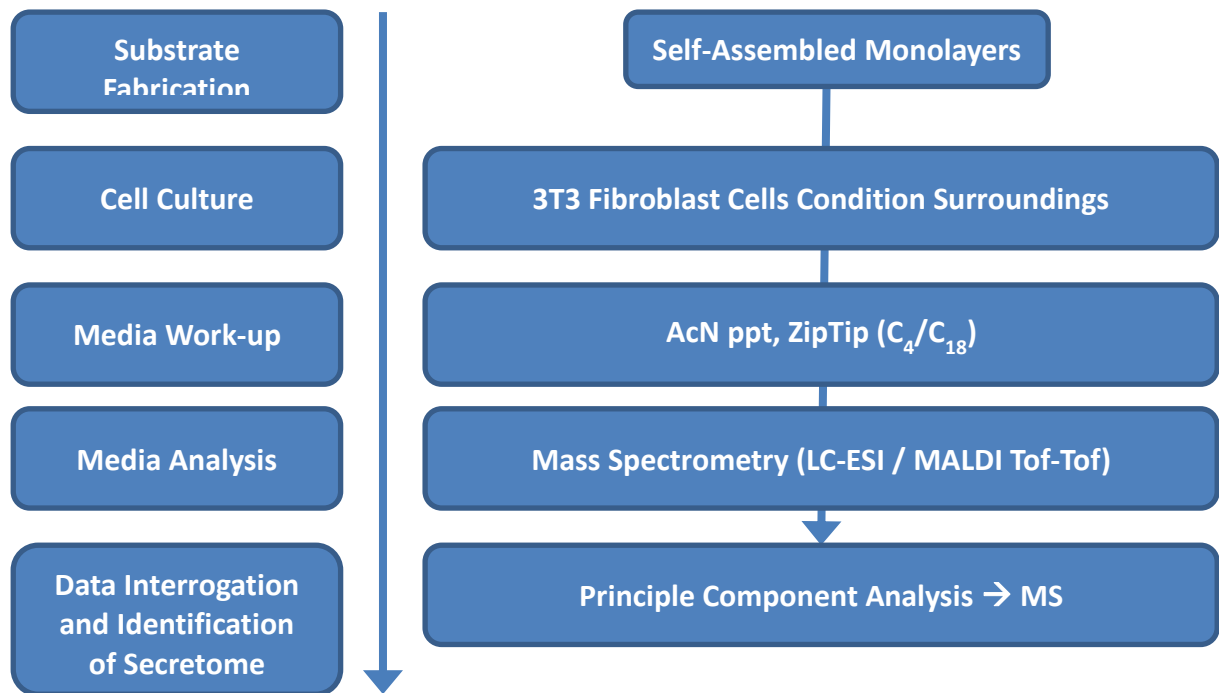


Figure 2.19 The different stages of secretome analysis using Mass spectrometry

2.16 References

1. Schreiber, F. Structure and growth of self-assembling monolayers. *Prog. Surf. Sci.* **65**, 151–257 (2000).
2. Ulman A , An introduction to ultrathin organic films: From Langmuir-blodgett to self assembly. *Academic Press*, Boston, MA (1991)
3. Plueddemann EP, Silane Coupling agents, 2nd edn. Plenum, New York, NY (1991)
4. Schwartz, D. K. Mechanisms and kinetics of self-assembled monolayer formation. *Annu. Rev. Phys. Chem.* **52**, 107–37 (2001).
5. Nuzzo, R. G. & Allara, D. L. Adsorption of bifunctional organic disulfides on gold surfaces. *J. Am. Chem. Soc.* **105**, 4481–4483 (1983).
6. Sagiv, J., Organized monolayers by adsorption. 1. Formation and structure of oleophobic mixed monolayers on solid surfaces. *J. Am. Chem. Soc.*; (1980), **102**, 92-98.
7. Bigelow, W. C.; Pickett, D. L.; Zisman, W. A., Oleophobic monolayers: I. Films adsorbed from solution in non-polar liquids. *J. Coll. Sci.* (1946), **1**, 513-538
8. Onclin, S., Ravoo, B. J. & Reinhoudt, D. N. Engineering silicon oxide surfaces using self-assembled monolayers. *Angew. Chem. Int. Ed. Engl.* **44**, 6282–304 (2005)
9. Malmqvist M, Method of silanisation of surfaces, (1989)
10. Ulman, A. Formation and Structure of Self-Assembled Monolayers. *Chem. Rev.* **96**, 1533–1554 (1996)
11. Mrksich M. Using self-assembled monolayers to understand the biomaterials interface. *Curr Opin Colloid Interface Sci* (1997); **2**:83–8
12. Mrksich, M. A surface chemistry approach to studying cell adhesion. *Chem. Soc. Rev.* **29**, 267–273 (2000).
13. Singhvi, R., et al. Engineering Cell Shape and Function. *Science* 264.5159 (1994): **696-8**.
14. Stöber, Werner. Controlled Growth of Monodisperse Silica Spheres in the Micron Size Range 1. **69**, 62–69 (1968).
15. Whitesides, G. M. & Laibinis, P. E. Wet chemical approaches to the characterization of organic surfaces: self-assembled monolayers, wetting, and the physical-organic chemistry of the solid-liquid interface. *Langmuir* **6**, 87–96 (1990).
16. Barnes, G. & Gentle, I. Interfacial Science: An Introduction *Oxford University Press*, (2011). 325
17. Inagaki N, Plasma Surface Modification and Plasma Polymerization; Lancaster, PA (1988).

18. Wenzel, R. N. Surface roughness and contact angle. *J. Phys. Colloid Chem.* (1949), 53(9), 1466–146
19. Kazarian, S. G. & Chan, K.L.A. ATR-FTIR spectroscopic imaging: recent advances and applications to biological systems. *Analyst* **138**, 1940–51 (2013)
20. Fuller, M. P. & Griffiths, P. R. Diffuse reflectance measurements by infrared Fourier transform spectrometry. *Anal. Chem.* **50**, 1906–1910 (1978).
21. Fadley, C. S., Baird, R. J., Siekhaus, W., Novakov, T. & Bergström, S. Å. L. Surface analysis and angular distributions in x-ray photoelectron spectroscopy. *J. Electron Spectros. Relat. Phenomena* **4**, 93–137 (1974).
22. Khorasani, M. T., Mirzadeh, H. & Kermani, Z. Wettability of porous polydimethylsiloxane surface: morphology study. *Appl. Surf. Sci.* **242**, 339–345 (2005).
23. Gregory, J., Particles in water: properties and processes. London: *CRC Press, Taylor & Francis Group*, (2006).
24. Khorasani, M. T., Mirzadeh, H. & Kermani, Z. Wettability of porous polydimethylsiloxane surface: morphology study. *Appl. Surf. Sci.* **242**, 339–345 (2005).
25. Hung, S., Shih, C., Chen, B., Tu, C. & Ling, Y. A New Detection Technique for Fluoroquinolone-Conjugated Proteins by High Performance Liquid Chromatography with UV / Fluorescence Detectors. *J. Food & Drug Anal.*, Vol. **15**, 71–74 (2007).
26. Carter, D. C., and J. X. Ho. Structure of Serum Albumin. *Adv in Protein Chem*; **45** (1994): 153-203.
27. Biswajit Pal, P.K. Bajpai, T.S. BasuBaul, *Spectrochim. Acta A*, **56** (2000), pp. 2453–2458
28. Zhao HW, M. Ge, Z.X. Zhang, W.F. Wang, G.Z. Wu *Spectrochim. Acta A*, 65 (2006), pp. 811–817
29. Jung, S.-Y. *et al.* The Vroman effect: a molecular level description of fibrinogen displacement. *J. Am. Chem. Soc.* **125**, 12782–6 (2003).
30. Thevenot, P., Hu, W. & Tang, L. Surface chemistry influences implant biocompatibility. *Curr. Top. Med. Chem.* **8**, 270–80 (2008).
31. Averett, L. E. & Schoenfisch, M. H. Atomic force microscope studies of fibrinogen adsorption. *Analyst* **135**, 1201–9 (2010).
32. Wiechelman, K. J., Braun, R. D. & Fitzpatrick, J. D. Investigation of the bicinchoninic acid protein assay: Identification of the groups responsible for color formation. *Anal. Biochem.* **175**, 231–237 (1988).

33. Brown, R. E., Jarvis, K. L. & Hyland, K. J. Protein measurement using bicinchoninic acid: elimination of interfering substances. *Anal. Biochem.* **180**, 136–9 (1989).
34. Smith, P. K. *et al.* Measurement of protein using bicinchoninic acid. *Anal. Biochem.* **150**, 76–85 (1985).
35. Clark, B. J. *UV Spectroscopy: Techniques, Instrumentation and Data Handling Textbook*; Chapman & Hall, London, UK (1993).
36. Yadav, L. D. S. *Organic Spectroscopy. Textbook. Page 324* ; Publisher-Springer, (2005)
37. Jeppu, G. P., Clement, T. P., Barnett, M. O. & Lee, K.-K. A Scalable Surface Complexation Modeling Framework for Predicting Arsenate Adsorption on Goethite-Coated Sands. *Environ. Eng. Sci.* **27**, 147–158 (2010).
38. Jeppu, G. P. & Clement, T. P. A modified Langmuir-Freundlich isotherm model for simulating pH-dependent adsorption effects. *J. Contam. Hydrol.* **129-130**, 46–53 (2012).
39. Foo, K. Y. & Hameed, B. H. Insights into the modeling of adsorption isotherm systems. *Chem. Eng. J.* **156**, 2–10 (2010).
40. Todaro, G. J. & Green, H. Quantitative studies of the growth of mouse embryo cells in culture and their development into established lines. *J. Cell Biol.* **17**, 299–313 (1963).
41. Barnes G, *Interfacial science: An introduction*, Oxford University Press, (2005).
42. Kopaciewicz, W, Rounds MA, Fausnaugh J and Regnier FE, *J. Chromatogr.*, 283 (1984) 37.
43. Cooley WW and Lohnes PR; *Multivariate data analysis*, John Wiley & Sons New York, (1971)
44. Morrison DF; *Multivariate statistical methods*; McGraw-Hill International, Auckland, (1978)
45. Mardia KV, Kent JT and Bibby JM, *Multivariate analysis*, Acad. Press, London (1989)
46. Deming SN, and Morgan SL, *Experimental design: A chemometric approach*, Elsevier, Amsterdam, (1993)
47. Wackernagel H; *Multivariate Geostatistics. An introduction with application*, 3rd edition, Springer; (2003)
48. Li YH, Geochemical cycles of elements and human perturbation. *Geochim. Cosmochim. Acta*, **45**, 2073 (1981)
49. Gonxalex G and Pena Mendez EM; *Eur. Food Res. Technol.*, **212**, 100 (2000)
50. Bermejo-Barral P., Moreda-Pineiro and Bermejo-Barrera A., Talanta, The multivariate optimisation of ultrasonic bath-induced acid leaching for the determination of trace elements in seafood products by atomic absorption spectrometry; **439**, pp. 211-227, (2001)

51. Flury B., and Riedwyl H. Multivariate statistics- A Practical approach, *chapman & Hall*, London, published online (2007)
52. Slater, TF., Sawyer, B., and Strauli, U. D. Studies on succinate-tetrazolium . Points of coupling of four different tetrazolium salts. *Biochim. Biophys. Acta.* **77**: 383-393. (1963)
53. Barbucci R *et al*; Conformation of human plasma proteins at polymer surfaces: the effectiveness of surface heparinization ; *Biom.* Vol. 15, Issue 12, (1994), Pages 955–962
54. Steadman, B. L. *et al.* The effects of surface adsorption on the thermal stability of proteins. *Biotechnol. Bioeng.* **40**, 8–15 (1992).
55. Dong A, Caughey WS. Infrared methods for study of hemoglobin reaction and structures. *Methods Enzymol* (1994), **232**: 139–175
56. Bowler BE, May K, Zaragoza T, York P, Dong A, Caughey WS. Destabilizing effects of replacing a surface lysine of cytochrome c with aromatic amino acids. *Biochemistry* (1993), **32**: 183–190
57. Bowler BE, Dong A, Caughey WS. Characterization of the guanidine hydrochloride-denatured state of iso-1-cytochrome c by infrared spectroscopy. *Biochemistry* (1994); **33**(9):2402-8.

CHAPTER 3

Protein Adsorption from Single Protein Solutions

3.1 Introduction

Protein adsorptions have been widely studied due to its great importance in industrial applications especially in biotechnology and nanotechnology. The interaction of proteins on surfaces is vital in biochip developments¹, biosensors², medical device coatings,³ fabrication of hybrid materials⁴ and clinical applications.⁵ Protein adsorption is a key role in biocompatibility since the majority of materials used in medical implants depends on the interaction of proteins with surfaces. However, research have been carried out in understanding protein adsorption on surface but many questions are unanswered in understanding the adsorption mechanism such as the adsorption process and protein conformational changes.

Proteins adsorb in differing quantities, densities, conformations and orientations, depending on the chemical and physical characteristics of the surface.^{6,7} Studies have shown that protein adsorption to solid surface induce structural changes that may affect the entire molecule. For example, structural changes may be induced in the protein by the physicochemical nature of the surface or the properties of the protein. Physicochemical cues such as surface chemistry; charge and topography of the material surface have been shown to affect protein adsorption and influence the biological performance of materials.⁸ Surface chemistry and topography are the two most studied and important factors that influence biological reactions.⁹

Surface chemistry and topography plays a vital role in protein adsorption and has been shown to affect amount of protein adsorbed.¹⁰⁻¹² Due to the high volume of research on surface chemistry and topography in understanding protein adsorption on flat surfaces, the research focus has now moved to nano-materials. Engineered nano-materials have been shown to have high potential for improving the treatment and diagnosis of disease.¹³⁻¹⁷ According to Cederevall *et al*, when a nanomaterial enters a physiological environment,

proteins rapidly adsorb to its surface and form either hard or soft protein corona.¹⁸ Other research on protein adsorption on nano-materials reveals that protein corona alters the size and interfacial composition of nano-materials, giving it a biological identity which is different from its synthetic identity.¹⁹ The biological identity is shown to be responsible for the kinetics, transport and reactivity of nano-materials in a physiological system²⁰ and plays a vital role in cellular interaction.²¹ However, there is less evidence in understanding the relationship of nano-materials to protein adsorption, linking the size, surface chemistry and topography of the nano-materials.

Surface Chemistry and topography has been shown to affect the conformation of bound proteins using colloidal substrates but little is understood of the process.²²⁻²⁴ Therefore, it is vital to investigate and quantify the mechanisms responsible for protein adsorption from single protein solutions on surface chemistry and topography. Protein adsorption is also strongly influenced by the surface density of the functional group and their influence on the substrate surface.²⁰ Therefore, a clear understanding of surface functionalization on protein adsorption needs to be reviewed which could be a potential application in biological systems.

In this chapter, protein adsorption from single protein solutions on functionalised silica nanoparticle is investigated. The protein used for the experiments were bovine serum albumin (BSA), a small globular protein and the most abundant plasma protein which transports fatty acids along with other small molecules throughout the circulatory system and fibrinogen (Fg), a rod-like protein involved in the coagulation cascade.

A large number of spectroscopic techniques are used to study protein structural conformational changes in solution such as circular dichroism,²⁵ total internal reflectance fluorescence,²⁶ nuclear magnetic resonance,²⁷ FTIR²⁸ and UV-Vis absorption.²⁹ Infrared spectroscopy (IR) is used for this study as it is best suited to compare secondary structures for

proteins in solution.³⁰ IR allows more thorough examination of the secondary structure of the bound protein.^{28,30}

Protein adsorptions on colloid particles are important for biomedical uses such as in drug delivery. High numbers of studies have shown that nanoparticle can pass through the cell membranes in organism for drug delivery,³¹⁻³³ but nanoparticle interactions with complex biological systems are still not fully understood.³⁴⁻³⁶ Silica nanoparticles having diameters in the range 11-215 nm have been synthesised and chemically modified to give four different functional groups (-OH, -NH₂, -COOH and -CH₃) which can be used to understand the driving forces of protein-surface interaction and the effect of particle surface charge and wettability. Infrared spectroscopy was used to assess the conformational and orientational aspects of proteins bound to a range of surfaces presenting contrasting surface chemistry and curvature. The bicinchoninic acid assay (BCA) was used for this study due to its stability under alkali conditions and its sensitivity for protein quantification.

Despite the high number of literature on protein adsorption onto nano-material surfaces, there are questions that need to be address such as how proteim interacts with surface and design of nanoscale surface and proteins to achieve its functionality. This chapter will investigate protein adsorption on functionalised silica nanoparticles which will provide information about protein interaction with nanoparticles, effect of surface chemistry and curvature on protein adsorbed, protein conformational changes that occurs on each functionalised silica nanoparticle.

3.2 Materials and Methods

3.2.1 Preparation of Silica Spheres

The Stöber process³⁷ was used to prepare mono-disperse silica spheres of varying sizes. The preparation of mono-disperse silica particles was carried out by the hydrolysis and condensation of TEOS in a mixture of water and ammonia which is used as a catalyst. The preparation and characterisation of silica sphere is discussed in chapter Two.

3.2.2 Preparation of Functionalised Silica Spheres

Chemically defined silica particles were prepared using silane (SAMs). The preparation and characterisations are explained in material and methods chapter, as described in Chapter Two.

3.2.3 Protein Adsorption from Single Protein Solution

The behaviour of proteins at the phase boundaries has become a major area of research due to its importance for the biocompatibility of medical implants. The adsorption of proteins on silica particles of modified surfaces was investigated. Albumin from bovine serum (Sigma, A2153) and Fibrinogen (Enzyme research Swansea, 3580AL) were dissolved in phosphate buffered saline (PBS, pH=7.0) at a concentration of 1 mg/mL and a serial dilution of 9-900 µg/mL respectively. The serial dilution calculation is in section 3.3.5. Fg and BSA were used because of their broad range in size.

Protein solutions were successfully diluted in 10 mL vials, 900 µL of each diluted proteins (BSA and Fg) was dispensed into a clean eppendorf tube. A volume of 100 µL of functionalised silica particles was added into the eppendorf containing the protein samples while 100 µL of PBS was added to a separate eppendorf as a control. Microstirrer bars were

placed inside the eppendorf tubes (particles + protein, PBS + Protein); stirred for 1 hour. The stirrer bars were removed and left for one hour. The eppendorf tubes were centrifuged using a micro centrifuge, 15k rpm for a few minutes. Proteins absorbed by the particles were measured using FTIR while 50 μ L of the samples were pipetted into 96 well plates with 150 μ L of assay to measure the protein adsorbed.

3.2.4 Bicinchoninic Acid Assay (BCA) Protein Quantification

BCA assay was used to calculate the protein concentration of the sample. BCA Protein assay reagent kit was obtained from Pierce (#23227) and contains the following reagent. BCA reagent A, 500 mL of reagent containing sodium carbonate, sodium bicarbonate, bicinchoninic acid and sodium tartrate in 0.1 M sodium hydroxide while Reagent B, 25 mL, contains 4% cupric sulphate. 50 parts of BCA reagents A was mixed with 1 part of BCA reagent B to form BCA solution.(ratio 50:1) Proteins standard was prepared by diluting 1 mg/mL of BSA stock standard with a phosphate buffer saline (PBS) and 50 μ L were pipetted into 96 well-plates. A volume of 200 μ L of the working reagents were added to the protein solution, the solution was mixed with a plate shaken for 30 seconds. The well-plate was incubated at 37°C for 30 minutes. After incubation, the plate was allowed to cool at room temperature and the absorbance measured at 562 nm on a plate reader (BioRad, Herts, UK). The concentration of the sample was calculated by plotting a standard curve, Section 2.7

3.2.5 Adsorption Isotherms

The experiment was conducted at room temperature. BSA (1 mg/mL) and Fg (1 mg/ml) were prepared using phosphate buffered saline (PBS). Dried silica spheres were sonicated in PBS to form homogenous dispersions prior to the addition of proteins for a certain period of time. With continuous stirring, the silica suspension was added to each

protein solution to give a substrate surface area per solutions of 1 m²/mL. Solutions were stirred for one hour and left for a further 2 hours to minimise shearing effects that might occur due to stirring. Solutions were centrifuged after two hours to induce sedimentation of the silica. A blank with protein only was carried out to rule out the possibility of protein sedimentation. The residual protein concentration in solution was determined using a Synergy 2 Multimode-microplate reader (Biotek) UV-Vis spectrometer using 96 well plates, measuring absorbance at 562 nm. Calibration was carried out using a series of protein solutions of known concentration. The experiments were performed in triplicate. The amount of protein adsorbed was calculated using the equation;

$$y = bx + c$$

$$x = ((y - c)/b) / \text{Available surface area}$$

Where x is the amount of protein adsorbed per m², c is the intercept; y is the protein concentration in µg/mL while the area is the available surface area in 1 m².

Kinetic adsorption of proteins was calculated using the Langmuir adsorption isotherm. Data is fitted to the isotherm where the binding constant 'K' and saturation value for the amount adsorbed can be estimated 'K' relates to the affinity of the adsorbent using OriginPro 9.0 software. Each exposure concentration and substrate combination was repeated three times and the data are presented as the mean ± standard deviation.

3.2.6 Statistical Analysis

Results were represented as mean ± SD using Microsoft Excel 2007 software and Origin Pro 9.0. The standard deviations are given as error bars.

3.2.7 Summary

A brief summary of the experiments carried out in understanding protein adsorption from single protein solutions is shown below in Figure 3.1

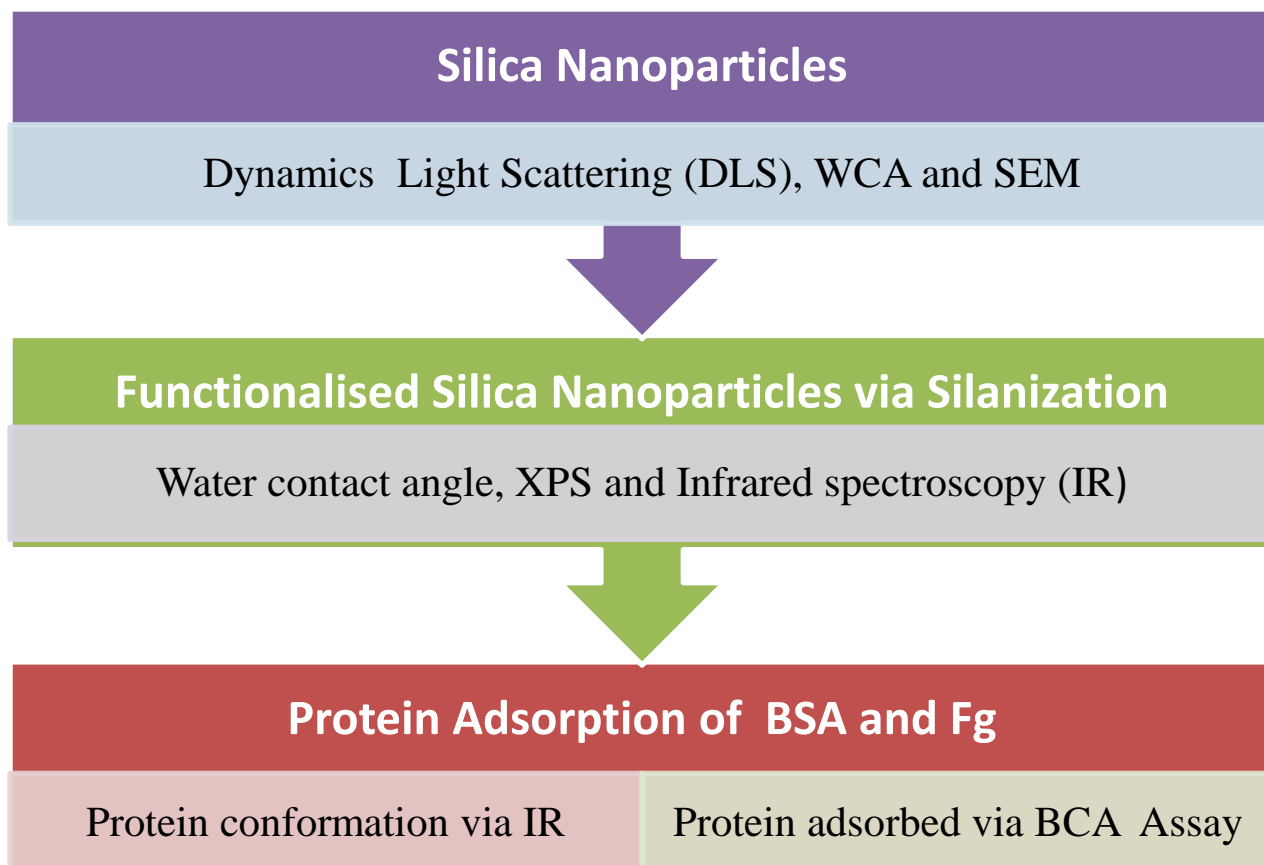


Figure 3.1 A detailed description of protein adsorption from single protein solution

3.3 Results

3.3.1 Surface Characterisation

The Stöber process is prepared through the hydrolysis and condensation of alkyl silicates under alkaline conditions in alcoholic solutions. Many researchers have conducted their experiments using the Stöber process such as Wang *et al*, produced silica particles ranging from 20 nm to 880 nm with TEOS of 0.05-0.67M⁴⁰ and Chen *et al*. prepared 73–300 nm sized particles with TEOS of 0.068-0.22M.⁴¹

Each sample batch was analysed by dynamic light scattering (DLS) to assess the average particle size. DLS measurements were performed after silica formation. Particles having diameters in the range 11-215 nm were used. Samples were freeze dried to minimise aggregation and phosphate buffer was added to the cuvette for measurement. Dynamic light scattering was used to measure the diameter of the silica particles as described in Section 2.5. Readings were taken thrice for each particle at a temperature of 25°C as shown in Figure 3.2. Data obtained from dynamic light scattering (DLS) surface area measurements are summarised in Figure 3.2.

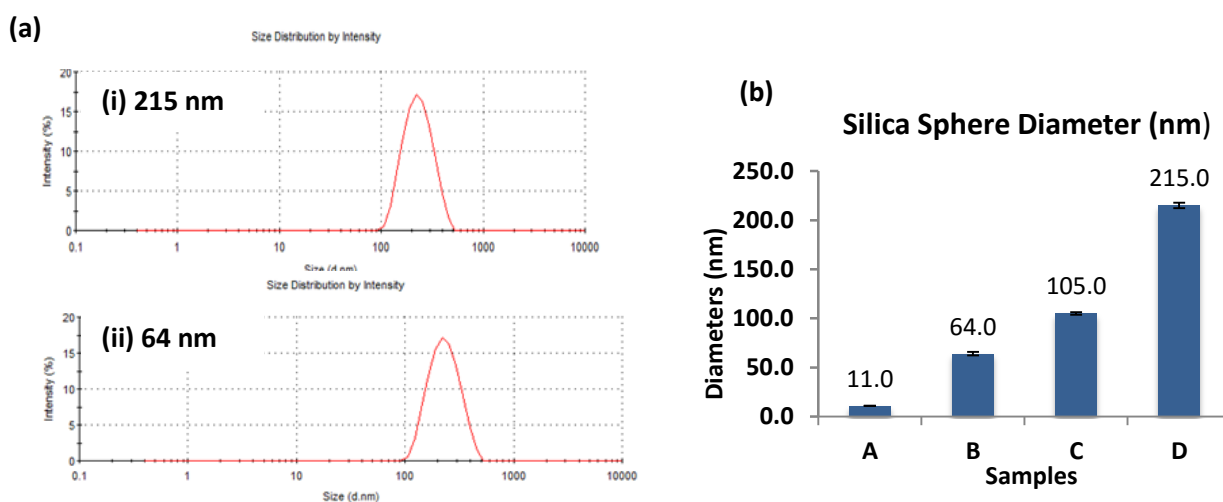


Figure 3.2 (a) DLS size distribution of Silica sphere nanoparticles taken at 25°C, (i) 215 nm (ii) 64 nm (b) Silica Spheres diameters. Data shown are the mean \pm SD of three replicate samples

3.3.2 Functionalised Silica Particles Characterisation

The functionalization of silica particle was used to activate the surface properties of particles to fit its application. Properties of silica include chemical inertness, ease of production, adjustable surface chemistry and unique porous architecture.⁴³ Functionalised silica particle used in this experiment were prepared using self-assembled monolayer formation of silane with different functional group as described in Section 2.1.3; Surface wettability was investigated to assess hydrophobicity as explained in Section 2.2. Water contact angle measurements were carried out for terminated surfaces respectively, Figure 3.3. The result correlates with results from other researchers.⁴³⁻⁴⁵

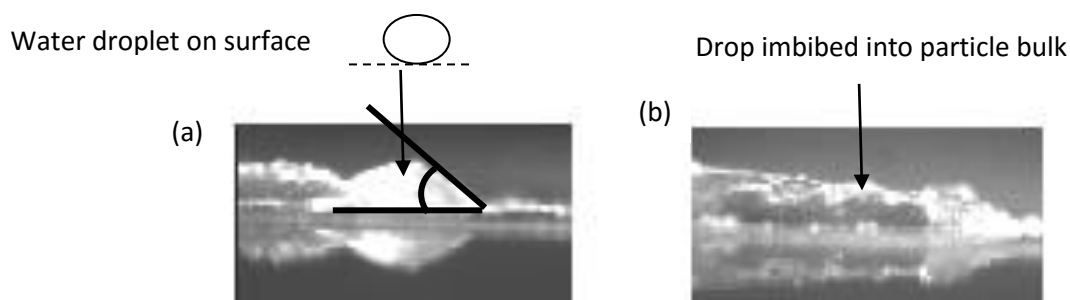


Figure 3.3 Water contact angles on (a) hydrophobic ($-\text{CH}_3$) and (b) hydrophilic ($-\text{OH}$) silica nanoparticle.

Contact angle measurements reveal the variation of solid-surface chemical composition. The ability of a water droplet to spread over a surface was used to assess the wettability of the nanoparticles.⁴⁶ The contact angle between the solid-liquid and the liquid-air interface depends on the relative interfacial energies of the surface and the liquid. Water contact angles shown in Figure 3.3 inserts demonstrate the difference in wettability observed for the treated substrates. The water droplet rested on the silica spheres showing that they were hydrophobic, in contrast to the hydrophilic samples onto which the water droplet rapidly spread over the surface and entered the space between the spheres.

3.3.3 Infrared Absorption Features and Chemical Function

The surface chemistry of functionalised silica particles was investigated by ATR-IR. Analysis by IR showed that after silanization, terminal ethoxy groups were still present on the silica spheres, Figure 3.4. ATR-IR spectra of modified silica terminal groups shows the wavenumber range from 950 to 1250 cm^{-1} , as it includes Si-O-Si vibrational modes which is in agreement with other researcher.⁴⁷⁻⁴⁹

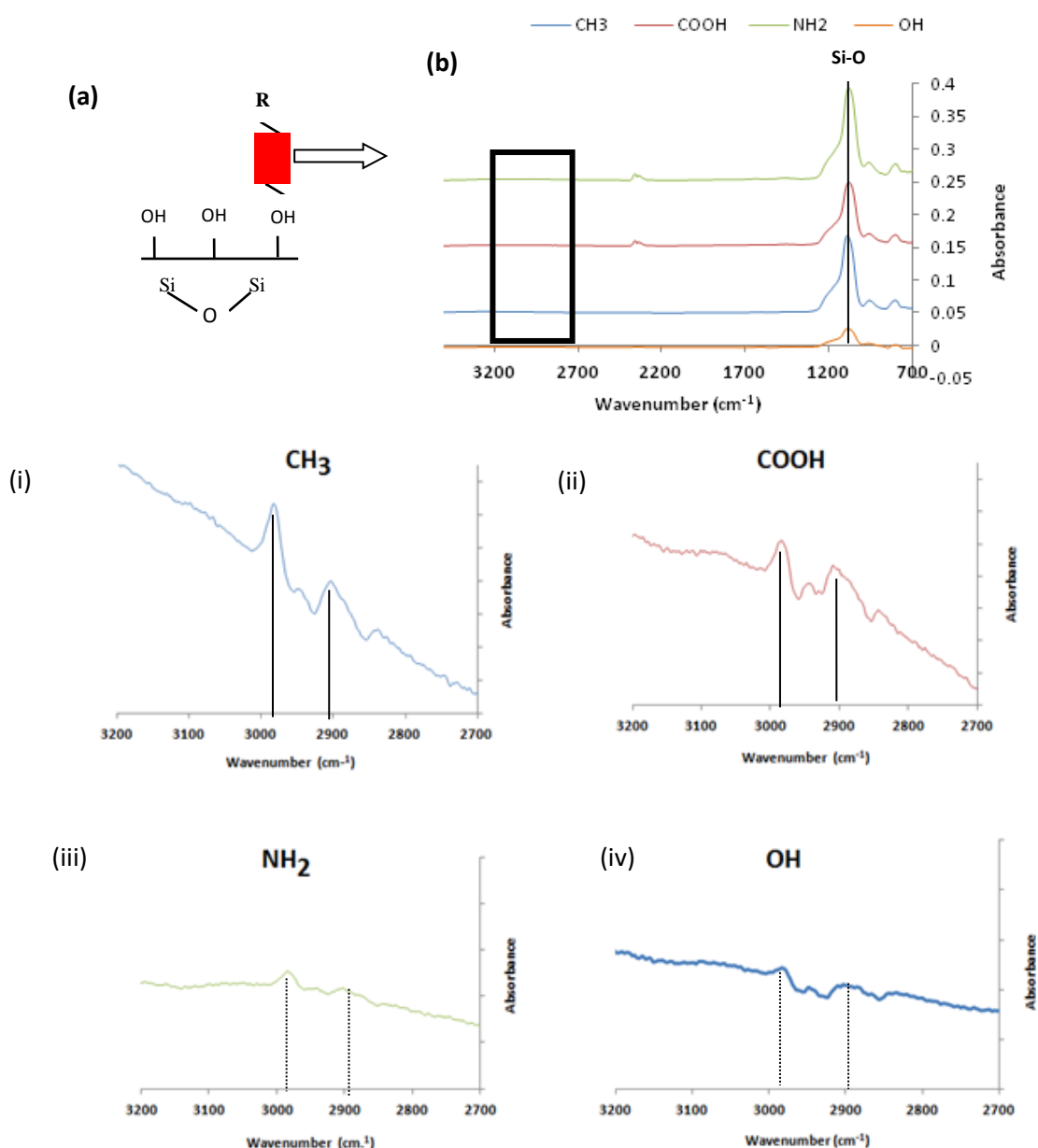


Figure 3.4(a) Functionalised Silica on a coverslip (b) ATR-IR spectrum of functionalised silica nanoparticle focusing on the wavenumber 2700-3200 cm^{-1} . Peaks on carboxylic, amine, methyl and hydroxyl surfaces were focused upon as shown in (i)-(iv)

The main characteristic peaks observed are shown in Figure 3.4 from 3200-2700 cm^{-1}
(A) The band appeared at 3000 -2850 cm^{-1} corresponds to the stretching of C-H from dative linking chain (CH_2 , CH_3) while (B) carboxylic acid, O-H stretch corresponds to 2890-3000 cm^{-1} , (C) amine N-H stretch appeared at 3500 -3300 cm^{-1} (medium) (D) hydroxyl O-H stretch band corresponds to 3300-2500 cm^{-1} .

3.3.4 X-ray Photoelectron Spectroscopy (XPS)

XPS was used to investigate the chemistries of functionalised silica spheres. The results are shown in Figure 3.5. The result shows the presence of carbon, nitrogen and oxygen atoms with XPS of C1s (285 eV), N1s (400 eV) and O1s (532 eV).

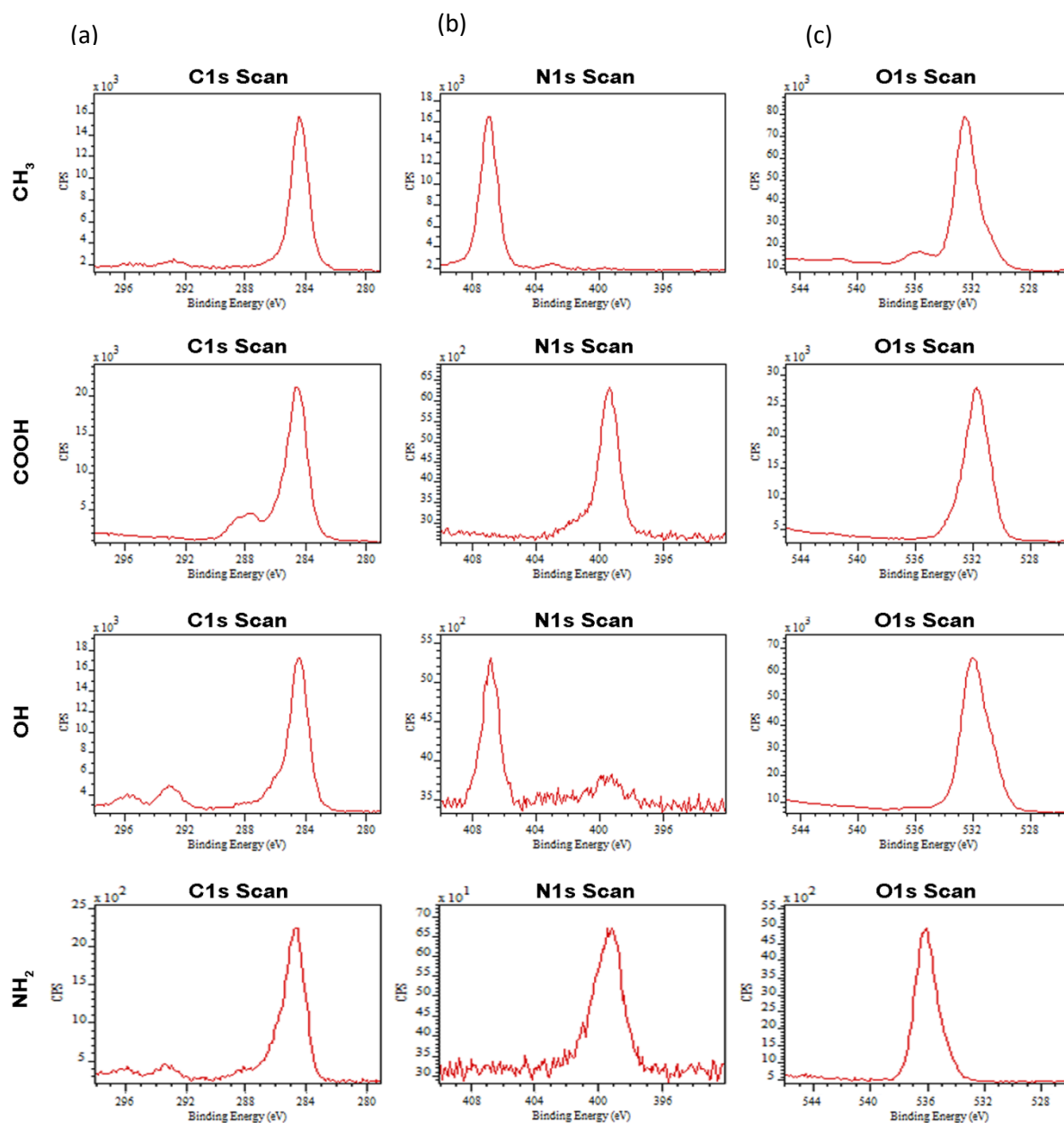


Figure 3.5 XPS spectra of functionalised silica spheres ($-\text{OH}$, $-\text{NH}_2$, $-\text{CH}_3$ and $-\text{COOH}$) of (a) C1s spectra (b) N1s and (c) O1s scan. The peaks at C1s are at ~ 284.8 eV (b) N1s binding energy is at ~ 400 eV while there are some contamination on N1s in CH_3 and OH [largely NO_3^- rather than NH] (c) O1s binding energy is at ~ 532.9 eV while NH_2 binding energy is at 536 eV.

3.3.5 Protein Serial Dilution

The working concentration of BSA (1 mg/mL) and Fg (1 mg/mL) stock were prepared as shown in Table 3.1. The serial dilutions were carried out to reduce error as shown in Figure 3.6 by preparation of stock and taking aliquots from each stock.. Sample 1 contains PBS only (control) while stock 1 has the highest protein concentration.

Table 3.1 Working Protein Concentration of BSA and Fg						
	Sample	Volume of sol. used/ mL	Volume PBS/ mL	Working Protein Conc. mg/mL	Final Protein Conc. µg/mL	
	1	0	2.50	0	0	Protein Stock =1mg/mL
Stock 1	2	7.5	0	1000.00	900.00	
	3	4.5	3	600.00	540.00	
	4	2.25	5.25	300.00	270.00	
Stock 2	5	1.6	14.5	99.38	89.44	
	6	4.5	3	59.63	53.67	
	7	2.25	5.25	29.81	26.83	
Stock 3	8	1.6	14.5	9.88	8.89	

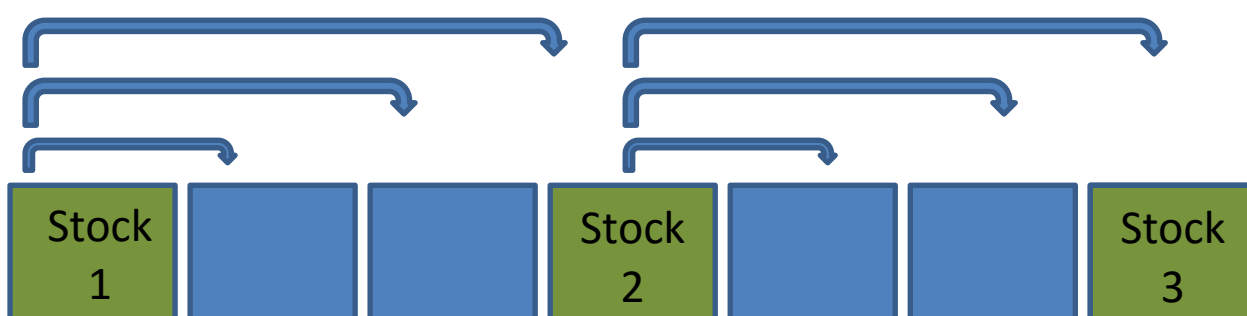


Figure 3.6 Serial dilutions of BSA and Fg concentration with less error

3.3.6 Bicinchoninic Acid Assay (BCA)

Bicinchoninic Acid assay protein quantification kit (Sigma Aldrich, BCA) is one of the most accurate measurements of protein concentration in the range 200-1,000 $\mu\text{g/mL}$. Bicinchoninic Acid Assay has less variation between different proteins than the Bradford assay. BCA assay builds a complex with peptide bonds and the reduction of Cu^{2+} ions to Cu^{+} by protein. The amount of reduced copper is proportional to the number of peptide bonds and thus to the number of protein molecules in the sample. The occurring complex has a strong optical absorption at 562 nm and the absorbance correlates directly with the number of protein molecules in the sample.⁵⁰ BCA assay is sensitive compared to other assays and display less interference. The results of BCA assay on BSA and Fg are shown in Chapter two.

3.3.7 Adsorption Isotherms

According to Lundstrom *et al*,⁵¹ adsorption isotherms often shows a step at low protein concentration, followed by an increase in adsorption as the concentration increases. Fibrinogen and albumin were used as model proteins due to their high abundance in plasma, different size, shape and variation which make the investigation applicable to biomaterial evaluation. The protein adsorption method is explained in Section 2.10. The adsorption isotherms of BSA on functionalised silica spheres is shown in Figures 3.7-3.8 showing the data presented in terms of particle chemistry and size respectively, Figure 3.9-3.10 shows similarly the adsorption profiles for Fibrinogen.

3.3.7.1 Bovine Serum Albumin -Surface Chemistry

BSA is used in protein-nanoparticle experiments due to its high abundance.

Adsorption profile of BSA at different concentration on functionalised silica nanoparticle based on physicochemical cues (chemistry and topography) is shown in Figure 3.7.

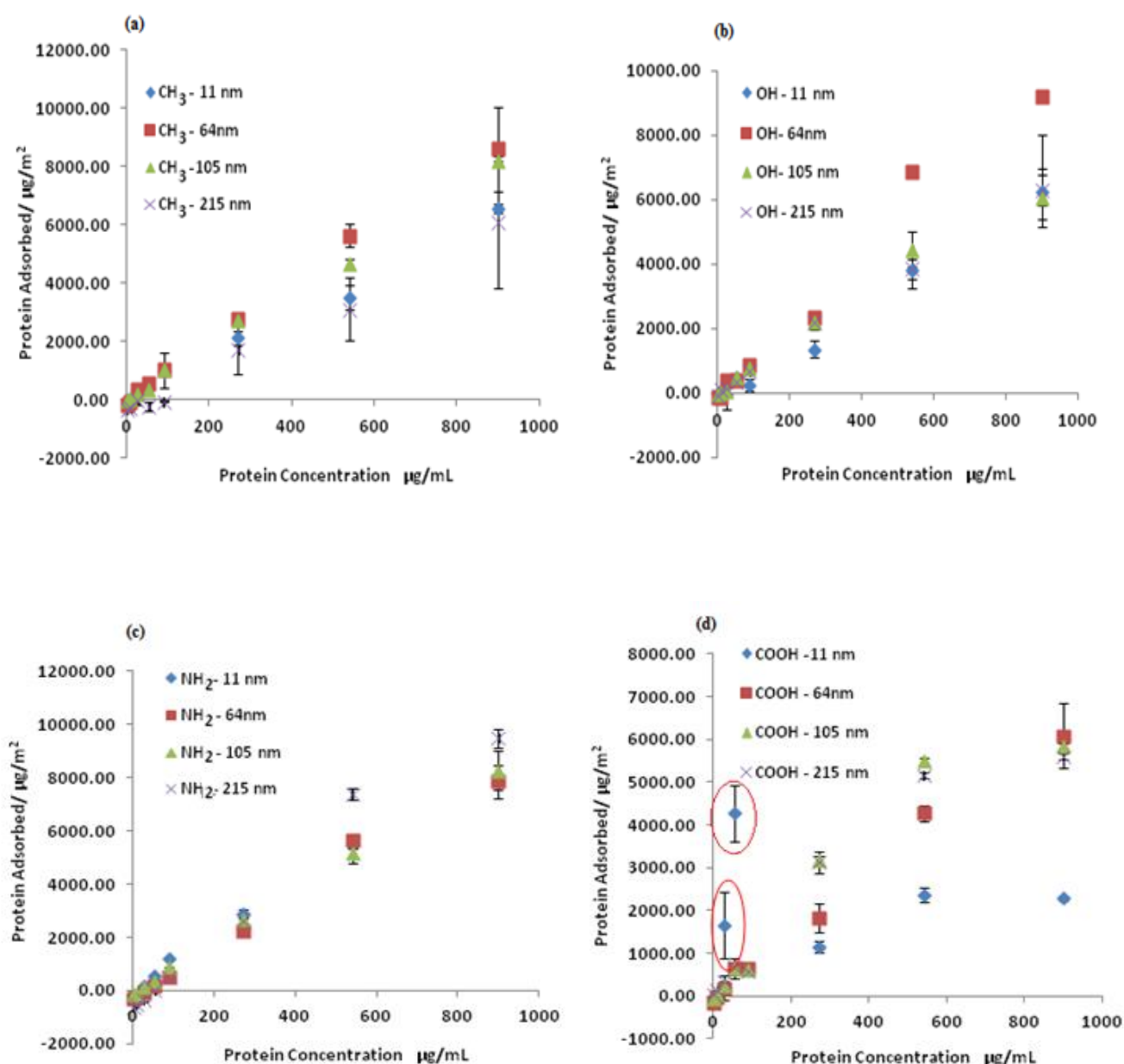


Figure 3.7 Adsorption isotherms of BSA on functionalised silica nanoparticle (a) methyl terminal group (CH_3) with different diameters of 11-215 nm (b) hydroxyl terminal group (OH) (c) amine terminal group (NH_2) and (d) carboxyl terminal group (COOH). Data shown are the mean \pm SD of three replicate samples

Figure 3.7 (a) to (d), reveals that BSA adsorption increase as concentration increases for all surface chemistry and most do not display saturation. There is variation in the amount of protein adsorbed for all particle sizes of tested reflecting difference in surface chemistry.

The adsorption of BSA on methyl surface (a) shows that 64 nm particles have the highest level of protein adsorbed as the protein concentration increases while 215 nm shows the lowest across all sizes. The spread of the variance of protein adsorbed increases as the protein concentration as illustrated; $64 > 105 > 11 > 215$ nm.

The hydroxyl terminated surface (b) shows that 64 nm particle have the highest amount of protein adsorbed compared to other sizes while the lowest amount of BSA adsorbed is for 105 nm particle. Less spread of variance was observed at lower protein concentration while an increase in spread variance is observed from 540 $\mu\text{g/mL}$ to 900 $\mu\text{g/mL}$. BSA adsorption on hydroxyl surface is illustrated from the highest to the lowest; $64 > 11 > 215 > 105$ nm.

The amine terminated surface (c) shows 215 nm particles have the highest protein adsorbed while 64nm particles have the lowest level of adsorption. There is less spread variance observed on amine surface compared to other surfaces from lower protein concentration to the highest protein concentration which is illustrate; $215 > 105 > 64.0 > 11$ nm.

The carboxylic terminated surface (d) shows wide spread variation compared to other surfaces. The massive variation makes the results inconsistent. A saturation level can be observed and two outliers (circled in red) can be seen which fit the trends on 11 nm particles. The outlier may be caused by the high tendency for aggregation due to the particle size. The highest level of adsorption is 64 nm while the lowest adsorption is 11 nm from the highest protein concentration.

Comparison of each surface chemistry shows the highest BSA adsorbed on OH is 9450 $\mu\text{g}/\text{m}^2$, NH_2 is 9500 $\mu\text{g}/\text{m}^2$, CH_3 is approximately 8600 $\mu\text{g}/\text{m}^2$ and the lowest amount adsorbed is COOH at 6033 $\mu\text{g}/\text{m}^2$.

3.3.7.2 Bovine Serum Albumin-Particle Size

The data used in section 3.3.7.1 is replotted to show relative variation of adsorption with respect to particle size differences.

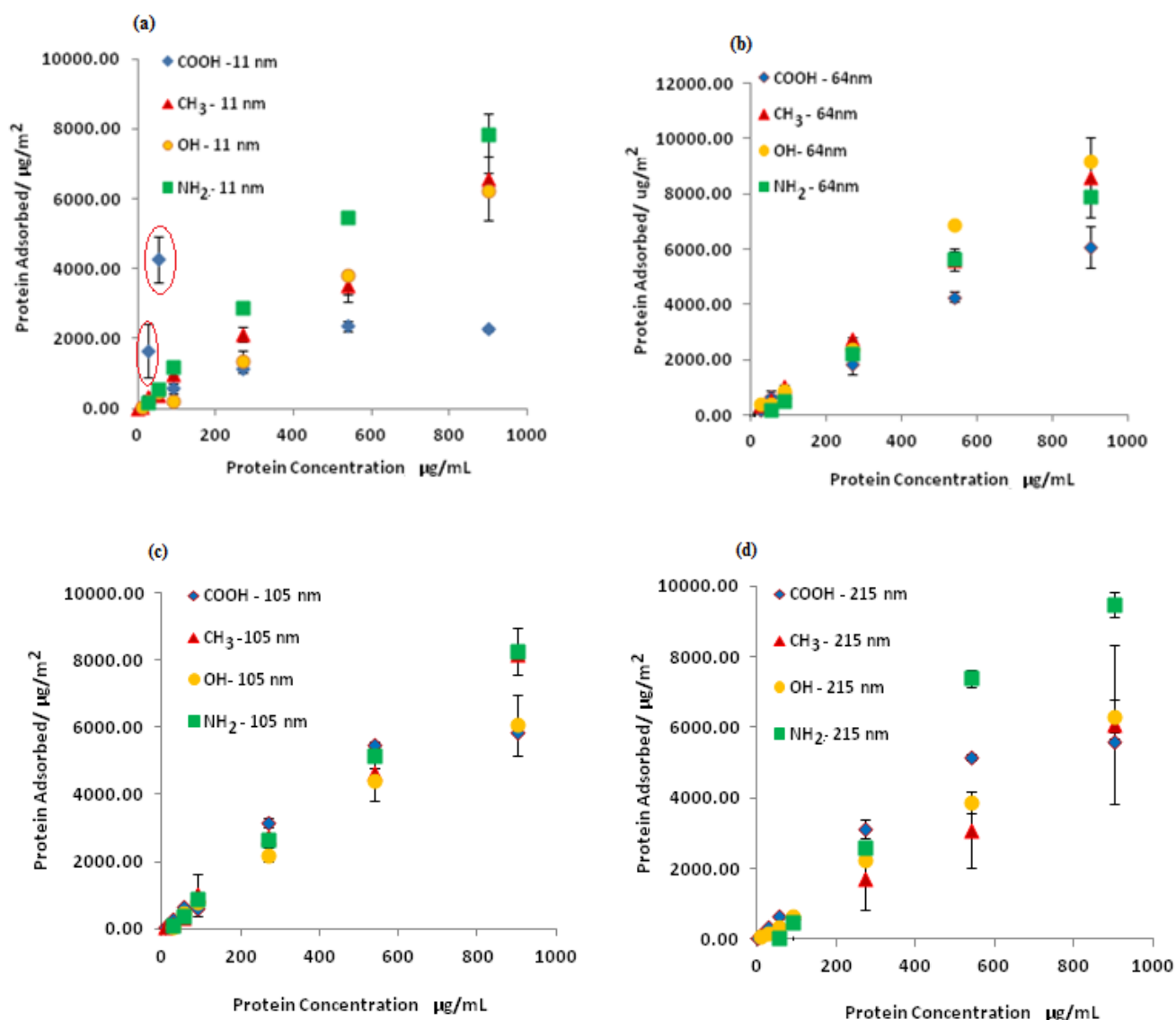


Figure 3.8 Adsorption isotherm of BSA on surface curvature (a) silane diameter size of (a) 11 (b) 64 (c) 105 and (d) 215 nm. Data shown are the mean \pm SD of three replicate samples. Error bars correspond to parameters standard deviations

The effect of particle size on BSA adsorption is shown in Figure 3.8. NH_2 has the highest amount of adsorption except at 64 nm particle where OH has the highest protein adsorbed. COOH have the least BSA adsorption from 11-214 nm.

Figure 3.8 (a) shows BSA adsorption on 11 nm nanoparticle. Saturation level is observed on COOH from 540 to 900 $\mu\text{g/mL}$. Despite the experiment being repeated three times, the same result is still obtained. Two outliers (circled in red) were observed which correlate to the result on COOH Figure 3.7 (d) where a separation variance between NH_2 and COOH at 11 nm was observed. Aside the two outlier on COOH, as the protein concentration increases, the amount of protein adsorbed on CH_3 , NH_2 and OH increases steadily from lower to higher protein concentration. NH_2 surface have the highest protein adsorbed of 7824 $\mu\text{g/m}^2$ at 900 $\mu\text{g/mL}$

Figure 3.8 (b) shows BSA adsorption on 64 nm particle. OH has the highest BSA adsorption of 8587 $\mu\text{g/m}^2$ at highest protein concentration of 900 $\mu\text{g/mL}$ while COOH have the lowest level of adsorption as the protein concentration increases. There is less spread of variance as the concentration increases while high spread is seen at the highest protein concentration, with no saturation level observed on surface chemistry.

Figure 3.8 (c) shows on 105 nm particle, there is less spread variance as the concentration increases. NH_2 has the highest BSA adsorption of 8185 $\mu\text{g/m}^2$ at 900 $\mu\text{g/mL}$. Saturation level is not observed as compared to Figure 3.8 (a).

A consistent spread separation is observed on 215 nm particle at 540-900 $\mu\text{g/mL}$, as shown in Figure 3.8 (d). NH_2 still maintain the highest level of adsorption while COOH and CH_3 have the lowest BSA adsorption as the protein concentration increases

Comparison of particle size shows 215 nm have the highest protein adsorbed of 9479 $\mu\text{g/m}^2$ while 11 nm have the lowest protein adsorbed of 7824 $\mu\text{g/m}^2$ at 900 $\mu\text{g/mL}$.

3.3.7.3 Fibrinogen (Fg) -Surface Chemistry

Adsorption profiles for Fg on functionalised silica nanoparticles are shown in Figure 3.10

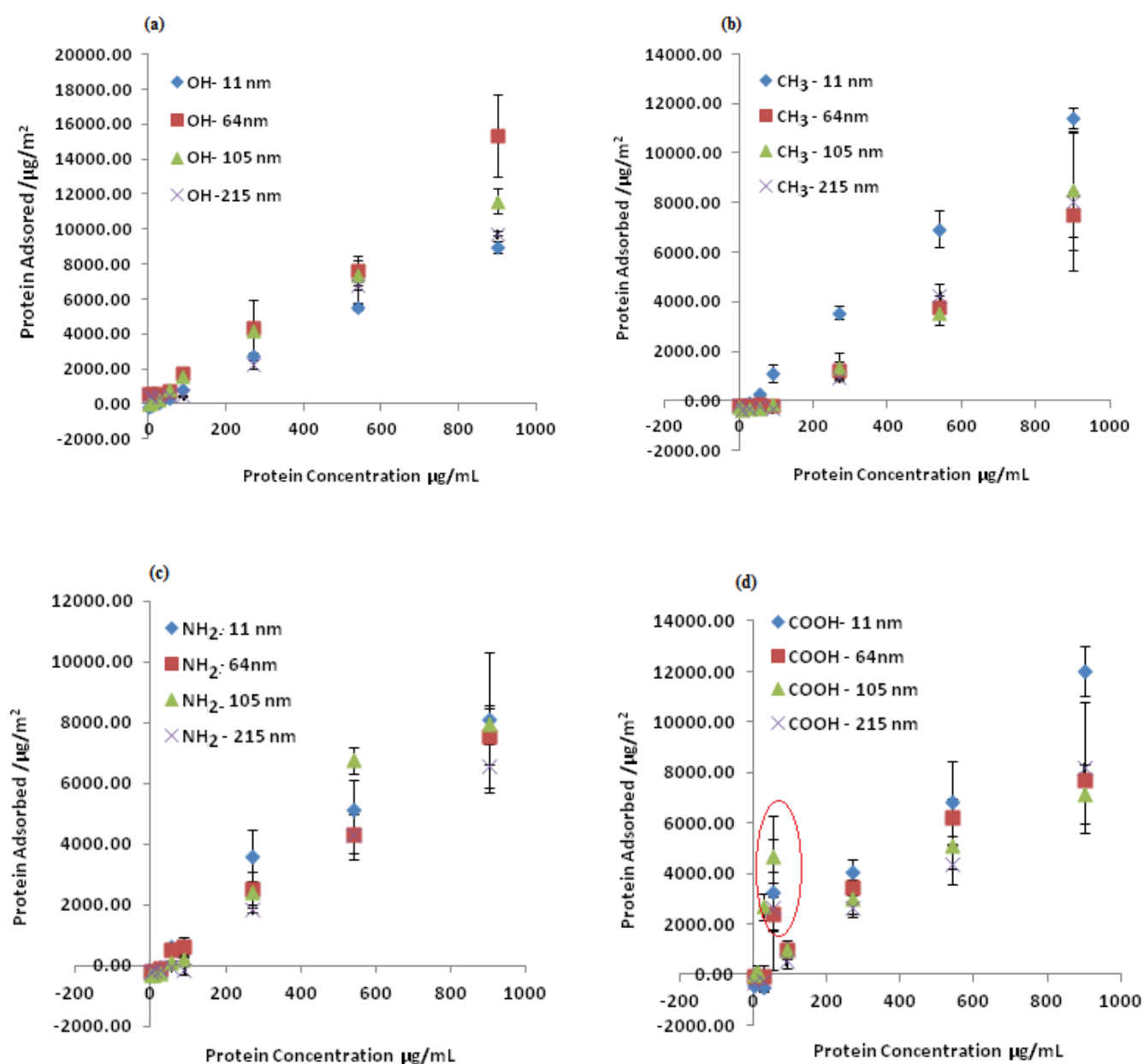


Figure 3.9 Adsorption isotherm of Fg on surface chemistry (a) OH (b) CH₃ (c) NH₂ (d) COOH. Data shown are the mean \pm SD of three replicate samples. Error bars correspond to parameters standard deviation

Fg adsorption increases as the concentration of Fg increases for all surface chemistry and there is no saturation observed on any surface. There is variation in amount of protein adsorbed for all particle size tested due to differences in surface chemistry.

Fg adsorption on hydroxyl surface, Figure 3.9 (a) shows that 64 nm particles have the highest amount of protein adsorbed compared to other sizes while the lowest amount of protein adsorbed is for 11 nm particles. Less spread variance was observed at lower protein concentration while an increase in spread variance is observed as the protein concentration increases, 900 µg/mL. Fg adsorption on hydroxyl surface is illustrated from the highest to the lowest; 64>105 >215 >11 nm.

Methyl surface in Figure 3.9 (b) shows that the 11 nm particles have the highest level of protein adsorbed as the protein concentration increases while the 64 nm particles shows the lowest adsorption level. The 11 nm particles show a consistent increase as the protein concentration increases from the lowest to the highest. The spread of the variance of protein adsorbed increases as the protein concentration as illustrated; 11 > 105 >215 > 64 nm.

The amine terminated surface in Figure 3.9 (c) shows the 11 nm particles have the highest protein adsorbed while 215 nm particles have the lowest level of adsorption. There is less spread variance observed initially, as the protein concentration increases, there is spread variance at 270 and 540 µg/mL but as the concentration reaches the highest, 900 µg/mL, there is less spread variance compared to on amine surface compared to other surfaces. The protein adsorption is shown below; 11 >105 >64 >215 nm.

The carboxylic surface as shown in Figure 3.8 (d) shows massive variation compared to other surfaces as the protein concentration increases. A few outliers (circled in red) can be observed on 11, 64 and 105 nm which may be due to aggregate and makes the results inconsistent. The highest level of adsorption is 11 nm while the lowest adsorption is 105 nm from the highest protein concentration. Comparison of each surface chemistry shows the

highest amount adsorbed on OH is 15340 $\mu\text{g}/\text{m}^2$, COOH at 12040 $\mu\text{g}/\text{m}^2$, CH_3 is approximately 11400 $\mu\text{g}/\text{m}^2$, and the lowest amount adsorbed is NH_2 is 7940 $\mu\text{g}/\text{m}^2$. Hydrophilic surface (OH) has the highest Fg adsorption while positively charge (NH_2) have the lowest Fg adsorption.

3.3.7.4 Fibrinogen-Influence of Particle Size

The data used in fibrinogen-surface chemistry is replotted to show the relative variation of adsorption with respect to particle size differences as shown in Figure 3.10

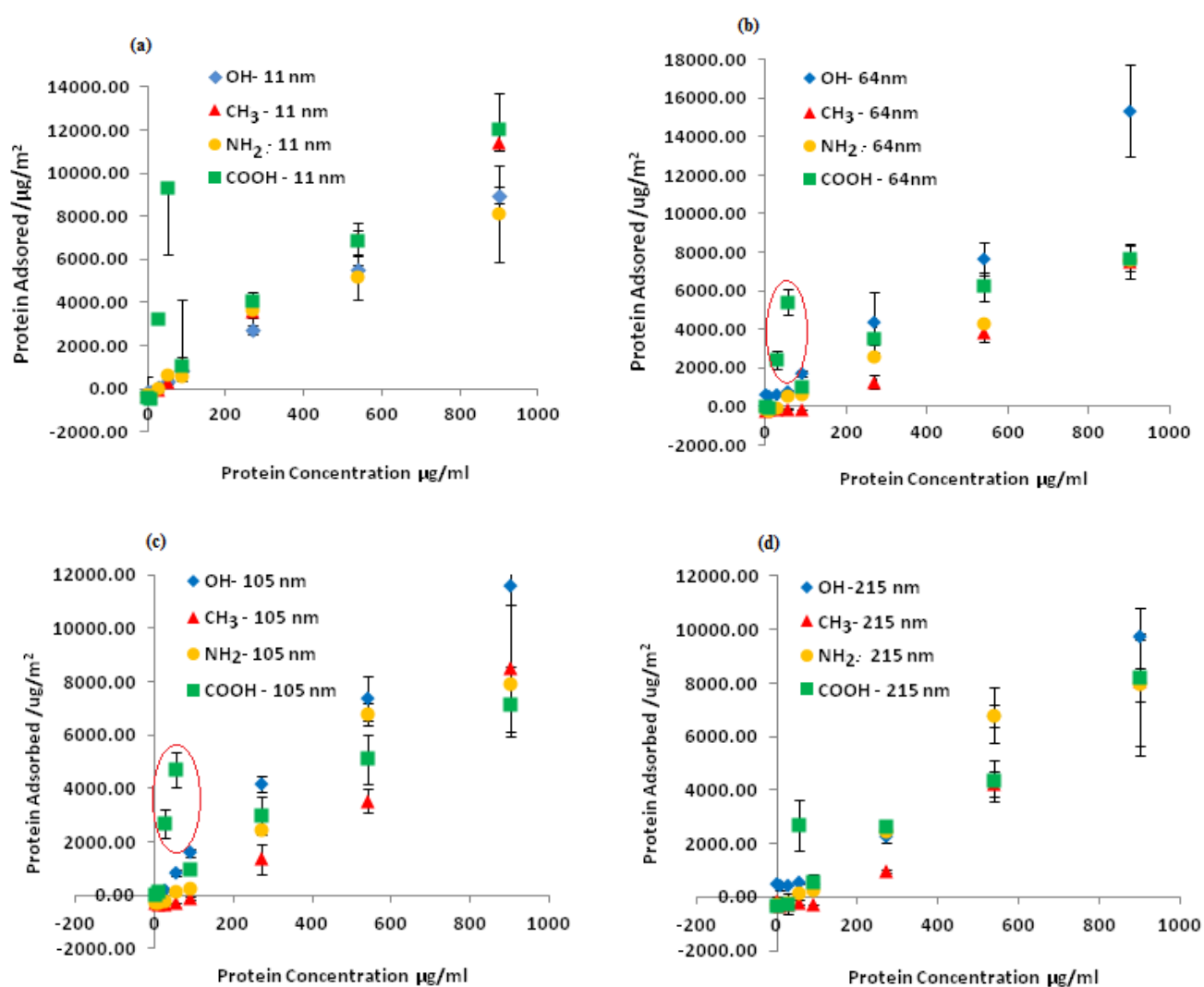


Figure 3.10 Fg adsorption isotherm on surface curvature (a) 11 nm (b) 64.0nm (c) 105 nm (d) 215 nm. Data shown are the mean \pm SD of three replicate samples. Error bars correspond to parameters standard deviations

Fg adsorption on particle size increases as the protein concentration increases for particle sizes. The smaller the size of the silica particles, the higher the amount of protein adsorbed. i.e. 215 nm particle adsorbed at $9753 \mu\text{g}/\text{m}^2$ while 64 nm particles adsorbed at $15,338 \mu\text{g}/\text{m}^2$. This may be due to the molecular size of the protein although as the protein concentration increases, protein adsorbed increases.

The adsorption of Fg on 11 nm particle, Figure 3.10 (a) reveals COOH display the highest level of adsorption with less spread variation observed. The highest protein adsorbed at highest protein concentration of $900 \mu\text{g}/\text{mL}$ is at $11,427 \mu\text{g}/\text{m}^2$ while NH_2 is the lowest protein adsorbed is $8102 \mu\text{g}/\text{m}^2$ at highest protein concentration.

Spread variation is observed on 64 nm particle, Figure 3.10 (b) with two outliers (circled in red) which fits outside the trends. An increase from lower protein concentration to highest protein concentration is observed on 11-215 nm particles. Hydroxyl surface ($-\text{OH}$) have the highest Fg adsorption at $900 \mu\text{g}/\text{mL}$ while NH_2 have the lowest Fg adsorption.

The Fg adsorption on 105 nm as display in Figure 3.10 (c) shows as the protein concentration increases, protein adsorbed increases. Few outliers are observed (circled in red) on COOH surface. The highest protein adsorbed at $900 \mu\text{g}/\text{mL}$ is at $11,604 \mu\text{g}/\text{m}^2$ on OH surface while COOH surface have the lowest protein adsorption.

Figure 3.10 (d) shows Fg adsorption on 215 nm, as the concentration increases, the amount of protein adsorbed increases. OH have highest Fg adsorption on concentration of $900 \mu\text{g}/\text{mL}$ at $9753 \mu\text{g}/\text{m}^2$ while NH_2 have the lowest protein adsorbed at highest protein concentration of $900 \mu\text{g}/\text{mL}$. The 64 nm have the highest Fg adsorption at $15,000 \mu\text{g}/\text{m}^2$ while 215 nm have the lowest Fg adsorption on silica functionalised surface.

3.3.8 Affinity Constant and Saturation Amount

The Langmuir adsorption Isotherm describes the adsorption equilibrium between solutes and solid surfaces having n binding sites.⁵² The Langmuir Isotherm is an equilibrium binding model which has been applied to several experimental studies of protein adsorption onto silica nanoparticles and polymer brushes.⁵³⁻⁵⁵ The Langmuir isotherm relates the adsorption sites on silica functionalised nanoparticle containing bound proteins, θ , to the binding constant, K_d which is given by this Equation 3.1 and Figure 3.11

$$\frac{Q}{Q_m} = \frac{K_d C}{1 + K_d C} \quad \text{Equation 3.1}$$

The Langmuir model describes the relationship between the adsorbate surface concentration ‘ Q ’ and the concentration in the phase adjacent to the surface ‘ C ’, ‘ Q_m ’ is the maximum adsorbate binding capacity and ‘ K_d ’ is a binding affinity constant.

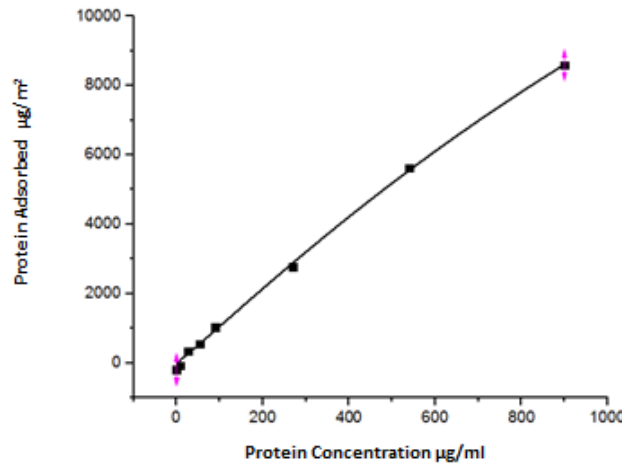


Figure 3.11: Curve fitting of BSA on particle size 64 nm of methyl (CH₃) functional group. Solid line represents the fit of Langmuir model. $R^2 = 0.9987$; $n=1$; $K_d = 1.74 \mu\text{gm}^2$; $Q_m = 2.3 \mu\text{gm}^2$.

Hill equation,⁵⁶⁻⁵⁸ was used to calculate the binding affinity of protein on each surface chemistry and curvature using the equation in Equation 3.2. OriginPro 9.0 was used to calculate the saturation amount (Q_m) and affinity constant (K_d) of protein adsorbed on each surface chemistry and curvature. The Hill coefficient, was fixed, $n=1$. The affinity constant (k_d) and saturation value (Q_m) was calculated for each of the data sets shown in Figures 3.7-3.10 to give the following data presented in Figure 3.12.

$$y = Q_m \frac{x^n}{k_d^n + x^n} \quad \text{Equation 3.2}$$

The affinity constant of BSA and Fg is shown in Figure 3.11 to understand the effect of surface chemistry and curvature on nanoparticles.

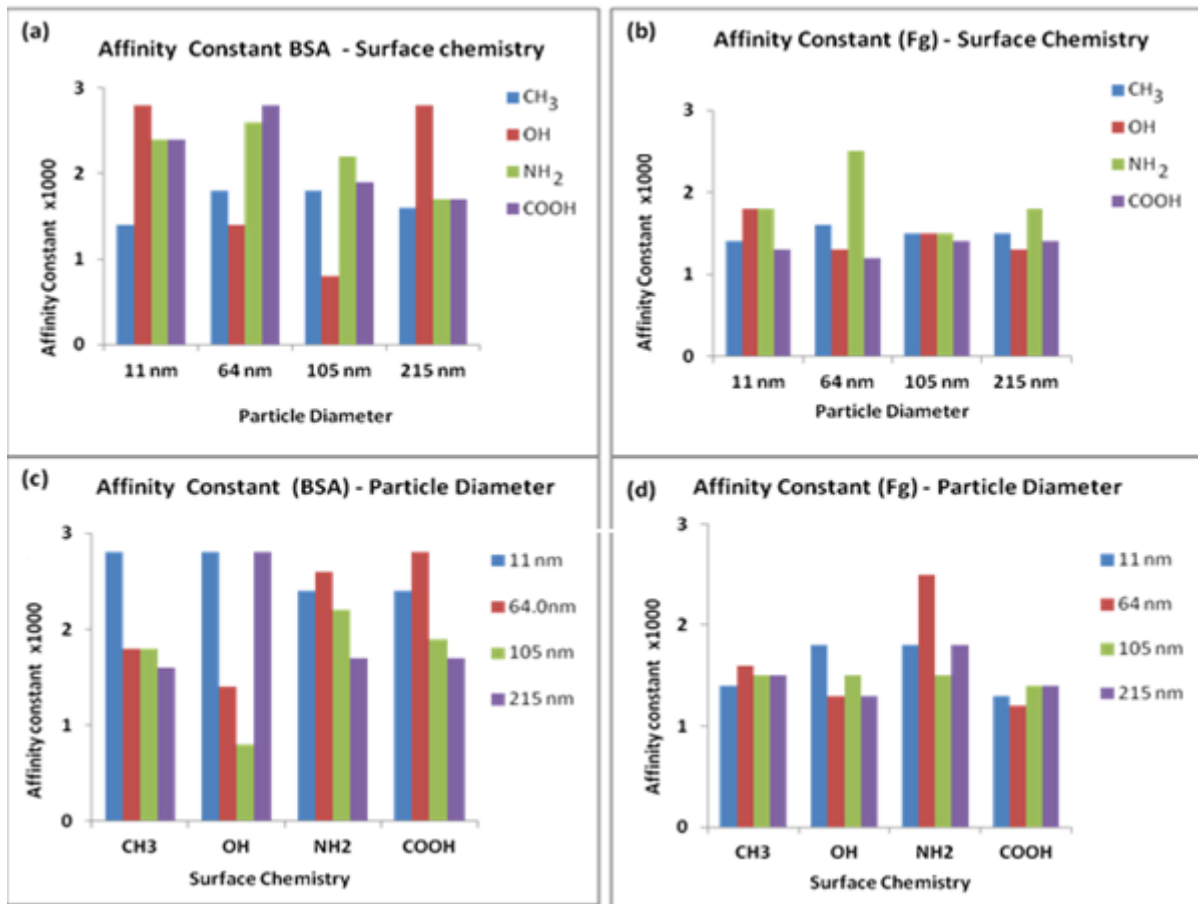


Figure 3.12 Summary of measured affinity constant, K_d , for BSA and Fg presented in terms of surface chemistry comparison (a) BSA (b) Fg and surface curvature comparison (c) BSA and (d) Fg

The affinity constant (k_d) describes the strength of the interaction between protein and the nanoparticle surface as shown in Figure 3.12 (a) and (b) shows the plot of surface chemistry vs affinity constant of varying sizes while (c) and (d) shows the affinity constant vs particle diameter using BSA and Fg on varying surface chemistries.

The affinity constant value of BSA and Fg in Figure 3.12 (a) and (b) shows that the binding constant value varies from the smallest to the largest sphere. The affinity constant of BSA on different surface chemistry shows a steady decrease as reported on the particle diameter effect in Figure 3.12 (a). The hydroxyl surface (OH) has the highest affinity constant on 11 nm particles while amine surface (NH_2) have the highest affinity constant value in Figure 3.12 (b). Although, as the particle size decreases, the binding affinity should increase, but BSA and Fg results is different and does not correspond to the general rule based on the effect of surface chemistry.

The affinity constant of BSA and Fg in terms of particle diameter is replotted using the data plot in Figure 3.12 (a) and (b). The 11 nm displays the highest affinity on CH_3 surface while 11nm and 215 nm particles have the highest affinity constant on OH surface and 64 nm particles have the highest affinity on NH_2 and COOH surface. The result of Fg in Figure 3.12 (d) shows lower affinity constant, i.e. majority of the surface site were saturated quickly. 64 nm on NH_2 surface have the highest affinity constant.

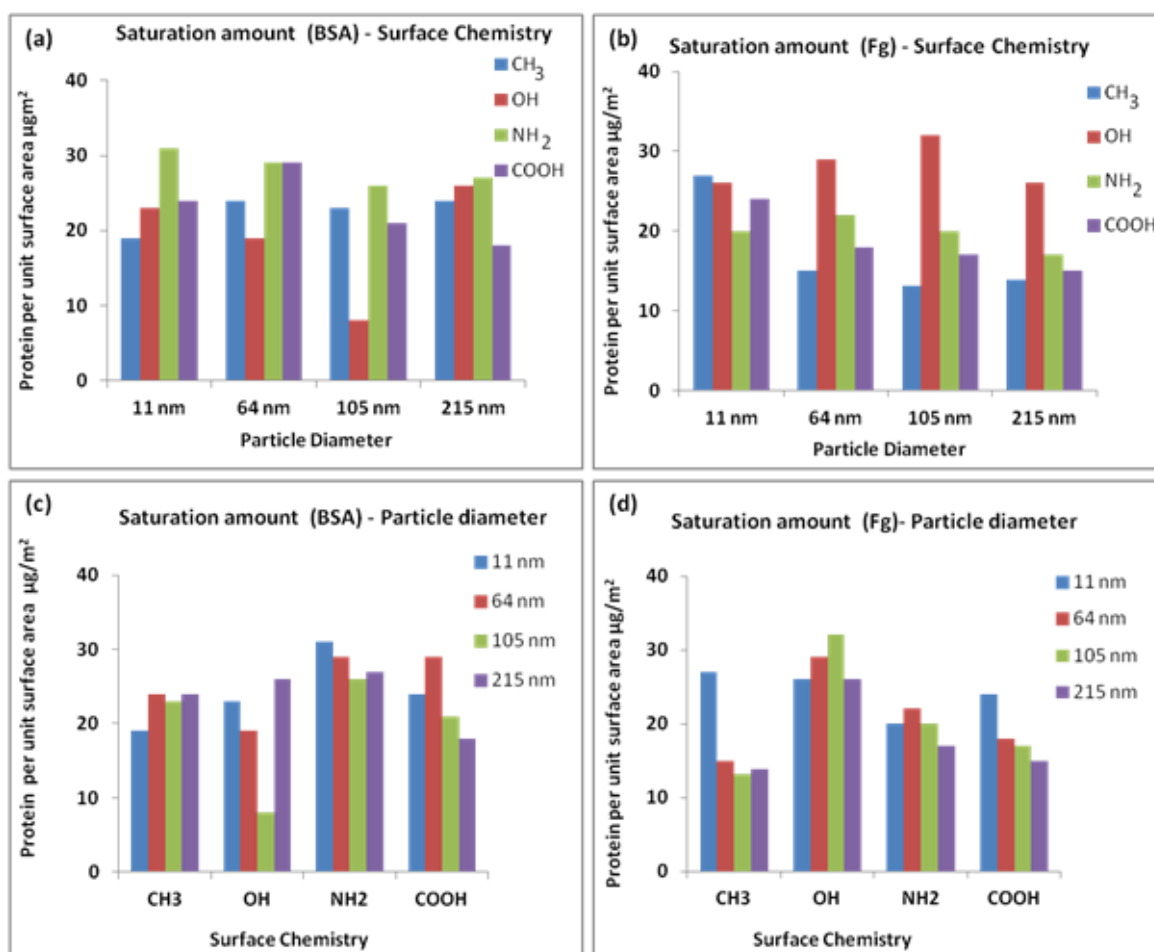


Figure 3.13 Summary of measured saturation amount (Q_{max}) for BSA and Fg on surface chemistry and particle diameter of saturation amount on (a) BSA- particle diameter, (b) Fg- particle diameter, (c) BSA-surface chemistry and (d) Fg-surface chemistry

The saturation amount shows the maximum capacity the protein had occupied on each functional groups and particle size. Figure 3.13 (a) shows the saturation amount of BSA on particle size. The highest saturation amount of BSA can be seen in 11 nm of (NH₂) while smallest saturation amount on OH surface is 105 nm particles. There is a steady increase in saturation amount of CH₃ surface on BSA as the particle size increases.

The saturation amount of BSA and Fg differs as seen on Figure 3.13 (a) and (b). BSA saturation amount in terms of surface chemistry shows NH₂ and COOH have the highest saturation amount per unit area while 11 nm and 64 nm have the highest saturation amount in terms of surface curvature. The saturation amount of BSA on NH₂ reduced from the lowest particle diameter of 11 nm to 215 nm. Fg increases from 11 nm to 105 nm on hydrophilic surface (-OH) while a steady decrease from 11 nm to 215 nm on hydrophobic surface CH₃ is observed.

Saturation amount of BSA and Fg in Figure 3.13 (c) and (d) shows BSA on NH₂ surface have the highest saturation amount at 11 nm particles and decrease as the particle size increases. Fg on OH surface have the highest saturation amount compared to other surface chemistry for the particle size of 11-215 nm. This may be due to feature of OH surface i.e. hydrophilic in nature while CH₃ and COOH shows a rapid decrease in saturation amount from the lowest particle diameter to the highest particle diameter, this is due to the wettability and the size of the surfaces. Different variations were observed on saturation amount of BSA and Fg on nanoparticle physicochemical cues (surface chemistry and curvature) which is similar to reports published by other researcher.⁶⁸

3.3.9 Analysis of Amide I band position for investigation of secondary structure

The conformation changes of proteins adsorbed on surfaces modified with hydrophilic (OH) groups were assessed using software known as GRAMS/A1. The amide I region of approximately ($1600\text{--}1750\text{ cm}^{-1}$) were focused upon which is due to its C=O stretching vibration. The amide I region shows a varying secondary structure of alpha helices, beta sheet, beta turn and random coil which gives to different vibrational frequencies as shown below in Figure 3.14 ;

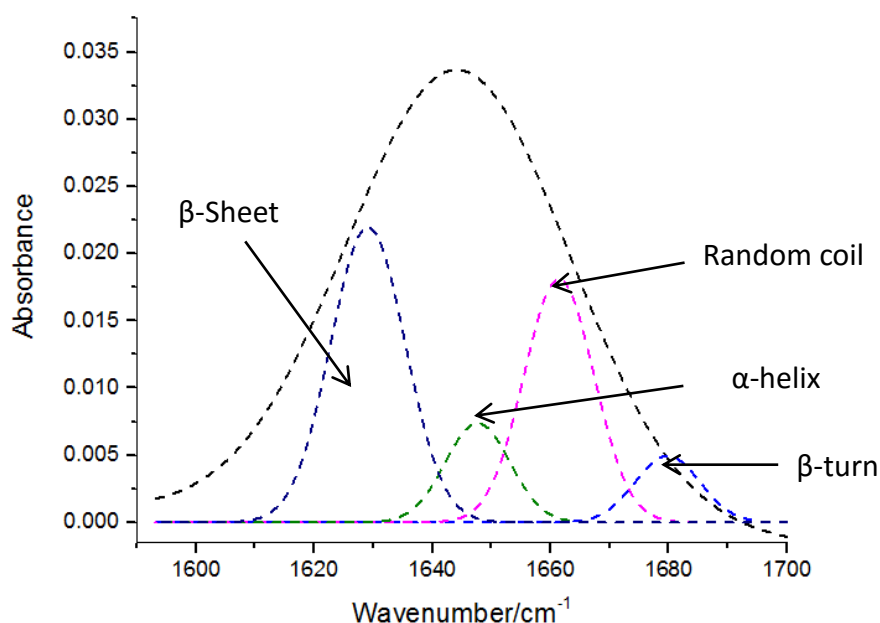


Figure 3.14 Results of FTIR analysis on the Amide I band for bovine serum albumin (BSA) on hydroxyl surface (OH) of particle size of 215 nm at protein concentration of 900 $\mu\text{g/mL}$.

The dataset were obtained from dataset which was used to analyse the secondary protein structure in terms of alpha, beta sheet, beta turn or random coil. The secondary structure of protein on different surface chemistries using BSA is shown in Figure 3.15, CH_3 and OH surface were only displayed while COOH and NH_2 are in Appendix A. Secondary structure equals 100, i.e at 900 mg/mL on 11nm, α -helix is 22.2%, β sheet is 30.8%, β turn is 33.3% while random coil is 13.7% all add up to 100%.

(I) Bovine Serum Albumin (CH₃)

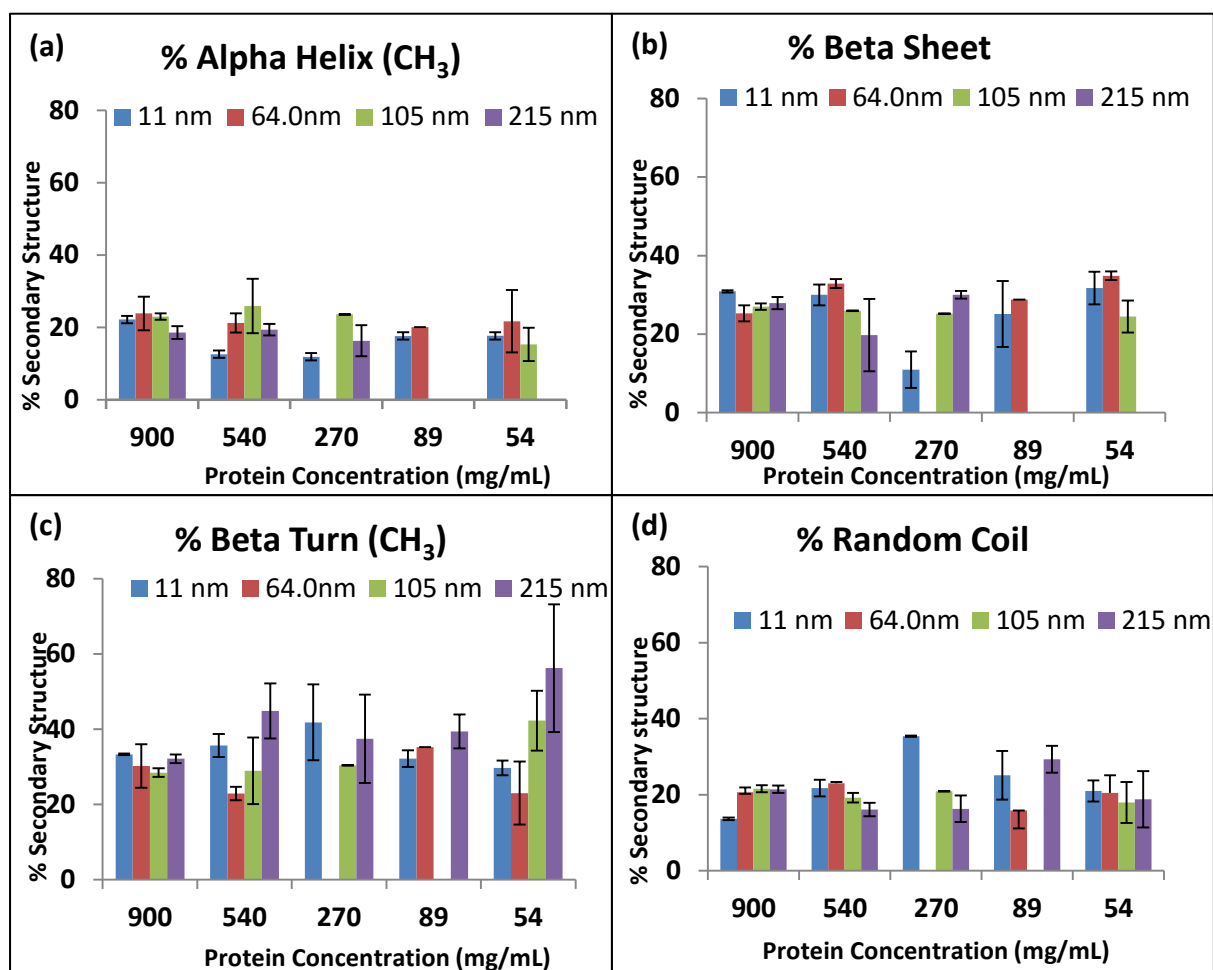


Figure 3.15 Conformation assessment of BSA on methyl surface (-CH₃) of curvature 11-215 nm (a) α - helix, (b) β -sheet (c) β - turn and (d) random coil .A blank chart illustrate a weak FTIR signal therefore a noisy spectra with low confidence in the fitting. Data shown are the mean \pm SD of three replicate samples.

The result in Figure 3.15 shows the effect of protein conformation on surface chemistry and curvature. The percentage of α -helix, β sheet, β turn and random coil on surface chemistry is represented on the bar chart.

Figure 3.15 (a) shows the percentage of secondary structure of α -helix vs protein concentration of BSA on methyl surface (CH₃) on particle size of 11-215 nm. Decrease in α -helix as protein concentration decreases from 900 and 270 mg/mL at 11 nm particle size

while an increase can be observed from 270 to 54 mg/mL. At 105 nm is observed to have the highest α -helix at 540 mg/L although there is high presence of alpha helix on 64 nm.

Figure 3.15 (b) shows the result for the percentage of β sheet result on methyl surfaces (CH_3) on different protein structure and particle diameter. Higher percentage of β sheet from higher protein concentration to lower concentration is observed. The 11 nm particle shows a lower presence of β sheet at 270 mg/mL while 64 nm have the highest percentage of β sheet on 11-215 nm.

At higher protein concentration of 900 mg/mL, 11 nm particle display an increase of beta turn until 270 mg/mL when decrease was observed from 27 mg/mL. The overall highest percentage structure of beta turn of 60 % is observed on 54 mg/mL at 215 nm particle in Figure 3.15 (c)

Figure 3.15 (d) display 11 nm particle have the highest percentage of random coil at 270 mg/mL. The percentage of secondary structure of BSA on hydrophobic surface (CH_3) shows a lower percentage of α -helix and random coil is observed while β sheet and β turn have the highest percentage structure, this result is not surprising since albumin is known to have a lower helical content when on hydrophobic surface.⁶⁵

(II) Bovine Albumin Serum (OH)

The percentage secondary structure change of BSA on hydroxyl surface (OH) at different nanocurvature is shown in Figure 3.16

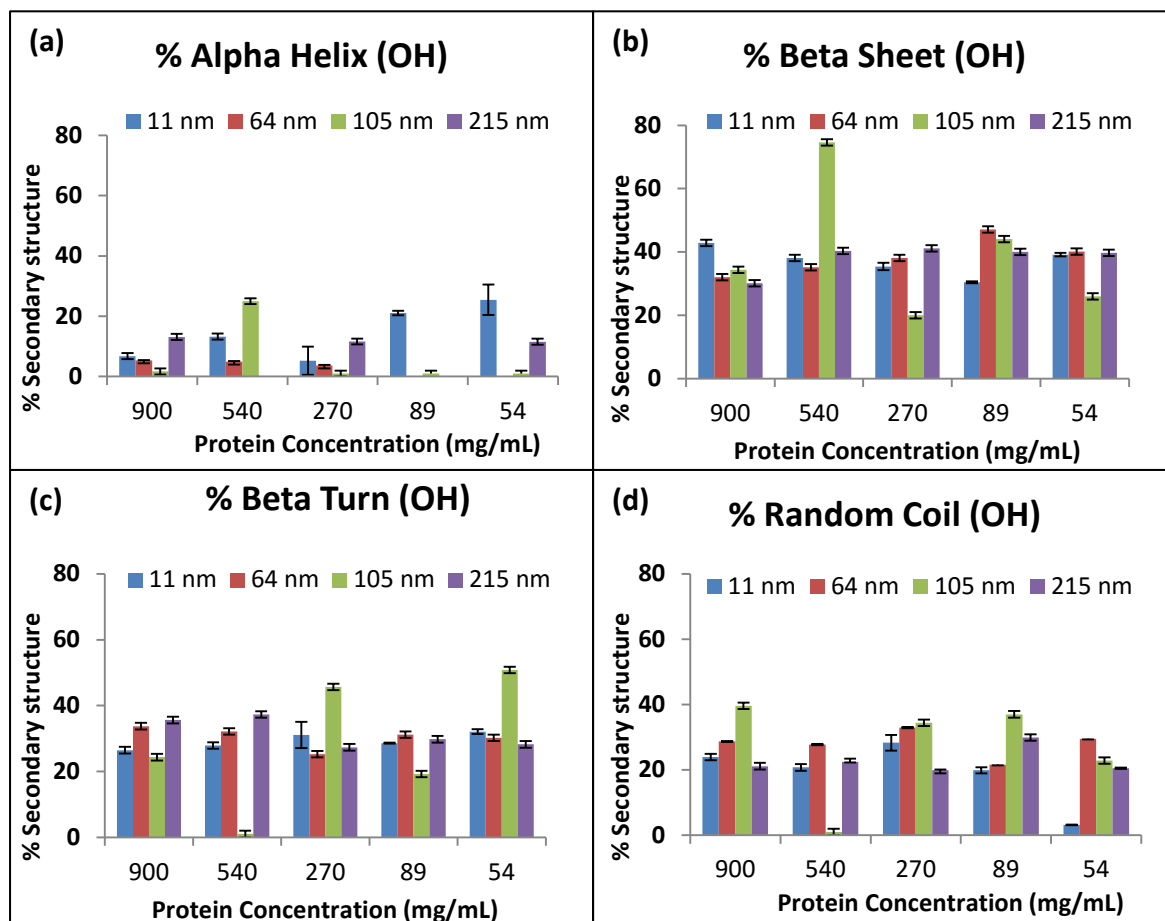


Figure 3.16 Conformation assessment of BSA on hydroxyl surface (OH) of curvature 11-215 nm (a) α -helix, (b) β -sheet (c) β -turn and (d) random coil. Data shown are the mean \pm SD of three replicate samples, n=3.

The conformation change on hydroxyl surface (OH) has a well organized structure from the β turn to the random coil as shown in Figure 3.16. There is less presence of α -helix structure on OH surface as shown in Figure 3.16 (a). The percentage of α -helix on 11 nm particle shows a decrease from the lowest protein concentration to highest protein concentration, i.e. 54 to 900 mg/mL. No major change was observed on the largest particles

from high BSA concentration to low BSA concentrations. The 105 nm particles have the highest BSA adsorption at 540 mg/mL.

High presence of β -sheet is observed on curvature of 11-215 nm on OH. The percentage of secondary structure is high in β -sheet results across all particle diameters. There is a major decrease observed on 64 and 105 nm from lower protein concentration to highest protein concentration as seen in Figure 3.16 (b). The 105 nm particles displays the highest BSA adsorption at 540 mg/mL.

There is no consistent result observed on Figure 3.16 (c) from the lower protein concentration to higher protein concentration on β -turn on hydroxyl surface. At 11 nm on 54 mg/mL, 32% of β -turn is achieved while the larger spheres of 105 nm have 28% of β -Turn. The highest protein concentration shows an opposite result of higher percentage of β -Turn on 215 nm compared to 11 nm particles. The trend observed on CH_3 (hydrophobic) and OH (hydrophilic) surface is different. BSA adsorbed more on the hydrophilic surface compared to the hydrophobic surface with an increase rate observed in beta sheet on all particle sizes.

BSA adsorbed more on larger spheres of 105 nm particles with a high percentage secondary structure of β -turn and random coil across the protein concentration while the smallest sphere of 11 nm particles displays the lowest percentage structure of approximately 30 % on β -Turn and random coil. As the concentration increases, there is an increase of random coil on 64 nm particles as shown in Figure 3.16 (d).

Conformation assessment of Fg on functionalized silica nanoparticle is shown in Figure 3.17. The result of CH₃ and OH surface is discussed in this chapter while COOH and NH₂ surface results can be found in Appendix 2.

(III) Fibrinogen (CH₃)

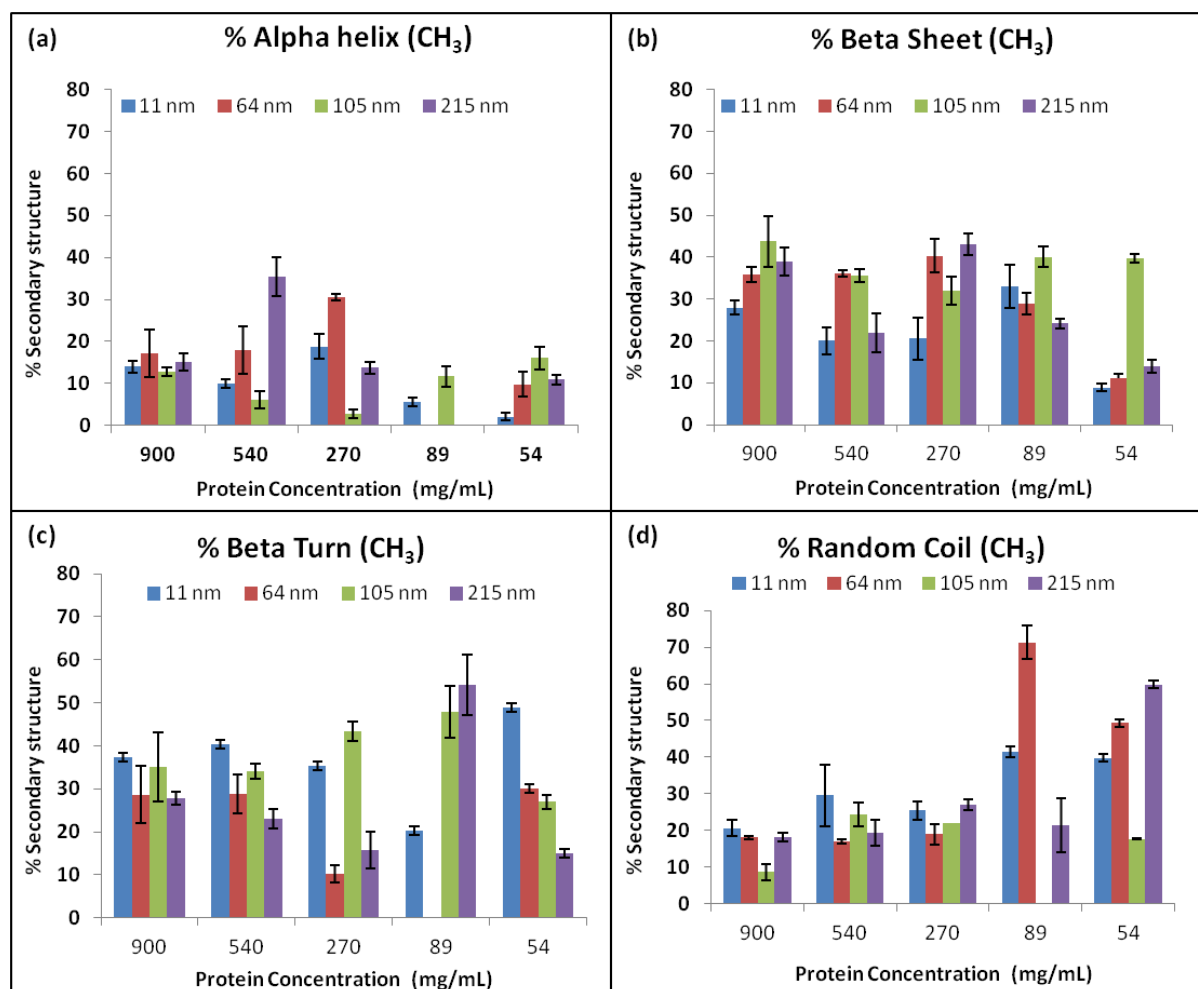


Figure 3.17 Conformation assessment of Fg on methyl surface (CH₃) of 11-215 nm (a) α - helix, (b) β -sheet (c) β - turn and (d) random coil. Data shown are the mean \pm SD of three replicate samples, n=3.

The presence of α -helix structure is lower compared to other secondary structures as shown in Figure 3.17 (a). The percentage of secondary structure of α -helix on 64 nm is approximately 30% on Fg concentration of 270 mg/mL; 215 nm display the highest

percentage (35%) of alpha helix at 540 mg/ml while 11 nm display the lowest presence of α -helix on majority of the Fg concentration.

There are more presence of β -sheet data on Figure 3.17 (b) from 11 -215 nm particles. The percentage of β -sheet is high on 64 and 105 nm particles compared to 11 nm particles at protein concentration of 900 mg/mL. At lower Fg concentration (54 mg/mL), the percentage of β sheet is lower on all particle sizes while at higher Fg concentration, there is high presence of β sheet on particle sizes.

There are variations in β -turn results as Fg concentration increases. 215 nm particles have the highest percentage of β - turn at 89 mg/mL, 11 nm have the highest percentage of β -turn at 540-900 mg/mL. 105 nm particle on methyl surface (CH_3) decreases steadily on Fg concentration of 89 to 270 mg/mL. Rapid decrease of β -turn on 215 nm is observed from 89-900 mg/mL as shown in Figure 3.17 (c).

Less presence of random coil is observed at higher protein concentration of 270 to 900 mg/mL as seen in Figure 3.17 (d). As the Fg concentration increases, the percentage of random coil decreases rapidly from 89-900 mg/mL. The 64 nm have the highest presence of random coil at Fg concentration of 270 mg/mL.

The conformation assessment of Fg on hydroxyl (OH) is shown below in Figure 3.18, the percentage of alpha helix, beta sheet, turn and random coil on each curvature.

(IV) Fibrinogen (OH)

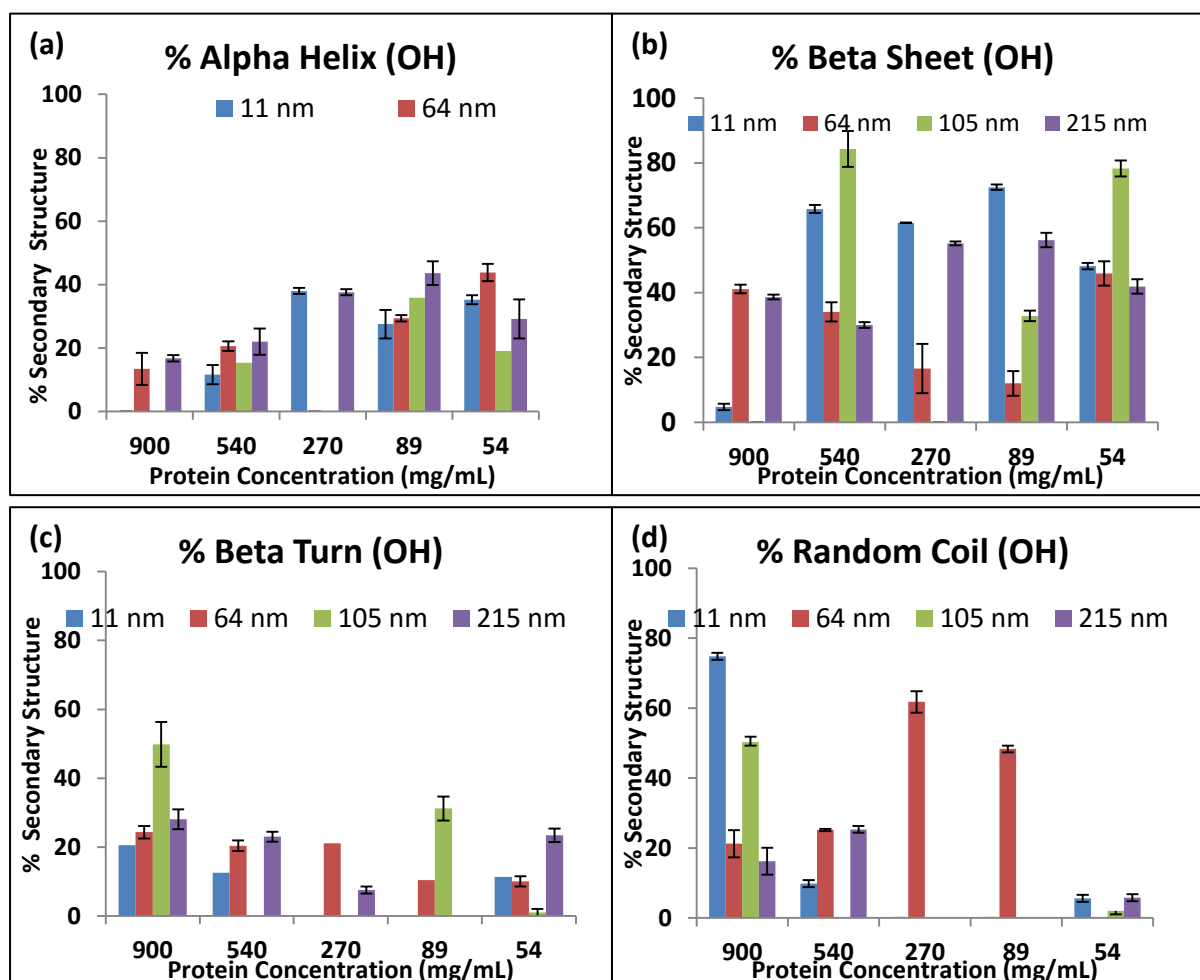


Figure 3.18 Conformation assessment of Fg on hydroxyl surface (OH) of 11-215 nm (a) α -helix, (b) β -sheet (c) β -turn and (d) random coil. Data shown are the mean \pm SD of three replicate samples, n=3

Secondary protein structure of Fg on OH surface is shown in Figure 3.18. The conformation change on hydroxyl (OH) surface is more disordered compared to the methyl (CH_3) surface.

The percentage of alpha helix on Figure 3.18 (a) shows high percentage on 64 nm and 215 nm only at lower protein concentration. The 64 nm particles at lower Fg concentration of 54 mg/mL have the highest percentage of α -helix at 43.8 % compared to 215 nm particle of 29 % at 54 mg/mL. Fg concentration of 900 mg/mL, shows a lower presence of α - helix on 64 and 215 nm particles.

The percentage of β -sheet to alpha helix, beta turn and random coil is higher as shown in Figure 3.18 (b). β - sheet on 105 nm particles have a high percentage at 540 and 54 mg/mL. 64 nm have a lower percentage of β -sheet at 89 and 270 mg/mL.

Figure 3.18 (c) and (d) shows less presence β - turn and random coil at each protein concentrations. The presence of β - turn is observed on 64 nm particles at Fg concentration of 54-900 mg/mL in Figure 3.22 (c) .The 105 nm particles have the highest presence of β -turn at 900 mg/mL. The 64 nm particles have the highest presence on random coil on Fg concentration of 89 and 270 mg/mL while 11 nm particles have the highest percentage of random coil at Fg concentration of 900 mg/mL as shown in Figure 3.18 (d). There are major differences observed on each secondary protein structure of surface chemistry and curvature.

3.4 Discussion

Functionalised silica nanoparticles of NH_2 (positively charge), CH_3 (Hydrophobic), COOH (negatively charge) and OH (Hydrophilic) were successfully synthesis and characterised to confirm the chemical structure of each functional groups. The four functional groups were used for this experiment to give insight and understanding of how surface chemistry and topography affects protein- adsorption since surface functionalization is known to influence protein-particle interactions.⁵⁹⁻⁶⁴ Silica nanoparticles ranging from 11-215 nm were used to understand and compare effects of surface chemistry and particle size on protein-nanoparticle interactions.

BSA and Fg have different property which may affect the conformation and regulate protein adsorption on the nanoparticle surface. The results show that nanoparticle size and chemistry strongly influence BSA-silica nanoparticles and Fg-silica nanoparticle interactions. The adsorption Isotherms of BSA (Figure 3.7-3.8) and Fg (Figure3.9-3.10) for different surface chemistry and curvature shows an increase in adsorption as the protein concentration increase,⁶⁵⁻⁶⁶ although a few outliers were observed which may be due to particle aggregation, especially on 11 nm and carboxyl terminated surfaces (COOH). Fg adsorbed in greater amount on OH surface at 64 nm compared to NH_2 and COOH as illustrated in Figure 3.19.

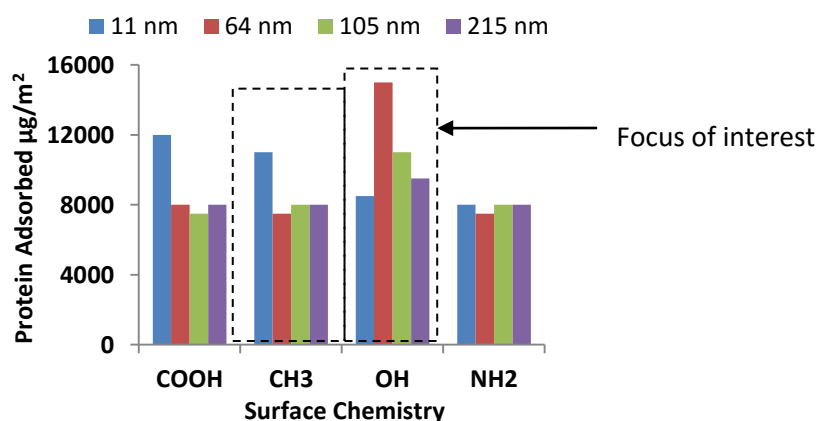


Figure 3.19 Effect of Surface Chemistry on Fg Adsorption at 900 mg/mL

The hydrophobicity of nanoparticle surfaces has been investigated and shown to influence the identities of the bound proteins and the amount of protein bound to the particles.⁶⁷⁻⁶⁹ In the present work, hydrophilic surfaces display the highest amount of Fg adsorption at 900 mg/mL and 64 nm compared to other particles of the same size presenting differing surface chemistry. Amine terminated surfaces (NH₂) have the least amount of Fg adsorption across all sizes of particles tested. The effect of surface chemistry and curvature is illustrated in Figure 3.20. Amine (NH₂) and hydroxyl (OH) terminated surface have the highest amount of BSA adsorption at 64 nm and 215 nm respectively while carboxylic terminated surface (COOH) have the least BSA-adsorption at 900 mg/mL.

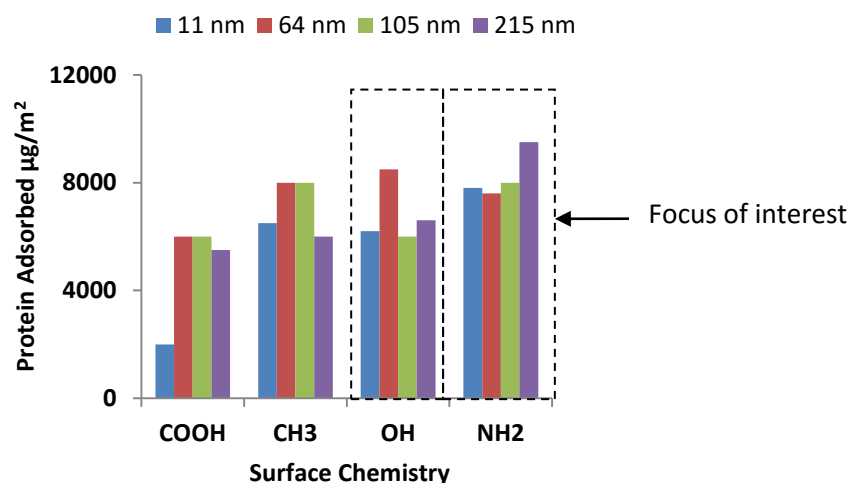


Figure 3.20 Effect of Surface Chemistry on BSA Adsorption at 900 mg/mL

BSA adsorption on positively charged terminated surface (NH₂) is 9478 µg/m² while on Fg is 15340 µg/m², this indicate a higher saturation of Fg on OH surface compare to BSA which may be due to the size of the protein since the Fg size is 40 x 4 nm while albumin is 14 x 4 nm.⁸⁸

The adsorption profile of BSA and Fg shows wide spread variation in terms of surface curvature. The 215 nm particle size have greater amount of BSA adsorption on NH₂ (positively charge) surface while Fg adsorbed at greater amount on 64 nm on OH

(hydrophilic) surface. This result shows protein adsorption varies with respect to both surface chemistry and curvature which correlates to some previous findings.^{70,71} This result may be due to the arrangement of Fg and BSA on the surface as shown in Figure 3.21 which shows possible protein adsorption process.

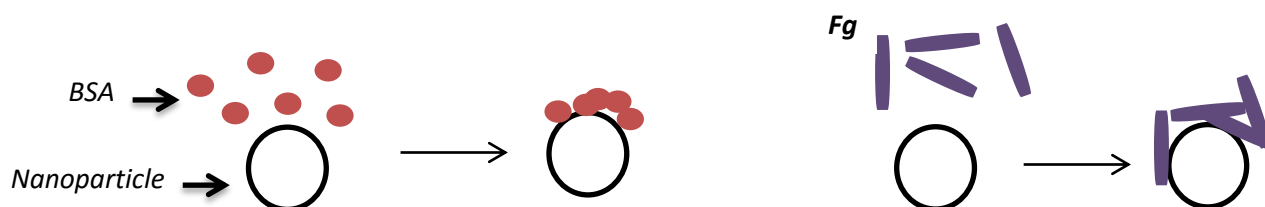


Figure 3.21 Schematic of protein adsorption of globular protein (BSA) and rod like protein (Fg) shows how they might undergo conformational and/or orientational change when they interact with silica nanoparticle.

Particle size is known to have an impact in particle-protein interaction, several studies have shown that biological to nanoparticles tend to scale with surface area^{72,73}, i.e. as the size responses become smaller, their surfaces areas shrink much more slowly causing greater surface to volume ratios than larger particle. This may be the case of the 64 nm silica nanoparticles which display higher adsorption amount with Fg than with BSA. Vertegel *et al*⁶⁹ studied the conformational changes that chicken egg lysozyme undergo upon adsorption to nanoparticles with different diameter of 4, 20 and 100 nm. The results show that the protein retains most of its secondary structure and enzymatic activity when adsorbing to silica nanoparticles of smaller size. BSA adsorbed mostly to 64 nm particles compared to other curvature size while Fg displays the highest protein adsorbed on 11 nm particle.

Several studies have confirmed that protein molecules change conformation when adsorbed onto surface (silica nanoparticle) due to the many factors such as physicochemical cues, type of protein and protein concentration.^{68,69} The concentration is known to have an

impact on protein adsorption on physicochemical cues as shown in our experiment. According to the results of this work, Fg adsorption at different concentrations (Figure 3.7 and 3.10) the result is summarised below in terms of chemistry Figure 3.22.

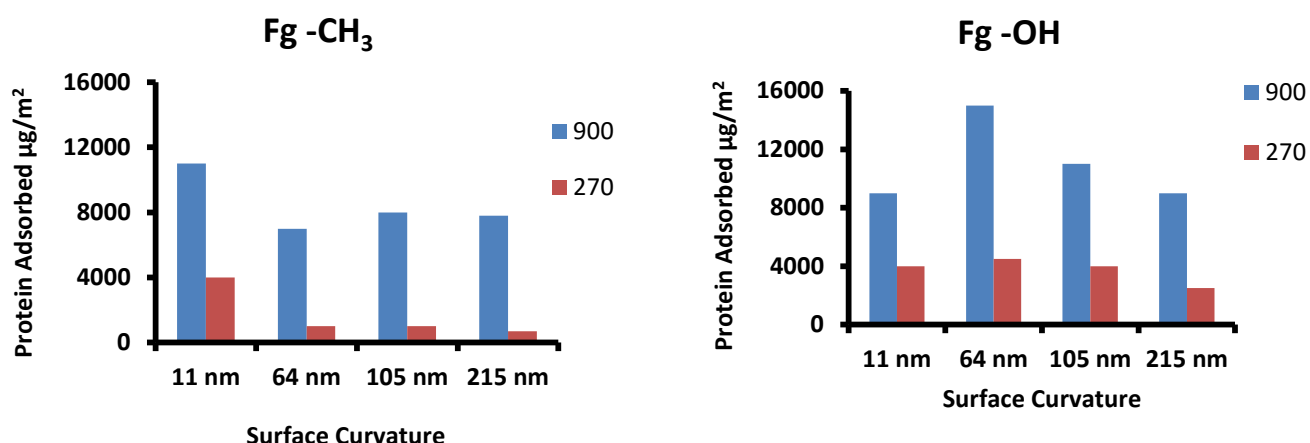


Figure 3.22 Protein adsorption at two concentrations of 900 and 270 mg/mL on hydrophobic and hydrophilic surfaces, n=3

The results in Figure 3.22 shows there is more Fg adsorption at 900 mg/mL compared to 270 mg/mL on each surface curvature, although on Hydrophobic surface, 11 nm displays the highest adsorption at 900 mg/mL while on hydrophilic surface, 64 nm shows the highest Fg adsorption at 900 mg/mL which may be due to it being locked into conformation during adsorption. BSA adsorption at two different concentrations of 900 and 270 mg/mL on amine terminated surface (NH₂) and hydroxyl surface (OH) across each surface curvature of 11 -215 nm is shown in Figure 3.23

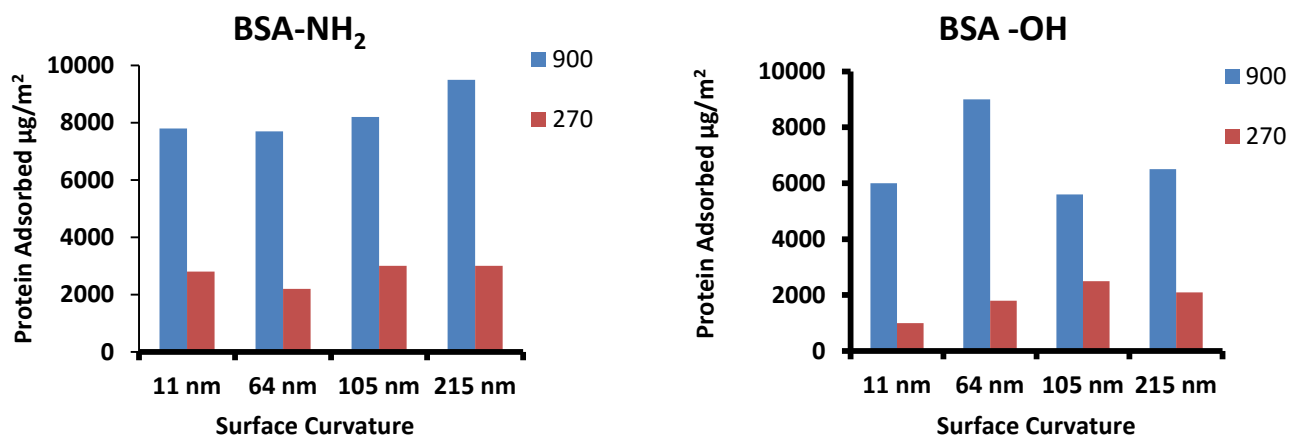


Figure 3.23 BSA adsorption on amine surface (NH₂) and hydroxyl surface (OH) on two different concentrations of 900 and 270 mg/mL

The effect of protein (BSA) concentration on NH₂ and OH chemistry shows higher adsorption on 11- 215 nm particle size at 900 mg/mL as seen in Figure 3.23, while at lower BSA concentration of 270 mg/mL, lower protein adsorption was observed on NH₂ and OH chemistries.

The colorimetric assay shows the affinity of BSA and Fg on different nanotopography using particles as models with respect to surface chemistry. The affinity constants found for Fg are generally higher on surfaces presenting NH₂ compared to other chemistries tested. This result may be due to the positive charge driving interaction with the protein. Conversely, the COOH surfaces present a more negative charge by zeta potential, broadly resulting in a lower affinity for Fg, for all particle sizes. Likewise, COOH surfaces have the lowest affinity for BSA while positively charged amine terminated surfaces have the highest affinity constant on BSA.

The percentage change of secondary structure of BSA and Fg shows different results on each surface chemistry and curvature at different protein concentration.

The saturation amount of Fg on CH₃ and OH were compared to validate the findings from the adsorption data below, in Figure 3.24.

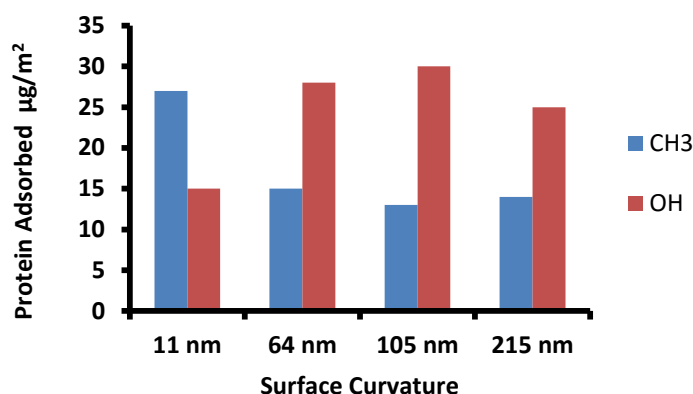


Figure 3.24 Saturation amount of Fg on CH₃ and OH

The saturation amount was calculated using a modified Langmuir Isotherm (Hill equation). All data was normalised for surface area. It is possible that proteins are orienting differently or changing their conformation due to different particle surface curvature. The 11 nm diameter particle shows highest saturation on the methyl surface (CH₃) whereas, a lower saturation amount was observed on particles at 64-215 nm. Fg on NH₂ surface is found to adsorb with little amount of protein in comparison to other surface analysis, i.e the amount of Fg adsorbed was observed to be CH₃ < NH₂ < COOH < OH as might be expected from previous report demonstrating Fg hydrophobic interaction.⁷⁴

The saturation amount of on NH₂ surface display BSA was found to adsorb with the highest saturation amount on NH₂ surface on 11-215 nm particle size. A comparison of NH₂ and OH saturation amount on each surface curvature is shown in Figure 3.25. BSA adsorption on OH, at 105 nm possible indicates denaturation of protein, therefore reducing the amount of available surface area for more protein molecule to adsorb.

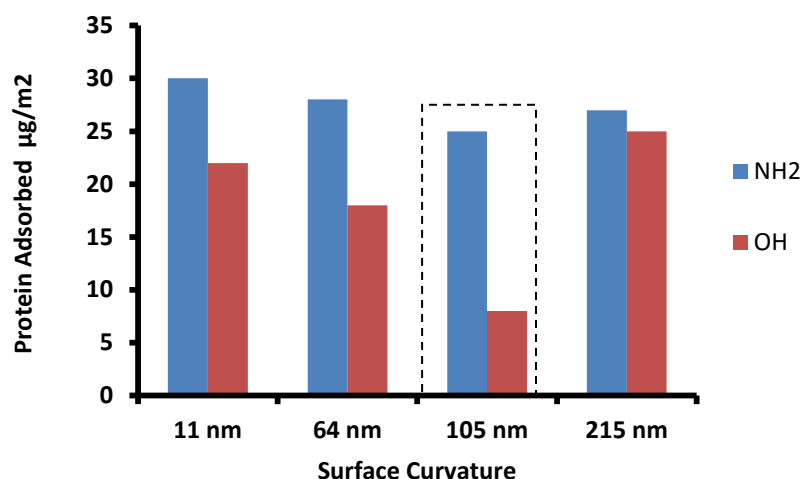


Figure 3.25 The effect of saturation amount of BSA on NH₂ and OH

FTIR was used to examine conformational changes of adsorbed proteins structure. Due to the difficulties associated with background subtraction, some of the results were noisy in amide I region. Difficult in atmospheric water bands, overlay the amide I band of interest, giving rise to sharp noise peaks. In these cases, component fitting of amide I was sometimes difficult with spectra noise being more prominent in samples with lower amounts of protein, i.e those sample prepared to cover the lower region of isotherm. Data is only presented in Figure 3.14 – 3.17 where I have confidence that fitting is correct.

The curve fitting analysis of secondary protein structure shows that on the hydrophilic surface, proteins lose a large amount of their α -helix structure on each surface curvature at different protein concentrations. Fibrinogen loses a greater amount compared to albumin on hydrophilic and hydrophobic surfaces on α -helical and β turn which is different from previous reports. The change in conformation may be due to several factors such as stronger interaction with hydrophilic surface, as discussed earlier.

Secondary structural change of Fg can be observed clearly on methyl ($-\text{CH}_3$) and hydroxyl (OH) surface, comparing adsorbed proteins on 64 nm diameter particles as shown in Figure 3.26. Particle-Protein complexes have the clearest FTIR spectra at 900 mg/mL.

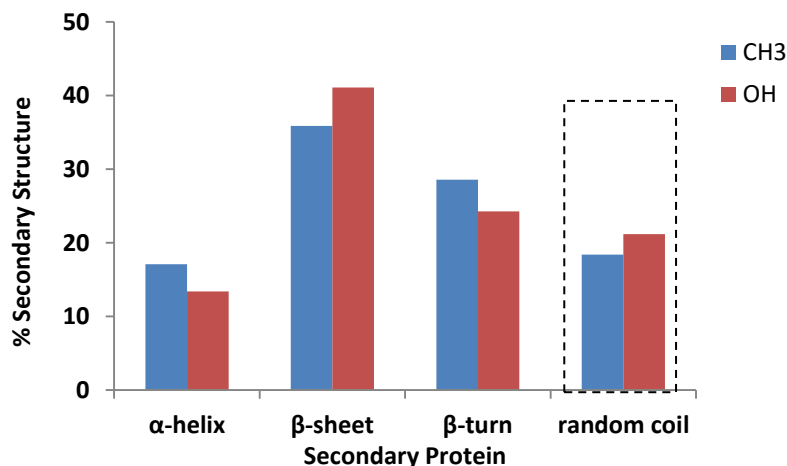


Figure 3.26 The percentage of secondary structure on CH_3 and OH at Fg concentration of 900 mg/mL, on 64 nm, $n=3$

The results in Figure 3.26 shows high percentage of random coil component suggests increase disorder on CH_3 surface, likely due to stronger affinity of interaction skewing the conformation during adsorption. Likewise, lower affinity binding on OH surface results in lower random components, suggesting that protein was not structurally altered as much in composition.

Secondary structural change of BSA on amine (NH₂) and hydroxyl surface (OH) were compared as shown in Figure 3.27,

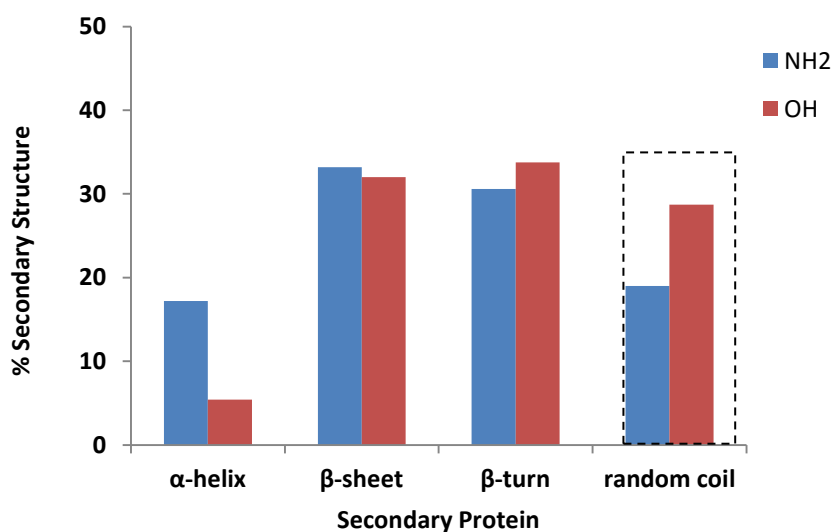


Figure 3.27 The percentage of secondary structure on NH₂ and OH on BSA concentration of 900 mg/mL, on 64 nm, n=3

Figure 3.27 shows amine surface (NH₂) display the lowest random component compared to hydroxyl (OH) with highest random component. More random coil components of OH shows more disorder on affinity constant which correspond to our result in Figure 3.12. Lower affinity binding on NH₂ surface results in lower random components.

The effect of surface chemistry, curvature concentration and conformation of protein on BSA and Fg adsorption have being reviewed. Finally, the effect of concentration needs to be understand as shown in Figure 3.28

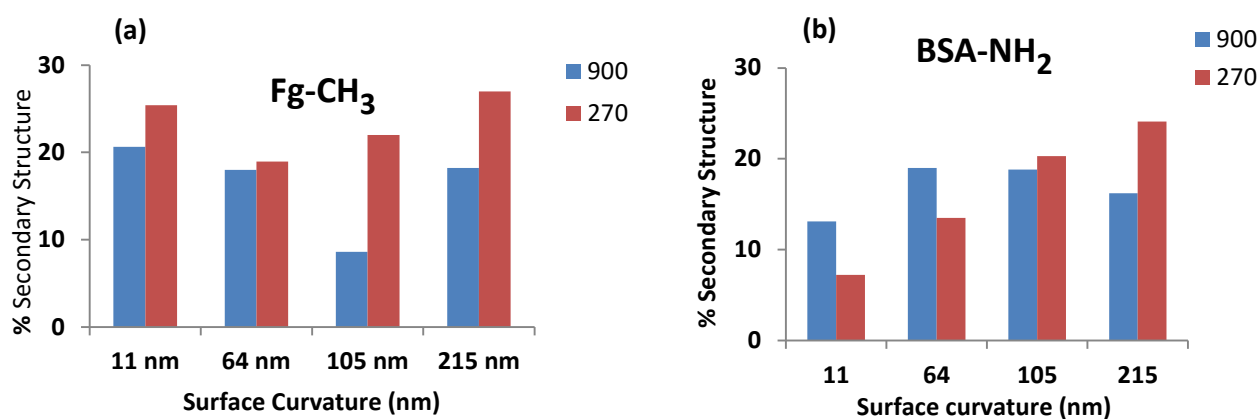


Figure 3.28 Effect of Fg and BSA concentration on random coil.

The result in Figure 3.28(a) shows at lower concentration of Fg at 270 mg/mL, 11nm have the highest percentage of random coil which correspond to our result in Figure 3.18, Majority of the result shows at lower protein concentration, there is high percentage of secondary structure compare to higher protein concentration of 900 mg/mL. Figure 3.28 (b) shows as the curvature size increase, BSA concentration at 900 and 270 mg/mL increases but BSA concentration at 900 mg/mL has the highest secondary.

3.5 Conclusions

This chapter demonstrated that Stöber process was successfully used to prepare monodispersed silica spheres. It has been shown that the use of self assembled monolayer technique to modify the surface of Silica nanoparticles to produce four functional groups (-OH, -NH₂, -CH₃ and -COOH). Characterisations with DLS, TEM, water contact angle, XPS and FTIR confirmed the formation of monolayer modification.

BSA and Fg interact differently on each surface chemistry and curvature as the protein concentration increases. Amine surfaces (NH₂) have the highest adsorption using BSA solution while hydroxyl surface (OH) has the highest adsorption using Fg solution in terms of surface chemistry. The 215 nm sphere have the highest adsorption on BSA solution while on Fg solution, 64 nm have the highest adsorption in terms of surface curvature. Carboxyl surface (COOH) has the least adsorption using BSA solution while NH₂ have the least adsorption using Fg solution. The finding in this chapter shows clearly that surface chemistry and curvature affect on protein adsorption.

The affinity and saturation of Fg and BSA solutions on surface chemistry and curvature reveals the lower the affinity constant, the higher the saturation amount on each surface chemistry and curvature. The lower the saturation amount adsorbing possibly indicates denaturation of protein, therefore reducing the amount of surface area for protein molecules to adsorb.

The results in this chapter show that the concentration of protein has an effect on protein-surface interaction. There is more Fg adsorption at 900 mg/mL compared to 270 mg/mL on each surface curvature, although on hydrophobic surfaces, 11 nm has the highest adsorption at 900 mg/mL while on hydrophilic surface (OH), 64 nm has the highest Fg adsorption at 900 mg/mL which may be due to it being locked into conformation during adsorption. BSA concentration, at 900 mg/mL, has the highest adsorption compared to lower

concentration. BSA and Fg conformation changes shows, the higher the random coil, the lower the α -helix while the percentage of β -sheet and β -turn have a higher percentage.

In Summary, it has been shown that surface chemistry, concentration and particle size affects protein conformation as shown on secondary structure of protein. The conformation changes in secondary structure reveal surface chemistry, curvature and concentration have effect protein-nanoparticle interactions. More understanding and insight is required to understand the effect of competitive binding of protein solutions on nanoparticle.

3.6 References

1. Lee, Y.-S. & Mrksich, M. Protein chips: from concept to practice. *Trends Biotechnol.* **20**, S14–8 (2002).
2. Nam JM; Thaxton CS; C.A. Mirkin, Nanoparticle-Based Bio-Bar Codes for the Ultrasensitive Detection of Proteins, *Science*, 301(5641) 1884-1886, (2003)
3. Webster, T. J., Schadler, L. S., Siegel, R. W. & Bizios, R. Mechanisms of enhanced osteoblast adhesion on nanophase alumina involve vitronectin. *Tissue Eng.* **7**, 291–301 (2001).
4. Srivastava, S., Verma, A., Frankamp, B. L. & Rotello, V. M. Controlled Assembly of Protein-Nanoparticle Composites through Protein Surface Recognition. *Adv. Mater.* **17**, 617–621 (2005).
5. Lawrence NJ, Wells-Kingsbury JM, Ihrig MM, T.E. Fangman, F. Namavar, C.L. Cheung, *Langmuir* 28 (2012) 4301–4308
6. Pitt, W. G. & Cooper, S. L. Albumin adsorption on alkyl chain derivatized polyurethanes: I. The effect of C-18 alkylation. *J. Biomed. Mater. Res.* **22**, 359–82 (1988).
7. Sigal, G. B., Mrksich, M. & Whitesides, G. M. Effect of Surface Wettability on the Adsorption of Proteins and Detergents. *J. Am. Chem. Soc.* **120**, 3464–3473 (1998).
8. Castner, D. G. & Ratner, B. D. Biomedical surface science: Foundations to frontiers. *Surf. Sci.* **500**, 28–60 (2002).
9. Galli, C., Coen, M. C., Hauert, R., Katanaev, V. L. & Gro, P. Creation of nanostructures to study the topographical dependency of protein adsorption. **26**, 255–267 (2002).
10. Hu, Y.-J., Liu, Y., Zhao, R.-M., Dong, J.-X. & Qu, S.-S. Spectroscopic studies on the interaction between methylene blue and bovine serum albumin. *J. Photochem. Photobiol. A Chem.* **179**, 324–329 (2006)
11. Lenk, T. J., Horbett, T. A., Ratner, B. D. & Chittur, K. K. Infrared spectroscopic studies of time-dependent changes in fibrinogen adsorbed to polyurethanes. *Langmuir* **7**, 1755–1764 (1991).
12. Ta, T. C. & McDermott, M. T. Mapping Interfacial Chemistry Induced Variations in Protein Adsorption with Scanning Force Microscopy. *Anal. Chem.* **72**, 2627–2634 (2000).
13. Choi, C. L. & Alivisatos, A. P. From artificial atoms to nanocrystal molecules: preparation and properties of more complex nanostructures. *Annu. Rev. Phys. Chem.* **61**, 369–89 (2010).
14. Xia, D., Ku, Z., Lee, S. C. & Brueck, S. R. J. Nanostructures and functional materials fabricated by interferometric lithography. *Adv. Mater.* **23**, 147–79 (2011).

15. Nie, S., Xing, Y., Kim, G. J. & Simons, J. W. Nanotechnology applications in cancer. *Annu. Rev. Biomed. Eng.* **9**, 257–88 (2007).
16. Mamo, T. *et al.* Emerging nanotechnology approaches for HIV/AIDS treatment and prevention. *Nanomedicine (Lond)*. **5**, 269–85 (2010).
17. Lobatto, M. E. *et al.* Multimodal clinical imaging to longitudinally assess a nanomedical anti-inflammatory treatment in experimental atherosclerosis. *Mol. Pharm.* **7**, 2020–9 (2010).
18. Cedervall, T. *et al.* Understanding the nanoparticle-protein corona using methods to quantify exchange rates and affinities of proteins for nanoparticles. *Proc. Natl. Acad. Sci. U. S. A.* **104**, 2050–5 (2007).
19. Walkey, C. D., Olsen, J. B., Guo, H., Emili, A. & Chan, W. C. W. Nanoparticle size and surface chemistry determine serum protein adsorption and macrophage uptake. *J. Am. Chem. Soc.* **134**, 2139–47 (2012).
20. Nel, A. E. *et al.* Understanding biophysicochemical interactions at the nano-bio interface. *Nat. Mater.* **8**, 543–57 (2009).
21. Chithrani, B. D.; Ghazani, A. A.; Chan, W. C. W. *Nano Lett.* (2006), 6, 662.
22. Wojciak BS, A. Curis, W. Monhagan, K. Macdonald, C. Wilkinson, *Exp. Cell Res.* 223 (1996) 426–435.
23. Higushi A, S. Tamiya, T. Tsubomura, A. Katoh, C.S. Akaik, M. Hara, *J. Biomater. Sci-Polym. Ed.* 11 (2000) 149–168.
24. Dufrene YD, Marchat TG, Rouxhet PG, *Langmuir* 15 (1999) 2871–2878
25. Billsten, P., Freskgård, P.-O., Carlsson, U., Jonsson, B.-H. & Elwing, H. Adsorption to silica nanoparticles of human carbonic anhydrase II and truncated forms induce a molten-globule-like structure. *FEBS Lett.* **402**, 67–72 (1997).
26. Czeslik, C., and R. Winter. 2001. Effect of temperature on the conformation of lysozyme adsorbed to silica particles. *Phys. Chem. Chem. Phys* 3:235–239.
27. Shaw, W. J., Campbell, A. A., Paine, M. L. & Snead, M. L. The COOH terminus of the amelogenin, LRAP, is oriented next to the hydroxyapatite surface. *J. Biol. Chem.* **279**, 40263–6 (2004).
28. Brandes N, Welzel PB, Werner C, Kroh LW: Adsorption-induced conformational changes of proteins onto ceramic particles: Differential scanning calorimetry and FTIR analysis. *J Colloid Interface Sci* (2006), 299:56–69.
29. Lunov O, Syrovets T, Loos C, Beil J, Delacher M, Tron K, Nienhaus GU, Musyanovych A, Mailänder V, Landfester K, Simmet T: Differential Uptake of Functionalized Polystyrene

- Nanoparticles by Human Macrophages and a Monocytic Cell Line. *ACS Nano* (2011), 5:1657–1669
30. Baron MH, M. Revault, S. Servagent-Noinville, J. Abadie, H. Quiquampoix *J. Colloid Interface Sci.*, 214 (1999), p. 319
31. G. Decher, *Science*, 1997, 277, 1232–1237
32. De, M., Ghosh, P. S. & Rotello, V. M. Applications of Nanoparticles in Biology. *Adv. Mater.* **20**, 4225–4241 (2008).
33. Pan, Z. *et al.* Adverse effects of titanium dioxide nanoparticles on human dermal fibroblasts and how to protect cells. *Small* **5**, 511–20 (2009)
34. Compton SJ and Jones CG, Mechanism of dye response and interference in the Bradford protein assay, *Anal Biochem* 151, 369–374 (1985)
35. Pierce net website, <http://www.piercenet.com/>; accessed on the 15th July 2014
36. Aldrich website, <http://www.sigmaaldrich.com/life-science/proteomics/protein-quantitation/bicinchoninic-acid-kit.html>, accessed on the 15th July (2014)
37. Stöber, W., A. Fink, and E. Bohn. Controlled Growth of Monodisperse Silica Spheres in the Micron Size Range. *Journal of colloid and interface science* 26.1 (1968): 62-9
40. Wang HC, C.Y. Wu, C.C. Chung, M.H. Lai, T.W. Chung, *Ind. Eng. Chem. Res.*, 45 (2006), pp. 8043–8048
41. Chen, X. *et al.* Chemical and Morphological Analysis of Surface Enrichment in a Biodegradable Polymer Blend by Phase-Detection Imaging Atomic Force Microscopy. *Macromolecules* **31**, 2278–2283 (1998).
42. Caetano, W., Duarte, E. L. & Itri, R. Small angle X-ray scattering studies to access the influence of bovine serum albumin (BSA) and carbonic anhydrase (Boca) on the size and interaction among Aerosol-O T reversed micelles as a function of the micellar hydration degree. (2004).
43. Grieve, K., Mulvaney, P. & Grieser, F. Synthesis and electronic properties of semiconductor nanoparticles/quantum dots. *Curr. Opin. Colloid Interface Sci.* **5**, 168–172 (2000).
44. Graf, G. A. *et al.* ABCG5 and ABCG8 are obligate heterodimers for protein trafficking and biliary cholesterol excretion. *J. Biol. Chem.* **278**, 48275–82 (2003).
45. Jana NR, Gearheart L, Murphy CJ. Seed-mediated growth approach for shape-controlled synthesis of spheroidal and rodlike gold nanoparticles using a surfactant template. *J Adv Mater*, 13:1389–93, (2001)

46. Rosenholm JM., Mamaeva V, C. Sahlgren, M. Linden, Nanoparticles in targeted cancer therapy: mesoporous silica nanoparticles entering preclinical development stage *Nanomedicine (Lond)*, 7 (2012), pp. 111–120
47. Kluth GJ, Thermal behaviour of alkylsiloxane self assembled monolayers on the oxidized Si (100) surface, (1997)
48. Peña-Alonso, R., Rubio, F., Rubio, J. & Oteo, J. L. Study of the hydrolysis and condensation of γ -Aminopropyltriethoxysilane by FT-IR spectroscopy. *J. Mater. Sci.* **42**, 595–603 (2006).
49. Socrates G, infrared characteristics group frequencies: tables & charts
50. Sigma Aldrich website, <http://www.sigmaaldrich.com/life-science/proteomics/protein-quantitation/bicinchoninic-acid-kit.html>, accessed July (2014)
51. Lundstrom I, Model of protein adsorption on solid surfaces, *Progress in Colloid & Polymer Science*, 70:76-82, (1985)
52. Welsch, N., Lu, Y., Dzubiella, J., & Ballauff, M. Adsorption of proteins to functional polymeric nanoparticles. *Polymer*, 54(12), (2013), 2835–2849.
53. Bharti, B., Meissner, J., & Findenegg, G. H. Aggregation of silica nanoparticles directed by adsorption of lysozyme. *Langmuir: The ACS Journal of Surfaces and Colloids*, 27(16), (2011), 9823–33.
54. Felsovalyi, F., Mangiagalli, P., Bureau, C., Kumar, S. K., & Banta, S. Reversibility of the adsorption of lysozyme on silica. *Langmuir: The ACS Journal of Surfaces and Colloids*, 27(19), (2011), 11873–82.
55. Louguet, S., Kumar, A. C., Guidolin, N., Sigaud, G., Duguet, E., Lecommandoux, S., & Schatz, C. Control of the PEO chain conformation on nanoparticles by adsorption of PEO-block-poly(L-lysine) copolymers and its significance on colloidal stability and protein repellency. *Langmuir: The ACS Journal of Surfaces and Colloids*, 27(21), (2011).
56. Dominguez-Medina, S.; McDonough, S.; Swanglap, P.; Landes, C. F.; Link, S. In situ measurement of bovine serum albumin interaction with gold nanospheres. *Langmuir* (2012), 28, 9131-9139.
57. Rocker, C.; Potzl, M.; Zhang, F.; Parak, W. J.; Nienhaus, G. U. A quantitative fluorescence study of protein monolayer formation on colloidal nanoparticles. *Nat. Nanotechnol.* (2009), 4, 577-580.
58. Hill A.V The possible effects of the aggregation of the molecules of haemoglobin on its dissociation curves. *J. Physiol.* (1910), 40, iv-vii

59. Ang, YW. *et al.* Large-area self assembled monolayers of silica microspheres formed by dip coating. **28**, (2010).
60. Mao CB, Li, F.Z. Cui *et al.* Oriented growth of hydroxyapatite on (0 0 1) textured titanium with functionalized self-assembled silane monolayer as template *J. Mater. Chem.*, 8 (1998), pp. 2795–2805
61. Tedja, R. *et al.* Effect of TiO₂ nanoparticle surface functionalization on protein adsorption, cellular uptake and cytotoxicity: the attachment of PEG comb polymers using catalytic chain transfer and thiol–ene chemistry. *Polym. Chem.* **3**, 2743 (2012).
62. Van der Maaden, K., Sliedregt, K., Kros, A., Jiskoot, W. & Bouwstra, J. Fluorescent nanoparticle adhesion assay: a novel method for surface pK_a determination of self-assembled monolayers on silicon surfaces. *Langmuir*, **28**, 3403–11 (2012)
63. Freeman, R. G.; Grabar, K. C.; Allison, K. J.; Bright, R. M.; Davis, J. A.; Guthrie, A. P.; Hommer, M. B.; Jackson, M. A.; Smith, P. C.; Walter, D. G.; Natan, M. J. *Science* **1995**, 267, 1629.
64. Sato, T.; Brown, D.; Johnson, B. F. G. *Chem. Commun.* **1997**, 1007.
65. Norde, W. & Favier, J. P. Structure of adsorbed and desorbed proteins. *Colloids and Surfaces* **64**, 87–93 (1992).
66. Kondo, S., Igarashi, M. & Nakai, K. The properties of silica surfaces treated at high pH. *Colloids and Surfaces* **63**, 33–37 (1992).
67. Cedervall, T.; Lynch, I.; Lindman, S.; Berggard, T.; Thulin, E.; Nilsson, H.; Dawson, K. A.; Linse, S. Understanding the Nanoparticle-Protein Corona Using Methods to Quantify Exchange Rates and Affinities of Proteins for Nanoparticles. *Proc. Natl. Acad. Sci. U. S. A.* (2007), 104, 2050–2055.
68. Lundqvist M, Sethson I, Jonsson BH. Protein adsorption *onto* silica nanoparticles: conformational changes depend *on the* particles' curvature *and the* protein stability. *Langmuir* (2004); 20(24):10639
69. Vertegel AA, Siegel RW, Dordic IS. Silica nanoparticle size influences *the* structure *and* enzymatic activity *of* adsorbed lysozyme. *Langmuir* (2004); 20:6800—680
70. Roach P, Farrar D, Perry CC, Surface Tailoring for Controlled Protein Adsorption: Effect of Topography at the Nanometer Scale and Chemistry, *Journal of the American Chemical Society* **2006** 128(12), 3939-3945
71. Walkey, C. D., Olsen, J. B., Guo, H., Emili, A. & Chan, W. C. W. Nanoparticle size and surface chemistry determine serum protein adsorption and macrophage uptake. *J. Am. Chem. Soc.* **134**, 2139–47 (2012).

72. Brown DM, Wilson MR, W. MacNee, V. Stone, K. Donaldson, Size-dependent proinflammatory effects of ultrafine polystyrene particles: a role for surface area and oxidative stress in the enhanced activity of ultrafines *Toxicol. Appl. Pharmacol.*, 175 (2001), pp. 191–199
73. Donaldson K, D. Brown, A. Clouter, R. Duffin, W. MacNee, L. Renwick, L. Tran, V. Stone The pulmonary toxicology of ultrafine particles *J. Aerosol Med.*, 15 (2002), pp. 213–220
74. Lassen B and M. Malmsten, Competitive protein adsorption at plasma polymer surfaces; *J. Colloid Interface Sci.*, (1997), 186, 9–16.

CHAPTER 4

Competitive Binding of Proteins

4.1 Introduction

Competitive protein adsorption is of relevance in many interfacial phenomenon as such as cellular adhesions on substrates and compatibility of biomaterials. Several factors can affect protein adsorption on biomaterials such as the concentration of protein, surface properties and the contact time the proteins have to adsorb onto a surface. Studies on competitive protein adsorption to nanoparticles are now emerging^{1,2} due to its importance in cellular response and biomaterial design. However, the process is not well established and has not yet been well explored.

One of the principles of competitive protein adsorption is the “Vroman effect” which explains how small proteins (albumin) present in high concentration will control the adsorption at early stages of the competitive adsorption processes and the larger protein (fibrinogen) will adsorbed at later stage which have been investigated using competitive adsorption.^{3,4} Despite the principle of the Vroman effect, there are still unsolved questions regarding the factors affecting competitive adsorption such as the affinity of the protein for the adsorbing surface and the conformation of adsorbed proteins.

Competitive protein adsorption processes cannot be predicted by considering the adsorption from single protein solution due to numerous factors such as the dilution, the pH, temperature, surface charge, surface chemistry and particle size. A large amount of research has been carried out on protein adsorption on single protein solution⁵⁻¹⁰ but there are fewer reports on competitive protein adsorption. Ying *et al*, showed albumin adsorbed preferentially on hydrophobic surfaces while less collagen adsorbed on hydrophilic surfaces.¹¹ Ding *et al*, also investigated competitive adsorption of fibrinogen, albumin and immunoglobulin onto gradient surface showing differences in the affinity for the surface.¹² A greater understanding of competitive adsorption process needs to be investigated.

To understand the competitive binding of proteins, the use of variable surface chemistry and curvature will be a better model for the molecular richness found in biological systems.^{13, 14} Functionalised silica nanoparticles were synthesised using the Stöber process and the self assembled monolayer technique was used to produce four different functional group (OH, NH₂, OOH and CH₃) which were used for this experiment. Two plasma proteins were used namely human serum albumin (HSA)- the most abundant protein in serum and plasma with a high mobility and human fibrinogen.

The chapter will investigate the effect of surface chemistry and curvature on competitive protein adsorption. Functionalised silica nanoparticles were used presenting four different functional groups of particle size of 11-215 nm at different timepoints of 10-180 mins. Variance in timepoint was used since it is deduced that the composition of adsorbed protein layer changes within a short period of time, after exposure to different types of proteins due to their competitive adsorption.^{41,42} The result will give in-depth knowledge and understanding of the role of surface chemistry and curvature on competitive adsorption of protein, affinity and conformational changes.

4.2 Materials and Methods

4.2.1 Protein Solutions

4.2.1.1 Human serum albumin (HSA)

HSA is used for conjugation in antibody production and acts as a standard for measuring protein concentrations. HSA is a water soluble globular protein which is synthesised by the liver.¹⁵ It is the most abundant protein, with an approximately 60% of the total globular protein in blood plasma. FITC-conjugated human serum albumin (1 mg/mL) used for this study was purchased from abcam (ab8030).¹⁴ The conjugate has an excitation of 493 nm and emission of 528 nm. HSA has a molecular weight of 66 kDa with a concentration of approximately 50 mg/mL plasma.

4.2.1.2 Human Fibrinogen (Fg)

Fibrinogen is a protein produced by the liver; present in the human blood plasma at a concentration of 2.5 mg/mL. Fibrinogen is vital for wound healing, inflammation and other biological functions. Fibrinogen is an elongated molecule with approximate molecular dimensions of $6.0 \times 6.0 \times 45.0$ nm, molecular weight of 350 kDa¹⁵ Fibrinogen conjugates fluorescent dye (5 mg) was purchased from life technologies (F-13192).The dye has an excitation of 540 nm and emission of 590 nm. Stock solutions were prepared by adding 3.33 mL of 0.1 M sodium bicarbonate (pH 8.3) at room temperature to 5 mg of Fg to give a final solution of 1.5 mg/mL. The solution was gently mixed for one hour.¹⁶

4.2.2 Protein Adsorption from Multiple Protein Solutions

Stock solutions of HSA of 15 µg/mL and 0.8 µg/mL of Fg were prepared in PBS. A 500µL stock solution of functionalised silica nanoparticles (-OH, -NH₂, CH₃, and -COOH) was prepared. A volume of 8.87µL of Fg was diluted with 415 µL of PBS while 249.6 µL of HSA is diluted with 415 µL PBS. Fg diluted solution was added to HSA. A volume of

1000 μL of mixed protein solution was delivered to a clean eppendorf tube while 500 μL of the functionalised silica particles in PBS and left for few minutes. A volume of 160 μL of protein solution (HSA and Fg) was added to each 500 μL of functionalised silica particle, and on adding protein solution to particles, they were vortexed quickly and left for each timepoints (10, 30, 60, 90, 120 and 180 mins). After each time points, sample was centrifuge for after each timepoints. A volume of 50 μL supernatant was pipetted into a fluorescence microplate reader, Biotek Synergy 2 Multimode Reader at an excitation of 485 nm/emission 540 nm (HSA) and excitation of 528 nm/emission 590 nm (Fg) respectively in a reader. After the measurements, samples were freeze dried and kept in the freezer (-20°C).

4.2.3 Infrared Spectroscopy

The Alpha Platinum ATR (A220/ D-01) Quicksnap spectrometer (Bruker Optic) was used for obtaining all the infrared spectra of samples. This system makes use of a single bounce diamond crystal, with an adjustable sample pressure, 360° rotatable pressure applicator and a spectral range of $7,500\text{--}375\text{ cm}^{-1}$. Infrared adsorption spectra of the samples were acquired by using OPUS software. A blank background measurement was carried out prior to each sample taking an average of 100 scans. The spectral range of the data was taken from $4000\text{--}375\text{ cm}^{-1}$. An average of 100 scans was also taken for each sample, with 4 spectra being taken to determine reproducibility.

4.2.4 Adsorption of Proteins to Nanoparticles

To visually demonstrate protein uptake on particles, we used fluorescently labelled albumin and Fg, prepared in solutions of the same concentration and ratio.

Functionalised silica particle with multiple protein solution (HSA, Fg) were washed once with PBS and before being immersed in Alexa Fluor 488 dye, life technology for 10 minutes in the dark at room temperature (RT) following the protocol from Molecular Probes¹⁷ at

excitation of 495 nm and emission of 519 nm. Samples were then washed three times with PBS and examined under a fluorescent microscope (Nikon Eclipse Ti-ST, Japan) to confirm the presence of protein in the particles.

4.2.5 SUMMARY

A schematic layout plan for the experiment that will be carried out is shown in Figure 4.1.

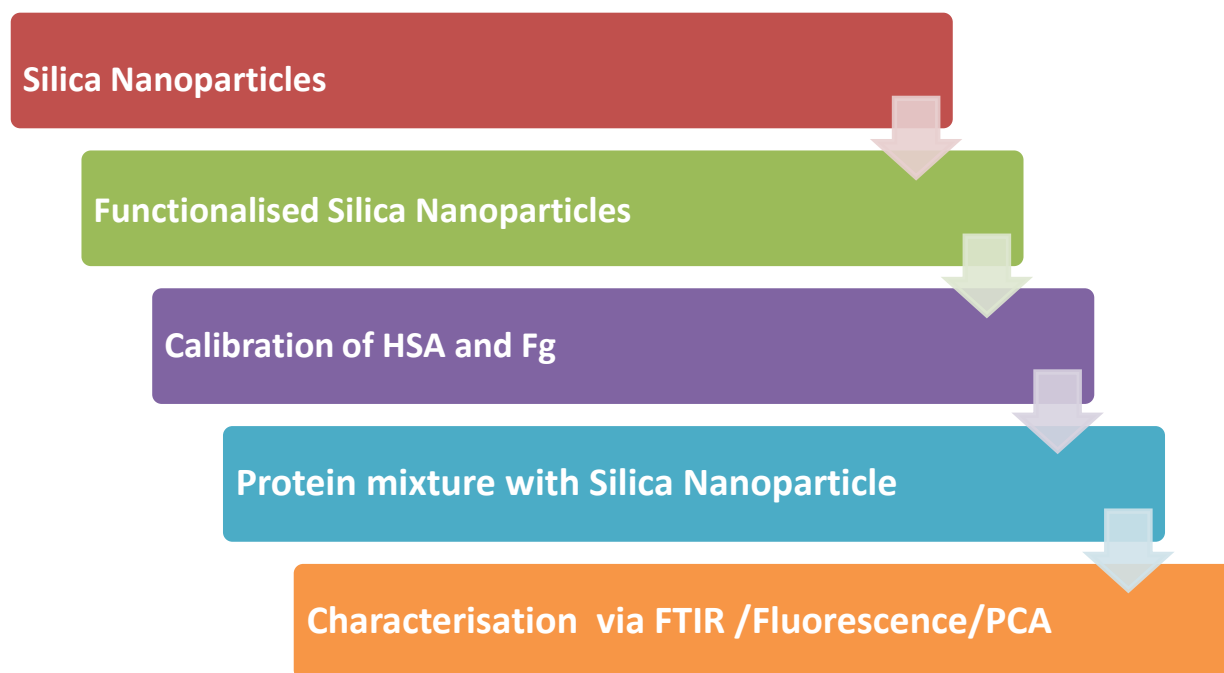


Figure 4.1 Schematic layout plan of the experiment

4.3 Results

4.3.1 Calibration Plot of HSA and Fg

A fluorescence calibration of HSA was plotted using different protein concentrations. The sensitivity factor of the plate reader was assessed to ensure optimal calibration over the widest sampling concentration range (sensitivity of 50 and 100 tested) at a temperature of 25°C as shown in Figure 4.2.

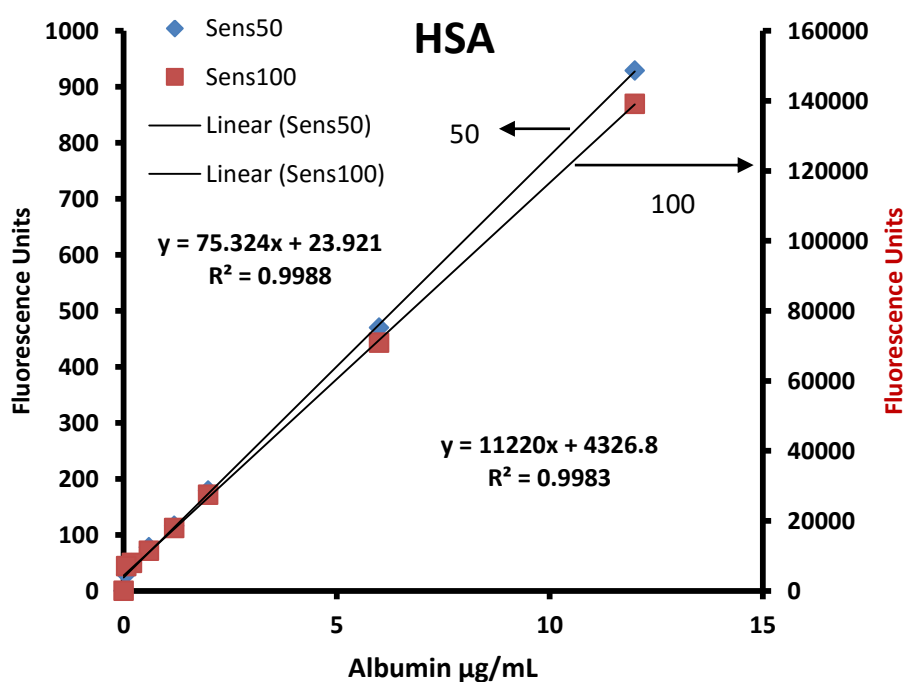


Figure 4.2 Calibration of HSA vs Fluorescence units of two sensitivity, 50 and 100. The results show a good level of accuracy between 0.059-12 µg/mL for both sensitivity 50 and 100 with lower end below 0.059 µg/mL shown on the right. Sensitivity of the calibration is much better when using sensitivity 100 (red squares).

The calibration plot of HSA of sensitivity of 50 and 100 shows a linear graph, as the protein concentration increases, the fluorescence unit increases. Due to higher sensitivity of 100, this was used for all following experiments. The calibration plot for Fg is shown in Figure 4.3

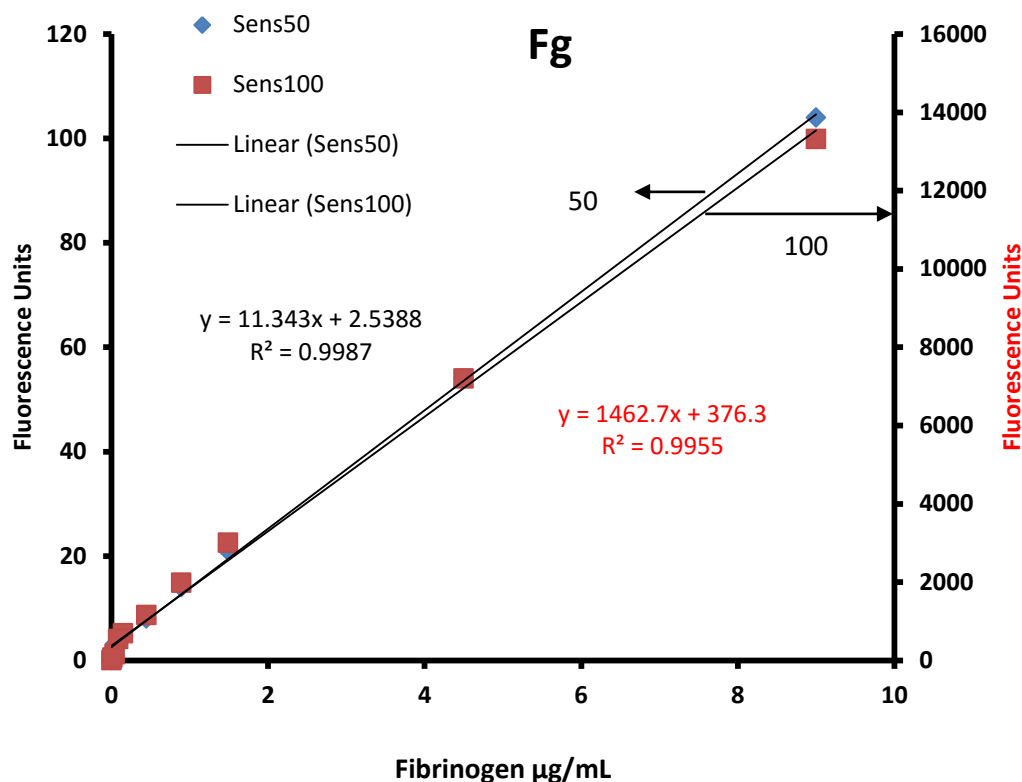


Figure 4.3 Calibration of Fg vs Fluorescence units of two sensitivity, 50 and 100 shows good level of accuracy between 9-0.015 µg/mL for both sensitivity 50 and 10 with lower end below 0.015 µg/mL. Sensitivity of calibration at 100 is much better than sensitivity at 50.

As the protein concentration of Fg increases, both sensitivity of 50 and 100 increases i.e. linear graph, as shown in Figure 4.5. Sensitivity of 100 is more sensitive compared to sensitivity of 50 which is similar to HSA. Due to higher sensitivity of 100, this was used for all following experiments.

4.3.2 Adsorption of Proteins to Nanoparticles

The adsorptions of protein to silica functionalised nanoparticles were observed using fluorescence labelled proteins as shown below in Figure 4.4.

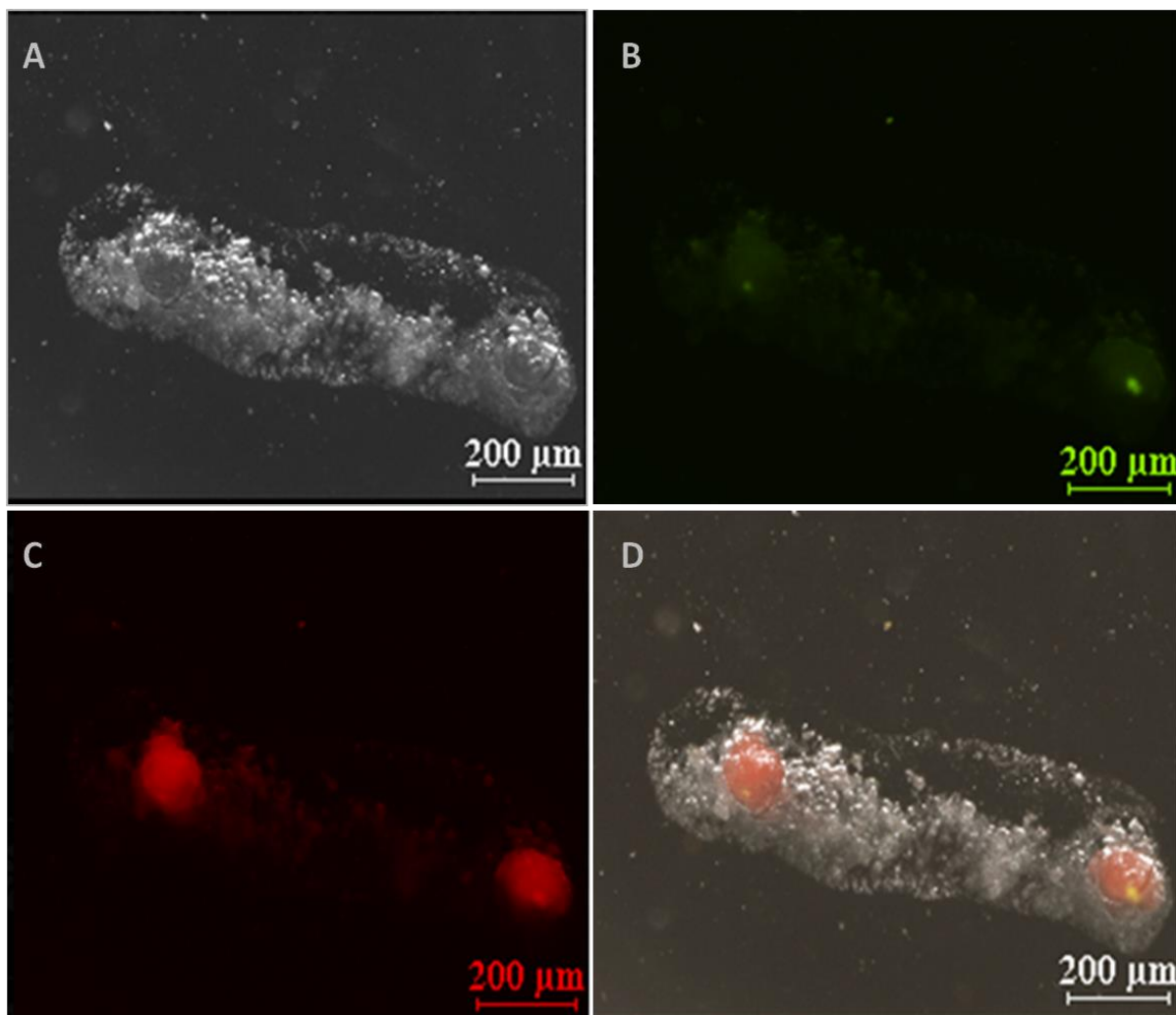


Figure 4.4 A representation experiment of adsorbed proteins on silica nanoparticles using fluorescence labelled Fg and HSA on to hydroxyl (OH) terminated 64 nm silica particles in (A) Brightfield image shows the binding of protein with nanoparticle (B) TRITIC (Fg) (C) FITC (HSA) (D) overlaid image of both proteins (HSA and Fg) binded with the nanoparticle

4.3.3 Competitive Adsorption of Proteins

The variation of albumin and fibrinogen adsorption from solution to different functionalised surfaces with adsorption times ranging from 10 to 180 mins are shown in Figure 4.5- 4.8.

4.3.3.1 Effect of Surface Chemistry on HSA Adsorption

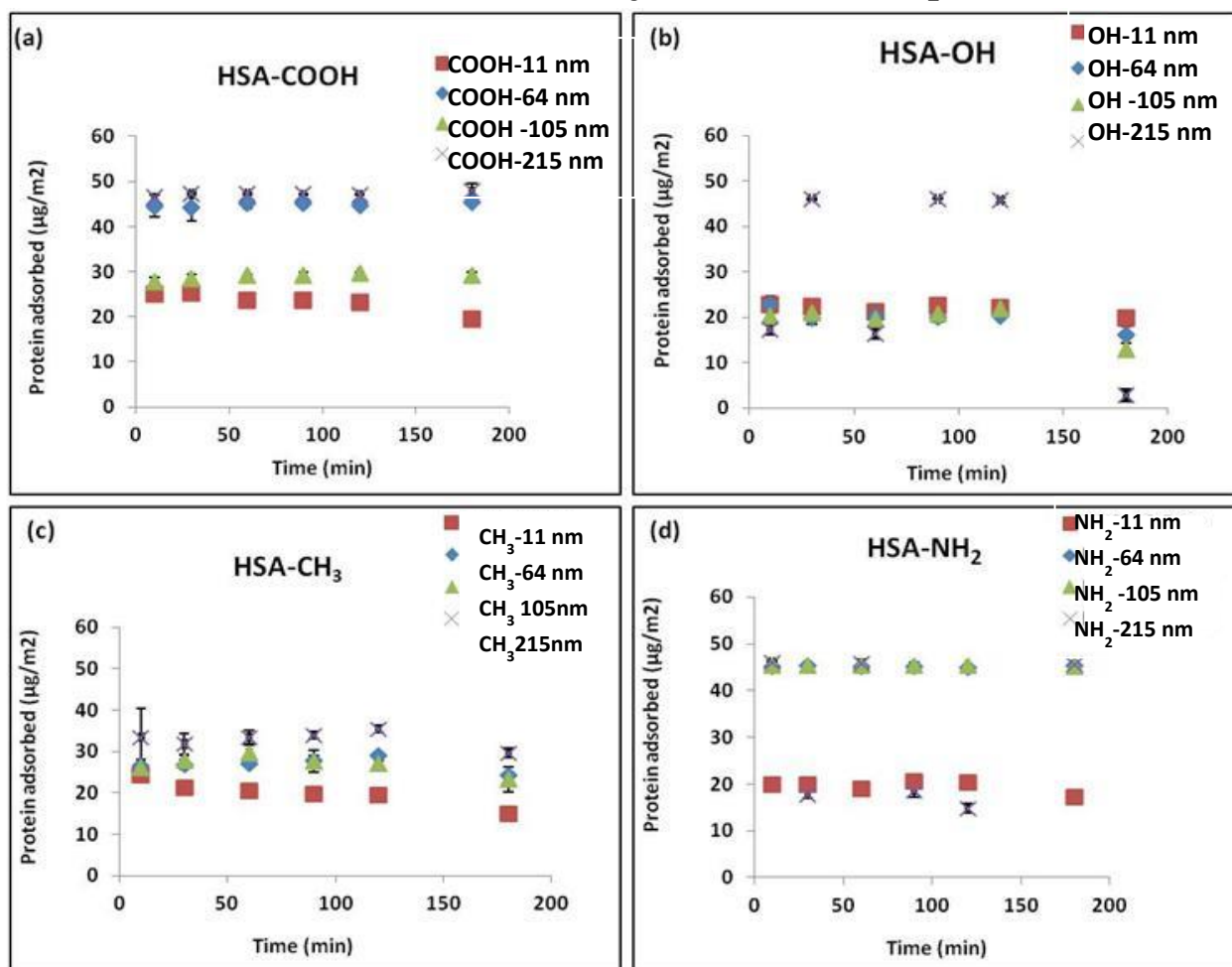


Figure 4.5 Variation of HSA adsorption and timepoints on different functionalised silica surface (a) COOH, (b) OH (c) NH₂ and (D) CH₃ surface. Data shown are the mean ± SD of three replicate samples.

The amount of individual protein (albumin and Fg) was monitored showing competitive binding to defined chemically modified silica nanoparticles. Adsorption was followed for over 180 minutes; Figure 4.7 shows data for HSA only.

On the carboxyl surface (COOH), little variation is observed with respect to time. The 11 nm samples have the least adsorption as time increases. The 64 and 215 nm adsorption is further apart from 11 and 105 nm. The 215 nm display the highest adsorption at $49 \mu\text{g}/\text{m}^2$; $215 > 64 > 105 > 11$ nm, see Figure 4.5 (a).

Figure 4.5 (b) shows less variation on 11, 64 and 105 nm as the time increases on hydroxyl surface. The 215 nm displays a higher level of adsorption at 30 mins, 90 and 120 mins respectively compared to other surface curvature. The 215 nm has the highest protein adsorbed on hydroxyl surface (OH) at $45 \mu\text{g}/\text{m}^2$. The results shows 215 nm particles adsorbed more compare to other nanoparticle; $215 > 11 > 105 > 64$ nm

Figure 4.5 (c) shows HSA adsorption changes with respect to time on methyl surface (CH_3). The 11 nm samples have the least adsorption and the rate of adsorption decreases with respect to time. Particle size of 11-105 nm decreases with respect to time while 215 nm particles show little increase at 90 to 120 mins, adsorption decrease from 120 -180 minutes when experiment halted, $215 > 64 > 105 > 11$ nm.

The NH_2 surface shows a wide variation between the smaller (11 nm) and larger (215 nm) curvature compared to all other surface chemistry. A similar pattern of adsorption is observed for COOH. No major change with respect to time, except for 11 nm which displays the lowest adsorption is observed on amine surface (NH_2). The 215 nm samples shows some changes as the time increases, an oscillation behaviour pattern is observed across the timepoint on surface bound albumin as shown in Figure 4.5 (d), $215 > 105 > 11 > 64$ nm

The highest HSA adsorption is on COOH surface at $48 \mu\text{g}/\text{m}^2$ at 180 mins, OH surface at $46 \mu\text{g}/\text{m}^2$ at 30 mins, NH_2 surface at $45 \mu\text{g}/\text{m}^2$ at 180 mins and CH_3 at $35 \mu\text{g}/\text{m}^2$ at 120 mins.

4.3.3.2 Effect of Surface Chemistry on Fg Adsorption

The effect of surface chemistry on Fibrinogen adsorption is shown in Figure 4.6. The Fg adsorption rate is focused between the region of 15-21 $\mu\text{g}/\text{m}^2$ for all surface chemistry as shown in Figure 4.8.

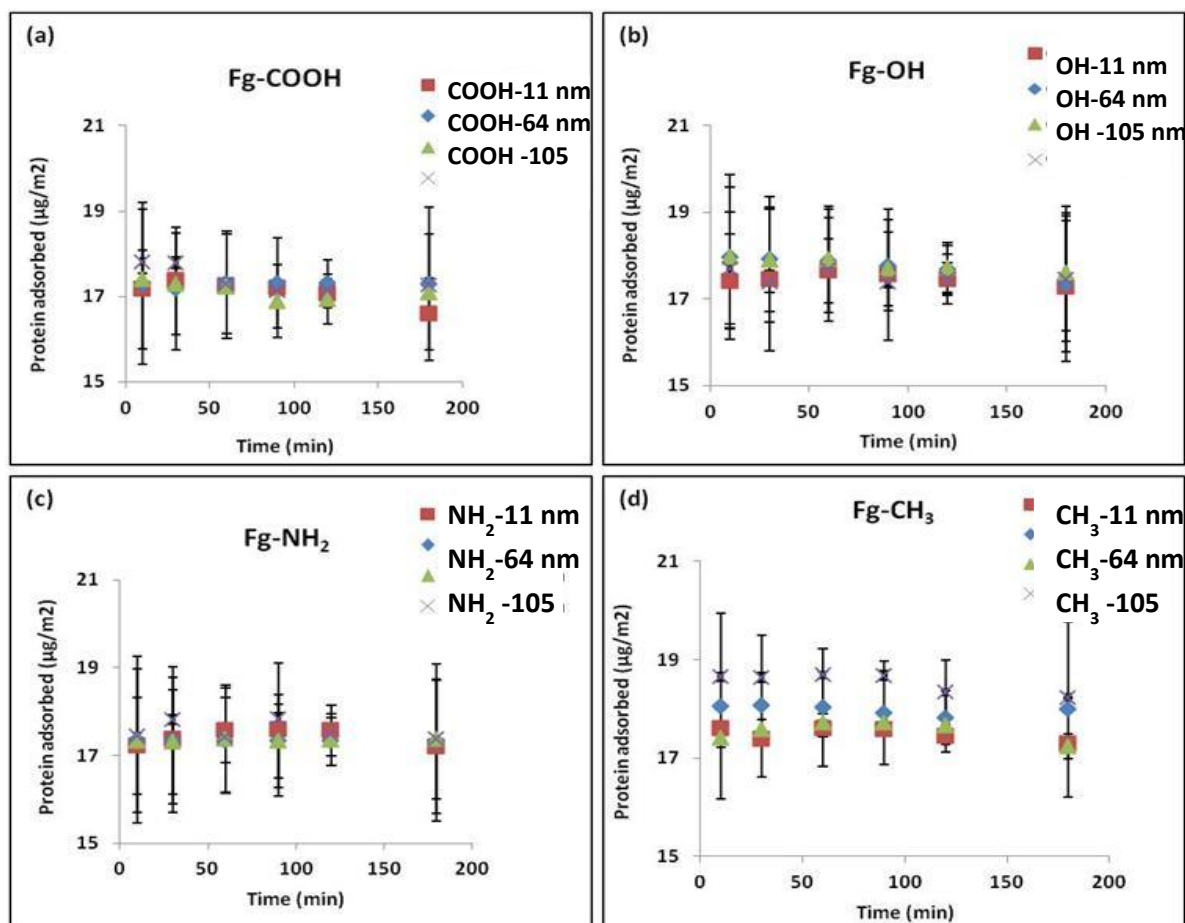


Figure 4.6 Fg adsorption at different timepoints (10, 30, 60, 90, 120 and 180 mins) on functionalised silica particle, (a) COOH, (b) OH (c) NH₂ and (d) CH₃ surface. Data shown are the mean \pm SD of three replicate samples

The amount of individual protein (albumin and Fg) were monitored showing competitive binding to defined chemically modified silica nanoparticles. Adsorption was followed for 180 minutes; Figure 4.6 shows data for Fg only. Less spread and variation is observed on carboxyl, hydroxyl and amine surface as the timepoint increases.

Figure 4.6 (a) shows a decrease in Fg adsorption with respect to time for 11 and 215 nm particle on carboxyl surface (COOH). The 105 nm sample decreases with time until 90 mins and little increases were observed from 90 mins to 180 mins when the experiment was halted. The Fg adsorption on 64 nm particles was constant throughout as the timepoint increases, 215>64>11>105 nm

Figure 4.6 (b) shows less variation on surface curvature as the time increases. The 11 nm and 105 nm particles decreases with respect to time while 64 nm remain constant as the timepoint increases. 64>105>11>215 nm

An oscillatory behaviour pattern was observed for 215 nm samples as the timepoint increases. No major changes and difference were observed on Figure 4.6 (c). The 215 nm samples show little increase and decreases as the timepoint increases, 215>64>11>105 nm

The NH₂ surface shows a wide variation as observed on Figure 4.6(d). The 215 nm particles have the highest level of Fg adsorption with respect to time. The 11 and 215 nm samples have the least Fg adsorption while an increase in adsorption is observed till 90 mins. Changes were observed on 64 nm particle, as adsorption decreases as the time increases, the adsorption rate increases from 180 mins and the experiment was halted, 215>64>105>11 nm

4.3.3.3 Effect of Surface Curvature on HSA Adsorption

The dataset shown in Figure 4.5 was replotted to understand the effect of surface curvature on HSA adsorption at different timepoints as shown in Figure 4.7.

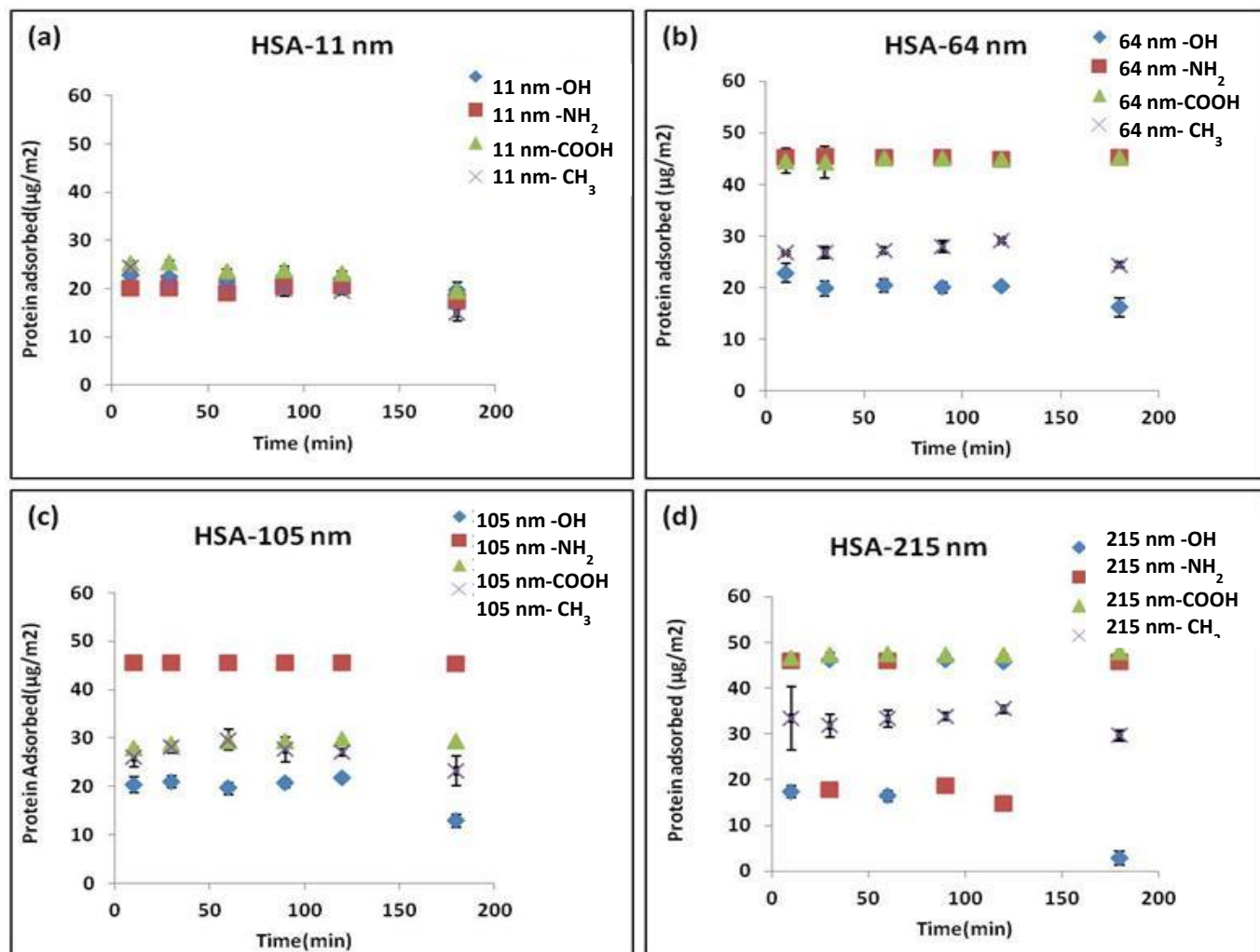


Figure 4.7 HSA adsorption on surface curvature at different timepoints (10, 30, 60, 90, 120 and 180 mins) on (a) 11 (b) 64 (c) 105 and (d) 215 nm. Data shown are the mean \pm SD of three replicate samples

The effect of surface curvature on HSA was measured from 10-180 minutes as illustrated in Figure 4.7. Figure 4.7(a) indicates no major changes in HSA adsorption to 11 nm particles over time, or with major differences observed between particles presenting different terminal chemistries. However, a small reduction in the amount of adsorbed HSA was possibly observed for all particle chemistries at 180 minutes compared to previous time points.

Figure 4.7 (b) shows HSA adsorption on 64 nm. NH_2 and COOH were constant as the timepoint increase. The least adsorption is observed on hydroxyl surface (OH) as it decreases as the timepoint increases. CH_3 was constant till it reaches 120 mins and reduces as it reaches 180 minutes. NH_2 and COOH are distinctly different from CH_3 and OH, with a trend in the amount of HSA adsorbed following $\text{NH}_2 > \text{COOH} > \text{CH}_3 > \text{OH}$.

A wide spread of adsorbed HSA levels is observed on all nanoparticles sizes above 11nm. Figure 4.7 (c) shows the changes associated with 105 nm as an example. Levels of adsorbed HSA on NH_2 terminal chemistry were found to be constant as the time increases, with the highest HSA adsorption found on this surface chemistry. COOH remains constant as the time increases, while OH and CH_3 decreases as the time increases from 10 mins to 180 mins. Amine surfaces present the highest HSA adsorption while hydroxyl surfaces have the least adsorption on 64 nm particles. Adsorption trend generally followed $\text{NH}_2 > \text{COOH} > \text{CH}_3 > \text{OH}$.

Figure 4.7 (d) shows hydroxyl surface decreases as the time increases from 10 mins to 180 minutes. COOH remain constant with respect to time while an oscillatory pattern is observed on amine surfaces. An oscillatory behaviour pattern is observed on amine and hydroxyl surfaces, which may indicate a change in presentation of the protein adsorbed and therefore the available surface area for adsorption at later time points. Wide spread variation

across the surface curvature is observed on 64, 105 and 215 nm. Generally, more HSA was adsorbed to carboxyl surfaces following a trend $\text{COOH} > \text{OH} > \text{NH}_2 > \text{CH}_3$.

4.3.3.4 Effect of Surface Curvature on Fg Adsorption

The effect of Fg adsorption on surface curvature is shown in Figure 4.8 at different timepoints of 10 -180 mins. There are less spread and variation in Figure 4.8 (a) to (d).The highest Fg adsorbed is between 16-20 $\mu\text{g}/\text{m}^2$.

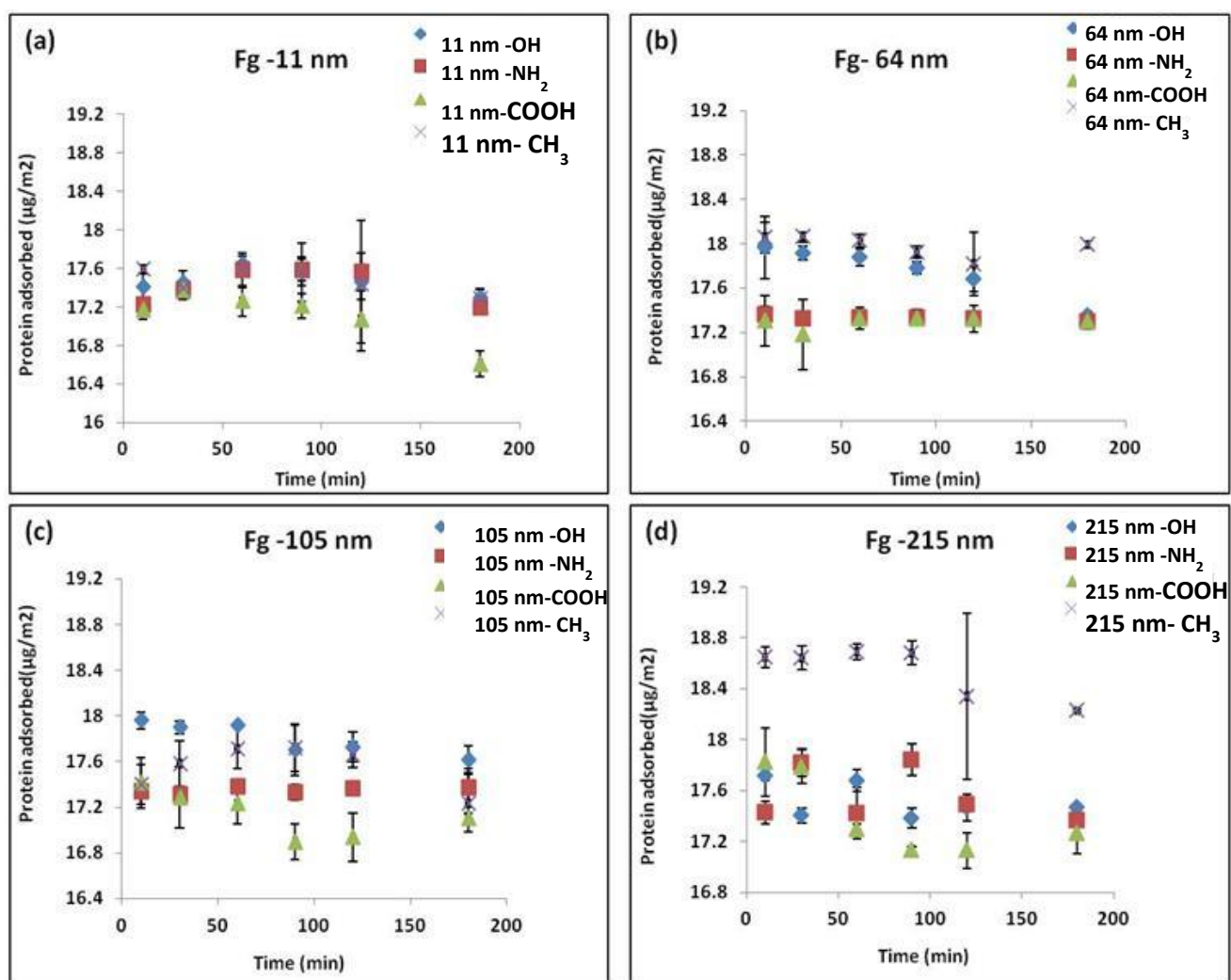


Figure 4.8 Fg adsorption on surface curvature at different timepoints (10, 30, 60, 90, 120 and 180 mins) on (a) 11 (b) 64 (c) 105 and (d) 215 nm. Data shown are the mean \pm SD of three replicate samples

Figure 4.8 (a) - (d) shows Fg adsorption on surface chemistries of CH₃, NH₂, OH and COOH at timepoints of 10, 30, 60, 90, 120 and 180 minutes. The Fg adsorption increases on COOH surface at 10 mins to 30 min, then, rapidly decrease at 60 -180 mins on 11 nm. Fg adsorption increases on NH₂, OH and CH₃ surface as the timepoint increases from 10 to 90 mins, at 120 mins, adsorption rate decreases on each surfaces till the experiment was halted. NH₂ and COOH surface have the highest Fg adsorption at 11 nm as shown in Figure 4.8 (a).
CH₃>NH₂>OH>COOH

Fg adsorption on 64 nm on Figure 4.8 (b) shows NH₂ have a constant adsorption from 10 to 180 mins. Fg adsorption on COOH surface decreases at 10-30 mins and become constants from 60 -180 mins. As the timepoint increases from 10-180 mins, adsorption rate on OH surface decreases till the experiment was halted. Adsorption rate on CH₃ surface decreases as timepoint increase till 120 mins. At 180 mins, adsorption rate increases until experiment was halted. OH and CH₃ surface have the highest adsorption compare to NH₂ and COOH surface, although CH₃ surface have the highest Fg adsorption on 64 nm. CH₃>OH>NH₂>COOH

Figure 4.8 (c) shows Fg adsorption on 105 nm at different surface curvature. NH₂ surface have a constant Fg adsorption rate as the timepoint increases. CH₃ surface shows an increase in Fg adsorption up to 90 mins, then decreases rapidly from 120-180 mins. COOH have the least adsorption rate while OH have the highest adsorption rate on 105 nm. OH>CH₃>NH₂>COOH

At 215nm, CH₃ surface have the highest Fg adsorption while COOH surface, have the least adsorption amount at 90, 120 ad 180 mins. Oscillatory pattern is observed on NH₂ and OH surface as shown in Figure 4.8 (d). CH₃>OH>NH₂>COOH

4.3.3.5 Ratio of Surface Chemistry on HSA/Fg Adsorption

The ratio of HSA and Fg adsorption using the data in Figures 4.5-4.8. The ratio of the results are shown in Figure 4.9. The ratios are important because composition of layers changes. We used solution ratios of 19:1 to mimicked physiological ratio. The effect of surface chemistry on HSA/Fg ratio is shown in Figure 4.9,

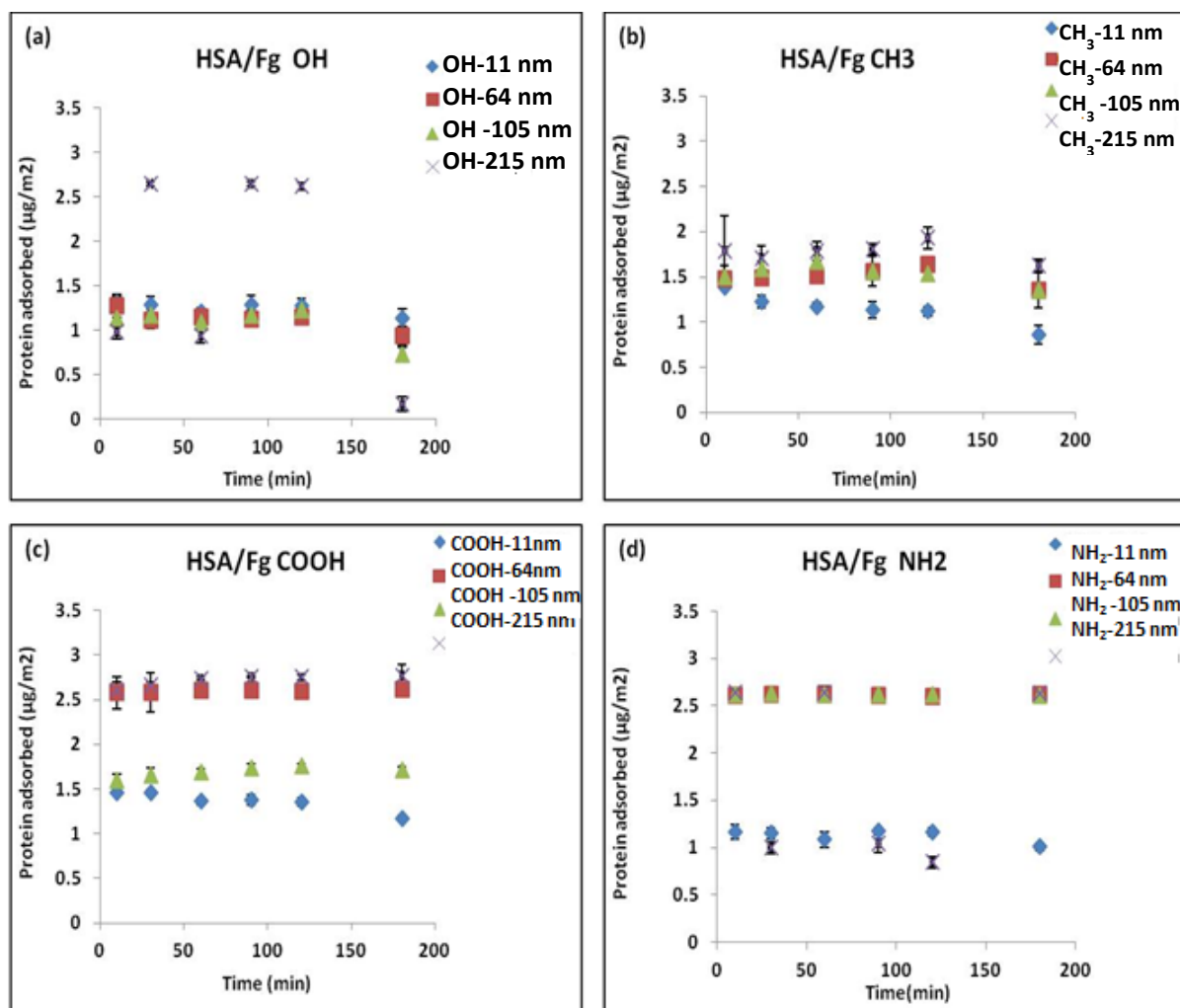


Figure 4.9 Ratio of HSA/ Fg (19:1) adsorption on surface chemistry at different time points (10, 30, 60, 90, 120 and 180 mins) (a) OH (b) CH₃ (c) COOH and (d) NH₂. Data shown are the mean ± SD of three replicate samples.

The hydrophilic surface (OH) in Figure 4.9 (a) shows the largest sphere, 215 nm have the highest adsorption of $2.7 \mu\text{g}/\text{m}^2$ at 30, 90 and 120 mins with an oscillatory pattern observed. Oscillatory pattern is observed on 215 nm while 11, 64 and 105 nm decreases as the time increases.

Figure 4.9(b) shows wide spread of results on methyl surface (CH_3). 11 nm have the least adsorption and decrease as the timepoint increases and have the highest adsorption. 215 nm adsorption increases as the timepoint increase, it have the highest adsorption on methyl surface.

Figure 4.9 (c) on carboxyl terminated surface (COOH) shows wide spread variation across the surface curvature. 64 and 215 nm have the highest adsorption as the time increases but the results was constant from 10 minutes to 180 minutes. 11 nm adsorption reduces as the time increase. 105 nm adsorption increases as the timepoint increases. 11 nm have the least adsorption.

Figure 4.9 (d) shows a distinctive result on positively charge surface (NH_2). 64 and 105 nm have the highest adsorption at $2.5 \mu\text{g}/\text{m}^2$. As the timepoint increases, adsorption on 64 and 105 nm remain constant. 215 and 11 nm have the lowest adsorption as the time point increases. A major change is observed on 215 nm, at 120-180 mins, there is a rapid increases observed.

4.3.3.6 Ratio of Surface Curvature on HSA/ Fg Adsorption

FTIR Analysis of HSA/Fg is shown in Figure 4.10 (i) while the difference of the dataset obtained in Figure 4.9 was replotted to understand the effect of surface curvature on competitive protein adsorption of HSA/Fg in Figure 4.10 (ii)

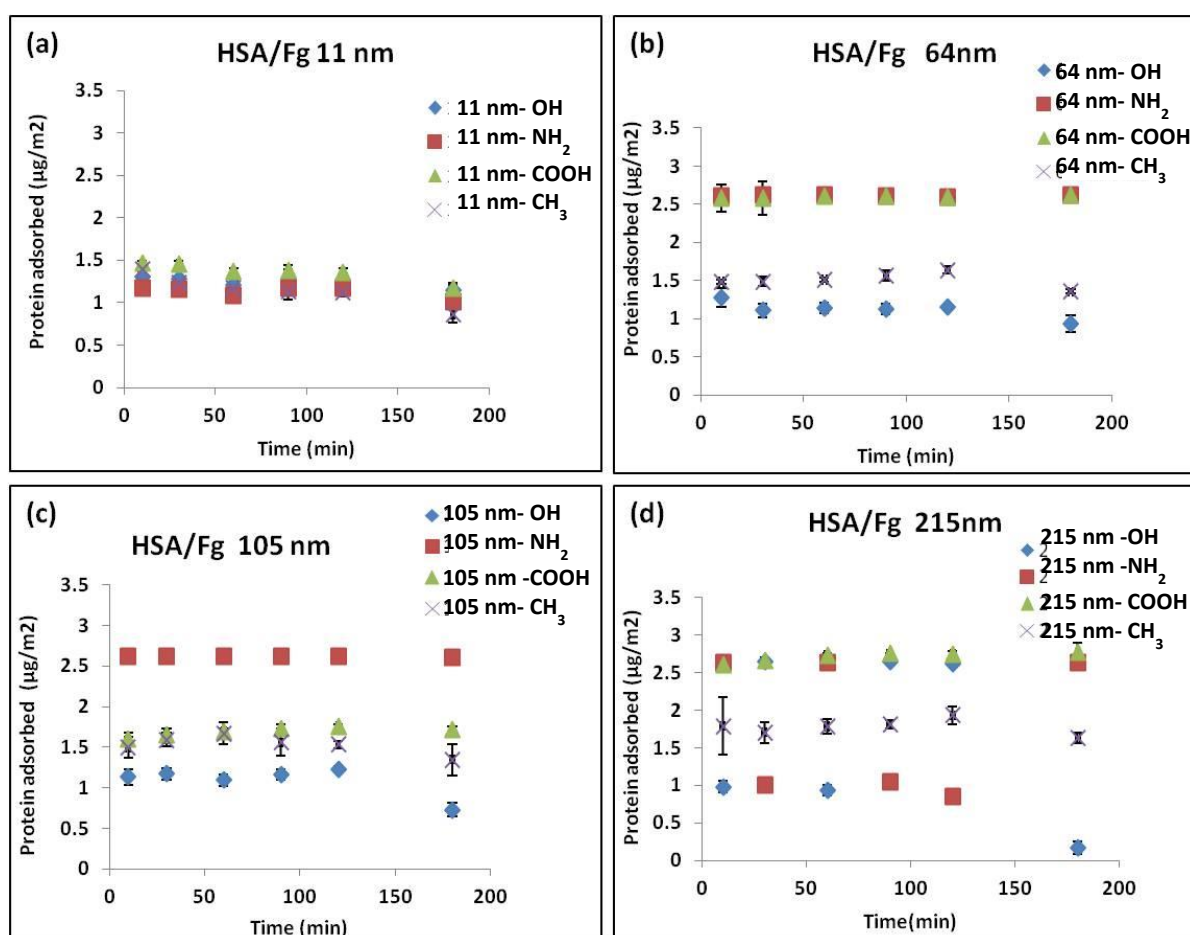
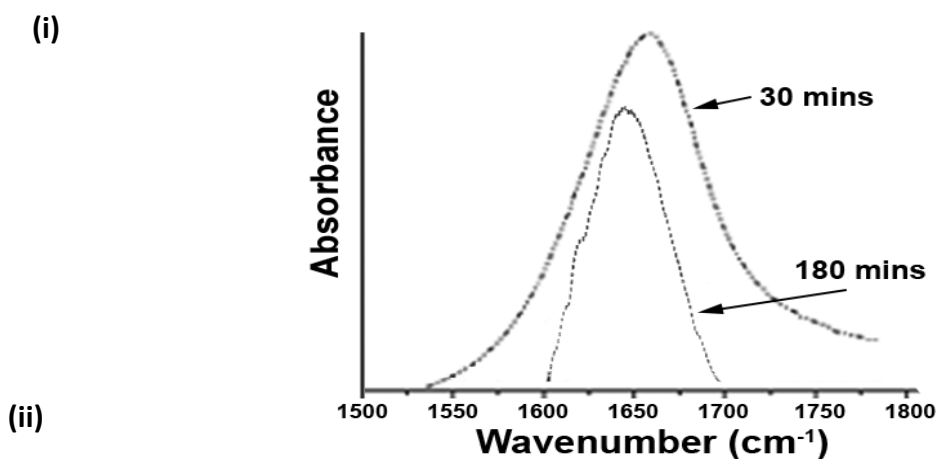


Figure 4.10 (i) FTIR Amide I band of HSA/Fg ratio of HSA/ Fg (19:1) adsorption on surface curvature at different timepoints (10, 30, 60, 90, 120 and 180 mins) (a) 11 (b) 64 (c) 105 and (d) 215 nm. Data shown are the mean \pm SD of three replicate samples, n=3.

Figure 4.10 (i) shows the result of FTIR analysis on Amide I band of HSA/Fg on hydroxyl surface (-OH) of particle size of 11 nm at 30 and 180 mins. A clear shift of the peak, as well as its shape change, highlights secondary structure change.

Figure 4.10 ii (a) shows a less spread variation on surface chemistry on 11nm. The highest amount of adsorption is on carboxylic surface (COOH) at $1.5 \mu\text{g}/\text{m}^2$. Surface chemistry decreases as the timepoint increases. Figure 4.10 (b) shows a wide spread variation on 64 nm. Surface charge has a great impact on this surface. NH_2 (negatively charge) and COOH (positively charge) have the highest amount of adsorption, $2.5 \mu\text{g}/\text{m}^2$, as the timepoint increases compared to OH and CH_3 . The adsorption on NH_2 and COOH surface is further apart to OH and CH_3 surface. OH and CH_3 surface decreases as the timepoint decreases. OH surface have the least adsorption on 64 nm.

A wide spread variation is observed on 105 nm as shown in Figure 4.10 (c). NH_2 adsorption is constant as the time increases from 10 mins to 180 mins. The adsorption on amine surface (NH_2) is further apart from CH_3 , NH_2 and COOH surface. OH surface have the lowest adsorption. The adsorption decreases as the timepoint increases on OH and CH_3 surface. Figure 4.10 (d) shows HSA/Fg adsorption on 215 nm. An oscillatory pattern is observed on hydroxyl surface (OH) and amine surface (NH_2). Steady increase in adsorption is observed on carboxylic surface (COOH). Methyl surface (CH_3) adsorption increases as the timepoint increases. Carboxylic surface (COOH) has the highest adsorption on 215 nm.

4.3.4 Fitting of Amide I

The collected protein-silica particles were further assessed by FTIR to give insight into protein structural changes with respect to time, surface chemistry and curvature. The fitting of amide I was carried out for HSA/Fg at different timepoints focusing on the effect of surface chemistry and curvature at different timepoints of 10, 30, 60, 90, 120 and 180 minute. The secondary structure of α - helix, β -sheet, β -turn and random coil adds up to 100%, e.g. at 11 nm on CH₃ Surface have an α - helix of 15 %, β -sheet of 33 %, β -turn of 25 % and random coil of 27 % adds up to 100% as shown in Figure 4.11.

(A) 10 Mins

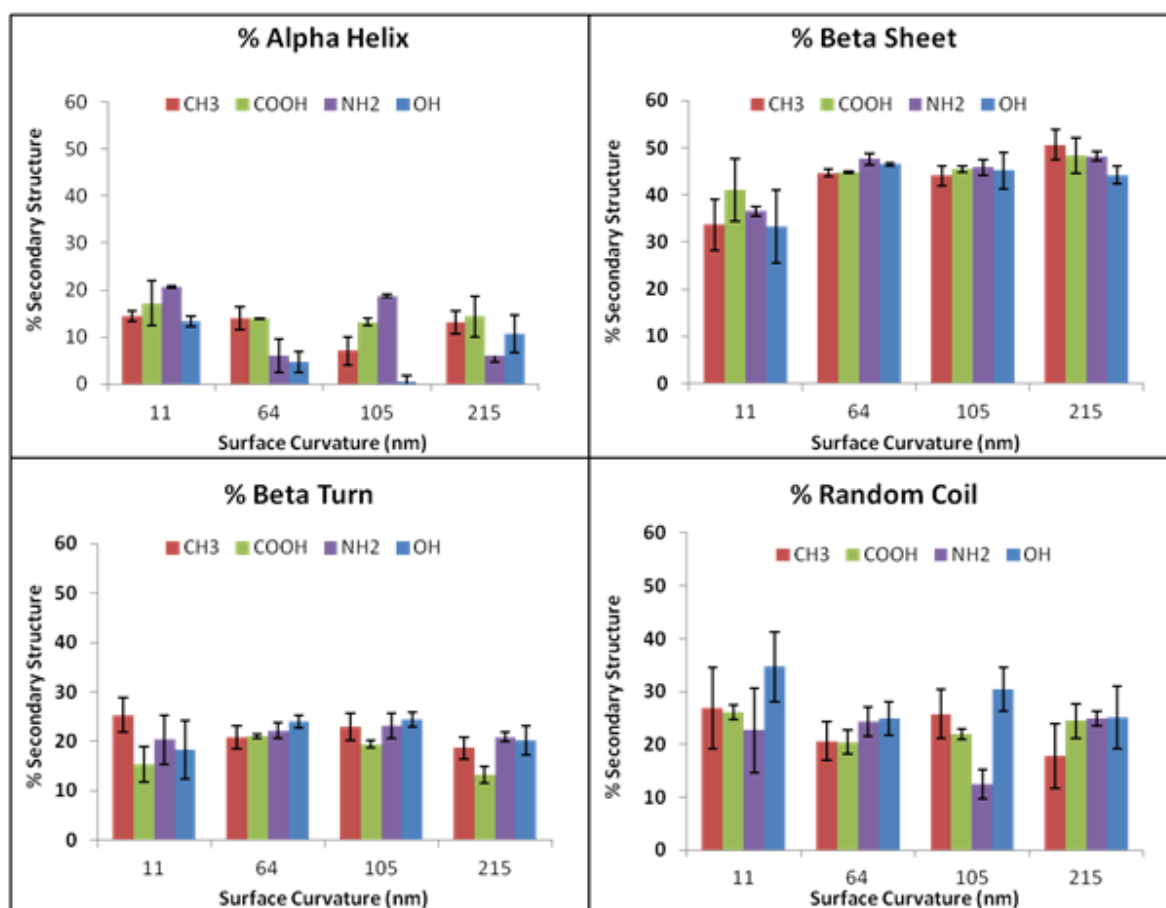


Figure 4.11 The percentage of secondary structure of HSA/Fg at 10 mins (a) α -helix (b) β -sheet (c) β - turn (d) random coil. Data shown are the mean \pm SD of three replicate samples, n=3.

The conformational changes at different time-points on surface chemistry and curvature at 10 minutes is shown in Figure 4.11. There is presence of α -helix but high percentage of β -sheet, turn and random coil is observed.

A lower percentage of α -helix of less than 30% is recorded on each surface curvature. An oscillatory pattern is observed on amine surface (NH_2) while a major decrease in α -helix is observed from lower curvature to higher curvature on methyl (CH_3), carboxyl (COOH) and hydroxyl surface (OH) at 10 minutes, as shown in Figure 4.11 (a).

A high percentage of β -sheet is observed in Figure 4.13 (b). Major increases from 11- 215 nm are observed on surface chemistry of OH , CH_3 , NH_2 and COOH at 10 minutes. The methyl surface (CH_3) has the highest percentage of β -turn at 11-215 nm while little increase is observed on hydroxyl surface (OH) at 11-64 nm. An oscillatory trend is observed on carboxyl surface (COOH) while amine surface (NH_2) remains constants from 11-215 nm; see Figure 4.11 (c).

The COOH surfaces have a high percentage of random coil on curvature of 11-215 nm while amine (NH_2) have the lowest percentage of random coil on 105 nm. An oscillatory trend is observed on hydroxyl surface (OH) and methyl surface (CH_3) on curvature of 11-215 nm as shown in Figure 4.11 (d).

The fitting of amide I was carried out for HSA/Fg at different time-points focusing on the effect of surface chemistry and curvature at timepoint of 30 mins.

(B) 30 Mins

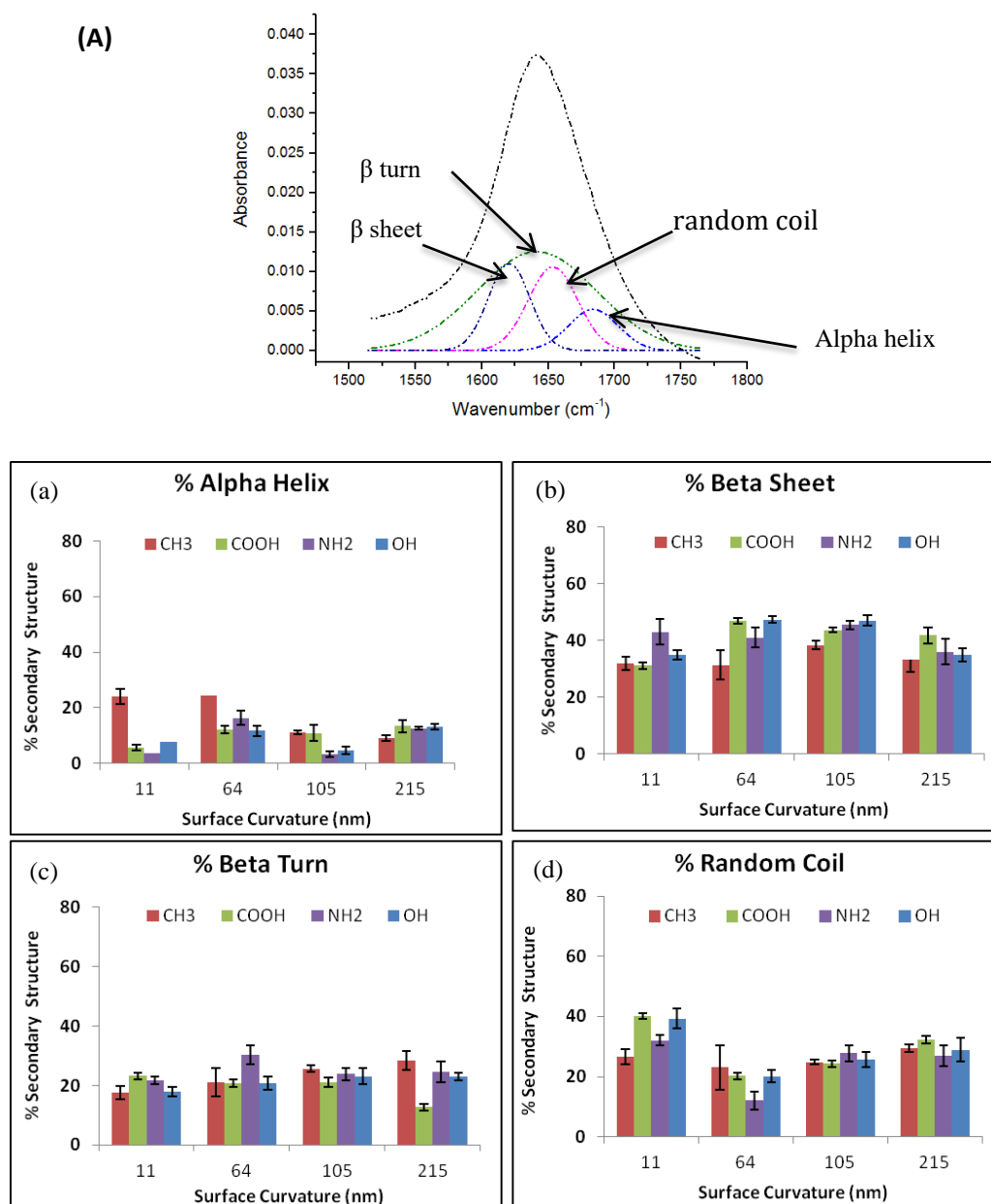


Figure 4.12 (A) Results of FTIR analysis on the Amide I band of HSA/Fg on hydroxyl surface (OH) of particle size of 11 nm at 30 minutes. (B) The percentage of secondary structure of HSA/Fg at 30 minutes, (a) α -helix (b) β -sheet (c) β - turn (d) random coil. Data shown are the mean \pm SD of three replicate samples, $n=3$.

There are high percentages of random coil at 11 nm for each surface chemistry as shown in Figure 4.12.

Low presence of α -helix is recorded on Figure 4.12 (a) for surface curvature of 11-215 nm. Methyl surface (CH_3) remains constant at 11 and 64 nm, rapid decreases in alpha helix at 105 and 215 nm were observed. Methyl surface have the highest percentage of α -helix at 11 and 64 nm.

There is high percentage of β -sheet at 30 minutes as shown in Figure 4.12 (b). Methyl surface increases from 11-64 nm and become constant from 105-215 nm. Hydroxyl surface (OH) remains constants from 11-215 nm while carboxyl (COOH) and amine surface (NH_2) increases from 11- 105 nm and decreases at 215 nm as shown in Figure 4.12 (b).

Hydroxyl surface (OH) on Figure 4.12 (c) shows decreases of β -turn from 11 nm to 64 nm, thereby remain constant from 64 -215 nm. Amine surface (NH_2) have the highest percentage of beta turn at 64 nm, an increase is observed from 11-64 nm and also remain constant from 105 -215 nm. Carboxyl surface decreases as the particle size increase from 11- 215 nm at 30 minutes.

Carboxyl surface (COOH) has the highest percentage of random coil at 11 nm samples. A rapid decrease occurs on all surface chemistry as curvature increases from 11 to 64 nm. Steady increase occurs from 105 – 215 nm particle sizes for all chemistries as shown in Figure 4.12 (d)

The fitting of amide I was carried out for HSA/Fg at different time-points focusing on the effect of surface chemistry and curvature at timepoint of 60 mins.

(C) 60 Mins

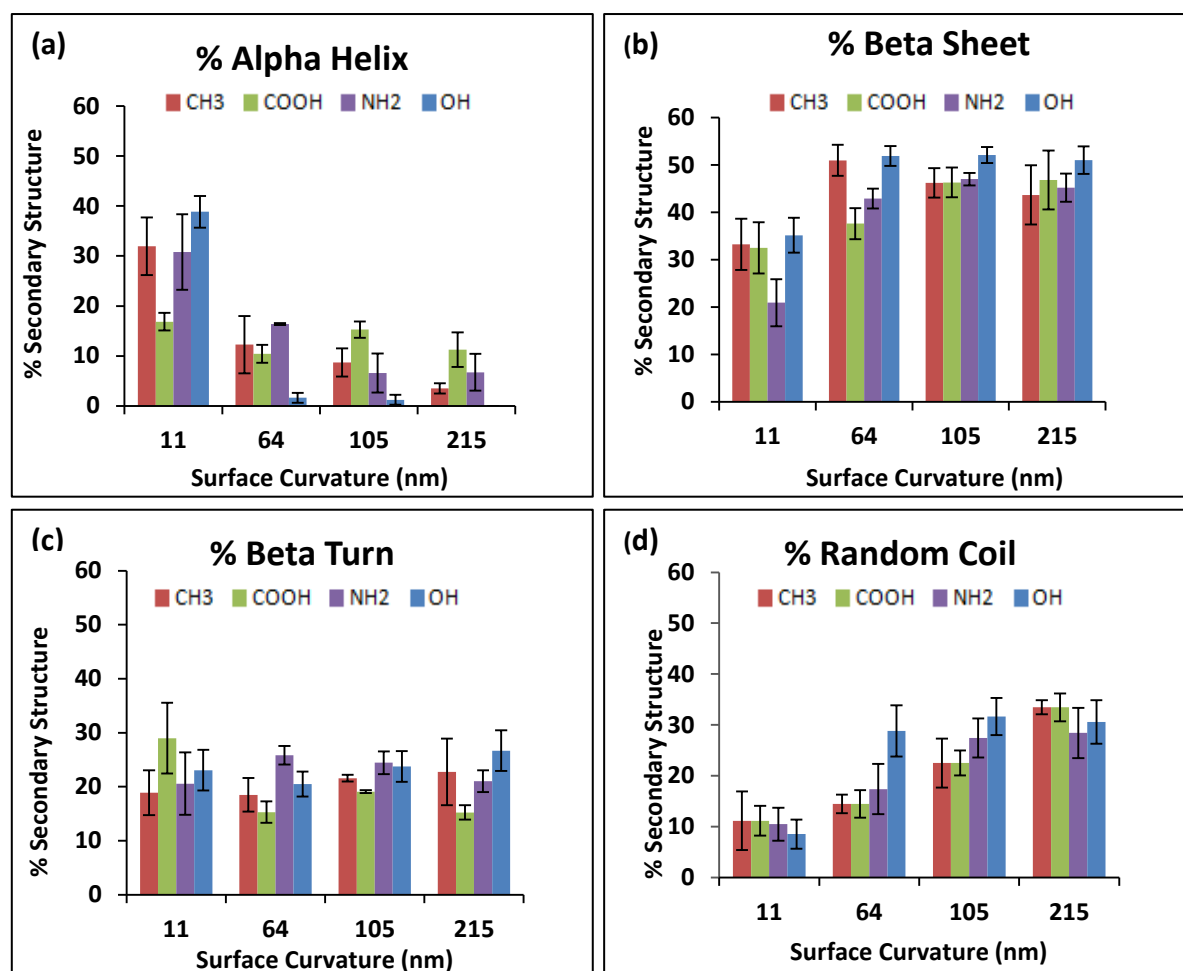


Figure 4.13 The percentage of secondary structure of HSA/Fg at 60 minutes, (a) α -helix (b) β -sheet (c) β -turn (d) random coil. Data shown are the mean \pm SD of three replicate samples, n=3.

As time increases up to 60 mins, there is lower percentage of α -helix observed on 64-215 nm which relates to a higher percentage of random coils on 64-215 nm on surface chemistry. As the curvature size increases, the random coil component increases. There is a high percentage of β -sheet especially on functional groups at 11-215 nm samples as shown in Figure 4.13 (a)-(d)

The fitting of amide I was carried out for HSA/Fg at different time-points focusing on the effect of surface chemistry and curvature at 90 mins.

(D) 90 Mins

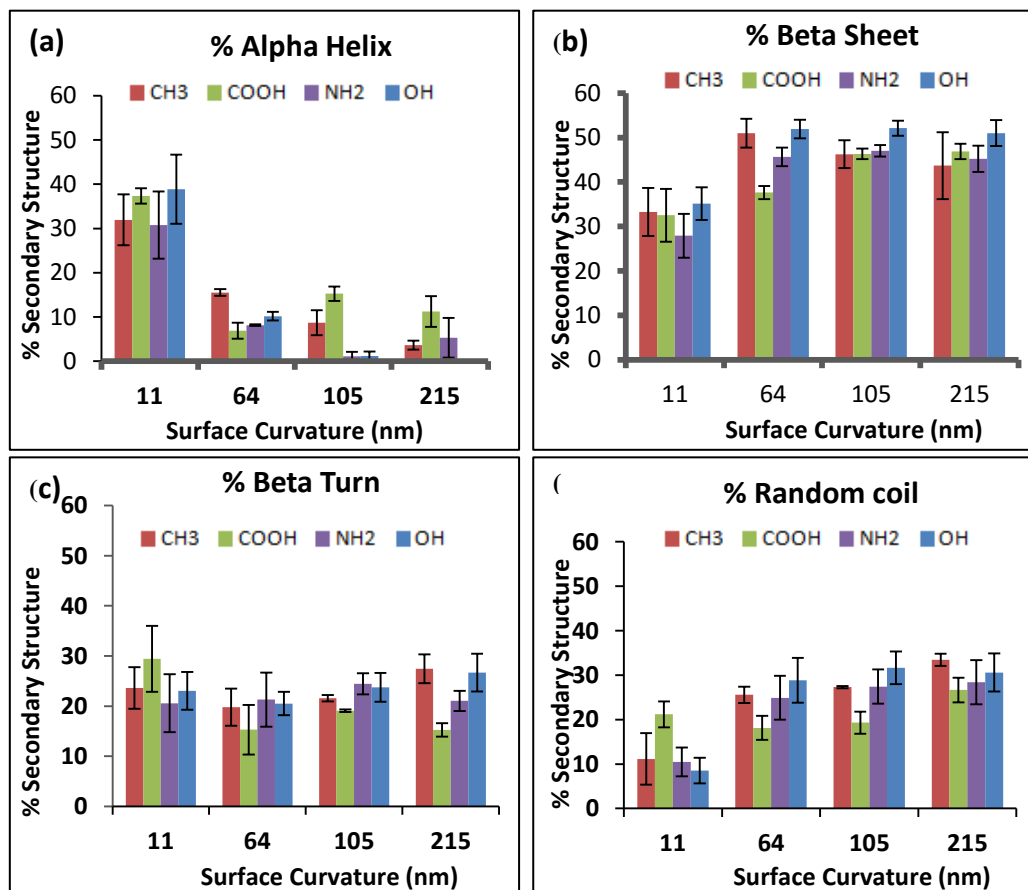


Figure 4.14 The percentage of secondary structure of HSA/Fg at 90 minutes (a) α -helix (b) β -sheet (c) β -turn (d) random coil. Data shown are the mean \pm SD of three replicate samples, n=3.

A similar trend at 60 mins is observed at 90 mins but there is lower percentage of α -helix on amine (NH_2) and hydroxyl surface (OH) at 105 nm. There is a high percentage of random coils present at 11-215 nm. A high presence of Beta Sheet is observed on 11-215 nm at 90 mins. A low presence of α -helix is observed at each size especially on amine (NH_2) and hydroxyl (OH) surface while higher level of random coil is observed on 64-215 nm on surface chemistry as shown in Figure 4.14 (a)-(d)

The fitting of amide I was carried out for HSA/Fg at different timepoints focusing on the effect of surface chemistry and curvature at 120 mins

(E) 120 Mins

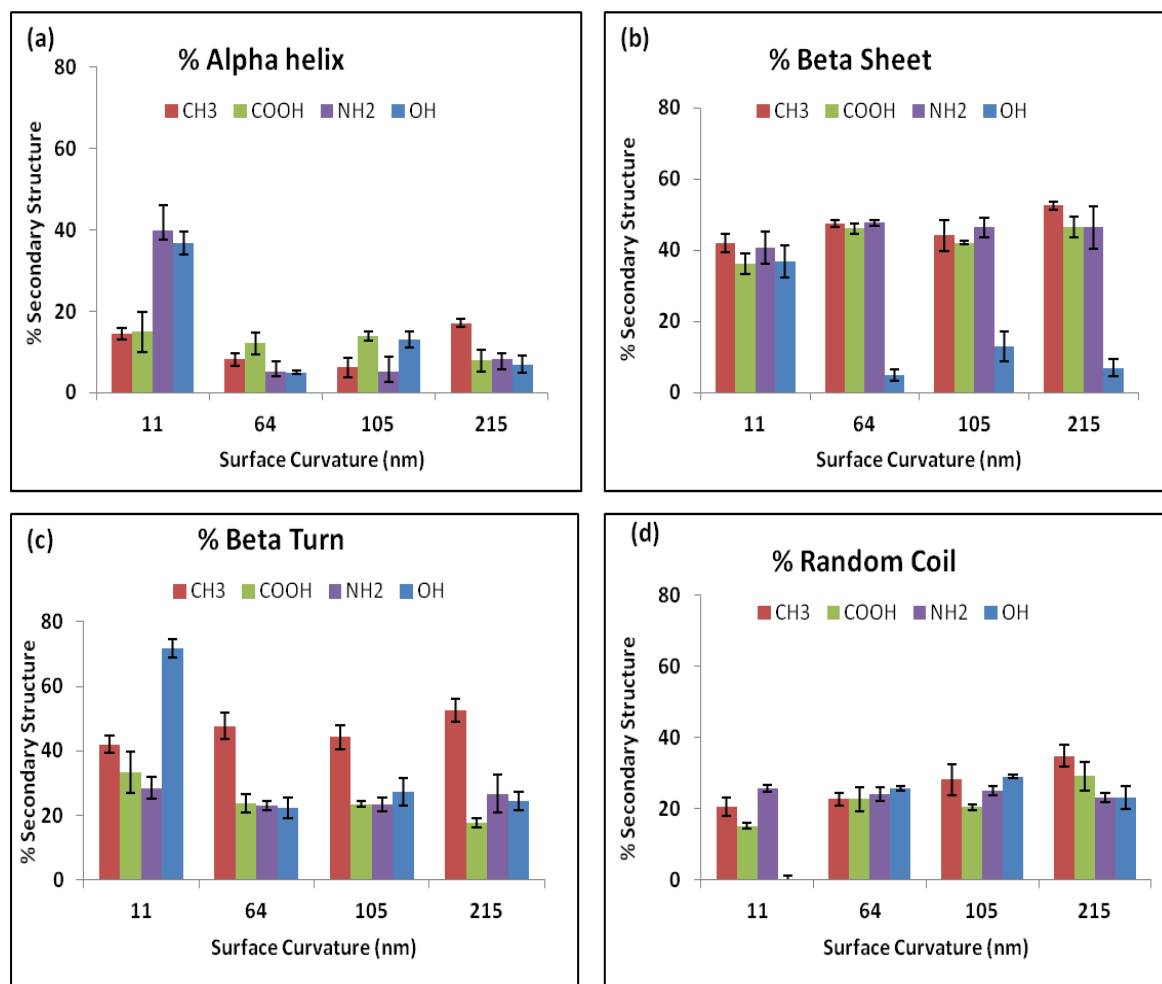


Figure 4.15 The percentage of secondary structure of HSA/Fg at 120 minutes (a) α -helix (b) β -sheet (c) β -turn (d) random coil. Data shown are the mean \pm SD of three replicate samples, n=3.

There is a lower presence of alpha helix still observed at 120 mins on 64-215 nm which relates to higher presence of random coil at 64-215 nm. There is a high presence of β -sheet observed but there is low percentage of β -sheet on hydroxyl surface (OH) as shown in Figure 4.17(a)-(d)

The fitting of amide I was carried out for HSA/Fg at different timepoints focusing on the effect of surface chemistry and curvature at time-point of 180 mins.

(F) 180 Mins

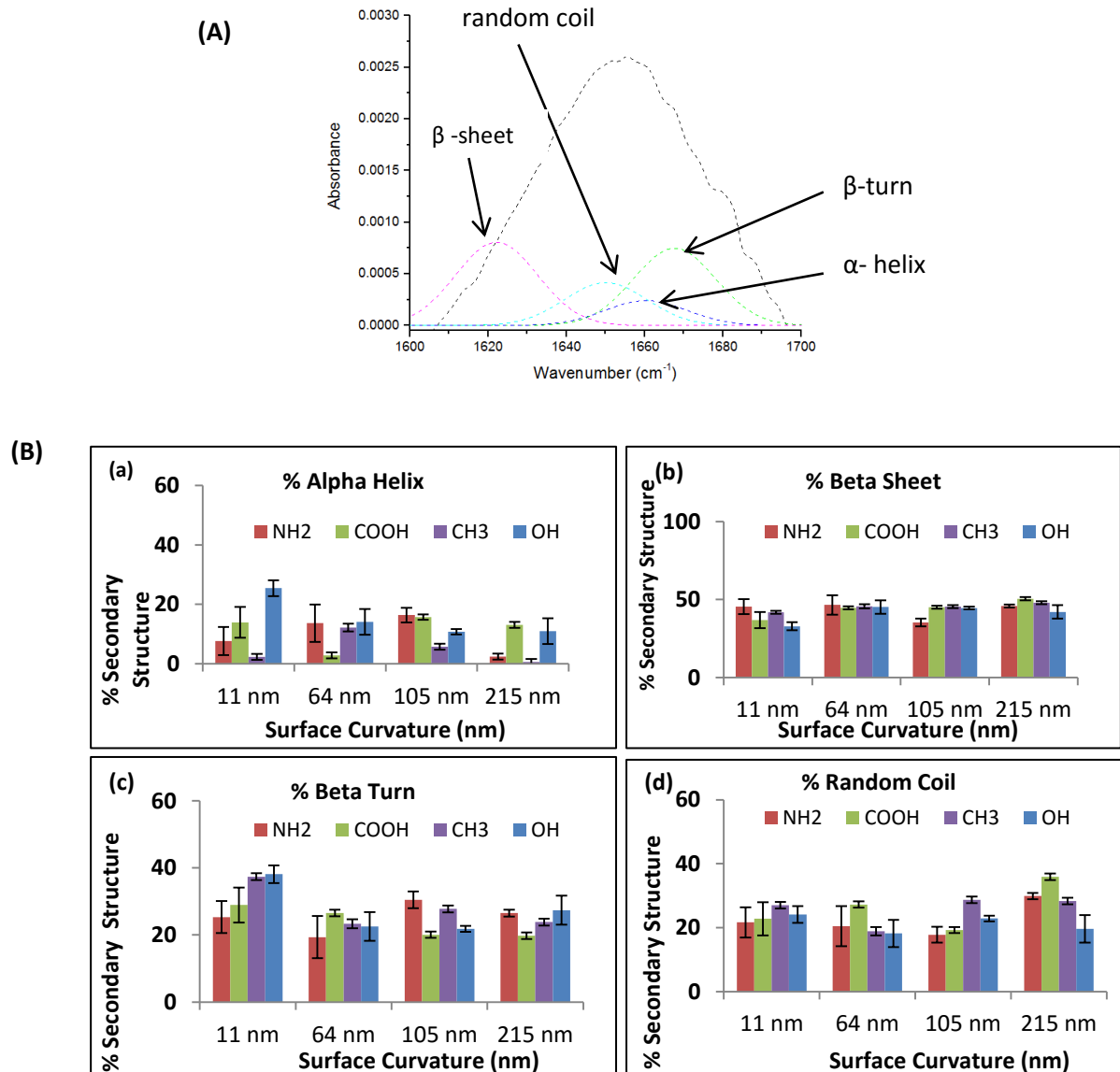


Figure 4.16 (A) Results of FTIR analysis on the Amide I band of BSA/Fg on hydroxyl surface (OH) of particle size of 215 nm at 180 minutes (B) The percentage of secondary structure of HSA/Fg at 180 minutes (a) α -helix (b) β -sheet (c) β -turn (d) random coil. Data shown are the mean \pm SD of three replicate samples, n=3.

At 180 mins, lower percentage of alpha helix is observed on surface curvature and chemistry while β -sheet has a high percentage on 11-215 nm. Carboxyl surfaces (COOH) have the highest percentage of random coil on 11, 64 and 215 nm. The β -turn conformations has a high percentage at 11 nm compare to other surface curvature at 64-215 nm.

4.3.5 PCA Analysis

PCA is a multivariate analysis technique that helps in the interpretation of datasets by identifying the major differences and bunching them together in *principal components*. The principal components (PCs) can then be used as a means of correlating patterns in data. PCA analysis was done on the FTIR data to understand the array pattern of amide I with respect to surface chemistry and curvature. The principal components (PCs) are used as a means of correlating patterns in the data, for instance variance associated with a particular sample subset. Each of these PCs has a score relating the degree of variance associated with it as seen in Figure 4.17. PC1 having the highest difference between datasets while PC3-PC20 have the lowest value of eigenvalue. PC1-2 were focused upon .

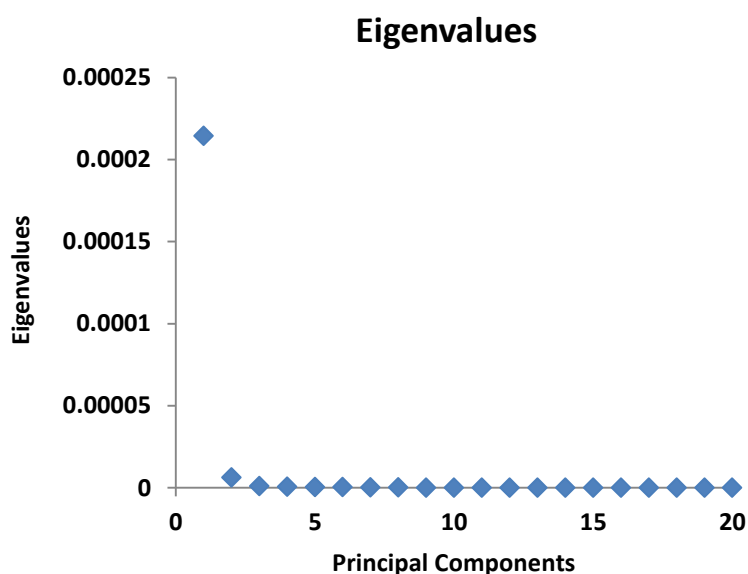


Figure 4.17 Eigen values of each principal component

4.3.5.1 Loading Plots

Each of the principal components is a packet of variables which highlight discrimination between samples in the datasets. Figure 4.18 represents the loading from PC1 and PC2 for datasets at different timepoints. Each of the datasets with negative and positive loadings corresponds to the position of the sample point within the scores plot. For instance a higher score for PC1 will have an overall higher proportion of positive PC1 loading peaks, along with less negative PC1 peaks.

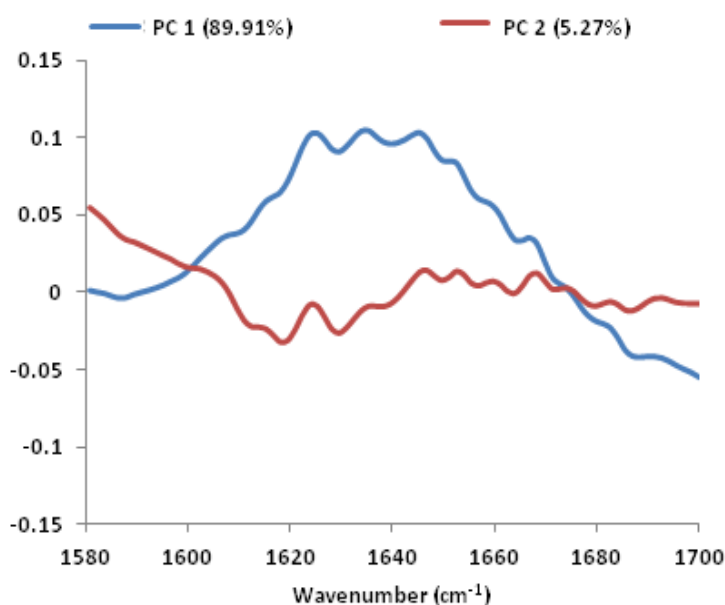


Figure 4.18 Amide I loading plot of PC1 vs PC2

PC 1 (89.91%) shows a broad amide I band between 1610 and 1680 cm⁻¹ while PC 2 (5.27%) has a wavenumber value between 1620 and 1640 cm⁻¹ as shown in Figure 4.20.

4.3.5.2 Score Plots

The score plot shown in Figure 4.19 captures 89.91% of the variance in the data in PC1, 5.27% of the variance in PC2. The data is presented such that amide I ($1600\text{-}1680\text{ cm}^{-1}$) is focused upon for the dataset for protein conformation change. The remaining dataset for surface chemistry at different timepoints are shown in the appendix.

PC1 and PC2 in terms of Surface Chemistry

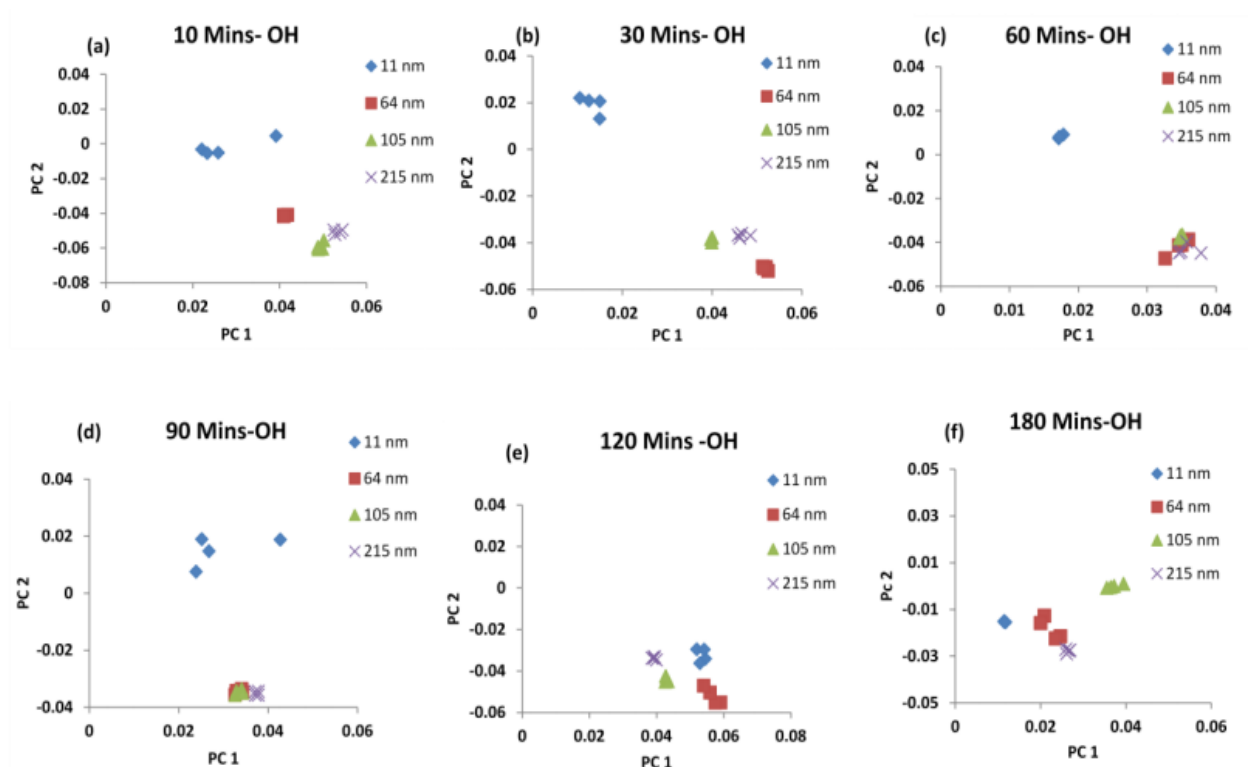


Figure 4.19 Score plots on the first two multivariate axes from PCA of the Amide I FTIR spectra on surface curvature of 11-215 nm on hydroxyl surface (OH) at 10-180 minutes.

At 10 mins, there is a distinctive difference between curvature sizes of 11- 215 nm on hydroxyl surface. The 11 nm samples were further apart from 64, 105 and 215 nm. Clustering of 105 and 215 nm samples is observed while 64 nm samples stand out from 105 and 215 nm. At 30 mins, The 11 nm samples moves further away from the rest of the curvature size while 64 nm samples moves further away from 105 and 215 nm. 11 nm samples is further apart as reported in 10 mins but the samples are moving close towards the

other samples. There is a clustering of samples observed on 64, 105 and 215 nm at 60 mins. At 10, 30 and 60 minutes all samples on each surface curvature are closely packed.

Clustering of dataset is observed at 64, 105 and 215 nm while scattering of samples at 11 nm is observed although the samples on 11 nm is further apart from other curvature size at 90 mins. At 120 mins, clustering of all samples is observed between PC 1 (0.04, 0.06) and PC2 (-0.03, -0.06). The dataset on each curvature of 11, 64, 105 and 215 nm stands apart. At 180 mins, all the samples moves further away from PC1 value of 0.04-0.06. 105 nm samples are further apart from 11, 64 and 215 nm samples. The score plots of amide I spectra shows the curvature size and time have an effects on protein-nanoparticle interaction. The score plot of amide I spectra on methyl surface (hydrophobic) is shown below in Figure 4.20 at different timepoints.

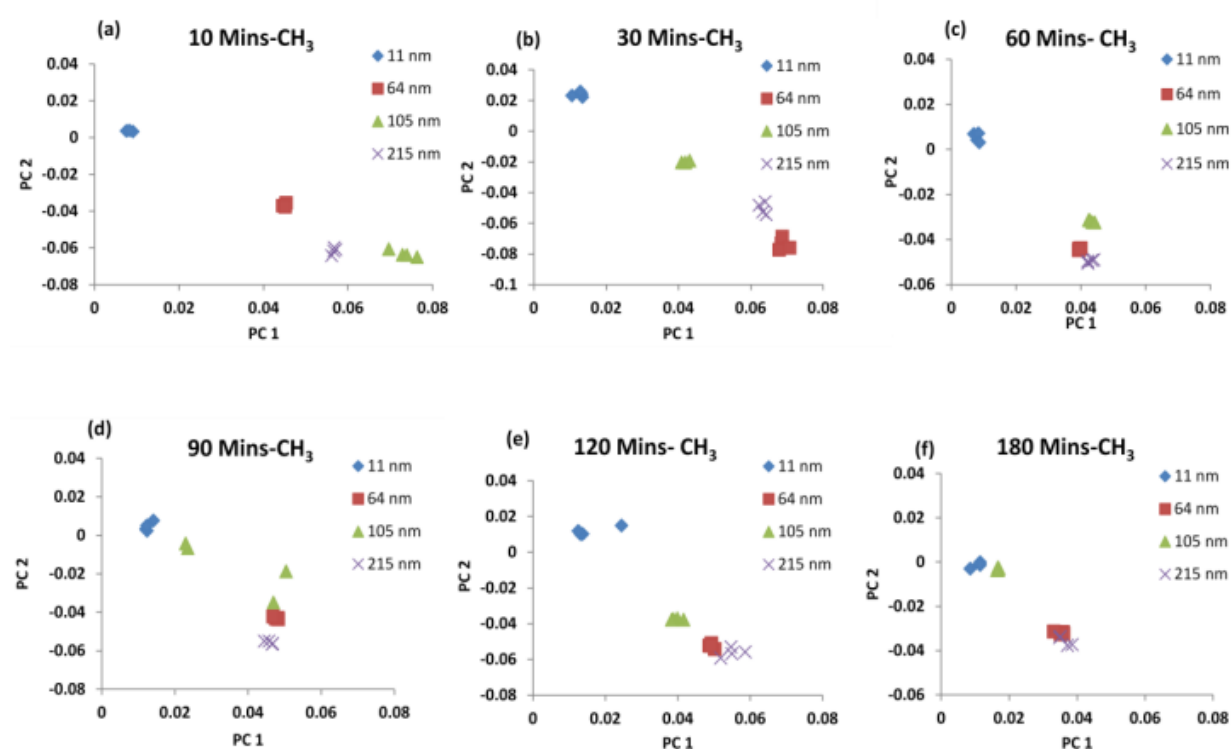


Figure 4.20 Score plots on the first two multivariate axes from PCA of the Amide I FTIR spectra on surface curvature of 11-215 nm on methyl surface (CH₃) at 10-180 minutes.

Figure 4.20 shows amide I spectra results on CH₃ surface at 10-180 mins. At 10, 30 and 60 mins, samples are further apart from other curvature size at each timepoints. The 105, 215 and 64 nm samples were apart from each other at 10 mins and 30 mins. At 60 mins, clustering of 64, 105 and 215 nm samples is observed.

Scattering of the 11 nm dataset is observed at 90 mins. The 11 nm samples still remain further apart at 120 and 180 mins till experiment was halted. Clustering of 64 and 215 nm samples is observed at 90, 120 and 180 mins. Scattering of 105 nm dataset is observed at 90 mins. Some of the dataset at the 105 nm is seen moving towards 11 nm while the others are clustering around 64 and 215 nm.

PC 1 and PC 2 on Surface Curvature

The dataset obtained in Figure 4.21 and 4.22 was replotted to investigate the effect of surface curvature of 11 and 215 nm on PC1 and PC 2, which is shown in Figure 4.21 and Figure 4.22

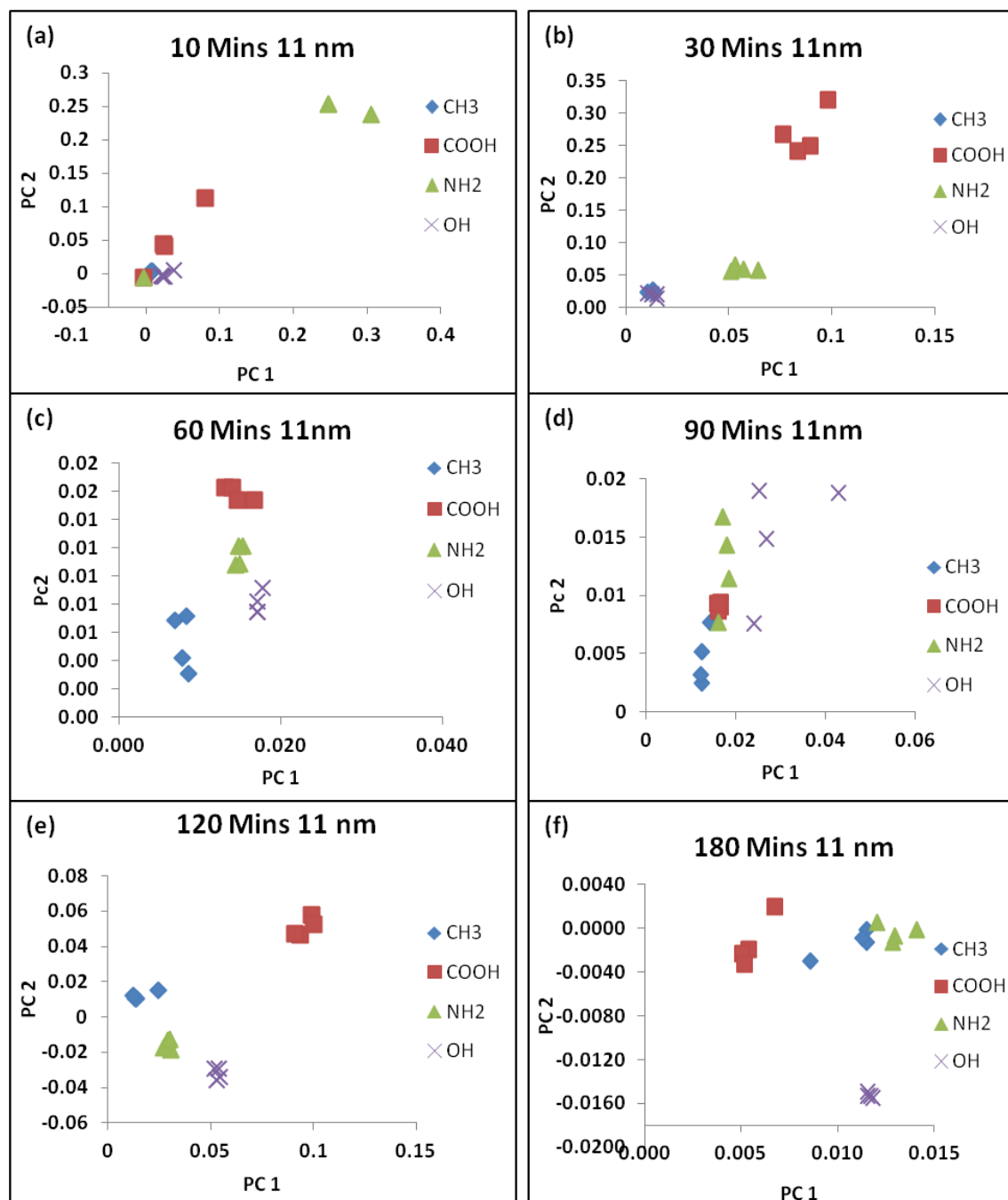


Figure 4.21 PC1 and PC2 score plots of amide I of 11 nm at different timepoints (10, 30, 60, 90,120 and 180 mins)

The results in Figure 4.21 (a)-(f) shows the PC1 and PC2 spectra of amide I at different timepoints and surface chemistry at curvature size of 11 nm.

Figure 4.21 (a) shows clustering of the dataset of carboxylic (COOH), hydroxyl (OH) and methyl surface (CH₃) at 10 mins. Some of the dataset of amine surface (NH₂) were far apart from other surface chemistry at 11 nm.

At 30 mins, Figure 4.21 (b) shows COOH and NH₂ dataset were observed to be far apart from other chemistries. Clustering of OH and CH₃ is observed near the origin. Little scattering of dataset is observed on each surface chemistry at 60 mins as shown in Figure 4.21 (c). The COOH is still further apart from OH, NH₂ and CH₃.

At 90 mins, scattering of OH and NH₂ is observed and the majority of the dataset of each surface chemistry aligned close to each other as shown in Figure 4.21 (d).

At 120 mins, the COOH dataset is still further apart while CH₃, NH₂ and OH aligned closed to each other as shown in Figure 4.21 (e). Figure 4.23 (f) shows different pattern compared to other timepoints. Clustering is observed on COOH, CH₃ and NH₂ dataset is observed to be further apart from OH dataset at 180 mins.

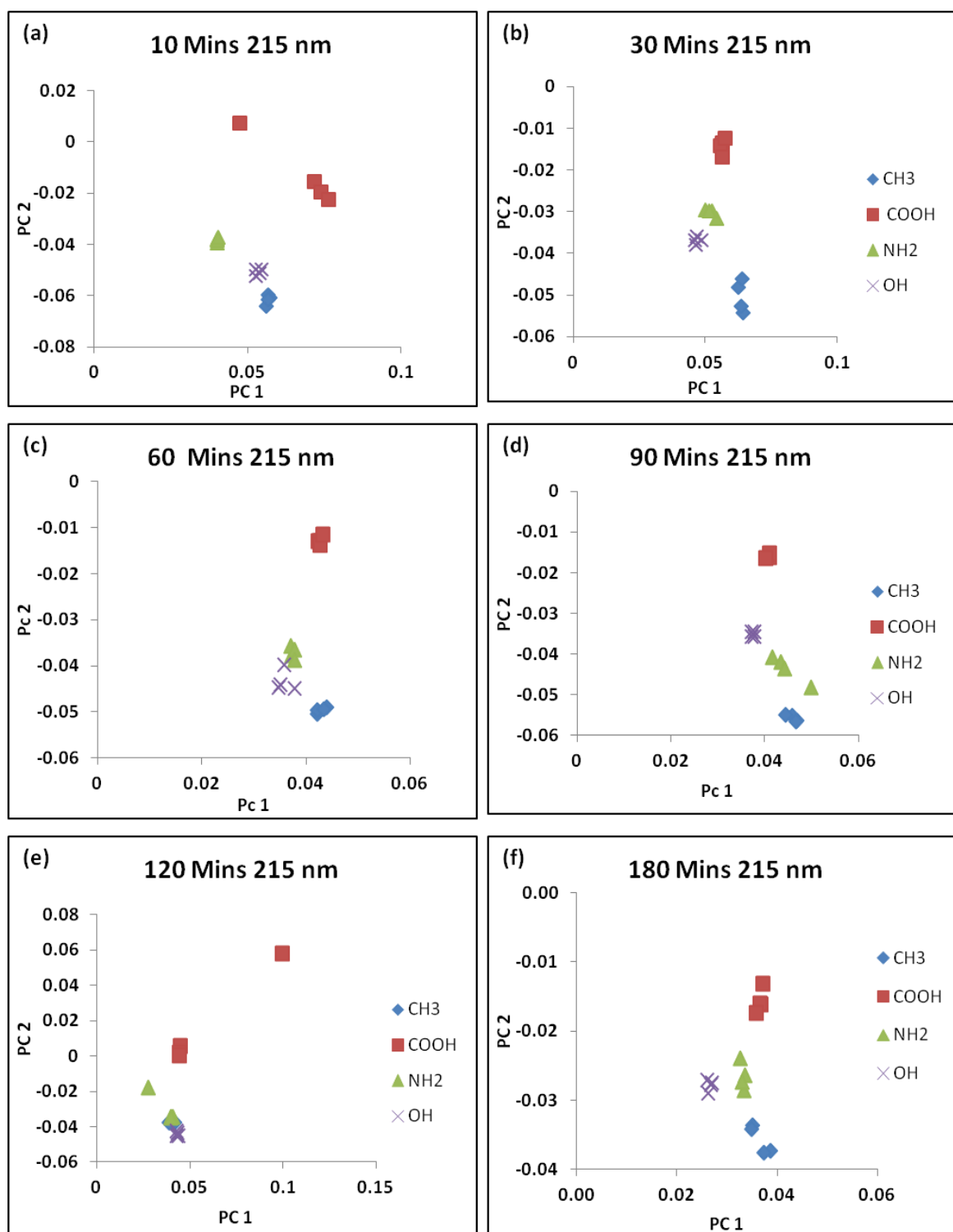


Figure 4.22 PC 1 and PC 2 score plots of amide I of 215 nm at different timepoints (10, 30, 60, 90, 120 and 180 mins)

The results in Figure 4.22 (a)-(f) shows PC1 and PC2 spectra of amide I at different timepoints and surface chemistry on curvature size of 215 nm. The COOH dataset is observed to be further apart from other surface chemistry at 10-180 mins. The NH₂ dataset is observed to be clustered at each timepoint although little scattering is observe at 60 and 180 mins. The NH₂ dataset is observed to be close to OH surface at 10- 180 mins. The CH₃ dataset also stands apart from other surface chemistry although clustering of CH₃ dataset is observed at 120 mins with OH and NH₂ dataset.

The OH dataset is observed to be clustered around the NH₂ and CH₃ dataset at 10-90 mins. Clustering of the OH dataset with NH₂ and CH₃ is observed at 120 mins. The OH dataset is observed to be surrounding the NH₂ dataset at each timepoints.

4.4 Discussion

Silica has been widely used for the coating of nanoparticles due to its properties, chemically inert, stable and biocompatible properties.^{19, 20} Functionalization of silica is well established using the self assembled monolayer technique which is used by other researchers.²¹⁻²³ The results of this work show a successful functionalization and a high colloidal stability of the particles in ethanol. The FTIR, WCA and XPS results confirm the presence of functional groups after the functionalization of silica spheres. Calibration of both HSA and Fg was carried out, showing a linear range response in the working range of 0-15 µg/mL.

Adsorption of HSA and Fg have been widely studied using single protein solution. The competitive adsorption of proteins on surfaces with regard to changing surface properties is challenging and not well understood. The effect of surface chemistry and curvature on competitive adsorption of HSA and Fg at different time-points has being reported in this Chapter. The study of surface chemistry is vital in understanding the adsorption kinetics in protein adsorption since some studies show adsorption on hydrophobic surfaces have adsorbed higher protein.²⁴

The results of the competitive adsorption of HSA and Fg as shown in the results section shows the effects of surface chemistry and curvature of HSA only, Fg only and the ratio of HSA/Fg at different time-points. Different timepoints were set for this experiment to understand the dynamic conformation changes that take place with respect to surface chemistry and curvature. HSA and Fg mixed solutions (HSA and Fg) of physiological ratio of 19:1 is assessed and measurement was carried out and the relative ratio of adsorbed proteins is assessed. HSA and Fg have been used to understand competitive adsorption on nanoparticles.²⁵

In this work, fluorometric assay is used to determine the amount of protein adsorbed in combination with infrared spectroscopy to assess conformational changes/differences with

respect to both surface properties and time of adsorption. PCA was also carried out to further understand similarities/differences with respect to the global vibrational data.

The effect of surface chemistry on HSA adsorption shows carboxylic surface (COOH) has the highest adsorption at $48 \mu\text{g}/\text{m}^2$ while methyl surface (CH_3) has the least adsorption of $35 \mu\text{g}/\text{m}^2$ at 180 mins. No major difference in adsorption is observed on methyl surface (CH_3) as the time-point increases for all surface curvature as shown in Figure 4.23. In chapter 3, section 3.3.8, higher affinity of albumin for CH_3 as curvature sizes increases was observed. This suggests that upon initial adsorption, no further change occurs i.e. the compositional with respect to HSA does not change with time.

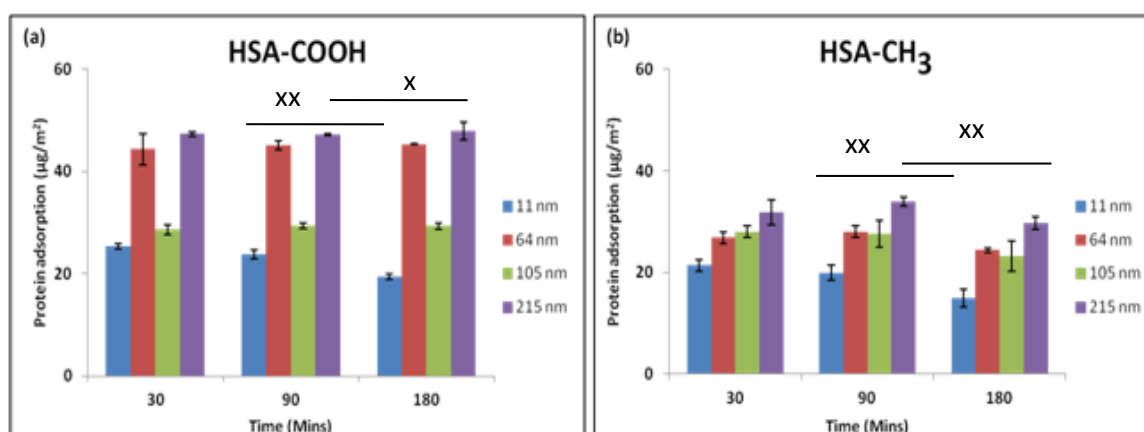


Figure 4.23 HSA adsorption on carboxylic (COOH) and methyl (CH_3) surface. Data shown are the mean \pm SD of three replicate samples. T test value shows $p < 0.5$ (x), $p < 0.05$ (xx),

HSA adsorption on CH_3 shows a decrease in adsorption on 11, 64 and 105 nm. The 215 nm have the highest HSA adsorption on methyl surface and carboxylic surface as shown in Figure 4.23. The results shows that surface charge may give rise to greater amounts of adsorption compared to hydrophobic interactions which support the findings presented in Chapter 3. Fg adsorption on methyl surface (CH_3) have the highest adsorption in terms of surface chemistry while the carboxylic surface (COOH) displays the least adsorption as shown in Figure 4.24 as the time-point increases.

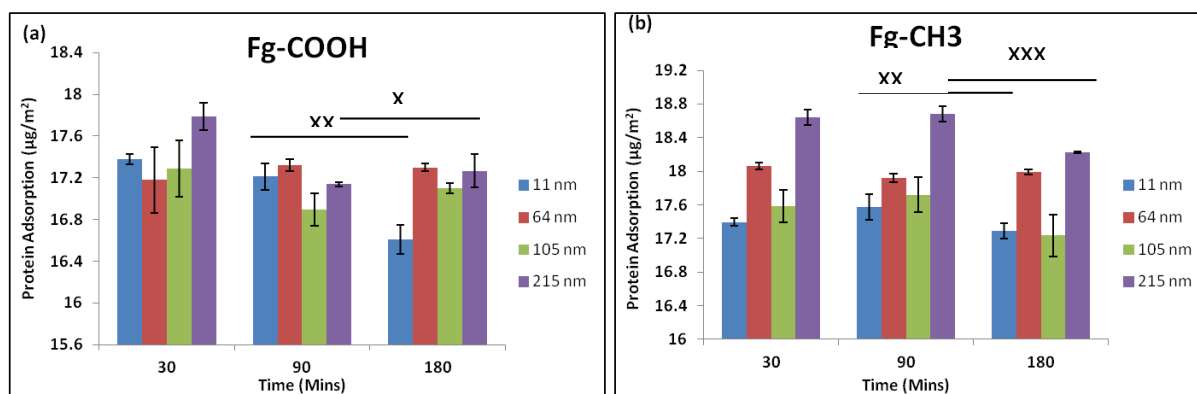


Figure 4.24 Fg adsorption on carboxylic (COOH) and methyl surface (CH₃). Data shown are the mean \pm SD of three replicate sample. T test values indicate $p < 0.5$ (x), $p < 0.05$ (xx), $p < 0.005$ (xxx).

On CH₃ surface, HSA stays constants over time, yet fibrinogen decreases, suggesting a possible change in configuration of the protein layer. Fg adsorption on methyl surface (CH₃) shows a constant value on 64 nm as the time-point increases whereas on other particle sizes, a slight decrease is observed between 90-180 min, with a p value of 0.004, $p < 0.005$. The results confirms the findings of previous researchers which shows Fg interacts with methyl surface greatly compared to other surface chemistries.²⁷⁻²⁹

The adsorption of Fg and HSA in competition were further analysed by fitting the IR spectra result at different time-points to understand the effect of surface chemistry and curvature on protein conformation as the time increases. More in-depth analysis was carried out using amide I component peak fitting. This gives detailed information on the secondary structure, but it should be clearly noted that again this is global structure encompassing HSA and Fg. The fitting of amide I shows the higher the random component present, the lower the presence of alpha-helix as the timepoint increases. A higher percentage of β sheet and β turn is observed at each timepoint. Secondary structural change of HSA/Fg on COOH and CH₃ surface at 30, 90 and 180 mins is shown in Figure 4.25 (a)-(f).

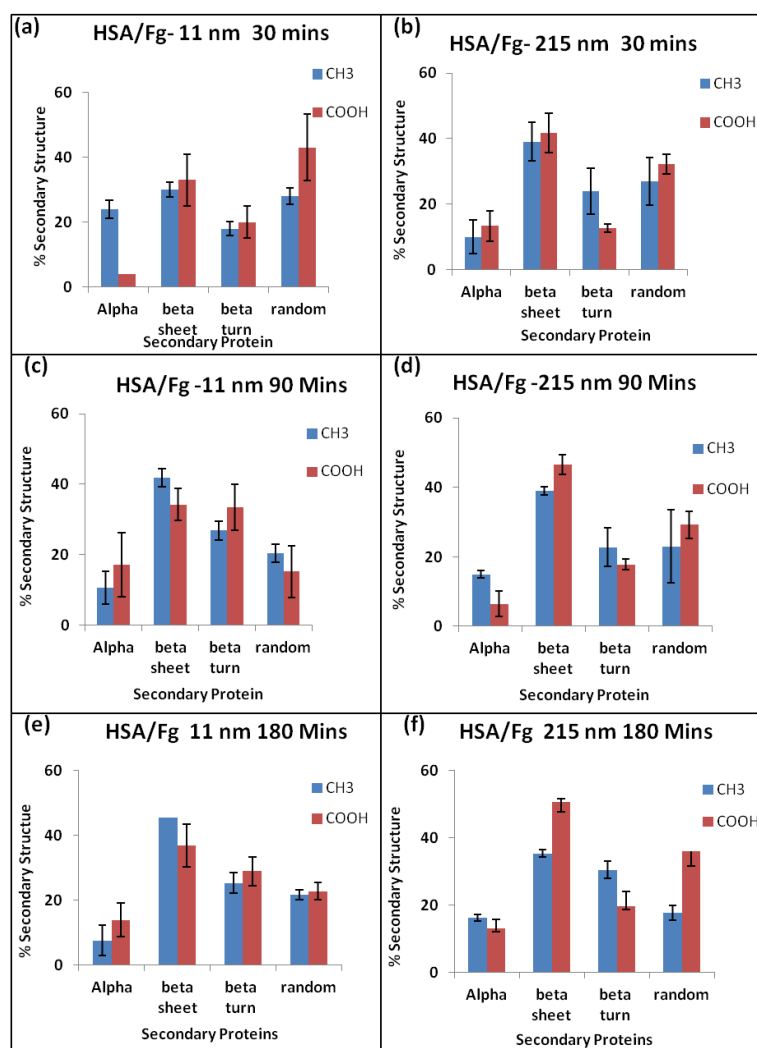


Figure 4.25 The percentage of secondary structure on CH₃ and COOH on 11 and 215 nm, at 30, 90 and 180 mins. n=3.

At 90 min, Figure 4.25 (c) and (d) shows a higher presence of beta sheet on surface curvature of 11 and 215 nm and chemistry of CH₃ and COOH surface. The percentage of alpha helix on surface curvature of 11 and 215 nm is lower while high random coil component is observed on COOH surface compared to CH₃ surface at 90 mins which corresponds to the results in Figure 4.25 of higher adsorption of 50 µg/mL on COOH surface at 90 mins. As time increases to 180 mins, the percentage of alpha helix is found to have the lowest percentage compared to all other protein structures as shown in Figure 4.25 (e) and (f).

The uses of PCA to study protein adsorption has been explored previously.^{30,31} The data from the eigenvalues of secondary protein structure over various surface chemical functionalities and different time-points was examined, and the first two PC's were taken, giving 89.91% confidence in the variance. Principal component variability in FTIR dataset shows the difference or similarity of secondary structure on the whole dataset, including chemistry, size and time.

PCA analysis of the amide I alone was carried out to assess global difference/similarity in the secondary structure of adsorbed proteins as shown in Figure 4.28, there is a change in the PC1 and PC2 scores relative to the time change from 30-90-180 mins with respect to CH₃ terminated particles. This demonstrates clearly, a change in global secondary structure.

Score plots of PC1 and PC2 on CH₃ surface at 30, 90 and 180 mins is shown in Figure 4.26. In terms of surface chemistry, 11 nm on OH and CH₃ surface is further apart from other curvature size, but as the time increases, 11 nm is observed to be closer to other surface curvature while some clustering is observed. In terms of surface curvature, results shows at 11-215 nm, no major clustering observed on surface chemistry as time increases, although some scattering is observed on carboxylic surface (COOH).

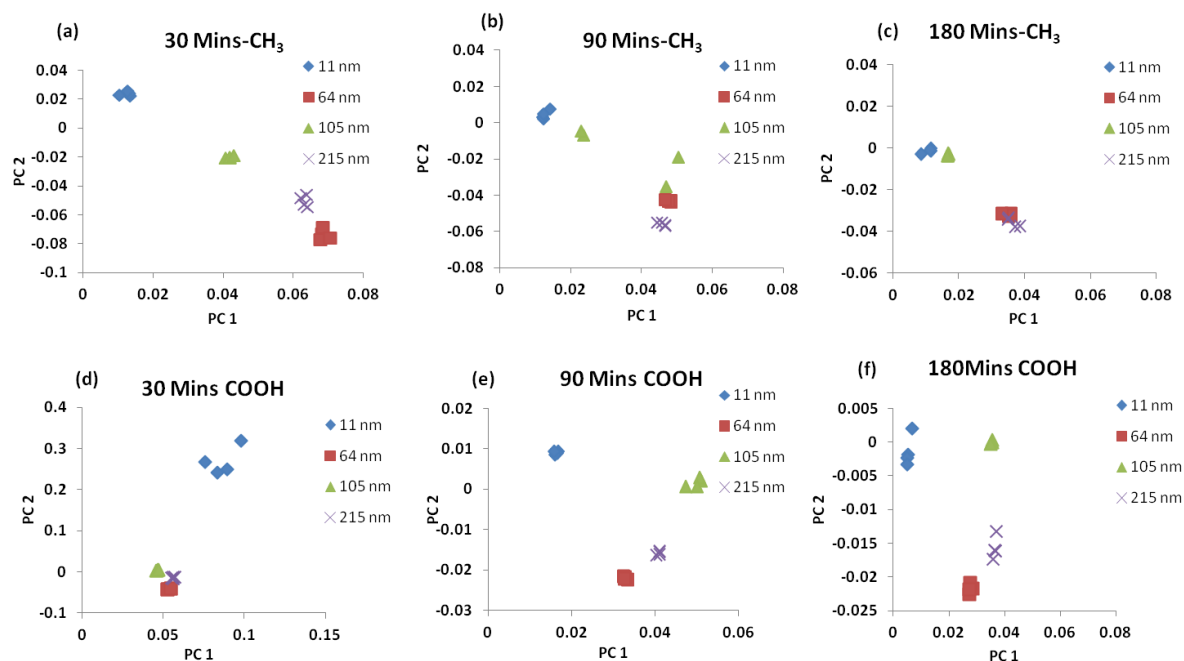


Figure 4.26 PC 1 and PC2 show the variability in amide I dataset on COOH and CH_3 surface

The interaction process between HSA and Fg differs on each surface chemistry. HSA adsorption on COOH surface shows a constant adsorption as the time increases on 64, 105 and 215 nm while a steady decrease in measured adsorbed amount is observed on 11 nm as the time-point increases between 90-180 mins with a p value of 0.006, $p < 0.05$. The affinity data in Chapter 3, section 3.3.8 shows higher affinity on carboxylic surface which may indicate that this affects the strength of binding during competitive adsorption.

Negatively charged surfaces (COOH) have the highest amounts of HSA compared to all other surfaces tested. Hydrophobic surface are widely known to adsorb higher amounts of protein, depending on the nature of the interaction and conformational distribution during adsorption. Hydrophilic surfaces can inhibit adsorption according to some researcher^{32,33} Protein adsorption results vary based on the type of nanoparticle and type of protein. Deng *et al*³⁴ and Fertsch-Gapp *et al*³⁵ have demonstrated that surfaces with no charge bind less protein than their negatively-charged (COOH) or positively charged (NH_2). Fg adsorption on

carboxylic (COOH) surfaces display the least adsorption in terms of surface chemistry and adsorption decreases as the time-point increases from 30-180 mins, as shown in Figure 4.24, with a p value of 0.41, $p < 0.5$. The PCA analysis in Figure 4.26 confirms changes in PC1 and PC2 as time increases from 30-90-180 mins with respect to COOH terminated particles. Scattering and clustering of the datasets is observed at the initial timepoint of 30 mins while variations in samples were observed as the timepoint increases from 90-180 mins in PC1 and PC2. The secondary structure of COOH surface as time-point increases shows an increase in random coil component and beta sheet as time increases while a lower percentage of alpha helix is recorded. The results relate to the finding in Chapter 3, i.e the lower the alpha helix present, the higher the random coil component.

Fibrinogen is known to denature as the surface curvature of silica nanoparticles increases from 7-82 nm according to Roach *et al.*³⁶ HSA adsorption reveals 215 nm has the highest adsorption while 11 nm has the least HSA adsorption as shown in Figure 4.27. On 11 nm particles no major changes are observed in HSA adsorption over time and over all chemistries tested. This is in contrast to data reported for HSA binding from single protein solutions (Chapter 3). This indicates that when in competition with Fg for surface sites the amount of HSA is 'buffered'. As there is much more HSA in solution compared to Fg (mimicking biological ratios of 19:1) it is likely that HSA rapidly adheres to the surface reaching equilibrium more quickly in a competitive scenario due to simultaneous binding of much stronger adhering Fg. A slight reduction in HSA adsorbed component is observed at 180 minutes on CH₃ terminated surfaces. This is not reflected in the amount of Fg adsorbed on similar particles as shown in Fig. 4.8, highlighting the possibility for a change in protein structure during adsorption. There is also a suggestion of time dependant protein structural change highlighted by the oscillatory adsorbed amount of HSA on both amine and hydroxyl 215 nm particles. A decrease in the amount adsorbed is demonstrated on these particles after

~100 minutes, Figure 4.7, with similar somewhat more pronounced trends for these surfaces being shown for Fg in Figure 4.8. One hypothesis may be that the larger particles, presenting lower surface curvature, allow re-orientation of the protein molecules after initial binding. This would be consistent with previously reported finding from single protein adsorption systems.³⁶

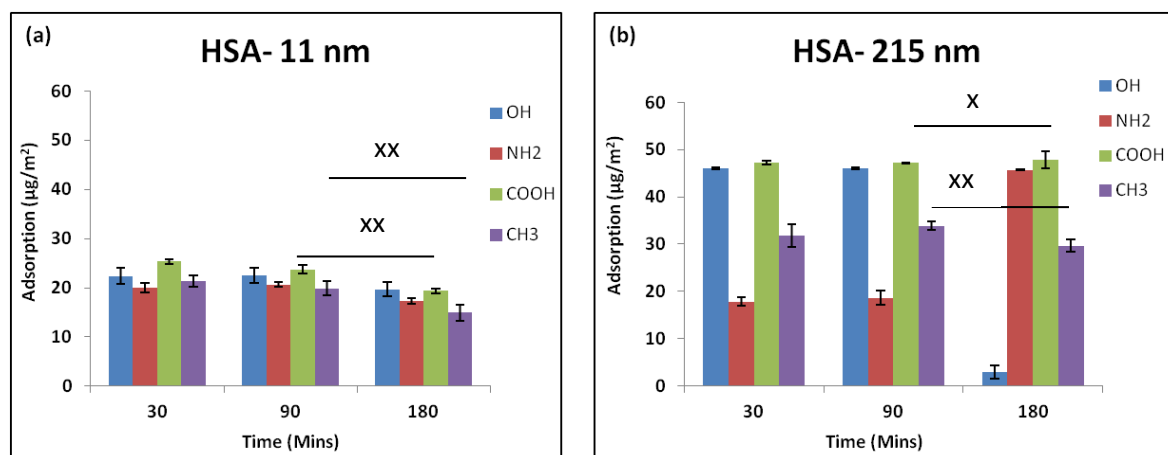


Figure 4.27 HSA adsorption on 11 and 215 nm. Data shown are the mean \pm SD of three replicate samples. T test value indicates $p < 0.5$ (x), $p < 0.05$ (xx).

A higher affinity of HSA on 11 nm is observed in the previous chapter which confirms lower adsorption while Fg adsorption on 11 nm has a lower affinity. Secondary structure on 11 nm at 30, 90 and 180 mins confirms the low percentage of random coil component as the time increases on CH₃ and COOH surface. This suggest the higher the affinity, the adsorption of HSA decreases as time increases. PCA analysis shows changes in PC1 and PC2 score plot of 11 nm on each of functional group (OH, COOH, NH₂ and CH₃) as the time increases. Clustering of samples is not observed but a variance between particle sizes as the time increases on surface chemistries. Fg adsorption also shows 215 nm have the highest adsorption while 11 nm have the lowest Fg adsorption as summarised in Figure 4.26

Cai *et al*²³ reveals nanoparticle size affects protein adsorption on titanium films of 2- 21 nm which confirms the finding in this Chapter as shown in Figure 4.28 of Fg adsorption on 11 and 215 nm.

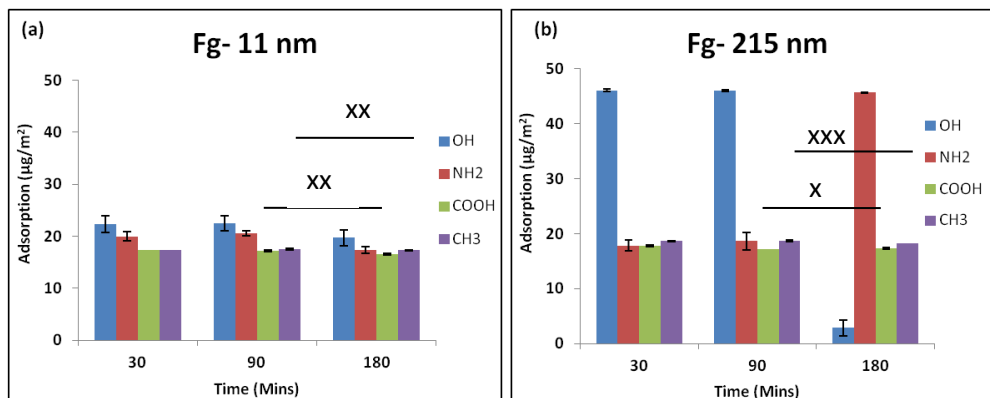


Figure 4.28 Fg adsorption on 11 and 215 nm. Data shown are the mean \pm SD of three replicate samples. T test value indicates $p < 0.5$ (x), $p < 0.05$ (xx), $p < 0.005$ (xxx).

The results shown in Figure 4.29 demonstrate that the carboxylic surface stabilises the protein layer adsorbed within the first 30 mins, with very little change to the HSA/Fg ratio after this time, In contrast, the OH surfaces alter the protein composition between 90 and 180 minutes suggesting that HSA is lost from the surface, while the amount of fibrinogen increases.

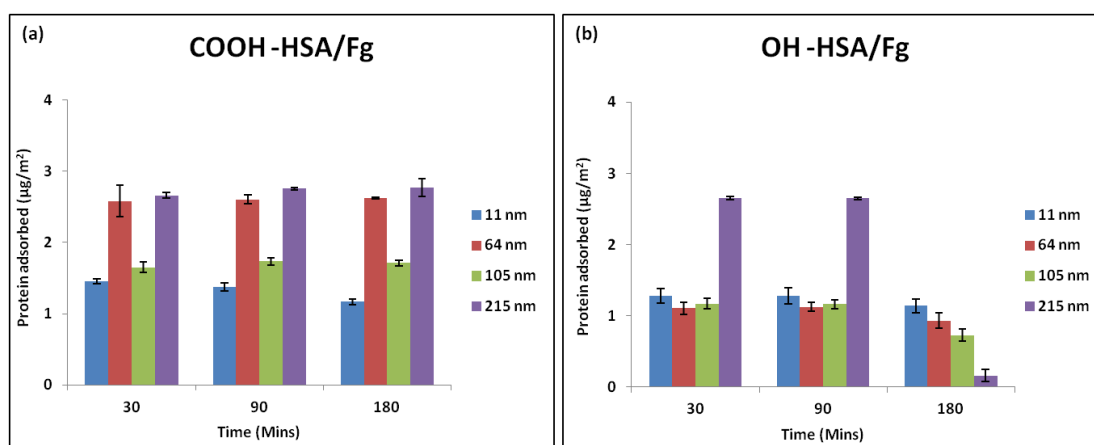


Figure 4.29 Effect of surface chemistry on HSA/Fg (19:1) adsorption. Data shown are the mean \pm SD of three replicate samples.

The results shown in Figure 4.29 confirm the principle of the Vroman effect which states that small protein molecules adsorbed more rapidly than larger molecules. The results in Figure 4.29 (a) correspond to HSA data in Figure 4.23(a). HSA of 66 kDa adsorbed more rapidly than Fg of 350 kDa as the time increases. The Vroman effect has been investigated by other researchers and observed on protein mixtures.^{39,40} The data here suggest that the Vroman effect is observed over the 180 minute timeframe for the OH presenting surface but not the COOH surface. One hypothesis, which is supported by other data in this chapter and from previous literature³⁶, could be the orientation/conformational constraints imposed on adsorbing proteins due to the surface curvature. Fibrinogen is known to wrap around curved surfaces, with higher interaction induced by surface chemistry, giving rise to enhanced binding. It is not known if similar effects would have been observed for the COOH surface at later time points, although due to the comparative binding strength of the two proteins in competition for these surfaces, it may be assumed that the effect would not be observed.

4.5 Conclusions

The results of this work have clearly shown how surface chemistry, curvature and timepoint affect protein adsorption using multiple proteins of HSA and Fg. Characterisation of functionalised silica nanoparticles were carried out successfully using FTIR, XPS and WCA.

Carboxylic surfaces (COOH) have the highest HSA adsorption and methyl surface (CH₃) has the least HSA adsorption at 180 minutes. The results relates to the finding in chapter 3 which shows higher affinity of BSA on methyl surface as curvature size increase. This suggests on methyl surface, upon initial adsorption, no further change occurs. The 215 nm particle have the highest HSA adsorption while 11 nm have the least HSA adsorption. i.e as the curvature size increases, there is more HSA adsorption. Methyl surface (CH₃) has the highest Fg adsorption while carboxylic surface (COOH) have the least adsorption as time

increases. The t-test confirms the strong evidence of the dataset with a p value less than 0.005.

The particle size of 215 nm have the highest adsorption on HSA, Fg and HSA/Fg adsorption as the timepoint increases while 11 nm have the least adsorption. The results correspond to other findings that curvature size affects protein adsorption.⁴³

As the timepoint increases, changes were observed on secondary structure. Random coil decrease on hydrophobic (CH₃) and negative charge (COOH) surface as the timepoint increases while β - sheet and β -turn increases as timepoint increases on 11 nm particles. Random coil increases on COOH surface as the timepoint increases (30-180 mins) on HSA adsorption. PCA analysis of the Amide I was used to assess global difference/similarities in secondary structure and as timepoint increases, there are clustering and variance between particle sizes on each functional group (OH, COOH, NH₂ and CH₃) which clearly demonstrates a change in global secondary structure.

The Vroman effect for HSA and Fg adsorption on different functionalised silica surfaces at different timepoints monitored by FTIR and PCA analysis confirms the influence of physicochemical cues on the competitive adsorption of proteins. The result shows how protein adsorption affects secondary protein structure at different timepoints. HSA of 66kDa adsorbed more rapidly on each functionalised silica nanoparticle especially on COOH surface at 11-215 nm at 10-180 mins compared to Fg of larger molecule of 350 kDa. Thus, the results obtained in this chapter can provide an insight for other researchers and industry into drug delivery systems and interfacial behaviour of biomaterial.

4.6 REFERENCES

1. Arai, T., and Norde, W., *Colloids Surf.* (1990) **51**, 17
2. Lindman, S. *et al.* Systematic investigation of the thermodynamics of HSA adsorption to N-iso-propylacrylamide/N-tert-butylacrylamide copolymer nanoparticles. Effects of particle size and hydrophobicity. *Nano Lett.* **7**, 914–20 (2007)
3. Vroman, L.; Adams, A. L. *Surf. Sci.* **1969**, *16*, 438.
4. Horbett, T. A. Mass action effects on competitive adsorption of fibrinogen from hemoglobin solutions and from plasma. *Thromb. Haemost.* **51**, 174–81 (1984).
5. Cedervall, T. *et al.* Understanding the nanoparticle-protein corona using methods to quantify exchange rates and affinities of proteins for nanoparticles. *Proc. Natl. Acad. Sci. U. S. A.* **104**, 2050–5 (2007). Green RJ, Davies J, Davies MC, Roberts CJ, Tendler SJB. Surface Plasmon resonance for real time in situ analysis of protein adsorption to polymer surfaces. *Biomaterials* 1997; *18*:405–13.
6. Roy RK, Choi HW, Yi JW, Moon MW, Lee KR, Han DK, Shin JH, *et al.* Hemocompatibility of surface-modified, silicon-incorporated, diamond-like carbon films. *Acta Biomater.* 2009; *5*:249–56.
7. Lü XY, Huang Y, Tang ZM, Hong QY, Lu ZH, Zhong YP, *et al.* Use of surface plasmon resonance (SPR) sensor for real time in situ study of adsorption of proteins onto surface of polyurethane. *Chin J Biomed Eng* 2003; *22*:165–70.
8. Li DJ, Huang Y, Lü XY, Zhang YY. Application of a modified Coomassie brilliant blue protein assay in study of protein adsorption on carbon thin films. *Surf Coat Technol* 2007; *201*:6843–6.
9. Huang Y, Zheng BZ, Wu AP and Lü XY,. Comparing adsorptive property of natural and synthesized hydroxyapatite to albumin, fibrinogen and IgG. *Key Eng Mater* 2007; *330–332*:869–72.
10. Taborelli M, Eng L, Descouts P, Ranieri JP, Bellamkonda R, Aebischer P. Bovine Serum-Albumin Conformation on Methyl and Amine Functionalized Surfaces Compared by Scanning Force Microscopy. *Journal of Biomedical Materials Research* 1995; *29*:707-714.
11. Cedervall, T. *et al.* Understanding the nanoparticle-protein corona using methods to quantify exchange rates and affinities of proteins for nanoparticles. *Proc. Natl. Acad. Sci. U. S. A.* **104**, 2050–5 (2007).
12. Cedervall, T. *et al.* Detailed identification of plasma proteins adsorbed on copolymer nanoparticles. *Angew. Chem. Int. Ed. Engl.* **46**, 5754–6 (2007).

13. Stöber, W., A. Fink, and E. Bohn. Controlled Growth of Monodisperse Silica Spheres in the Micron Size Range. *Journal of colloid and interface science* 26.1 (1968): 62-9
14. Life technology website, accessed on the 27th June 2014,
<http://www.lifetechnologies.com/order/catalog/product/F13192?ICID=search-f13192>
15. Vickerman JC, Gilmore IS. Surface Analysis Principal Techniques, second edition, Wiley, 2009
16. Stöber, W., A. Fink, and E. Bohn. Controlled Growth of Monodisperse Silica Spheres in the Micron Size Range. *Journal of colloid and interface science* 26.1 (1968): 62-9
17. Caetano, W, P. S. Haddad, R. Itri, *et al.*, Langmuir 23, 1307 (2007)
18. Graf, G. A. *et al.* ABCG5 and ABCG8 are obligate heterodimers for protein trafficking and biliary cholesterol excretion. *J. Biol. Chem.* **278**, 48275–82 (2003).
19. Iler, R. K. The Chemistry of Silica: Solubility, Polymerization, Colloid and Surface Properties and Biochemistry of Silica; Wiley: New York, 1979.
20. Cavaliere-Jaricot, S.; Darbandi, M.; Nann, T. Au-silica nanoparticles by “reverse” synthesis of cores in hollow silica shells. *Chem. Commun.* 2007, 20, 2031–2033.
21. Ketelson, H. A.; Brook, M. A.; Pelton, R. H. Sterically stabilized silica colloids: Radical grafting of poly(methyl methacrylate) and hydrosilylative grafting of silicones to functionalized silica. *Polym. Adv. Technol.* 1995, 6, 335–344.
22. He, X. X.; Wang, K. M.; Tan, W. H.; Li, J.; Yang, X. H.; Huang, S. S.; Li, D.; Xiao, D. Photostable luminescent nanoparticles as biological label for cell recognition of system lupus erythematosus patients. *J. Nanosci. Nanotechnol.* 2002, 2, 317–320.
23. Liu, S. H.; Han, M. Y. Synthesis, Functionalization, and Bioconjugation of Monodisperse, Silica-Coated Gold Nanoparticles: Robust Bioprobes. *Adv. Funct. Mater.* 2005, 15, 961–967
24. Brash JL, C.P. Sharma, M. Szycher (Eds.), Blood Compatible Materials and Devices, Technomic Publishing Company, Lancaster (1991), pp. 3–24
25. Nonckreman, C. J., Fleith, S., Rouxhet, P. G. & Dupont-Gillain, C. C. Competitive adsorption of fibrinogen and albumin and blood platelet adhesion on surfaces modified with nanoparticles and/or PEO. *Colloids Surf. B. Biointerfaces* **77**, 139–49 (2010).
26. Sigal, G. B., Mrksich, M. & Whitesides, G. M. Effect of Surface Wettability on the Adsorption of Proteins and Detergents. *J. Am. Chem. Soc.* **120**, 3464–3473 (1998)
27. Lassen and M. Malmsten, *Journal of Colloid and Interface Science*, 1997, 186, 9–16.
28. M. D. Bale, D. F. Mosher, L. Wolfarht and R. C. Sutton, *Journal of Colloid and Interface Science*, 1988, 125, 516–525.

29. Tegoulia, V. A. & Cooper, S. L. Leukocyte adhesion on model surfaces under flow: effects of surface chemistry, protein adsorption, and shear rate. *J. Biomed. Mater. Res.* **50**, 291–301 (2000).
30. Michel, R., Pasche, S., Textor, M. & Castner, D. G. Influence of PEG architecture on protein adsorption and conformation. *Langmuir* **21**, 12327–32 (2005).
31. Muramoto, S. *et al.* ToF-SIMS Analysis of Adsorbed Proteins: Principal Component Analysis of the Primary Ion Species Effect on the Protein Fragmentation Patterns. *J. Phys. Chem. C. Nanomater. Interfaces* **115**, 24247–24255 (2011)
32. Holmberg, M. & Hou, X. Competitive protein adsorption--multilayer adsorption and surface induced protein aggregation. *Langmuir* **25**, 2081–9 (2009).
33. Wertz, C. F. & Santore, M. M. Adsorption and Relaxation Kinetics of Albumin and Fibrinogen on Hydrophobic Surfaces: Single-Species and Competitive Behavior. *Langmuir* **15**, 8884–8894 (1999).
34. Deng Z. J., Liang M., Monteiro M., Toth I. & Minchin R. F. Nanoparticle-induced unfolding of fibrinogen promotes Mac-1 receptor activation and inflammation. *Nat. Nanotechnol.* **6**, 39–44 (2011).
35. Fertsch-Gapp, S., Semmler-Behnke, M., Wenk, A. & Kreyling, W. G. Binding of polystyrene and carbon black nanoparticles to blood serum proteins. *Inhal. Toxicol.* **23**, 468–75 (2011).
36. Roach, P., Farrar, D. & Perry, C. C. Surface tailoring for controlled protein adsorption: effect of topography at the nanometer scale and chemistry. *J. Am. Chem. Soc.* **128**, 3939–45 (2006)
37. Walkey, C. D., Olsen, J. B., Guo, H., Emili, A. & Chan, W. C. W. Nanoparticle size and surface chemistry determine serum protein adsorption and macrophage uptake. *J. Am. Chem. Soc.* **134**, 2139–47 (2012).
38. Dutta D, Sundaram S, Teeguarden J, Riley B, Fifield L, Jacobs J, Addleman S, Kaysen G, Moudgil B, Weber T: Adsorbed proteins influence the biological activity and molecular targeting of nano-materials. *Toxicol Sci* 2007, **100**:303-315
39. Gun'ko, V. M., Mikhalovska, L. I., Tomlins, P. E. & Mikhalovsky, S. V. Competitive adsorption of macromolecules and real-time dynamics of Vroman-like effects. *Phys. Chem. Chem. Phys.* **13**, 4476–85 (2011).
40. Jung, SY, S. M. Lim, F. Albertorio, G. Kim, M. C. Gurau, R. D. Yang, M. A. Holden and P. S. Cremer, *J. Am. Chem. Soc.*, 2003, **125**, 12782–12786; J.-H. Kim and J.-Y. Yoon, in

Encyclopedia of Surface and Colloid Science, ed. A. T. Hubbard, Marcel Dekker, New York, 2002, pp. 4373–4381.

41. Vroman L, Colloids Surf., B, 2008, 62, 1–4; W. J. Ma, A. J. Ruys, R. S. Mason, P. J. Martin, A. Bendavid, Z. Liu, M. Ionescu and H. Zreiqat, Biomaterials, 2007, 28, 1620–1628; N. King, C. T. Hittinger and S. B. Carroll, Science, 2003, 301, 361–363; A. van Blaaderen, Science, 2003, 301, 470–471.

42. Mandrusov E, J. D. Yang, N. Pfeiffer, L. Vroman, E. Puszkin and E. F. Leonard, AIChE J. Fluid Mech. Transport Phenom., 1998, 44, 233–244.

43. Reddy A, Implant debris particle size affects serum protein adsorption which may contribute to particle size-based bioreactivity difference. *J Long Term Eff Med Implants*. 2014;24(1):77-88.

CHAPTER 5

Investigation of Cell Secretome in Response to Surface Cues

5.1 Introduction

Stem cells have become the focus of research due to its vital role in understanding cellular response, and therapeutic targets.¹ Despite the high focus of research in stem cells, relatively few authors have investigated the secretome of stem cells using different proteomic technologies and techniques.

Secretome are defined as protein that cells secrete into the extracellular environment which control and coordinate vital biological processes. These proteins serve several purposes in signal transduction, immune defence and blood coagulation.² Secreted molecules are believed to be key mediators in cell-cell communication, which also influence the surrounding environment of the cells. The main reason to investigate stem cell secreted proteins is because the cell culture will closely resemble and mimic the *in vivo* conditions which are more suitable to study and understand how secreted factors affects cell proliferation and differentiation.³ The study on cell secretome will lead to discovery of novel therapeutic and effective biomarkers.

The recent studies of secretome of various stem cells have considered the potential for treating diseases such as renal failure,^{4,5} stroke,⁶ and lung injury.⁷ However, less information is known about various stem cell secretome and their key factors.

Secretome proteins are difficult to study because they are less often isolated and identified due to their low cellular abundance. The analysis of secreted protein is challenging due to different techniques/method being used, which is another major reason there is less research carried out. Examples of challenges faced in secretome analysis are the presence of protein concentrations in cell culture media, cell density incubation time, serum protein in cell culture media and the bioinformatics tools to analyse the dataset. Proteomic approaches are used in secretome analysis.

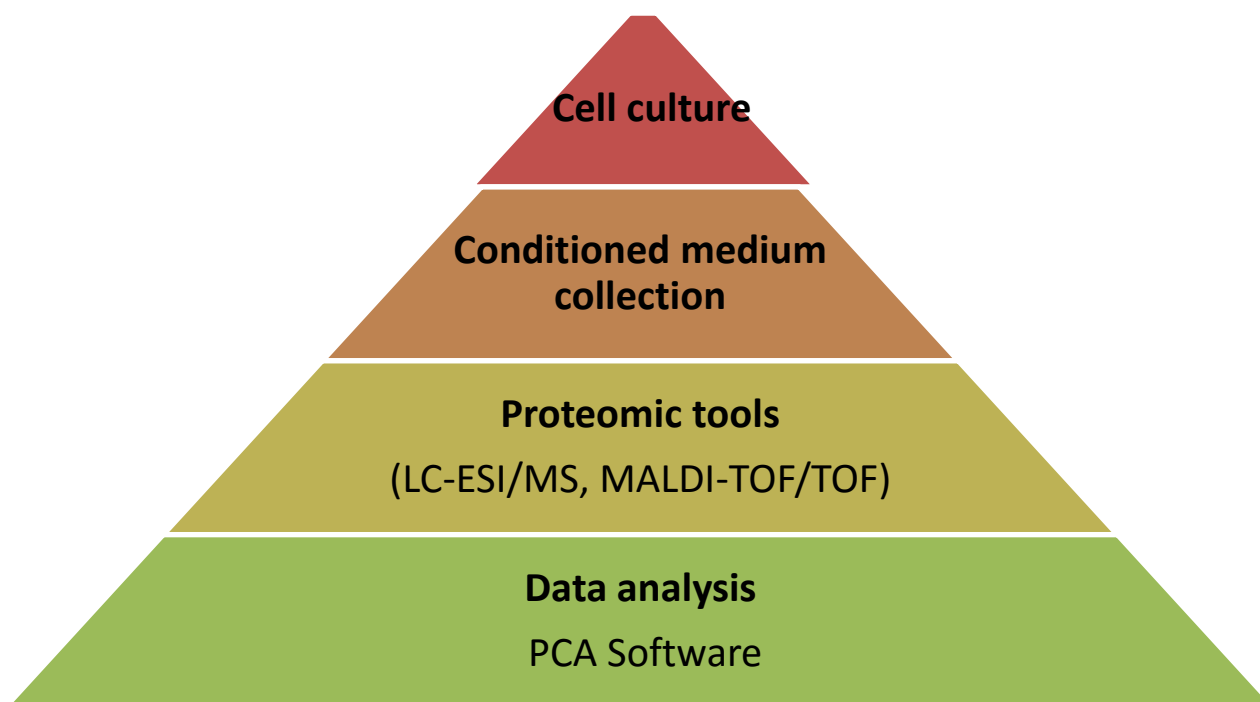


Figure 5.1 Challenges of secretome analysis

The isolation of cells and cell culture has a strong effect on the cell conditioned medium and detection of the secreted proteins. Cells were cultured in serum containing media and were removed so as not to contaminate the end result and prevent the detection of cell-produced proteins secreted at low concentration. Since cells strongly requires serum, it may be difficult for the cells to adapt to low or minimal serum concentration in the culture media.⁸⁻¹⁰ The cells were later washed in serum free medium at different timepoints depending on the cells type, cell density, concentration of media and timepoints. Mbeunkui *et al*,¹¹ used the procedure from medium collection, to serum collection, washing of cells in serum free medium (four times), incubation period and time intervals of 18-42 hours. Similar approaches were followed by some researchers to establish a protocol for medium collection such as Chevallet *et al*¹² and Lawlor *et al*,³² but different cells, different time points and mass spectrometry were used for secretome analysis. Mass spectrometry approaches have been widely used in proteomic analysis which is now used in secretome analysis for

separation and detection of large scale proteins present in a complex biological mixture. LC-ESI-MS technique for low molecular weight proteins and peptides have been shown to be the novel approach in secretome analysis¹⁴ while some make use of 1D and 2D electrophoresis. Each of this method has its advantages and disadvantages.¹⁵ Currently, proteomic analysis tool is used for identifying secreted proteins which rely predominantly on MS analysis of cell culture supernatant.

In this study, fibroblast cells were used with different media namely, Fetal calf serum (FCS), bovine serum albumin (BSA), Dulbecco modified eagle medium (DMEM), Fibrinogen (Fg) and phosphate buffer saline (PBS) of different concentrations to establish a methodology for secretome experiments. The effect of surface physicochemical cues was studied at different concentrations of 200 μ L, 400 μ L and 600 μ L and timepoints (30 minutes and 24 hours) were used. Two proteomics separation techniques were used to investigate fibroblast secreted protein on different surface chemistries at 30 mins and 24 hours namely, LC-ESI/MS and MALDI-Tof/Tof to detect low abundant proteins that have not been secreted or reported.

5.2 Materials and Methods

5.2.1 Self-Assembled Monolayer Formation using Silanes

As explained in materials and method in Page 49.

5.2.2 Characterisation of SAMs

5.2.2.1 Water Contact Angle Measurements

Static water contact angle measurement is the most preferable method used to measure a material's degree of wettability because it is quick, economical and a relatively simple technique.²⁰ Wettability is a property of surfaces that controls many phenomena such as the biological response to materials.²¹ Water contact angle measurements on SAMs were conducted at room temperature using the sessile drop method.^{22,23} The angle between the baseline of the drop and the tangent at the drop boundary is measured. A water droplet (10 μ L) of water was placed on the substrate and measured as shown in section 2.3. The procedure was repeated three times at different sites on the same surface and the contact angle of the sample was expressed as a mean value of three contact angle measurements. Three analysis techniques were used, two were drop analysis method²⁴ was used as seen in Figure 5.2 while the third one is an imageJ software application called angle measurement

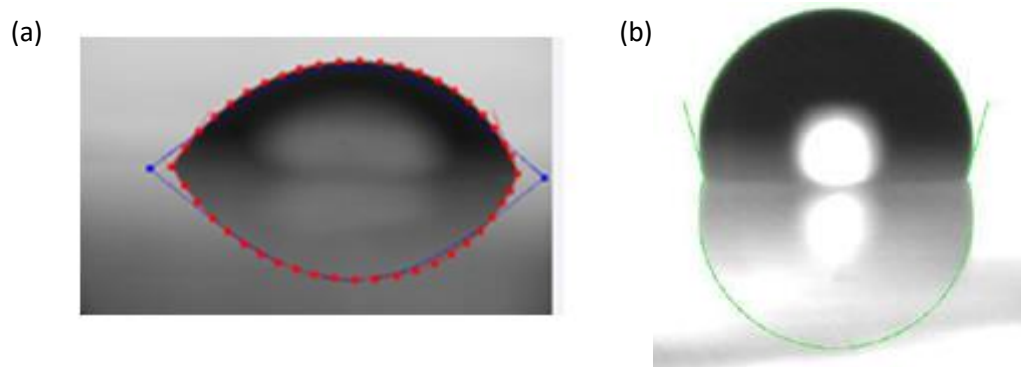


Figure 5.2 (a) Dropsnake method and (b) low-bond axisymmetric drop shape analysis (LBADSA).²⁴

5.2.2.2 Fourier Transform Infrared spectroscopy - Attenuated Total Reflectance (FTIR-ATR)

The Alpha Platinum ATR (A220/ D-01) Quicksnap spectrometer (Bruker Optic) was used for obtaining all the infrared spectra of SAM samples. This system makes use of a single bounce diamond crystal, with an adjustable sample pressure, 360° rotatable pressure applicator and a spectral range of 7,500-375 cm^{-1} . Infrared adsorption spectra of the SAMs were acquired by using OPUS software. A blank air background measurement was carried out prior to each sample taking an average of 265 scans. The spectral range of data was taken from 4000 – 375 cm^{-1} . An average of 265 scans was also taken for each sample, with 5 spectra being taken to determine reproducibility and surface variance across the sample area.

5.2.3 Cell Culture

All work using cell cultures was performed in a class 2 laminar flow cabinet using aseptic techniques. The cabinet was sterilized by UV light for at least 30 minutes prior to use and all equipment washed by 70% ethanol prior to use.

Materials

3T3 mouse embryonic fibroblasts were used for this study, preserved in freeze media in liquid nitrogen until required. Freezing media is made up of 95% Fetal calf serum (FCS) and 5% dimethyl sulfoxide (DMSO). The cells were removed from liquid nitrogen and maintained in complete medium; Dulbecco's modified eagles medium , DMEM (Biosera), supplemented with 10% Fetal calf serum (FCS), 2% L-glutamine and 1% penicillin/streptomycin were warmed in the 37 °C water bath before starting to passage.

5.2.3.1 Cell Passage

3T3 fibroblasts used in this study were used at second passage. The cells were plated in tissue culture flask; the media was changed every other day and passaged after reaching 90% confluence. The confluent culture in tissue culture flask (T-25/75cm²) was taken out of the incubator and examined for any colour change in the medium and under a phase contrast microscope for cell viability and taken into the laminar flow hood. The medium was aspirated and cells washed once with 4-5 mL of PBS. 1 ml of PBS and 150 μ L of trypsin was added and incubated for less than five minutes to detach cells. The flask was taken from the incubator after five minutes or when the cells have detached from the bottom of the flask. 10 mL of FGM medium was added and carefully pipetted in and out, using a 10 ml pipette, to break up the cell clumps. The cell suspension was transferred to a 30 mL tube and centrifuged at 800 rpm for 5 minutes and the supernatant was discarded. The cell pellets were re-suspended in 10 mL of fresh warm fibroblast growth media. The cell viability and cell count was determined using haemocytometer and trypan blue exclusion assay (Invitrogen, Paisely, UK) with 1 in 10 dilution of cells (5 μ L of cell suspension and 45 μ L of Trypan blue).

5.2.4 Cell Culture and Different Media Composition

Molecules secreted from cells are of extremely low abundance, especially when considering the initial response to materials. For this reason it is necessary to reduce the composition complexity of the media used in order to identify secreted proteins. The constituents of five test medias are detailed below and shown in Table 5.3

1. **Fetal calf serum (FCS)** media was prepared using 10% Fetal bovine serum (FBS) in Dulbecco's modified eagles medium (DMEM) supplemented with 1% penicillin/streptomycin. Medias with and without 2% L-glutamine were assessed. This was used as positive control for cell viability.

2. **Dulbecco modified eagle medium (DMEM)** was used with and without 2% L-glutamine.
3. **Bovine serum albumin (BSA)** supplemented media was made up with 0.3 mg/mL BSA (Sigma Aldrich) in phosphate buffered saline (PBS). The PBS was made by dissolving pre-formulated tablets in dH₂O, to make a final solution containing 137 mmol sodium chloride (NaCl), 2.7 mmol potassium chloride (KCl), 4.3 mmol sodium pyrophosphate (Na₂HPO₄) and 1.47 mmol potassium dihydrogen phosphate (KH₂PO₄) with a pH at 7.4 at 25°C. Medias with and without 2% L-glutamine were assessed.
4. **Fibrinogen (Fg)** supplemented media was made up with 0.02 mg/mL Fg in PBS (Sigma Aldrich) in phosphate buffered saline (PBS). The PBS was made by dissolving pre-formulated tablets in dH₂O, to make a final solution 137 mmol sodium chloride (NaCl), 2.7 mmol potassium chloride (KCl), 4.3 mmol sodium phosphate (Na₂HPO₄) and 1.47 mmol monopotassium phosphate (KH₂PO₄) with a pH at 7.4 at 25°C. Medias with and without 2% L-glutamine were assessed.
5. **Phosphate buffered saline (PBS)** was prepared as above, being supplemented with/without 2% L glutamine, serving as a negative control for cell viability.

Table 5.1 Different Medias Composition		Reduced media complexity ↓
Medias	Abbreviation	
Fetal Calf Serum 10% in DMEM	FCS	
Dulbecco Modified Eagle Medium	DMEM	
Bovine Serum Albumin 0.3 mgmL ⁻¹ in PBS	BSA/PBS	
Fibrinogen 0.02 mgmL ⁻¹ in PBS	Fg/PBS	
Phosphate Buffered Saline	PBS	

5.2.4.1 Cell culture in Serum Free-medium

Cells were re-suspended in each of the test solutions at a density of 3×10^4 3T3 fibroblasts per mL. Three replicate cell culture experiments were carried out examining cells via phase contrast microscopy after 1, 2, 24 and 48 hours. Image-J software with a cell counter plug-in was used to manually count the cell number and assess cell spreading areas.

5.2.4.2 Cell Culture in Serum Free-Medium with SAMs Chemistries

Cells were passaged and re-suspended in BSA media without glutamine. 3×10^4 cells were seeded in each 24 well containing three replicate of each of the SAMs, and incubated in humidified air with 5% CO₂. Three different media volumes were also assessed in order to find an optimum condition where secreted proteins were at sufficient concentration for analysis; media volumes of 200, 400 and 600 μ L were used. All media containing cell secretions were collected from sample wells after 30 minutes and 24 hours. The schematic of experiment layout for cell protein secretion is shown in Figure 5.3

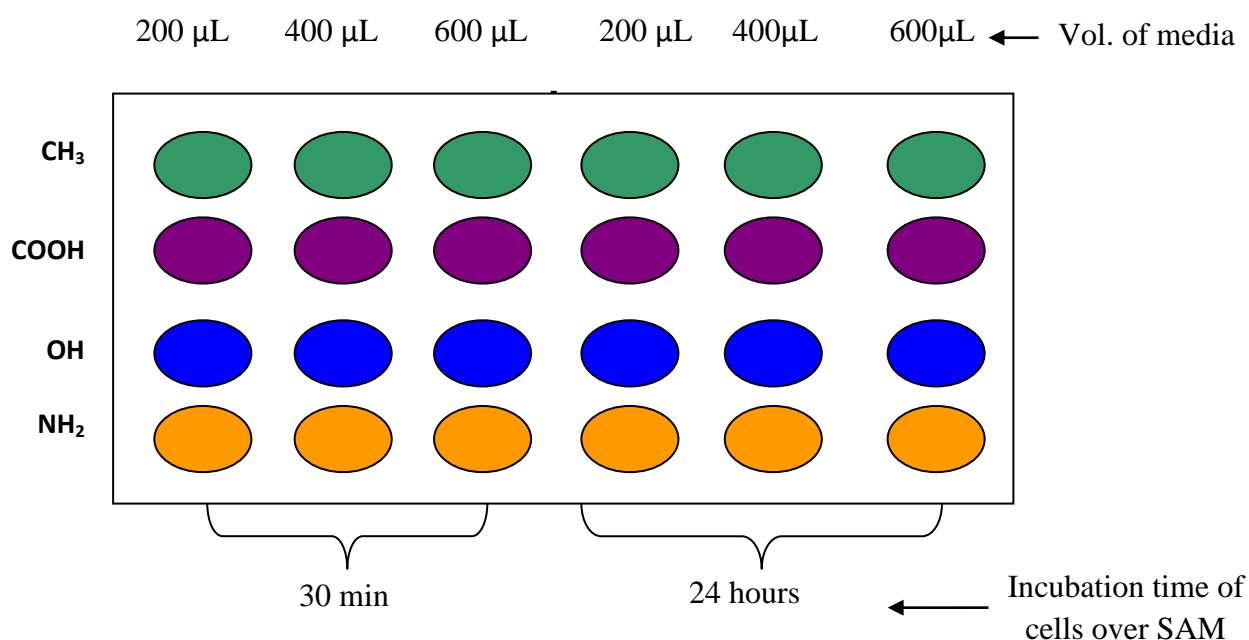


Figure 5.4 Schematic of experiment layout for cell protein secretion

5.2.5 Acetonitrile Precipitation

Acetonitrile (ACN) precipitation is a method used to reduce high abundant proteins and is widely used in laboratories for small molecule analysis.²⁵ All samples contained large amounts of BSA in comparison to the cell secreted proteins, so an ACN crash was used to remove this. A volume of 400 μ L acetonitrile was added into each of the sample volumes as shown in Figure 5.4 because the ratio of the same to ACN is ratio 2:1.

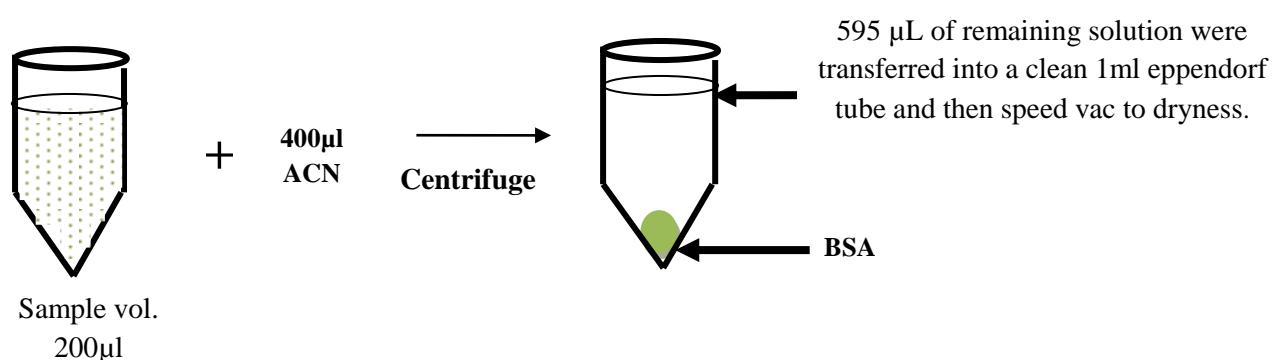


Figure 5.4 Protein precipitation using acetonitrile

After Speed Vac concentrating the solution, a white solid remained at the bottom of the 0.5 mL eppendorf tube. 50 μ L of 0.1% trifluoroacetic acid (TFA) in distilled water were added and Ziptip technique was carried out.

5.2.6 Ziptip

Ziptips are a commercial product used for purifying and concentrating femtomoles to picomoles of proteins or peptide samples to analysis. Each Ziptip is a 10 μ L pipette tip with a 0.6 or 0.2 μ L chromatography media fixed at its end. The sample is aspirated through the tip, with the species of interest binding to the packing. This allows washing, de-salting and prior to the sample being dispensed, giving rise also to a more concentrated sample.²⁶

5.2.6.1 Ziptip Procedure

The following procedure was carried out for sample analysis. Ziptip C₄ (Millipore) was attached to a 20 μ L Gilson pipette and set to dispense 10 μ L aliquots.

- The tip was wetted with 2 cycles of 50% acetonitrile/ water, ensuring that air bubbles were not introduced into the Ziptip. The tip was then equilibrated ready for sample binding with 5 cycles of 0.1% TFA in H₂O.
- Peptides were then bound to the tip (acidifies to 0.1% TFA) with 10 cycles of sample solution. The sample volume should be less than 100 μ L. The salts that bound to the tips were washed off with 2 cycles of 0.1% TFA in H₂O and dispense to waste.
- The last stage is the stripping solution; 4 μ L of 80% acetonitrile/water + 0.1% TFA were dispensed into a 500 μ L eppendorf tube using a Gilson pipette tip. The cycle solvents were done at least 3 times without introducing air into the sample. The sample is sent for ESI-MS analysis (acknowledgement to Dr Sarah Hart).

5.2.7 Mass Spectrometry (MS)

Mass spectrometry is used to determine the mass of a large range of molecules ranging from large to small biomolecules. The two most commonly used techniques in MS are electron spray ionisation (ESI) and matrix-assisted laser desorption ionisation (MALDI).

5.2.7.1 Liquid Chromatography-Electrospray Ionisation (ESI)

The samples were analysed by using liquid chromatography and electrospray ionisation mass spectroscopy (LC-ESI-MS). The instrument is an LTQ Velos (Thermo Fisher Scientific, Hemel Hempstead, Herts), coupled to a Dionex Ultimate3000 split flow system with Famos autosampler (Dionex Corporation, Crawley, Surrey). The gradient was a 35min

linear ramp from 2%-60% B (MeCN: 0.1% formic acid), with solvent A being 2% MeCN: 0.1% FA. the column was a 75 μ m i.d. 15 cm PepMap with 5 μ m beads, 200A pore size (Dionex), and the trap column was the same packing material in a 2mm guard. All solvents were from Fisher, and LC-MS grade formic was from Sigma. Samples (5 μ l loading volume) were loaded from zero dead-volume vials (Waters, Elstree, Herts) in buffer A. Columns were washed in 90% B for 5 min and re-equilibrated in 2% B for 15 min prior to the next injection. The MS program ran from 300 or 400 m/z up to 2000 m/z in survey (MS) mode only. (Acknowledgement to Dr Sarah Hart, Keele University)

5.7.2 Matrix Assisted Laser Desorption Ionisation (MALDI)

The samples were analysed by using matrix assisted laser desorption ionisation mass spectroscopy (MALDI). The instrument is MALDI 4800 ToF/ToF which can perform MS and MS/MS of samples in an automated, unbiased manner (Information-Dependent Acquisition), equipped with a Dionex Ultimate 3000 nano HPLC system and Probot MALDI spotting system for LC MALDI. Its resolving power is 18,000 (FWHM), mass accuracy of 50 ppm and sensitivity in low femtomoles range. MALDI 4800 ToF/ToF provide highest level of protein coverage throughout in proteomic analysis. Figure 5.8 shows the method used for secretome experiment. After Acetonitrile crash and C4 zip tip clean up proteins were mixed in a 1:1 ratio (v/v) with α -cyano-4-hydroxycinnamic acid (CHCA, 10 mg/mL MALDI target plate, and analysed by a MALDI time-of-flight (TOF/TOF) instrument (MALDI 4800, ABSciex, Warrington, Cheshire). MS data were acquired in a positive reflector mode in the mass range of 700-3,600 m/z, 800-1,000 laser shots were accumulated during survey scan acquisition. Close external calibration was performed using Calmix 5, a mixture of 5 protein standards (bradykinin, angiotensin, P14R, ACTH fragment 18-39, glufibrinopeptide). All spectra were externally calibrated using calibration spots. All chemicals were obtained from

Sigma-Aldrich (Poole, Dorset) in 0.1% TFA, 80% acetonitrile) on a stainless steel.

(Acknowledgement to Dr Sarah Hart & Dr Elzbieta Piatkowska)

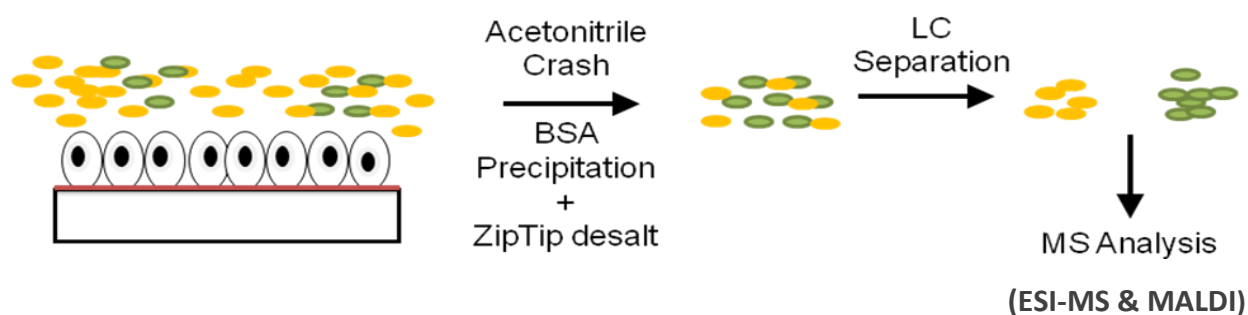


Figure 5.5 Schematic of method used in secretome experiment using MS

5.2.8 SUMMARY

A brief summary illustrating the experimental workflow carried out is shown in Figure 5.6

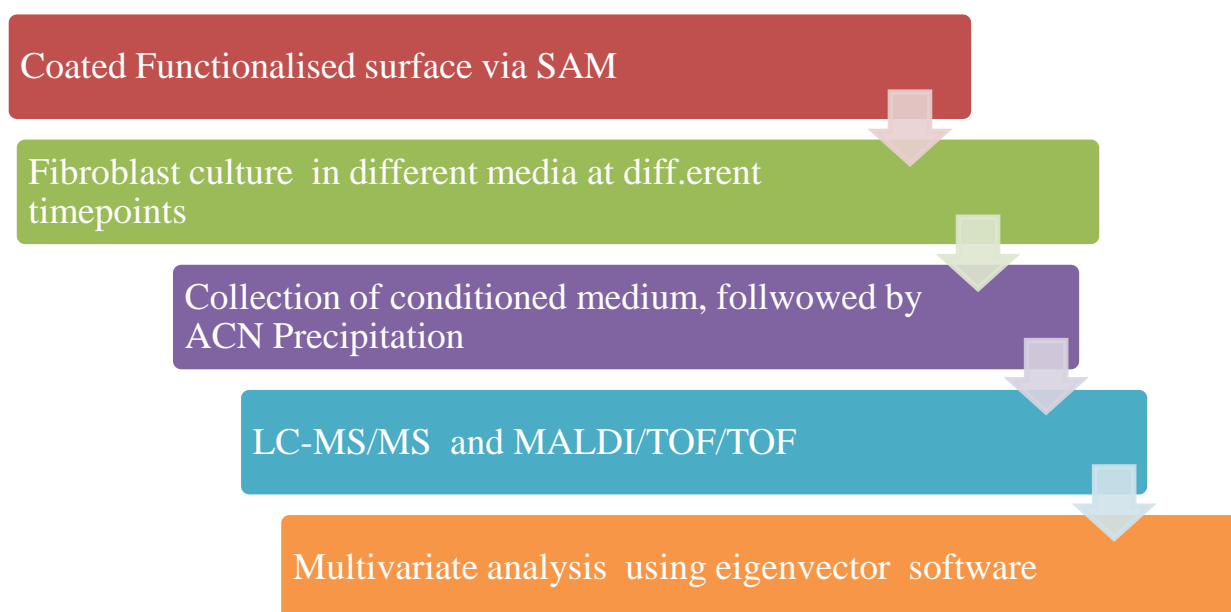


Figure 5.6 Schematic illustration of the procedure used for fibroblast secreted proteins.

5.3 Results

5.3.1 Characterisation of Self assembled monolayers (SAMs)

SAMs were analyzed using water contact angle (WCA) and attenuated total reflectance, Fourier transform infrared spectroscopy (ATR-FTIR)

5.3.1.1 Water Contact Angle

Water contact angle measurements were taken to assess the difference in wettability of the self assembled monolayers of varying functionality. Drop shapes were found to differ as expected as seen in Figure 5.7 with non-polar CH_3 surfaces presenting a higher WCA compared to more polar surfaces, e.g COOH , NH_2

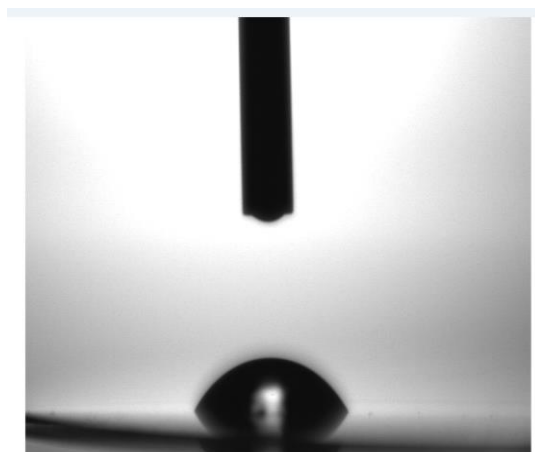


Figure 5.7 Images of water contact angle of surface chemistries

Water contact angle alters with respect to the interaction of water and surface functionality. Table 5.4 shows the difference between three measurements using drop analysis technique.

Chemistries	ImageJ angle measurement	Drop analysis	
	Angle tool	Drop snake	LB-ADSA
CH ₃	63.8 ± 3.0	78.0 ± 0.7	71.8 ± 0.9
OH	52.5 ± 2.2	50.3 ± 2.7	51.4 ± 3.4
NH ₂	43.3 ± 1.2	43.0 ± 1.4	47.1 ± 1.6
COOH	25.9 ± 3.9	25.1 ± 2.6	29.6 ± 2.8

Table 5.4 Difference between water contact angle measurement, standard deviation is used as the error bar, n=6 .The results in Table 5.4 demonstrate difference in wettability as expected for each of the SAMs

The results in Table 5.4 clearly demonstrate difference in wettability as expected for each of the SAMs.

5.3.1.2 Fourier Transform Infrared Spectroscopy (ATR)

FTIR-ATR was used to analyse the surface functionality of the SAM substrates prepared. This technique gives information on the presence of chemical groups evidenced in spectra by peaks at specific wavenumbers, which are related to the vibrational energy adsorbed by specific groups. FTIR confirmed the modification of the glass substrates by the SAMs, with peaks relating to amine, hydroxyl, carboxyl terminal groups as well as the hydrocarbon backbones of the SAMs, Figure 5.8. This is explain further in the discussion section

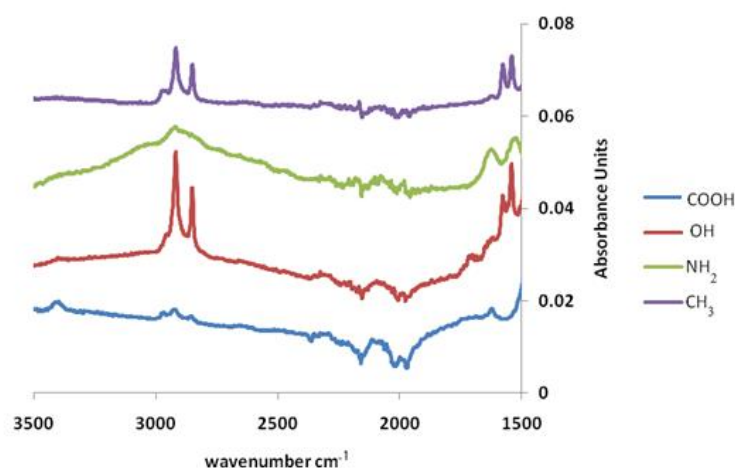


Figure 5.8 FTIR spectra of various SAM surfaces

5.3.2 Cell culture

3T3 fibroblast cells cultured in medias of varying composition were observed by brightfield phase contrast microscopy and images were taken at different timepoints of 1, 2, 24 and 48 hours as shown in Figure 5.9

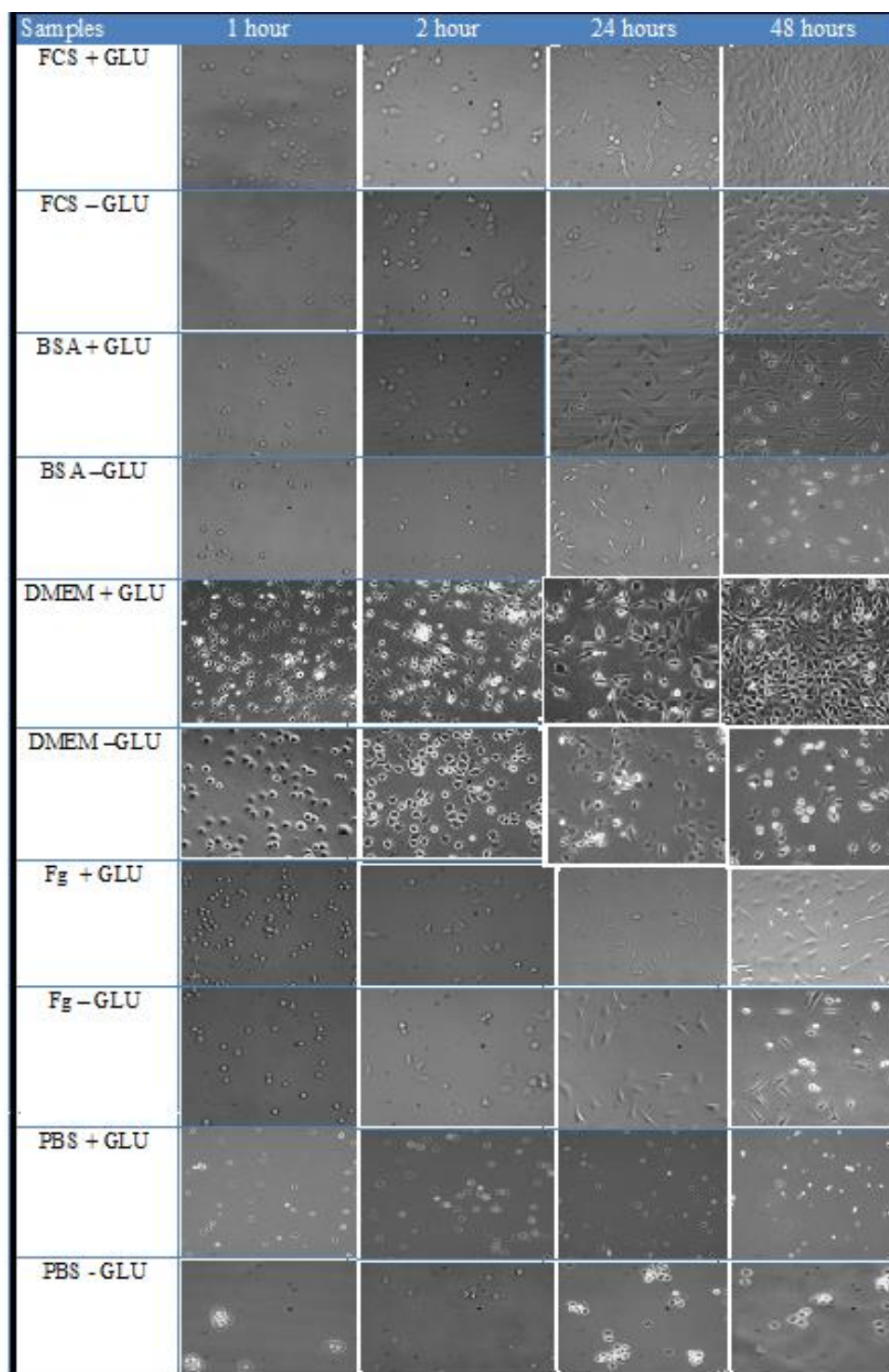


Figure 5.9 Phase contrast optical microscopy of 3T3 fibroblasts cultured in test medias of varying complexity. Images were taken at 20x magnification, at 1, 2, 24 and 48 hours after seeding. Scale Bar of 100 μm

The cells were counted manually using ImageJ software. The scale of the image was set to scale and the setting threshold was done using black and white background. The ROI manager setting was used to semi-automatically calculate cell areas as shown in Figure 5.10. The constituents of the media compositions are: FCS, DMEM, BSA, Fg and PBS supplemented with and without 2% glutamine (GLU). All cells were counted except the cells that are on the left and right edges were not counted. Also, the cells must be globular. The mean of cell numbers in each media composition was calculated and recorded using Microsoft Excel.

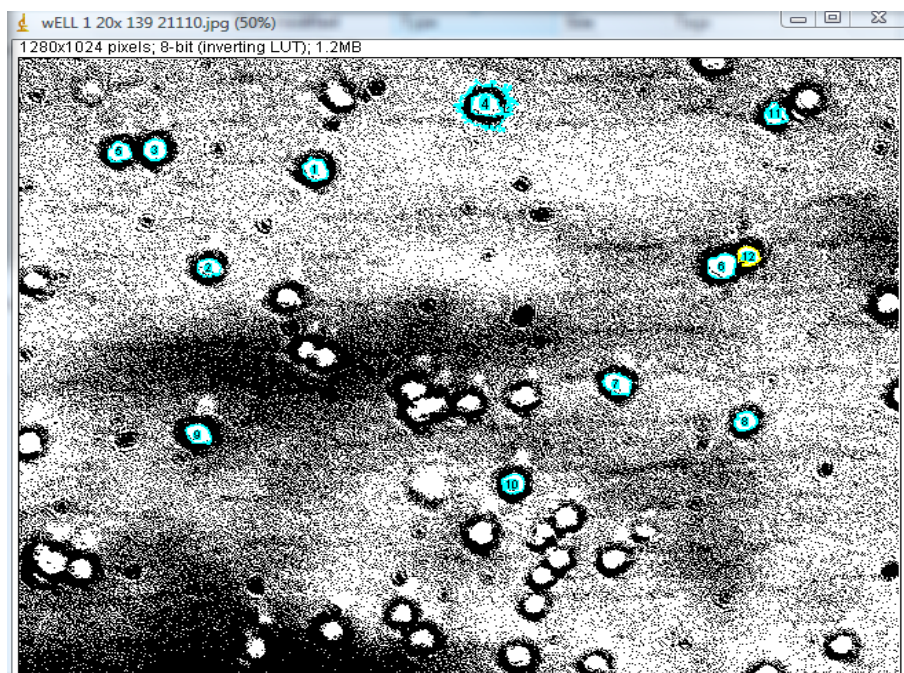


Figure 5.10 Illustration of how the cell numbers were calculated using ImageJ regions of interest (ROI manager). Example shown is threshold optical image of 3T3 fibroblast cultured for 1 hour in FCS + Glutamine media, taken at 20x magnification. Overlay in blue shows cell area measured using ImageJ software. Scale bar of 70 μm

The mean of cell numbers in each media composition was calculated and recorded using Microsoft excel. Cells that were adhere and spreading over the surface were differentiated and those that remained globular in shape were counted using ImageJ. ImageJ was used to count the number of cells that are adhered (globular in shape) and cells that are spreading at 1, 2, 24 and 48 hours. Although cells contract during proliferation this may give insight into the viability of cells in the various conditions and at different time points. Figure 5.11 illustrate how ImageJ was used to count the number of cells that were adhered and spreading using the same procedure as calculating cell number but the setting threshold was not changed to black and white.

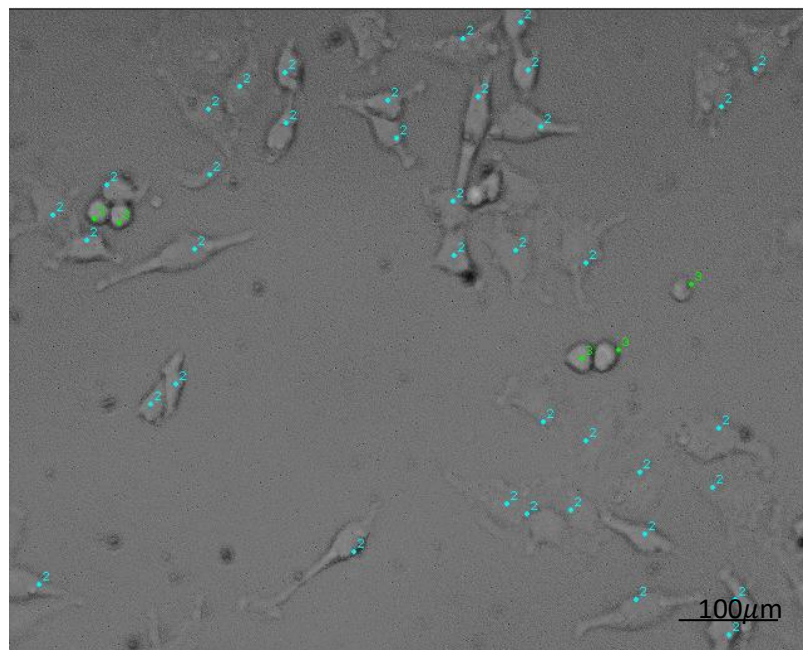


Figure 5.11 Illustration of how cell numbers were calculated, differentiating between those cells spread (shown in blue) and those adhered (shown in green) using ImageJ (ROI manager). Example shown is an optical image of 3T3 Fibroblast cultured for 1 hour in FCS + Glu media, taken at 20x magnification

The comparison of cell number within the different media was used to assess the viability of 3T3 fibroblasts over a range of timescales. Lower complexity of media was

required for subsequent secretome analysis, although cell viability during the culture period of interest was a major factor in selecting the media that will be used for secretome experiment as shown in Figure 5.12

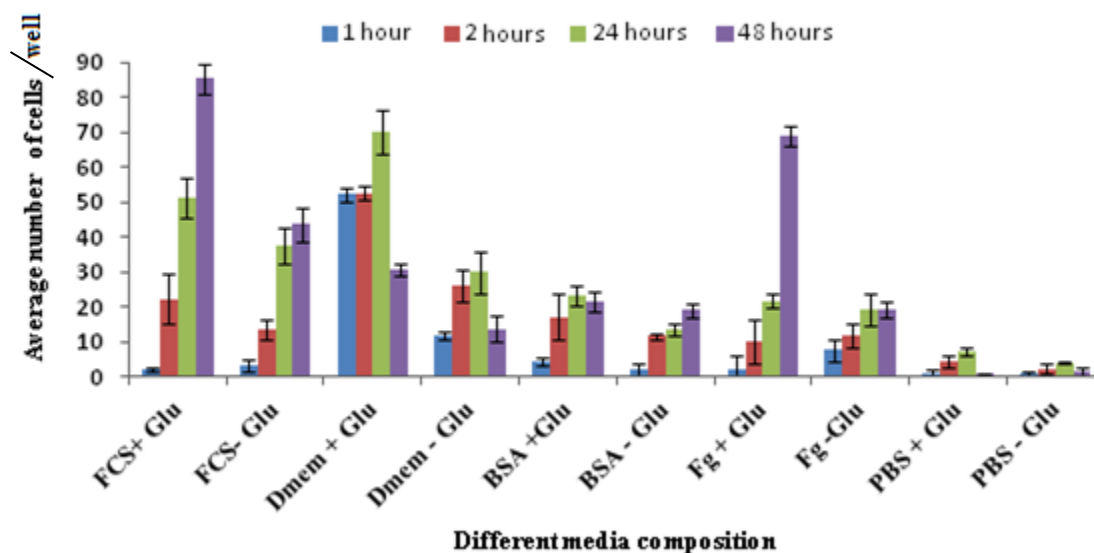


Figure 5.12 Different media composition at different timepoints of 1, 2, 24 and 48 hours

The number of spreading cells within the various test media at various time points of 1, 2, 24 and 48 hours over the time periods to assess how cell spread. Samples were run in replicate with four fields of view counted for each sample. Results clearly highlight differences in cell number with the different medias. For example, FCS + Glu from 1-48 hours indicates a gradual increase in cell spread while PBS -Glu from 1 – 48 hours shows much lower cell spread which decreases with increasing culture time.

The result of the test medias containing glutamine as seen in Figure 5.13 and without glutamine in Figure 5.14 to assess the impact of glutamine on 3T3 fibroblast.

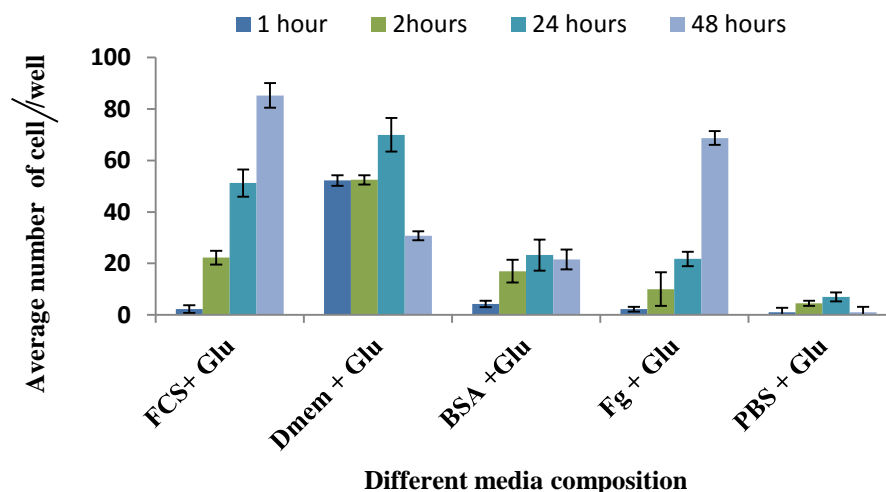


Figure 5.13 Spreading of 3T3 fibroblast with glutamine at different time point Data shown are the mean \pm SD of three replicate samples. Error bars correspond to the standard deviations of the parameters

The media composition with glutamine at 1, 2, 24 and 48 hours as shown in Figure 5.14, The cells in FCS and Fg media shows a rapid increase in cell spreading from 1 hour to 48 hours while less cell growth is observed using BSA media from 1 – 48 hours. Cell spreading in media without glutamine at different timepoints is shown in Figure 5.14

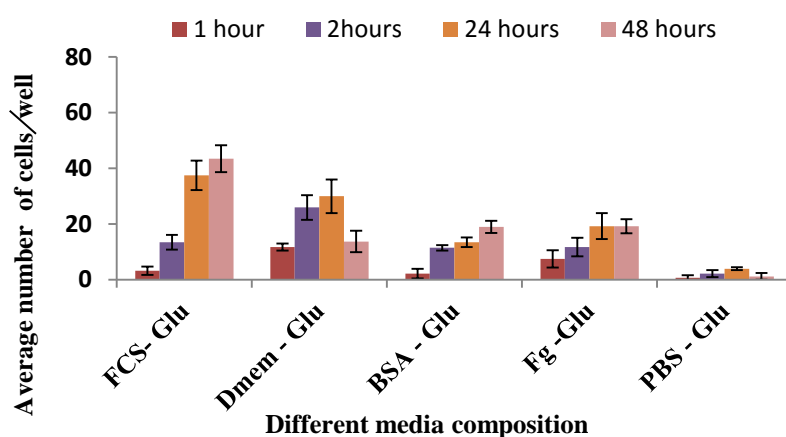


Figure 5.14 Different media composition without glutamine at different timepoints Data shown are the mean \pm SD of three replicate samples. Error bars correspond to the standard deviations of the parameters

Figure 5.14 reveals that cell in FCS - Glu have a high number of cell spread at time period of 1-48 hours compared to BSA -Glu and Fg - Glu. The average number of cell spread in FCS - Glu at 48 hours is 50. BSA and Fg maintain a steady cell spreading at 1 hour to 48 hours. The spreading of cells confirms FCS has the highest number of cell spreading with and without glutamine at 1hour to 48 hours while DMEM, BSA and Fg shows a steady growth at each timepoint.

Non-spreading of cells at each media composition were also counted and represented in Figure 5.15. Non spreading of cells with and without glutamine at different timepoints is shown in Figure 5.15.

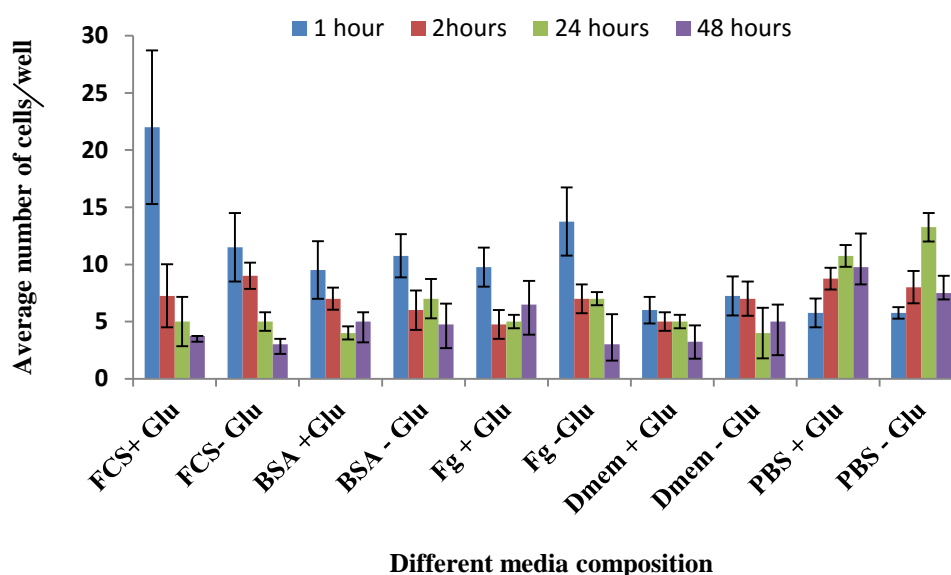


Figure 5.15 Non spreading at different media composition and timepoints Data shown are the mean \pm SD of three replicate samples. Error bars correspond to parameters standard deviations

The result in Figure 5.16 shows non spread of cell at 1- 4 hours. Non spread means the cells still maintain their globular shape.. Cells in FCS +Glu shows a decrease in non spread with increasing culture time while cells in PBS+ Glu shows an increase in non spread with increasing culture time.

The average area of cells with and without glutamine at 1, 2, 24 and 48 hours after seeding were calculated using ImageJ. The result in Figure 5.16 highlights the differences in cell area with the different media. For example, BSA-GLU has a constant cell area of 40 μm^2 at 2, 24 and 48 hours.

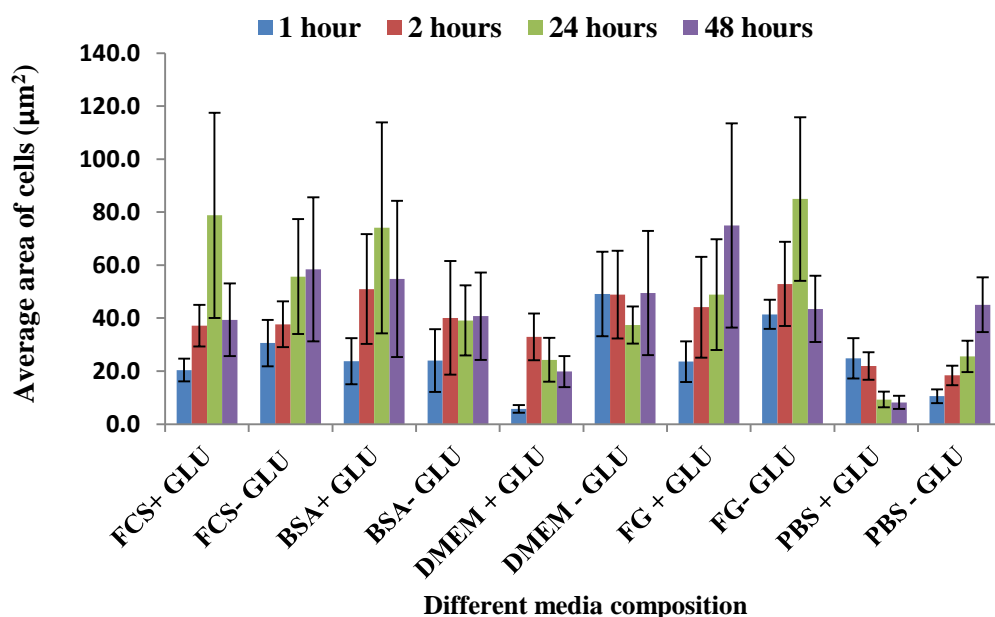


Figure 5.16 Area of cell on different media composition. Data shown are the mean \pm SD of three replicate samples. Error bars correspond to parameters standard deviations

5.3.3 Cell Culture of 3T3 Fibroblast in Bovine Serum Albumin (BSA)

3T3 fibroblasts was seeded onto SAMs chemistries of $-\text{OH}$, $-\text{NH}_2$, $-\text{CH}_3$ and $-\text{COOH}$ at 1, 2 and 24 hours. Phase contrast optical microscopy of 3T3 fibroblasts cultured in BSA-Glu media with SAMs. Images were taken at 20x magnification at 1, 2 and 24 hours after seeding. Further analysis was done to know how the cell spreads and adhered at each surface. ImageJ software was used to count the number of cells adhered and cell spreading in Figure 5.17 and 5.18

Adhered of cells were counted at 1, 2 and 24 hours .Fewer number of cell adhered is seen on amine surface (-NH₂) while high number of adhered cells is found on methyl surface (-CH₃).

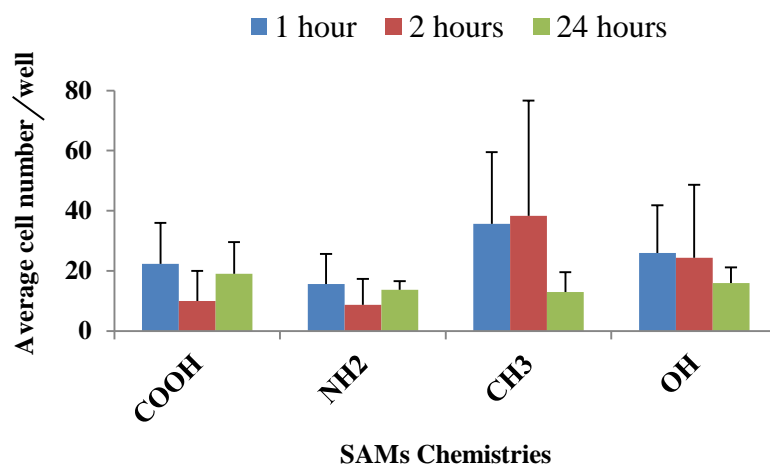


Figure 5.17 The average cell number of 3T3 fibroblast that adhered with SAMs chemistries. Positive error bars were used to show the variability of data. Data shown are the mean \pm SD of three replicate samples. Error bars correspond to parameters standard deviations.

The cell spreading at different timepoints and functionality on Figure 5.18 shows amine surface (-NH₂) have the highest cell spread at 2 and 24 hours while methyl surface (-CH₃) have the lowest number of cells spreads from 1 to 24 hours. The result confirms the results of cells adhered. The higher the number of cells adhered, the lower the spreading of cells.

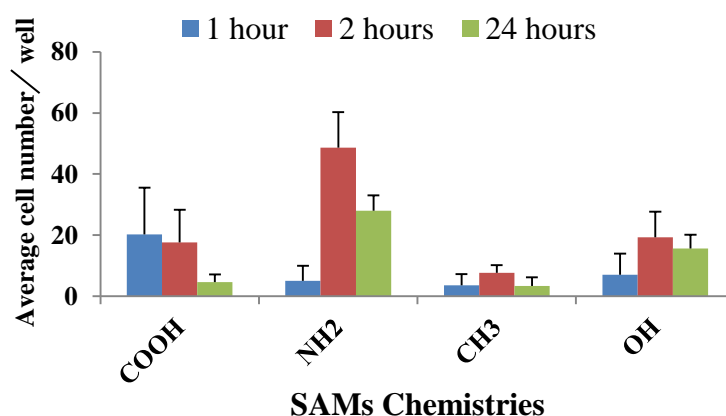


Figure 5.18 Spreading of cell with SAMs Chemistries

5.3.4 Liquid Chromatography-Mass Spectrometry (ESI-MS)

Secretome samples were collected at 30 min and 24 hours, and undergo acetonitrile precipitation (ACN) crash to remove the BSA and then spin dried. Samples were sent to Dr Sarah Hart for LC-ESI and MALDI analysis at Keele University. Liquid chromatography was used to separate the cell culture media after incubation with cells over various chemical functionalized surfaces.

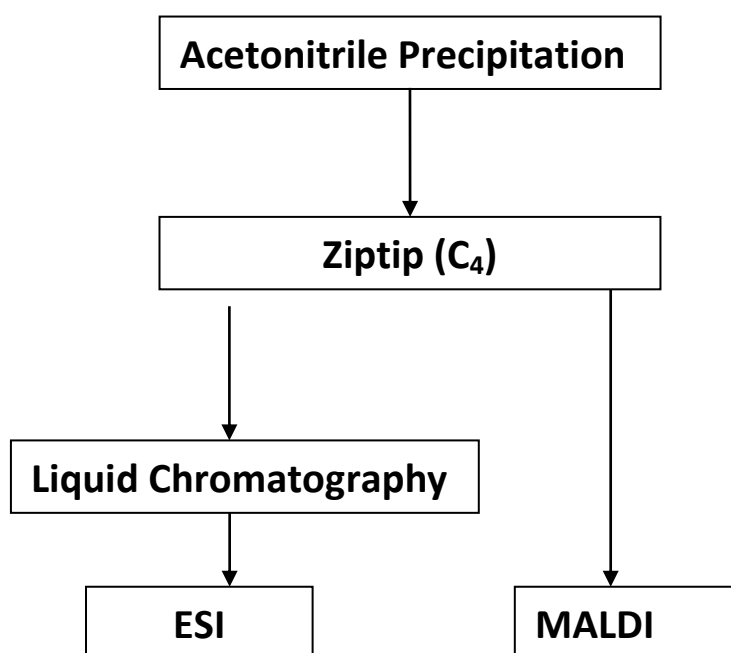


Figure 5.19 Schematic Illustration of mass spectrometry analysis

The LC trace, shown in Figure 5.19, demonstrates the complexity of the media with numerous fractions resulting from media components and cellular secreted molecules. The mass spectra were collected using Xcalibur software and pasted into Microsoft Excel spreadsheet. In order to interrogate the data, four sections of the LC trace were analysed separately.

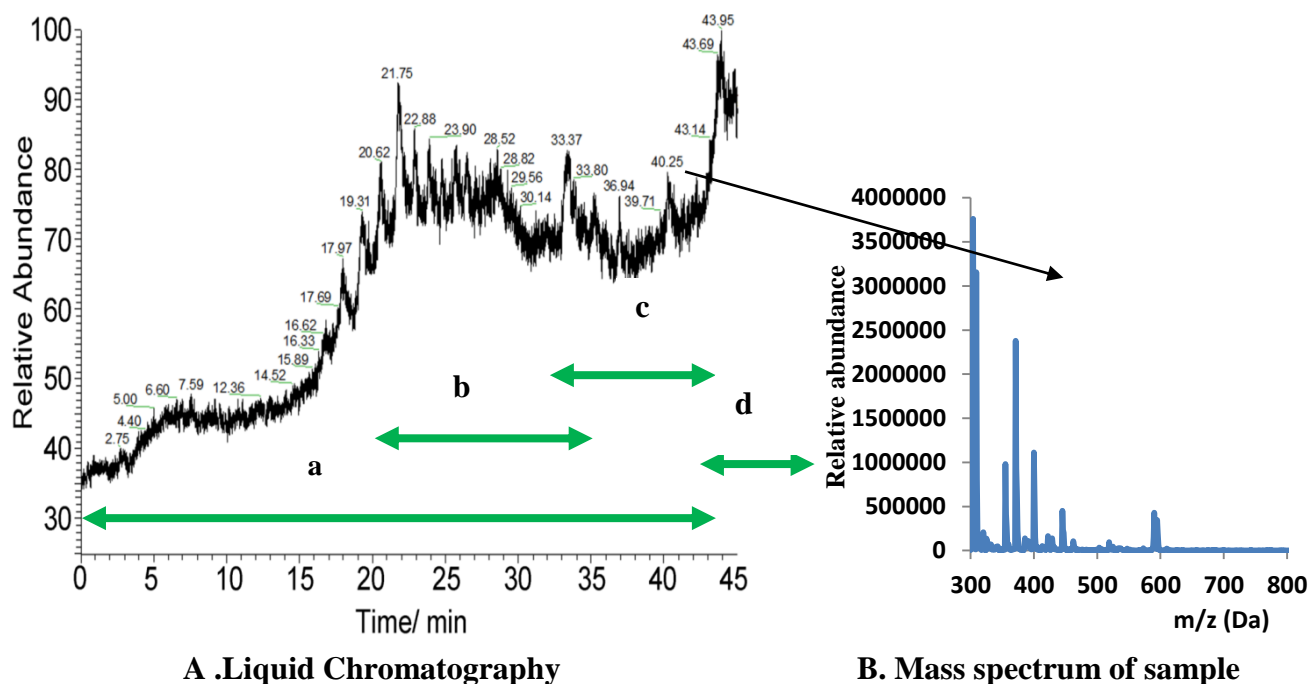


Figure 5.20 Liquid chromatography and mass spectrum of a sample.

The mass spectra were collected in to 4 sets combining spectra under the liquid chromatography trace over four time domains: 0-45 mins (denoted as 'a'), 20-30 mins (b), 30-40 (c) and 40-45 (d). The Liquid chromatography shows the relative abundance (which is the intensity of all ions in the spectra) vs time. While the mass spectrum of the sample reveals the relative abundance vs mass to charge ratio (Da). The MS data were interrogated using principal component analysis (PCA).

5.3.5 Matrix assisted Laser Desorption Ionization -Mass Spectrometry (MALDI-MS)

MALDI-TOF is analytical tool which has being widely used to analyse a range of macromolecules from samples such as cells and tissues. It is highly accurate and sensitive, coupled with a mass range of 1-300kDa²⁹⁻³¹ MALDI-TOF methods and applications have been widely used in research especially in the proteomics field and in detecting biomarkers.³²⁻
³⁴ The secretome samples were collected at 30 min and 24hours, and undergo acetonitrile precipitation (ACN) crash to remove the BSA and spin dried. The samples were labelled as shown in Figure 5.21 and sent to Dr Sarah Hart for MALDI-MS analysis at Keele University. The mass spectra were collected using Xcalibur software and pasted into Microsoft Excel spreadsheet and analysed using multivariate analysis method. .

	30 minutes			24 hours		
	n=1	n=2	n=3	n=1	n=2	n=3
CH ₃	a1 30	a2 30	a3 30	a1 24	a2 24	a3 24
OH	b1 30	b2 30	b3 30	b1 24	b2 24	b3 24
NH ₂	c1 30	c2 30	c3 30	c1 24	c2 24	c3 24
COOH	d1 30	d2 30	d3 30	d1 24	d2 24	d3 24

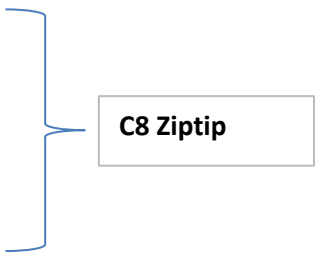


Figure 5.21 Illustrate the MALDI-Tof-Tof experimental setup label.

5.4 RESULTS AND DISCUSSION

Self assembled monolayer's (SAM) have being used as model surfaces to understand the effect of surface chemistry on protein adsorption and cell responses.³⁵⁻³⁷ Carboxylic acid (-COOH), amino (-NH₂) and hydroxyl (-OH) functional groups were found to have lower contact angles, as shown in Figure 5.22 using the ImageJ application with literature supporting these experimental values.³⁸⁻⁴⁰ Results of water contact angle measurements using all the three techniques confirm that methyl surfaces (-CH₃) had a WCA of $78 \pm 0.7^\circ$ being classed as relatively hydrophobic due to the low polarity of this functional group, therefore having low surface energy. A lower contact angle indicates a higher polarity and higher surface energy, allowing a water droplet to spread on such a surface. Previous reports by other researchers using silanization technique have varied results. Howarter *et al*,⁶⁴ showed the WCA of NH₂ is 70° ; Simon *et al*⁶⁵ and Yanqing *et al*⁶⁷ have WCA of NH₂ as 26° and 47° respectively. WCA of NH₂ in this thesis is in agreement with previous work. Functionalised COOH nanoparticles have a contact angle of 26° , which is more hydrophilic compared to NH₂ of 43° according to the result in Figure 5.22. The result is similar to previous work by Yanqing *et al*⁶⁷ and Toworfe *et al*⁶⁵ in which the contact angle of COOH is 15° and 27° respectively, and their results showed COOH is more hydrophilic.

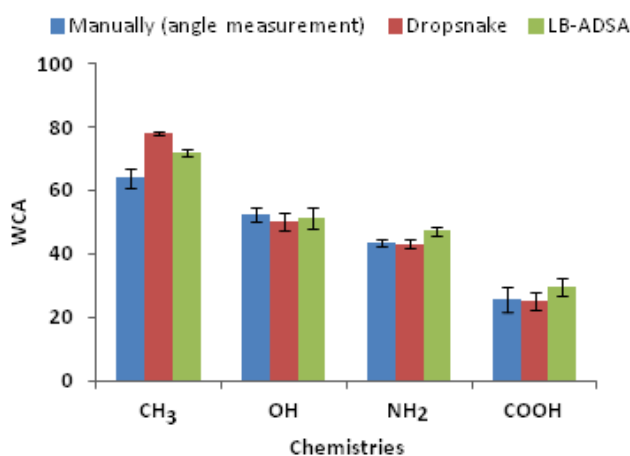


Figure 5.22 Wettability and polarity of surface functional groups

CH₃ has the highest water contact angle and polarity of 48 at pH 7.4, which indicates it is hydrophobic and non-polar. COOH, NH₂ and OH have WCA and pK_a values of 4.0, 9.0, and 16.0 at pH 7.4 respectively²⁴ which indicates they are hydrophilic and polar. There is no great difference between the three techniques, although the dropsnake techniques have a higher water contact angle of CH₃ compared to LB-ADSA and angle measurement technique. The OH SAMs did however show a higher WCA than was expected and previously reported (17-34°)^{41,42} possibly indicating that after silanisation a residual ethoxy groups may have been present. This hypothesis is supported by infrared spectroscopy as shown in Figure 5.23.

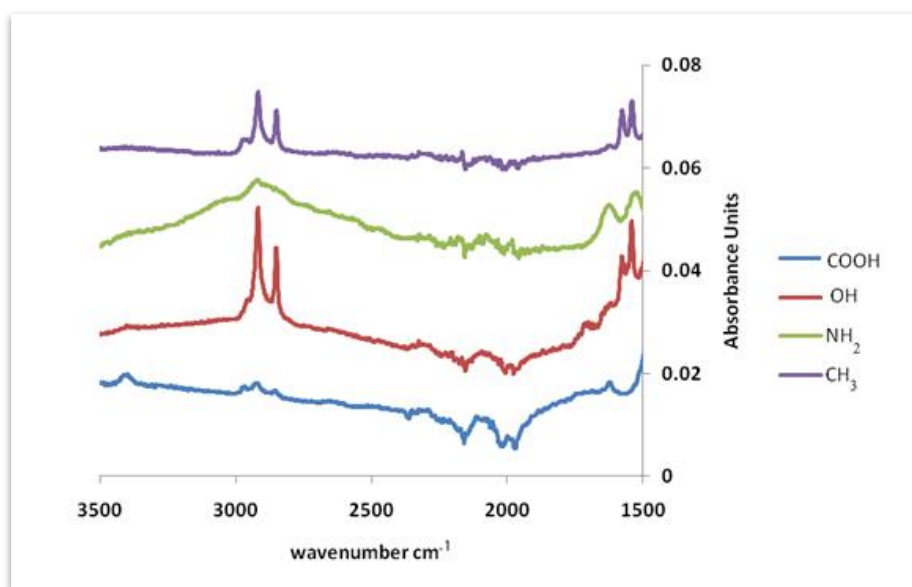


Figure 5.23 Infrared spectra of SAM modified surfaces

Infrared spectroscopy was used to confirm the surface functionality, with specific functional groups used to confirm SAM formation: C-O, N-H, C-H, O-H, C=O and C-N as seen in Figure 5.23. Peaks were observed and shown in Table 5.3

Table 5.3 Surface Functionality using Infrared Spectroscopy⁴³

Peaks cm^{-1}	Functional groups
3500-3300	N-H _{STRETCH} ,
3000-3200	O-H _{STRETCH} ,
2800-2600	C-H _{STRETCH}
2260-2220	C-N _{WAG}
1780-1710	C=O _{STRETCH}
1650- 1580	N-H _{WAG}

All glass surfaces were therefore shown to be modified with appropriate SAMs intended. The remaining ethoxy groups present in the hydroxyl functional surface were removed via acidification in further surface preparation.

The presence of serum in the cell culture medium is normally required *in vitro* for optimal growth of cells. However, addition of serum affects the ability to carry out analysis of secreted proteins during proteomic analysis as serum species mask low abundant proteins of interest. Most researchers interested in secretome analysis incubate their cells in serum free media for several hours to reduce solution complexity, an essential step in order to identify the molecules released from the cells easily. By reducing the complexity of the media in which cells are cultured in will allow any small differences in the secretome resulting from cell-surface interaction to be identified, as well as increasing reproducibility of the experiments.⁴⁴

Figure 5.9 shows phase contrast optical microscopy of 3T3 fibroblasts cultured in test medias of varying complexity. Cell numbers were counted with the results clearly highlighting differences with the different medias, Figure 5.24 show the number of fibroblasts cultured in various media increases from 1-48 hours. As there are no additional cells added during culture, an increase in cell number can only result due to proliferation.

Cells cultured in PBS + GLU, however, showed a much lower number of cells attaching to the tissue culture plastic, which decreased with increasing culture time. FCS and PBS were used as positive and negative controls respectively, being at each end of the media complexity scale.

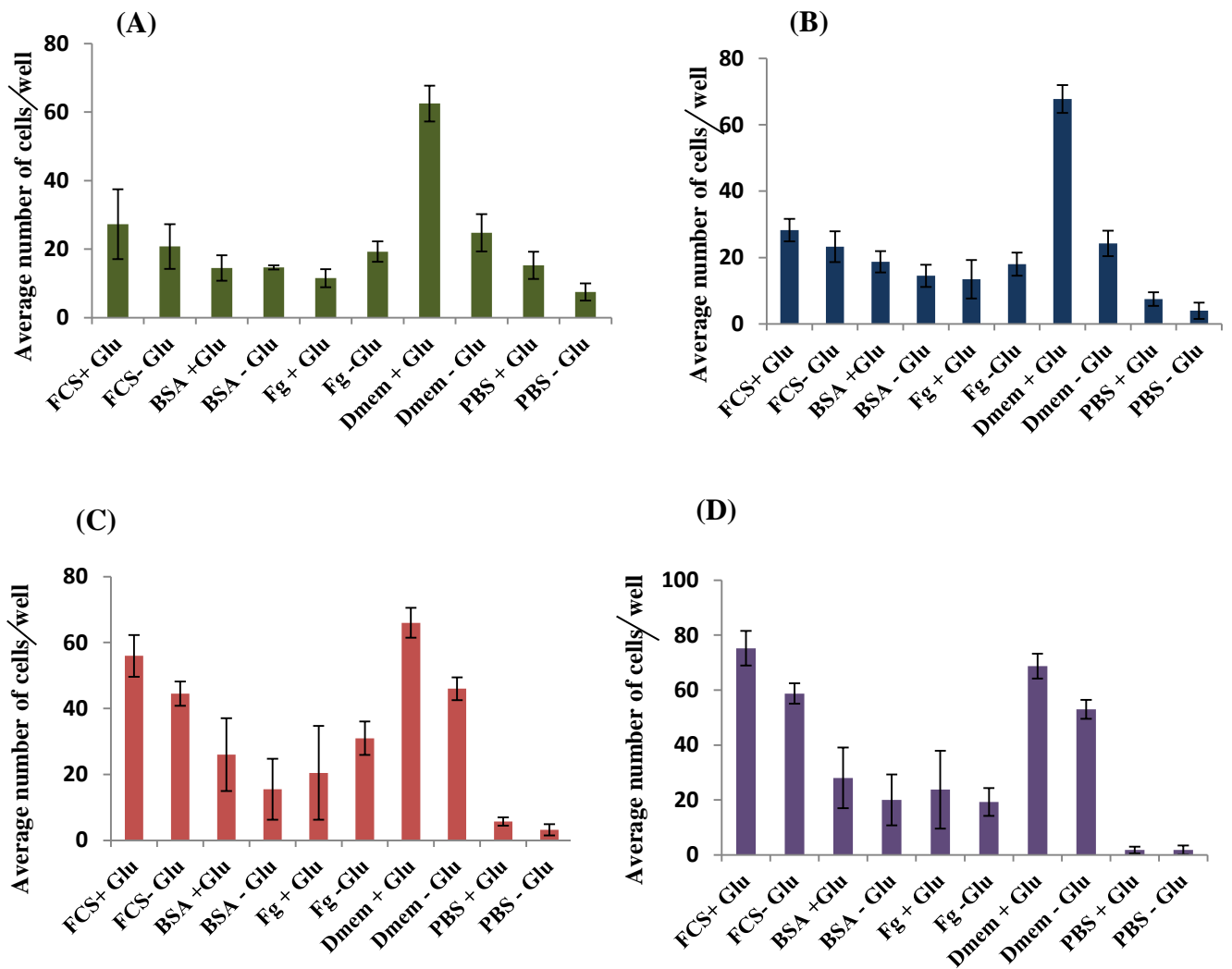


Figure 5.24 Cell numbers cultured in varying test medias over 48 hours. A-D Illustrate the average number of cells in different media complexity at 1 hour, 2 hours, 24 hours and 48 hours. Error is represented using standard deviation, n= 3

Even after only 1 hour a difference in cell numbers attaching to substrates can be seen. DMEM + GLU, for instance has almost double the cell number of other medias

initially, although this changes little over a 2 day period indicating that cell attachment to surfaces is promoted but insufficient nutrients are available for cell proliferation. Glutamine is used as a cell culture media supplement because it acts as a major energy and nitrogen source for mammalian cells.⁴⁵ Data shows that with the exclusion of glutamine cell proliferation over 2 days is reduced a little although over 2 hours, and in some cases 24 hours, little change is observed. This was especially observed with BSA and Fg medias.

The spreading of cells was also investigated, showing again a dependence of cell number on media composition and time of culture. With the exception of cells cultured in DMEM all other cell counts were similar up to 2 hours. Little difference was observed comparing FCS, BSA and Fg test medias indicating that each of these medias gave rise to similar cell responses over short time scales. Differences in the ability of cells to attach and spread are linked to cell well-being.⁴⁶ The areas of spreading cells attaching to the surface during culture also showed no differences between FCS, BSA and Fg containing medias over short time periods.

In an attempt to reduce media complexity such that secretome analysis could be strengthened, the addition of glutamine in culture media was deemed not necessary over short culture period. The initial interaction of cells was little affected by reduced complexity solutions containing proteins (BSA and Fg), with only phosphate buffered saline showing a reduction in cell attachment as expected. BSA/PBS was therefore a good candidate to be used for further cell culture and MS analysis of secreted molecules.

Bovine serum albumin (BSA/PBS) solution was used to culture 3T3 fibroblast over various functional SAMs for 1 hour, 2 hours and 24 hours. The results indicated in Figures 3.12 and 3.13 show that methyl surfaces ($-\text{CH}_3$) have the highest numbers of cells adhered yet the lowest number of cells spreading over the surface after 1, 2 and 24 hours in culture. These

results correspond to those reported by Lee *et al.* showing that NH₂ SAM surfaces have a greater adhesion strength compared to COOH, CH₃ and OH surface using bovine serum albumin as the media.³⁶ High number of cells spread on NH₂ SAM surfaces have been reported in previous studies using different cell types and standard culture conditions.³⁷⁻⁴¹

At pH 7.4, as buffered in culture media, amino groups may become positively charged to present NH₄⁺ groups. The high number of cells attaching and spreading on NH₂ SAMs may therefore be caused by the presence of a high density of positively charged species on the surfaces interacting with cell membranes. The charged surface may also lead to changes in the adsorption characteristics of proteinaceous species through electrostatic interaction. However, hydrophobic interaction usually dominates protein adsorption⁴¹

Higher number of cells attaching to methyl surface indicates more protein at the surface due to electrostatic interaction and also accounts for cell interaction; possibly once cells attach, they can more easily spread on charged surface due to electrostatic interaction with the cell membrane.

LC-ESI-MS

The mass spectrometric results of 24 secretome samples with multiple thousands of different peaks in each make it difficult to interpret the data. One way to simplify the manipulation of the data is by the use of principal component analysis (PCA), a multivariate analysis technique that helps in interpretation of datasets by identifying the major differences and bunching them together in *principal components*. The principal components (PCs) can then be used as a means of correlating patterns in the data, for instance variance associated with a particular sample sub-set. Each of these PCs has a score relating the degree of variance associated with it as seen in Figure 5.25. PC1 having the highest difference between datasets, etc.

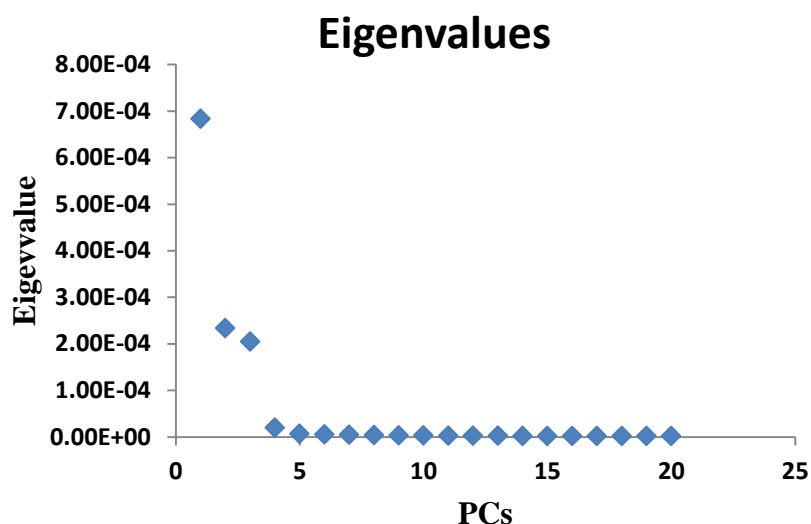


Figure 5.25 Eigen values of each principal component analysed for the LC-ESI data set.

The data from the LC-MS of culture media from fibroblasts cultured over various surface chemical functionalities was examined, and the first four PC's were taken, giving a 99.8% confidence in variance. The score plots for this data are shown below, Figure 5.26

Score Plots of ESI

The score plot shown in Figure 5.27 captures 57.6% of the variance in the data in PC1 19.7% of the variance in PC2. The data is presented such that each coloured data point corresponds to the media taken from cells cultured over the same chemistry. It is clear from the PC score plot that there are specific clusters in the data set, highlighted by circles in the Figure 5.26, showing a dependence of the media composition with respect only to the SAMs used. This demonstrates that cells certainly responding to each of the surface chemistries differently, with the media composition only being altered by cell secreted molecules. Others have shown similar secretome responses in terms of osteoblast differentiation⁴⁷ and human mesenchymal stem cell differentiation.⁴⁸⁻⁵⁰ To date, however, there have been no reports highlighting such surface chemistry effects on the proteins secreted by cells.

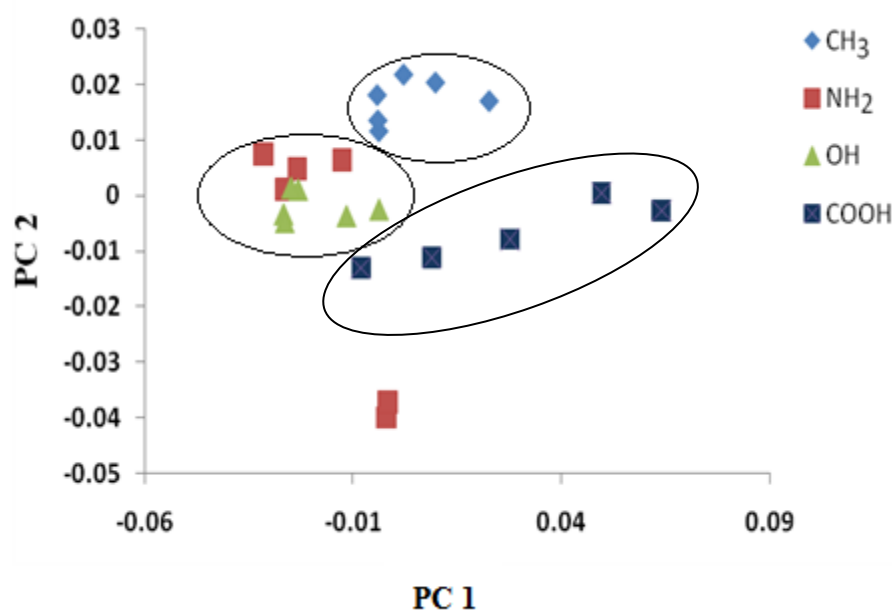


Figure 5.26 Score plot on the first two multivariate axes from PCA of the ESI-MS spectra. Clustering of PC1 vs PC2 mass spec data from cell secretome analysis

All data points cluster with others of the same chemistry, except for two outliers within the NH_2 SAM dataset. It should be noted also that 6 repeats are shown for each surface, with 3 samples taken from culture media at 30 minutes after initial seeding of cells and 3 from media at 24 hours. The two outliers correspond to one from each of these time periods, which will be discussed below.

Surface charge seems to play a major role in determining cell secretion response, with positively charged NH_2 and OH surfaces being different from less positively charged CH_3 and negatively charged COOH surfaces, at pH 7.4. CH_3 has the highest number of cell adhere while amine surfaces have highest number of cell spread. CH_3 was far apart from other chemistries in Figure 5.26 because it has high adhere cell number (i.e cells are still globular protein) and large cell area compared to hydroxyl and amine; while carboxyl has high cell spread in one hour compared to other chemistries.

A further investigation into principal components PC3 (17.25% variance) and PC4 (1.65% variance) was also carried out, although these are not good discriminators and therefore are not included in this discussion.

Loading Plots of ESI

Each of the principal components is a packet of variables which highlight discrimination between samples in the datasets. Figure 5.27 represents the loading from PC1 and PC2. Each of the peaks with negative and positive loadings corresponds to the position of the sample point within the scores plot. For instance a higher score for PC1 will have an overall higher proportion of positive PC1 loading peaks, along with less negative PC1 peaks. Figure 5.27 denotes the mass spectral variances attributed to each of the principal components. Several species having high discriminating scores are highlighted in both components, listed in Table 5.4 and Table 5.5

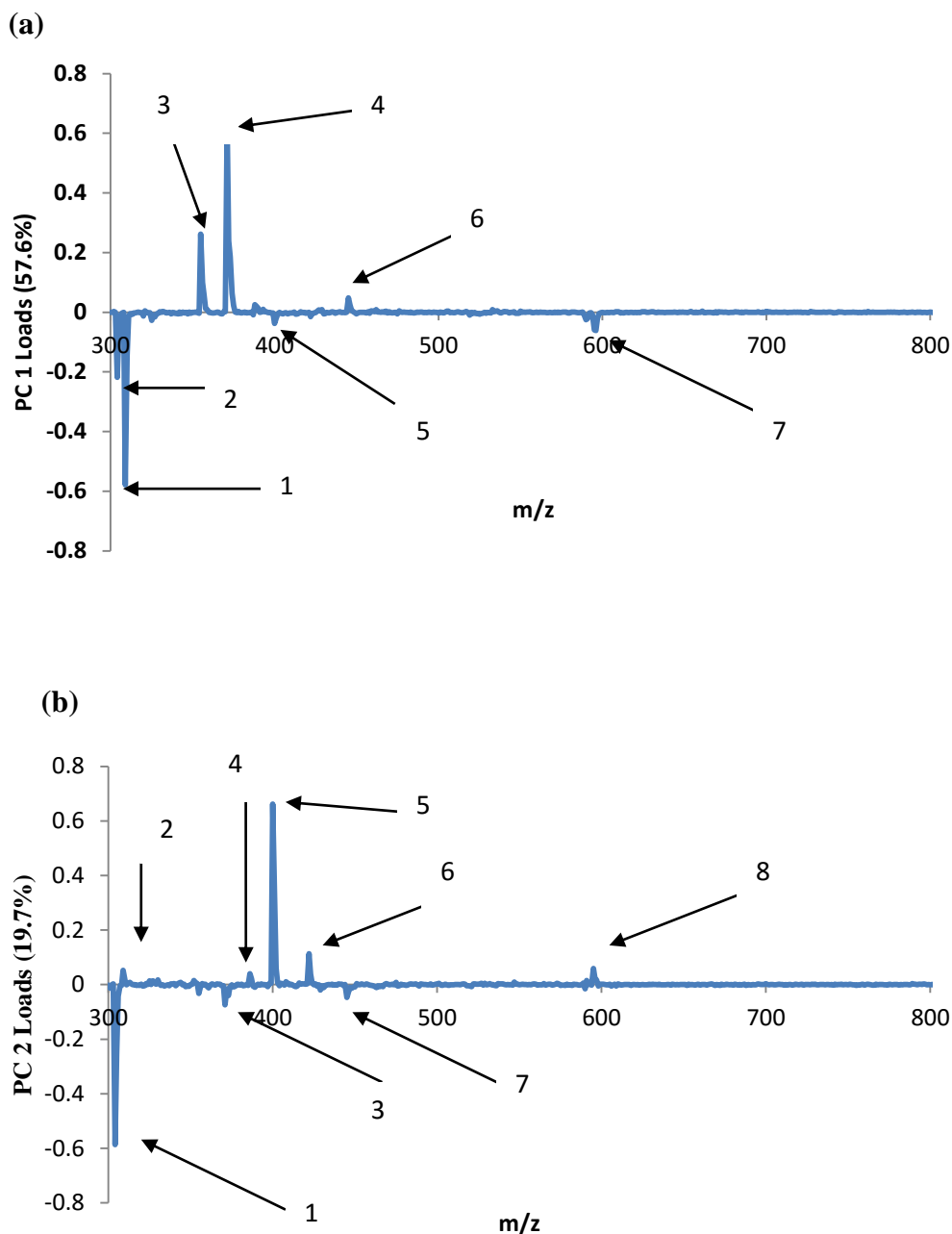


Figure 5.27 PC1 and PC2 loadings associated with (a) PC1 and (b) PC 2 due to secretome variance with respect to surface chemistry

Inspection of PC1 loadings plot (Figure 4.5), shows major peaks at m/z 371, 355, 445 and 393 loads positively while 304, 309, 400 and 596 loads negatively in PC1. PC2 loading plot has the following major peaks at m/z 304, 309, 355, 371, 387, 400, 422, 446 and 595. As an example, media analysed from CH_3 SAMs has a higher PC2 score compared to other

samples, and so will have a greater amount of species with m/z values 309, 387, 400, 422 and 595 Da, with a lesser amount of species with m/z values of 304, 371 and 446 Da.

Table 5.4 Loading value found in PC1 for ESI-MS Data

m/z (Da/e)	1	2	3	4	5	6	7	
PC1 (57.3%)	304	309	355	371	400	445	596	
Loadings	-0.218	-5.778	0.262	0.630	-0.037	0.048	-0.062	

Table 5.5 Loading value found in PC 2 for ESI-MS Data

m/z (Da/e)	1	2	3	4	5	6	7	8
PC2 (19.7%)	304	309	371	387	400	422	446	595
Loadings	-0.586	0.052	-0.074	0.022	0.662	0.113	-0.028	0.059

Table 5.4 and 5.5 shows the loading value in PC1 and PC2 for ESI-MS data. Same peaks are observed in PC1 and PC2 which may be due to the components picked out by PCA which identify sample differences are spread out across the whole LC trace as explained in result section in page 219. Further analysis must be carried out in order to identify the components shown in Table 5.4 and Table 5.5; Bendell *et al* have identified 550 proteins in mouse embryonic fibroblasts conditioned medium (MEF) and 2493 proteins in medium conditioned by embryonic stem cells (ESCs) relating to species indicative of these particular cell types compared to other cells.⁵¹ Prowse *et al* have identified secreted proteins such as insulin-like growth factor 1 (IGF-1), insulin-like growth factor- binding proteins 1,2,3,4,5 and 7 (IGBP-1,IGBP2,IGBP 3, IGBP 4, IGBP 5, IGBP 7) and secreted protein acidic and rich in cysteine (SAPRC).⁵² These identified proteins are known to help in the maintenance of human embryonic stem cells.

The initial attachment of cells with substrates has often been overlooked, due to the time periods thought to be relevant in terms of cell responses to materials. On short time scales, interaction of proteins is often considered to be the dominant role in determining cell-surface interaction. According to Planque *et al*⁵³ cells can only be incubated in serum free media for several hours (typically from 18-48 hours). The time interval will vary for a given cell type and also the type of medium used, or else dead cells or cells undergoing apoptosis will be in the culture medium. For this study, it is clearly shown that within 24 hours 3T3 fibroblasts showed little difference with respect to morphology (spreading/cell area) when cultured in BSA/PBS or FCS containing media. Assessment of the secretome was therefore carried out with respect to the time of culture.

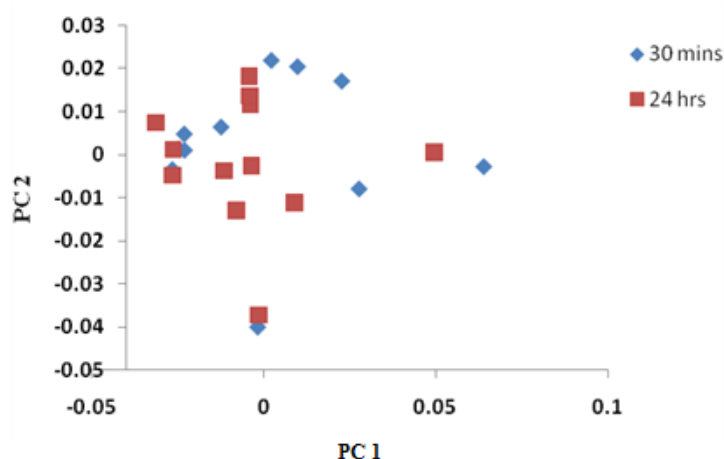


Figure 5.28 Effect of incubation time on cell secretion variance

The score plot in Figure 5.28 shows there is not any clustering in relation to time dependence for most of the surfaces, with red and blue dots overlapping. However, the CH₃ does show some clustering, with the 30 minutes sitting to the right and 24 hours sitting to the left. This means more CH₃ surfaces may give rise to some media changes/secretome responses over time, with those samples collected after 30 minutes in culture presenting more components from PC1; PC2 does not seem to add discrimination between the samples taken

after 30 mins and 24 hours. One reason for this surface having a time dependency could be due to protein adsorption effects. According to Pitt *et al*, protein molecules adsorb rapidly on surfaces with decreasing wettability.⁵⁴ Cells may well be responding to the surface chemistry by secreting proteins in relation to that specific response, but due to hydrophobic-hydrophobic binding such secreted molecules may well adsorb to the surface and not be available for analysis by the methodology used in this investigation. This may well be indicated by the higher PC1 values at 30 minutes compared to 24 hours. Further investigation needs to be carried out to understand this finding.

MALDI TOF/TOF

MALDI TOF/TOF has been used in proteomics research to identify biomarkers.⁵⁵⁻⁵⁷ MALDI datasets consist of many peaks which need to be analysed using eigenvector software since the peaks contain potential biomarkers that needs to be identified.

Secreted protein of fibroblast cells cultured over various surface chemical functionalities using MALDI/Tof were analysed using eigenvector software and Matlab. Eigenvalues are presented in Figure 5.29. The eigenvalue represents the amount of variance that can be captured by one component. The first four PC's were taken, giving a 99.8% confidence in variance. The first component has a higher eigenvalues component.

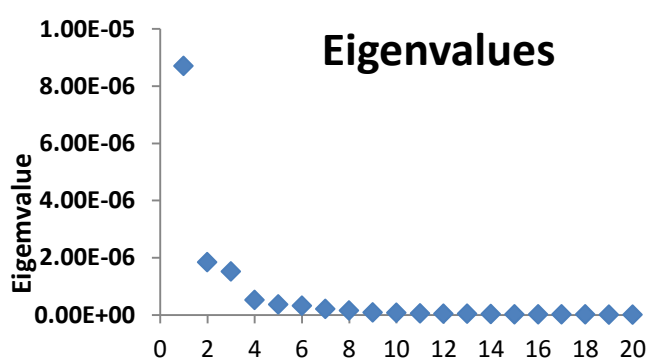


Figure 5.29 Eigen values of each principal component analysed for the MALDI-Tof-Tof data set.

Scores of MALDI-Tof/Tof

The score data presented in Figure 5.30 shows PC 1 (62.16% variance) and PC 2 (13.16% variance) and shows variation of data, whereby specific clustering of functional groups were observed in the dataset. The majority of the OH and CH₃ datasets cluster together while COOH SAM cluster in central region as shown in PC 1 and PC 2. PC3 (10.86% variance) and PC 4 (3.69% variance) shows more variations of chemistry and few outliers. It is odd that PC1 alone did not have a good ability to separate samples. However, using the MADLI the individual sample repeats were also quite widely spread, e.g. NH₂ or OH in Figure 5.30. This may have been due to the sample composition not being optimal, or some of the components not ionising or ‘flying’ well from a combined sample spot. Others have also highlighted better sampling for LC-ESI or MALDI with pre-separation. Difficulties associated with equipment moving sites and time of thesis submission did not allow for a thorough investigation of these issues.

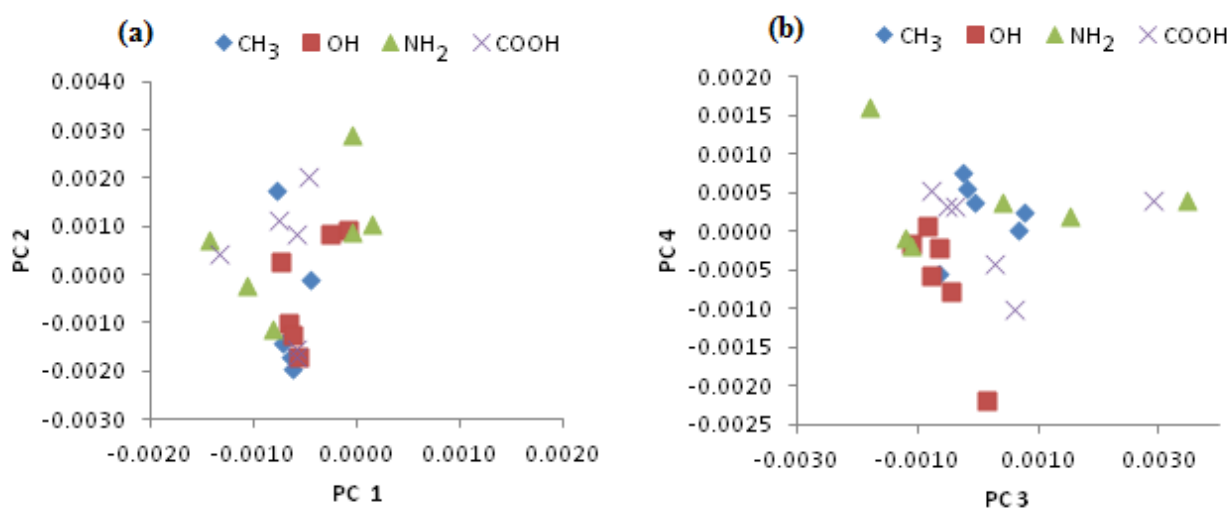


Figure 5.30 Score plots on the first four multivariate axes from PCA of the MALDI-Tof-Tof spectra. Clustering of PC1 vs PC2, PC3 vs PC 4 mass spec data from cell secretome analysis.

Surface charge played a vital role in the spectra result of MALDI-Tof-Tof. Negative charge COOH SAM clusters at the central region on PC 1 vs PC2, while NH₂ and CH₃ cluster together in another region and OH SAM is seen further apart. It is clear from the PC score

plot of PC 1 vs PC 2 and PC 3 vs PC 4 that there are specific clusters in the data set, showing a dependence of the media composition with respect only to the SAMs used. This demonstrates that cells certainly responding to each of the surface chemistries differently, with the media composition only being altered by cell secreted molecules.

All data points cluster with each other in PC 1 and PC 2 while there are few outliers with the NH_2 , OH and COOH SAM dataset. It should be noted also that 6 repeats are shown for each surface, with 3 samples taken from culture media at 30 minutes after initial seeding of cells and 3 from media at 24 hours. The effect of incubation time on cell secretion variance is shown in Figure 5.31. The two outliers correspond to one from each of these time periods in Figure 5.31. The time period for both PC 1 and PC 2 shows a big difference at 24 hours and 30 minutes. The result in Figure 5.30 show the clustering of COOH SAM at PC1 vs PC 2 take place at 30 mins, majority of the clustering of PC 3 vs PC 4 take place at 30 mins.

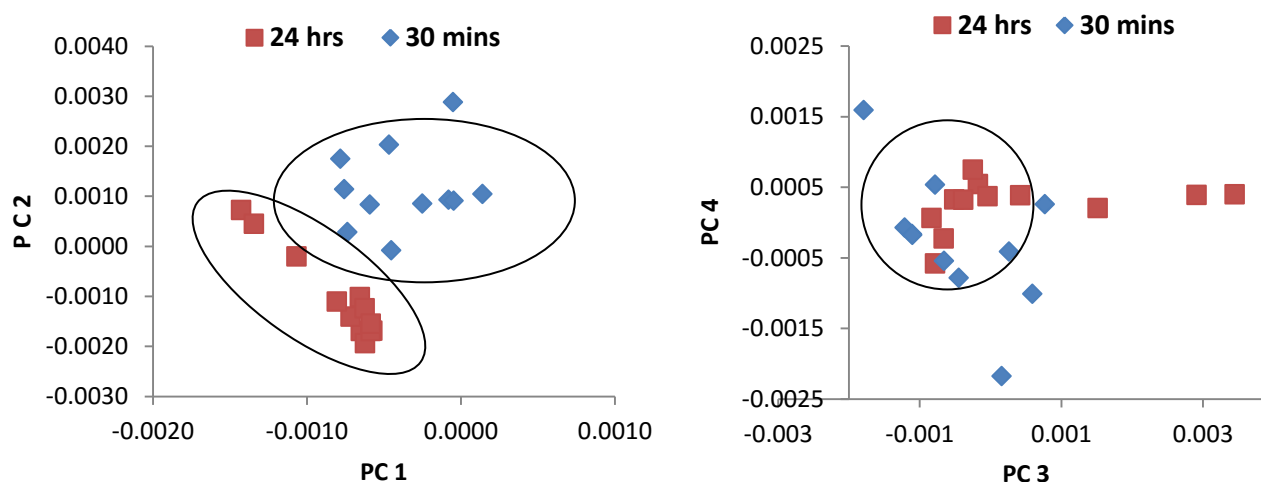
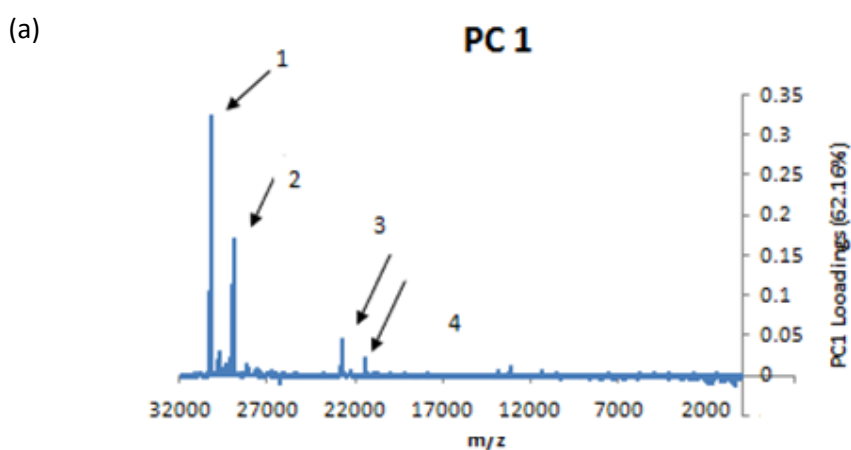


Figure 5.31 Score plot on the first four multivariate axes from PCA of the MALDI-Tof-Tof spectra showing the effect of incubation time on cell secretion variance

Loading Plot of MALDI-Tof/Tof

The loading plots for MALDI analysis of PC 1 and PC 2 are shown in Figure 5.33. The peaks with higher loading values were selected for further determination and analysis. Despite there was no variation difference between PC1 and PC2 in terms of surface chemistry, high peaks were identified in both PC 1 and PC2 in the loading plot. Peaks were identified after 17 kDa m/z with the highest peak obtained at 31,190 m/z while so many peaks can be seen on PC 2. The highest peak on PC 2 is located in 30,000 m/z Table 5.6

PC1 Loading - Surface Chemistry Variance



PC2 Loading - Surface Chemistry Variance

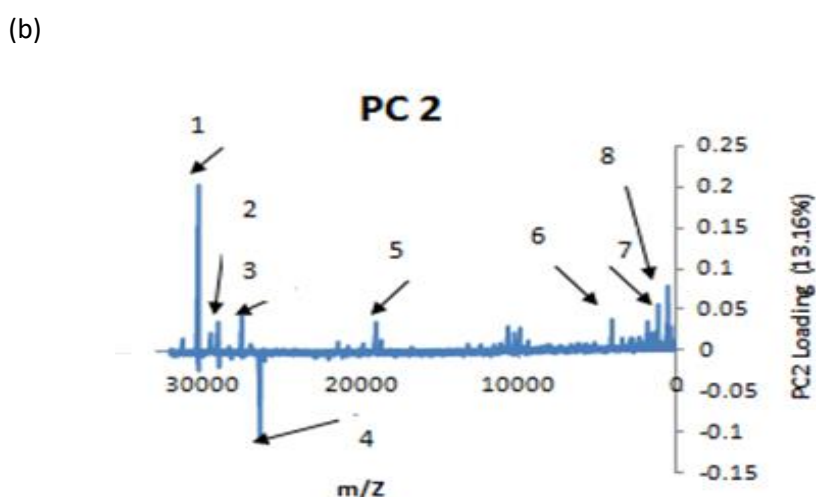


Figure 5.32 Loading plots of PC1 and PC2 from PCA of MALDI-Tof-Tof for the first two PCs. The loading are ordered in increasing mass to charge ratio.

Table 5.6 Loading values found in PC1 for MALDI -MS								
m/z (Da)	1	2	3	4	5	6	7	8
PC1 (62.16%)	31190	28500	22000	20000				

Table 5.7 Loading values found in PC2 for MALDI -MS								
m/z (Da)	1	2	3	4	5	6	7	8
PC2 (13.16%)	30209	28963	27486	26317	17607	4109	1186	569

Table 5.6 and 5.7 shows the loading values of PC1 and PC2. The PC model showed different spectra being produced using BSA on different surface chemistry and different time points. Research have been carried out using TOF-SIMS and PCA analysis technique to understand the effect of protein adsorption (fibrinogen) with different timepoints on a variety of substrates.^{58,59} Principal Component analysis methods have been shown as a reliable method which can be used to identify unknown spectra, although more future research and reports will be required.

A methodology in secretome analysis of fibroblast cell which can be used for any cell type has being achieved. The incubation time of cells in serum free media is another major challenge in secretome. Planque C *et al*⁵³ stated that cells can be incubated in serum free media for 18-48 hour to reduce complexity and avoiding interference from other protein in the media, while experiment was at 30 mins and 24 hours.

Reducing the complexity of media has being shown in detail in this chapter , from using glutamine and non-glutamine to less serum media .Few review or experiment paper being published showing the effect of surface chemistry and incubation timepoint on secreted protein which shows the experiment carried out is unique and novel.

MS is mostly used in secretome analysis such as ESI-MS and MALDI –Tof MS which have been used in identification of biomarkers of diseases.⁶⁰⁻⁶¹ Several reports on detection of serum biomarkers have make use of MALDI-MS or ESI-MS.

The use of Multivariate analysis technique is now widely used by researchers such as Wagner et al⁶² and Ohrlund et al⁶³, to give meaningful information from large datasets. PC analysis result on ESI and MALDI at different surface chemistry and incubation timepoints shows cells respond to surface chemistry differently and at different timepoint.

The overall findings in this chapter have demonstrated the successful methodology achieved for secretome experiments. The use of BSA without glutamine has proved a positive impact on the experiment whereby spreading cells attaching to the surface during culture also showed no differences between FCS, BSA and Fg containing medias over short time periods.

Surface Charge plays a vital role in cell secretion response in ESI-MS and MALDI-Tof-Tof result. Negatively charged COOH surfaces have the highest number of cells adhered and well clustered on both PC 1 and PC 2 of Spectra Plot. The timepoint also has a great impact on the cell secretion response as seen in Figure 5.32 on score plot of MALDI-Tof-Tof. A higher response is observed in 30 minutes compared to 24 hours on PC 1 and PC 2.

5.5 CONCLUSION

Fibroblasts have been shown to respond differently to a range of surface chemistries using self assembled monolayers (SAM), both in their morphology, adhesion and spreading of cells over time and their secretome as evidenced by MS. 3T3 fibroblasts with culture media BSA/PBS spread rapidly on amine ($-\text{NH}_2$) surfaces compared to hydroxyl ($-\text{OH}$) and carboxyl ($-\text{COOH}$) at 1, 2 and 24 hours while methyl surfaces have the highest number of cells adhering after 1, 2 and 24 hours.

Liquid chromatography electrospray mass spectrometry of media from cells cultured over differing surface chemistries (NH_2 , CH_3 , OH , COOH) at different time points (30 minutes and 24 hours) reveals different species are present using principal component analysis. Surface charge and wettability seem to play roles in determining cell responses. Variance is observed at very short incubation times, with no additional variance being observed at longer times. This indicates that initial cell-surface interactions are critical in determining the cell responses. Further investigation to identify the nature of the difference in secreted molecules is required, but may drive the design of novel materials to initiate desired cellular responses.

MALDI Tof/Tof results shows variation over differing surface chemistries at different points compared to LC-MS which may be due to several factors but there was variation in terms of incubation time in PC 1 vs PC 2 compared to PC 3 vs PC 4.

A method for the investigation of cell-surface responses has been designed and applied to 3T3 fibroblast cells cultured over surfaces presenting a range of chemical functionality. This method can be applied to other cell types and the investigation of other environmental factors. This work shows that surface chemistry affects cell response and also even within very short time periods after initial seeding.

Further investigation into the identity of the species were highlighted by principal components would allow better understanding of the mechanisms involved in cell mediation

of their micro-environment. A further work for this section will include MS-MS of main peaks of interest and the use of tandem MS database searching to identify these species will be possible.

5.6 REFERENCE

1. Vodicka, P., Skalnikova, H. & Kovarova, H. The characterization of stem cell proteomes. *Curr. Opin. Mol. Ther.* **8**, 232–9 (2006).
2. Ladunga, I. (2000) Large-scale discovery of secretory proteins from nucleic acid sequences. *Current Opinion in Biotechnology*, 11:13-18.
3. Skalnikova, H., Motlik, J., Gadher, S. J. & Kovarova, H. Mapping of the secretome of primary isolates of mammalian cells, stem cells and derived cell lines. *Proteomics* **11**, 691–708 (2011).
4. Bi, B., Schmitt, R., Israilova, M., Nishio, H. & Cantley, L. G. Stromal cells protect against acute tubular injury via an endocrine effect. *J. Am. Soc. Nephrol.* **18**, 2486–96 (2007).
5. Van Koppen, A. *et al.* Human embryonic mesenchymal stem cell-derived conditioned medium rescues kidney function in rats with established chronic kidney disease. *PLoS One* **7**, e38746 (2012).
6. Cho, Y. J. *et al.* Therapeutic effects of human adipose stem cell-conditioned medium on stroke. *J. Neurosci. Res.* **90**, 1794–802 (2012).
7. Ionescu, L. *et al.* Stem cell conditioned medium improves acute lung injury in mice: in vivo evidence for stem cell paracrine action. *Am. J. Physiol. Lung Cell. Mol. Physiol.* **303**, L967–77 (2012).
8. Wu, H.-Y., Chang, Y.-H., Chang, Y.-C. & Liao, P.-C. Proteomics analysis of nasopharyngeal carcinoma cell secretome using a hollow fiber culture system and mass spectrometry. *J. Proteome Res.* **8**, 380–9 (2009).
9. Perera, C. N., Spalding, H. S., Mohammed, S. I. & Camarillo, I. G. Identification of proteins secreted from leptin stimulated MCF-7 breast cancer cells: a dual proteomic approach. *Exp. Biol. Med. (Maywood)*. **233**, 708–20 (2008).
10. Huang, L.-J. *et al.* Proteomics-based identification of secreted protein dihydrodiol dehydrogenase as a novel serum markers of non-small cell lung cancer. *Lung Cancer* **54**, 87–94 (2006).
11. Mbeunkui, F., Fodstad, O. & Pannell, L. K. Secretory protein enrichment and analysis: an optimized approach applied on cancer cell lines using 2D LC-MS/MS. *J. Proteome Res.* **5**, 899–906 (2006).
12. Lawlor, K., Nazarian, A., Lacomis, L., Tempst, P. & Villanueva, J. Pathway-based biomarker search by high-throughput proteomics profiling of secretomes. *J. Proteome Res.* **8**, 1489–503 (2009).

13. Zwickl, H. *et al.* A novel technique to specifically analyze the secretome of cells and tissues. *Electrophoresis* **26**, 2779–85 (2005).
14. Chiellini, C. *et al.* Characterization of human mesenchymal stem cell secretome at early steps of adipocyte and osteoblast differentiation. *BMC Mol. Biol.* **9**, 26 (2008).
15. Sze, S. K. *et al.* Elucidating the secretion proteome of human embryonic stem cell-derived mesenchymal stem cells. *Mol. Cell. Proteomics* **6**, 1680–9 (2007).
16. Tadorelli, M. *et al.* Bovine serum albumin conformation on methyl and amine functionalized surfaces compared by scanning force microscopy. *J. Biomed. Mater. Res.* **29**, 707–14 (1995).
17. Lenk, T. J., Horbett, T. A., Ratner, B. D. & Chittur, K. K. Infrared spectroscopic studies of time-dependent changes in fibrinogen adsorbed to polyurethanes. *Langmuir* **7**, 1755–1764 (1991).
18. Ta, T. C. & McDermott, M. T. Mapping Interfacial Chemistry Induced Variations in Protein Adsorption with Scanning Force Microscopy. *Anal. Chem.* **72**, 2627–2634 (2000).
19. Wojciak BS, A. Curis, W. Monhagan, K. Macdonald, C. Wilkinson, Exp. Cell Res. 223 (1996) 426–435.
20. Whitesides GM, Laibins PE, Langmuir 1990, 6, 87-96
21. Barnes G, Interfacial science: An introduction, oxford University Press, 2005.
22. Membrane research, http://membranes.edu.au/wiki/index.php/Sessile_Drop_Method
23. Stalder AF, Kulik G, Sage D, Barbieri L, Hoffmann P. Physicochemical and engineering aspects, 2006.
24. <http://bigwww.epfl.ch/demo/dropanalysis/>
25. Barnes G, Interfacial science: An introduction, oxford University Press, 2005.
26. Kopaciewicz W *et al.* Zip...Tips...Millipore Corporation.
27. Vickerman JC, Gilmore IS. Surface Analysis Principal Techniques, second edition, Wiley, 2009.
28. Harvard university website. http://evans.harvard.edu/pdf/evans_pKa_table.pdf , Accessed on 20/09/2011.
29. Tanaka K, Waki H, Ido Y, Akita S, Yoshida Y, Yoshida T. Protein and polymer analyses up to m/z 100,000 by laser ionization time-of-flight mass spectrometry. *Rapid Commun Mass Spectrom* 1988;2:151 –3.
30. Karas M, Hillenkamp F. Laser desorption ionization of proteins with molecular masses exceeding 10,000 daltons. *Anal Chem* 1988;60:2299– 301.

31. Stults JT. Matrix-assisted laser desorption/ionization mass spectrometry (MALDI-MS). *Curr Opin Struct Biol* 1995;5: 691–8.
32. Bonk T, Humeny A. MALDI-TOF-MS analysis of protein and DNA. *Neuroscientist* 2001;7:6–12.
33. Harvey DJ. Matrix-assisted laser desorption/ionisation mass spectrometry of oligosaccharides and glycoconjugates. *J Chromatogr, A* 1996;720:429–46.
34. Zaluzec EJ, Gage DA, Watson JT. Matrix-assisted laser desorption ionization mass spectrometry: applications in peptide and protein characterization. *Protein Expr Purif* 1995;6:109–23.
35. Singhvi R, Kumar A, Lopez GP, Stephanopoulos GN, Wang DIC, Whitesides GM, Ingber DE. Engineering cell shape and function. *Science* 1994;264:696–8.
36. Mrksich M. Using self-assembled monolayers to understand the biomaterials interface. *Curr Opin Colloid Interface Sci* 1997;2:83–8.
37. Mrksich M. A surface chemistry approach to studying cell adhesion. *Chem Soc Rev* 2000; 29:267–73.
38. Singhvi R, Kumar A, Lopez GP, Stephanopoulos GN, Wang DIC, Whitesides GM, Ingber DE.
39. Faucheux N, R. Schweiss, K. Lutzow, C. Werner and T. Groth, *Biomaterials* **25**, 2721 (2004).
40. Keselowsky BG, Collard DM and Garcia AJ, *J. Biomed. Mater. Res. A* **66**, 247 (2003)
41. Tilton RD; Robertson CR, Gast AP, Manipulation of hydrophobic interactions in protein adsorption. *Langmuir*, 1991, 7 (11), pp 2710-2718
42. Capadona JR, Collard DM and Garcia AJ, Fibronectin adsorption and cell adhesion to mixed monolayers of tri(ethylene glycol)- and methyl-terminated alkanethiols, *Langmuir* 19 (2003), pp. 1847–1852
43. <http://www2.ups.edu/faculty/hanson/Spectroscopy/IR/IRfrequencies.html>
44. Inagaki, N. Plasma Surface Modification and Plasma Polymerization; Tenomi Publishing AG:
45. Thilly WG (1986) Mammalian cell technology. Butterworth, Boston .
46. Webb K, Hlady V, Tresco PA. Relationship among cell attachment spreading, cytoskeletal organization and migration rate for anchorage-depend cells on model surfaces. *J of Biom Med Volume* 49.362-368

47. Keselowsky BG, Collard DM, Garcia AJ. Surface chemistry modulates fibronectin conformation and directs integrin binding and specificity to control cell adhesion. *J Biomed Mater Res A* 2003;66: 247
48. Curran JM, Chen R, Hunt JA. The guidance of human mesenchymal stem cell differentiation in vitro by controlled modifications to the cell substrate. *Biomaterials* 2006;27: 4783.
49. Dalby MJ, Gadegaard N, Tare R, Andar A, Riehle MO, Herzyk P, et al. The control of human mesenchymal cell differentiation using nanoscale symmetry and disorder. *Nat Mater* 2007;6: 997.
50. Curran JM, Chen R, Hunt JA. Controlling the phenotype and function of mesenchymal stem cells in vitro by adhesion to silane-modified clean glass surfaces. *Biomaterials* 2005;26: 7057.
51. Bendall SC *et al.* An enhanced mass spectrometry approach reveals human embryonic stem cell growth factors in culture. *Mol. cell. Proteomics* 2009;8, 421-432.
52. Prowse AB *et al.*, Identification of potential pluripotency determinants for human embryonic stem cells following proteomic analysis of human and mouse fibroblast conditioned media. *J. Proteome Res.* 2007;6, 3796-3807.
53. Planque C *et al.* “ Identification of five candidate lung cancer biomarkers by proteomics analysis of conditioned media of four lung cancer cell lines” *Mol cell proteomics* 2009 8:2746-2758
54. Pitt WG and Cooper SL, *J. Biomed. Mater. Res.* 22 (1988) 359
55. Karas M, Hillenkamp F. Laser desorption ionization of proteins with molecular masses exceeding 10,000 daltons. *Analytical Chemistry* 1988; 60(20): 2299-2301.
56. Hillenkamp F, Karas M. Mass spectrometry of peptides and proteins by matrix-assisted ultraviolet laser desorption/ionization. *Methods Enzymol* 1990; 193: 280-295.
57. Hillenkamp F, Karas M, Beavis RC, Chait BT. Matrix-assisted laser desorption/ionization mass spectrometry of biopolymers. *Analytical Chemistry* 1991; 63(24): 1193A-1203A
58. Brash, J. L.; tenHove, P. *Thromb. Haemostasis* 1984, 51, 326.
59. Horbett, T. A. *Thromb. Haemostasis* 1984, 51, 174.
60. Stastna M, J.E. Van Eyk, Secreted proteins as a fundamental source for biomarker discovery *Proteomics*, 12 (2012), pp. 722–735
61. Makridakis M, A. Vlahou Secretome proteomics for discovery of cancer biomarkers *J. Proteomics*, 73 (2010), pp. 2291–2305

62. Wagner, M. S. & Castner, D. G. Characterization of Adsorbed Protein Films by Time-of-Flight Secondary Ion Mass Spectrometry with Principal Component Analysis. *Langmuir* **17**, 4649–4660 (2001).
63. Ohrlund, A.; Hjertson, L.; Jacobsson, S. P. *Surf. Interface Anal.* **1997**, 25,105-110
64. Howarter JA and Youngblood JP; Optimization of Silica Silanization by 3 Aminopropyltriethoxysilane; *Langmuir* 2006, 22, 11142-11147
65. Simon, A.; Cohen-Bouhacina, T.; Porte, M. C.; Aime, J. P.; Baquey, C. *J. Colloid Interface Sci.* 2002, 251, 278-283.
66. Toworfe GK , Composto IM, Ducheyne SP et al ;Nucleation and growth of calcium phosphate on amine, carboxyl and hydroxyl silane self assembled monolayers *Biomaterials* , 27 (2005), pg 631-642
67. Yanqing A, Chen M, Xue Q, Liu W et al; Preparation and self- assembly of carboxylic acid-functionalised silica. *J Colloid Interface Sci.* 2007 Jul 15;311 (2):507-13.

CHAPTER 6

General Discussion, Future Work and Conclusions

6.1 DISCUSSION

The chapters in this thesis have examined the effect of surface chemistry and topography on protein adsorption, and how the surface interaction with cells affects the proteins secreted to condition their environment. Functionalised silica nanoparticles of 11-215 nm have been shown to affect protein adsorption; also surface chemistry plays a vital role in the amount of protein adsorbed as described in Chapter 3 and 4. The study also highlights the major effect of adsorption on single and multiple proteins on particle size of 11-215 nm. This chapter will summarise all its results in previous chapters, including a discussion and future work that needs to be carried out from this thesis.

Functionalization of silica nanoparticles with four different chemistries were chosen to investigate the effect of surface wettability (hydrophobic and hydrophilic) and surface charge (negative and positive) on protein adsorption. Albumin and fibrinogen are two proteins used due to their different sizes, shapes and relevance within the extracellular matrix. The two proteins were used to examine the effect of surface chemistry and topography on protein adsorption, also the effect of protein size and shapes on protein adsorption were observed.

The results shown in Chapter 3 shows albumin and fibrinogen have different adsorption amount in terms of surface chemistry and curvature which is due to their different shape. Albumin, a globular protein, 14 x 4 nm can adsorb in different orientations but can only undergo single stage adsorption processes while fibrinogen is elongated, 40 x 4 nm in size and can only adsorb in two processes either parallel or horizontal as shown in Figure 3.20. The highest BSA and Fg adsorption is found on hydrophilic surfaces, while in terms of curvature 64 nm particles supported the highest adsorption.

Protein conformation changes that take place on surface-bound protein were investigated using FTIR, as shown in Chapter 3. The affinity constants were different for both

BSA and Fg. Albumin experiences stronger attraction affinity towards hydrophilic surfaces (OH) while a higher affinity of Fg is on amine surfaces (NH₂). The strong affinity observed on this surface caused a protein deformation as observed on the secondary protein structure. The influence of surface chemistry and curvature on competitive protein adsorption was investigated at different time-points as shown in Chapter 4. The adsorption of HSA and Fg varies in terms of surface chemistry and curvature.

The use of PCA to analyse FTIR spectra was applied to understand the effect of surface chemistry and curvature on competitive protein binding at different time-points, in Chapter 4. The analysis of PC1 and PC2 shows on hydroxyl (OH) and methyl surface (CH₃), 11 nm is further away from other curvature size at 10 mins but at 180 mins, 11 nm is found clustering around other surface curvature while on OH surface, 105 nm is seen moving further away which suggest that strong spectral difference impact on the variance, highlighting the differences in amide I band shape and therefore associated secondary structure. As the timepoint increases, the less the random coil present on each surface curvature and chemistry using HSA/Fg solution in ratio 19:1. The results may be due to differing shapes of albumin and Fg on each surface curvature at different timepoints.

Understanding material cell-surface interaction and cellular communication were investigated using a proteomic approach in Chapter 5. The investigation of secreted protein on physicochemical cues was carried out using a proteomic approach. A methodology and protocol was established on how fibroblast secreted protein can be investigated. Albumin was used due to its low abundance, since one of the main challenges of proteomics is the type of media being used. Fibroblast cells were seeded on albumin at different time-points and shown to survive between 1-24 hours. MALDI and ESI ionisation were used to analyse the secretome samples. PCA multivariate analysis was used to analyse the data and correlation of surface chemistry on secreted protein. To date, there have been no reports highlighting

such surface chemistry effects on the proteins secreted by cells. The results show a distinctive difference of surface chemistry while surface charge played a vital role on the ESI dataset. A similar result is observed on the MALDI dataset; negatively charge (COOH) data were aligned differently from other surface chemistry (CH₃, OH and NH₂).

Surface chemistry and curvature have been shown to have an impact on protein-surface interaction, as shown on the amount adsorbed, affinity and surface saturation in Chapter 3 and 4. The understanding of cellular communication has shown surface chemistry affects cell response. Secretome methodology is being achieved and the principle governing protein adsorption and conformation changes has being established.

We have clearly shown that surface chemistry and topography affect protein adsorption, from the result of protein adsorbed, conformation changes, affinity and saturation of protein. The use of PCA analysis has helped in understanding the correlation of the amide I spectra in terms of surface chemistry and topography, and also MS dataset. It has also been clearly shown that the type of protein, concentration and timepoint have an effect of protein adsorbed which shows protein-surface interaction differs. A methodology is achieved. The results obtained in this thesis have resulted in further investigation of cell adhesion and proliferation on nanoparticles.

6.2 Future Works

Further investigation that could be carried out to further understand protein-surface interactions and cellular communication are listed below;

6.2.1 Cell- Nanoparticle Interaction (Chemistry and Topography)

Nanoparticles have being widely used in biomedical application due to its importance in drug delivery and imaging tools.¹⁻³ Physicochemical cues such as size, shape, surface charge, chemistry and topography have being shown affect cell-nanoparticle interaction.⁴⁻⁶

The effect of surface chemistry and topography with biological response will be investigated. Progression of the experiment in Chapter 3 and 4 is to understand the effect of surface chemistry and nanoparticle size with cell interaction using functionalised silica nanoparticle. A closed packed layer of silica spheres of 11-215 nm is prepared, as shown in section 2.2.2. Functionalised silica nanoparticles of four chemistries, OH, COOH, NH₂ and CH₃ will be used for this experiment as explained in materials and methodology in Chapter 2. SEM, XPS, WCA and FTIR will be use to characterise the silica nanoparticle while fibroblast cell will be used a model for this experiment at different timepoints between 1-24 hours as shown in Figure 6.1

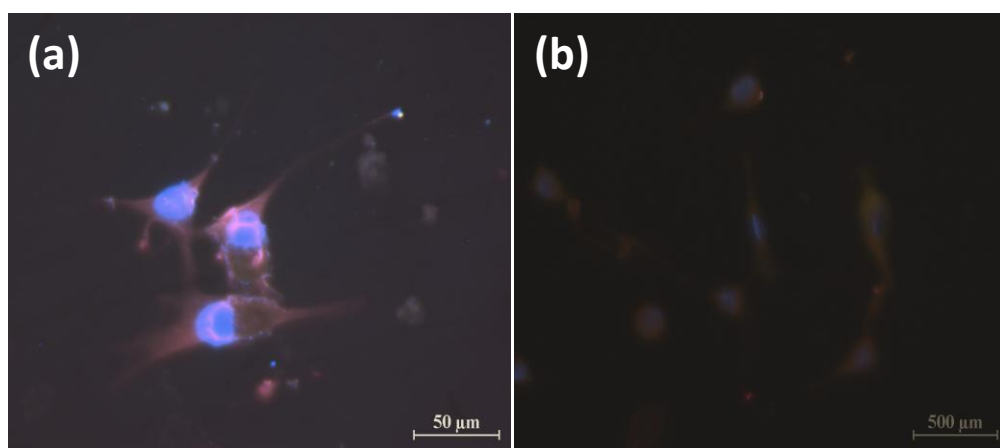


Figure 6.1 Fluorescence microscope image of Fibroblast cell seed on functionalised silica nanoparticle at 24 hours (a) NH₂ terminated surface (b) OH terminated surface. Overlaid image of Dapi, Tritc and Fitc.

The use of stem cells and primary cell line will be used for this study such as mesenchymal stem cells, neural and fibroblast cells. The results will give a broader understanding of the effect of functional chemistries and particle sizes on cell-nanoparticle interaction.⁷ To understand the possibilities of nanoparticles for (stem) cell therapy the interactions of nanoparticles with cells need to be investigated^{8,9}

6.2.2 Cell-Secretome-Chapter 5

A methodology and protocol for secretome analysis is successfully achieved, therefore, the use of primary cell, neural cells and stem cells will be used for the study. Further analysis of MALDI and ESI dataset will be carried out on the loading value shown in Table 5.5-5.7 using MS/MS analysis. Stem cells have been shown to respond to physicochemical cues such as surface chemistry and topography.^{10,11} Micro and nanostructures are vital when considering the contact guidance of cells on surfaces, e.g. their guidance along topographical features. Microstructures such as microgrooves, pits and pillars are known to induce changes in cell attachment, contact guidance, spreading and protein abundance. Nanotopography has being shown to affects cell adhesion, proliferation and motility.¹²⁻¹⁴ One area of major impact within regenerative medicine is the use of neural stem cells. Neurone cells will be used using the methodology and protocol achieved in Chapter 5 since neural stem cell plays a vital role in neuronal connection.

The effects of micro and nanoscale topography on neuron cells can be investigated by the use of a proteomic approach to assess the protein profile of the cell on different surface topography and chemistries known as secretome (secreted protein). Secreted molecules released from neurone cells will provide and give insight for the biological features characterising neuronal phenotype. By using the protocol achieved in Chapter 5 for secretome, it will use the approach to overcome the challenges of secretome such as the type of condition media, will be used time point and how to analysis dataset.

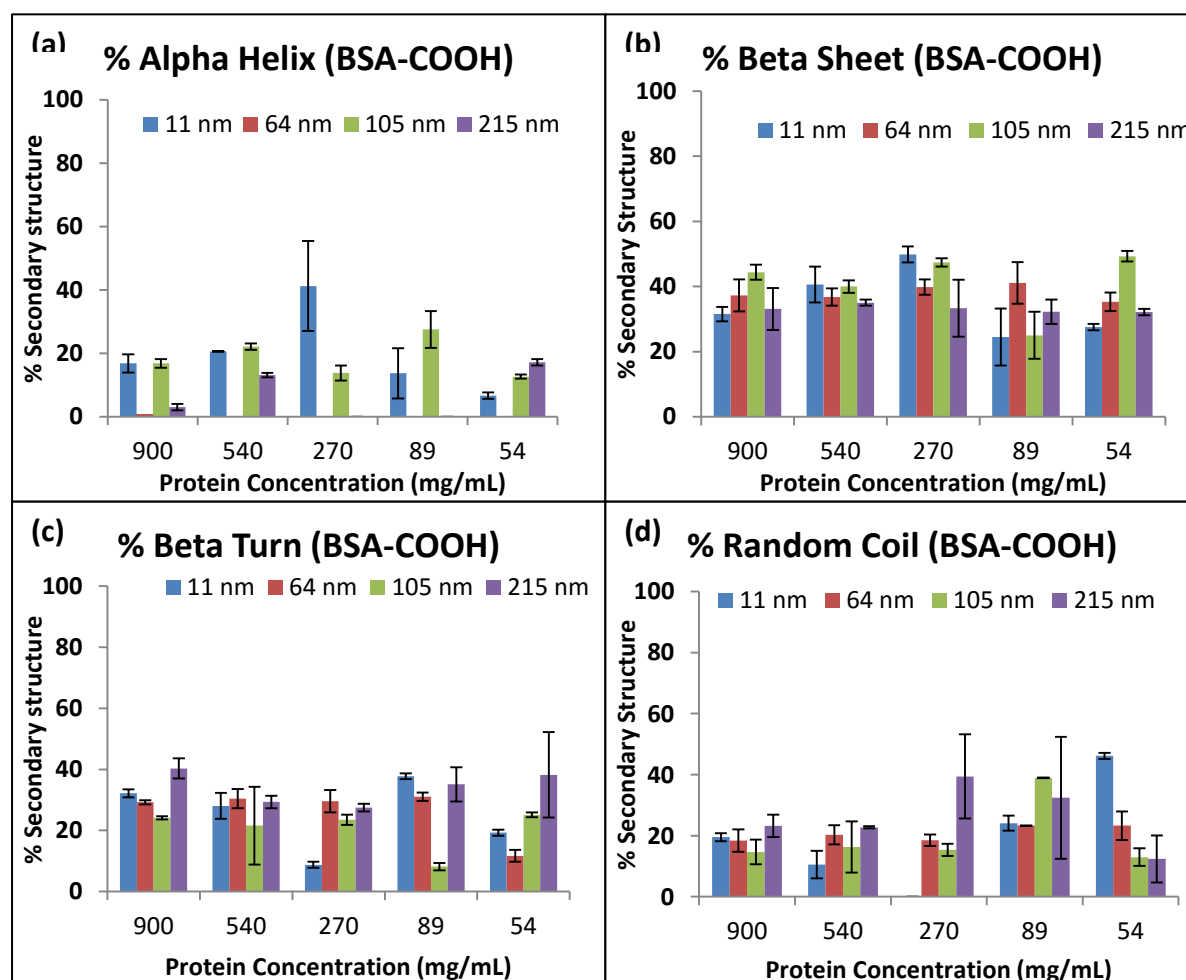
6.3 References

1. De, M.; Ghosh, P. S.; Rotello, V. M. Applications of nanoparticles in biology. *Adv. Mater.* 2008, 20, 4225–4241.
2. Kohane, D. S. Microparticles and nanoparticles for drug delivery. *Biotechnol. Bioeng.* 2007, 96, 203–209.
3. Giljohann, D. A.; Seferos, D. S.; Daniel, W. L.; Massich, M. D.; Patel, P. C.; Mirkin, C. A. Gold nanoparticles for biology and medicine. *Angew. Chem., Int. Ed.* 2010, 49, 3280–3294
4. Verma A, Stellacci F: Effect of surface properties on nanoparticle-cell interactions. *Small* 2010, 6:12–21.
5. Fleischer CC, and Payne CK Nanoparticle–Cell Interactions: Molecular Structure of the Protein Corona and Cellular Outcomes; *Acc. Chem. Res.*, 2014, 47 (8), pp 2651–2659
6. Mailander V and Landfester K; Interaction of Nanoparticles with Cells; *Biomacromolecules* , 2009, 10 (9), pp 2379–2400
7. Shang L, Nienhaus K and Nienhaus GU; Engineered nanoparticles interacting with cells: size matters; *Journal of Nanobiotechnology* 2014, 12:5
8. Li LW, Mu QX, Zhang B, Yan B: Analytical strategies for detecting nanoparticle-protein interactions; *Analyst* , 2010, 135:15191,530.
9. Saptarshi S, Duschl A, Lopata A: Interaction of nanoparticles with proteins: relation to bio-reactivity of the nanoparticle.; *J Nanobiotechnol* 2013, 11:26.
10. Dalby, M. J. et al. The control of human mesenchymal cell differentiation using nanoscale symmetry and disorder. *Nat. Mater.* **6**, 997–1003 (2007).
11. McBeath, R., Pirone, D. M., Nelson, C. M., Bhadriraju, K. & Chen, C. S. Cell shape, cytoskeletal tension, and RhoA regulate stem cell lineage commitment. *Dev. Cell* **6**, 483–95 2004.
12. Dalby M. J., et al, Nucleus alignment and cell signalling in fibroblasts: response to a micro-grooved topography. *Experimental Cell Research*, vol. 284 no. 2 pp. 274–282 2003
13. Gallagher J. O., McGhee K. F., Wilkinson C. D. W., Riehle M. O. Interaction of animal cells with ordered nanotopography. *IEEE Transactions on Nanobioscience*, vol. 1 no. 1 pp. 24–28 ,2002
14. Wojciak-Stothard B., Madeja Z., Korohoda W., Curtis A., Wilkinson C. Activation of macrophage-like cells by multiple grooved substrata. Topographical control of cell behaviour. *Cell Biology International*, vol. 19 no. 6 pp. 485–490 1995

APPENDIX

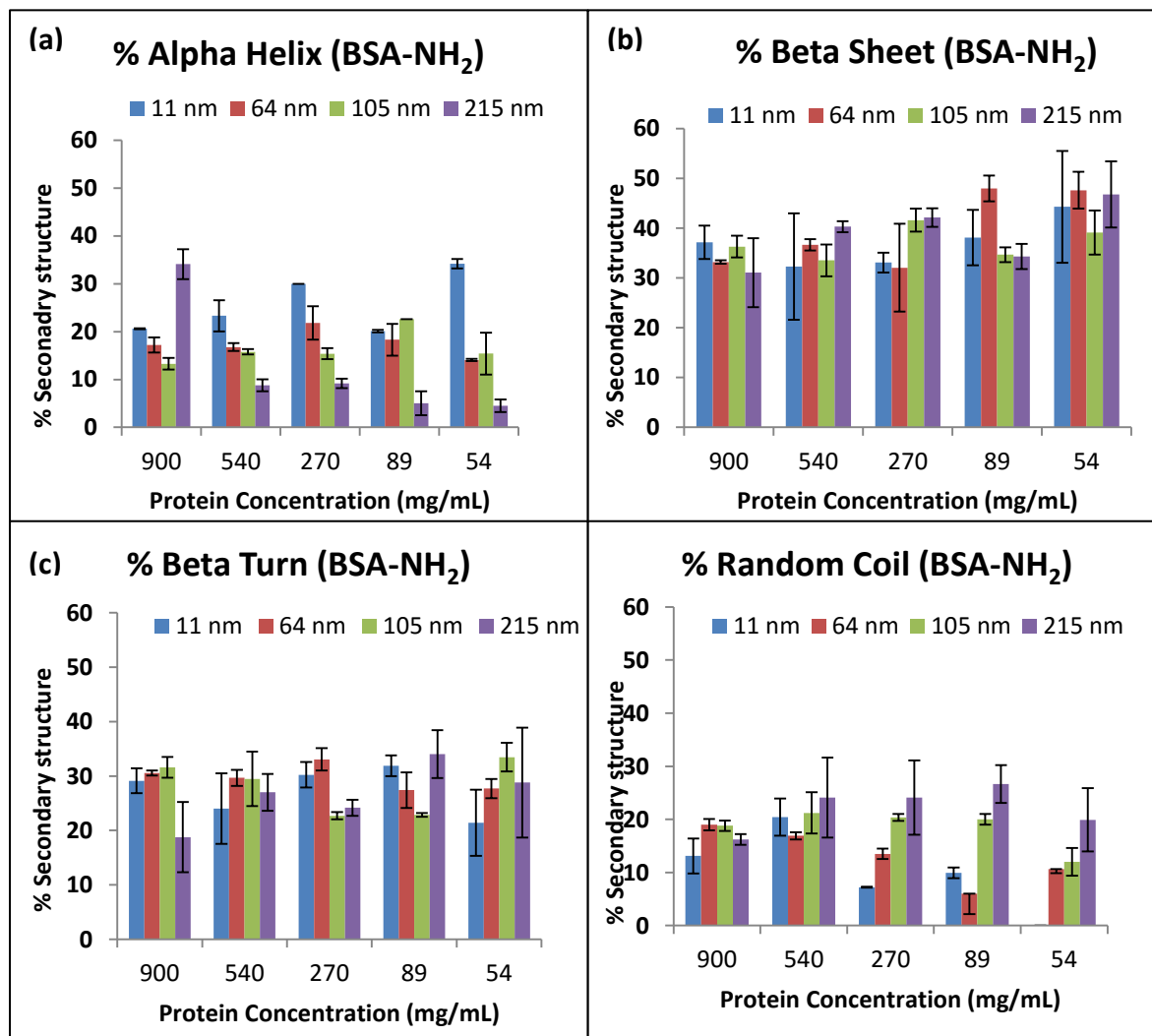
Appendix 1

The appendix shows the percentage of secondary structure of BSA on carboxyl surface (COOH) and amine surface (NH₂) at different sized spheres is shown in Appendix 1.1. Secondary structure equals 100, i.e at 270 mg/mL on 11nm, α -helix is 41.23%, β sheet is 49.85%, β turn is 8.77% while random coil is 0% all add up to 100%.



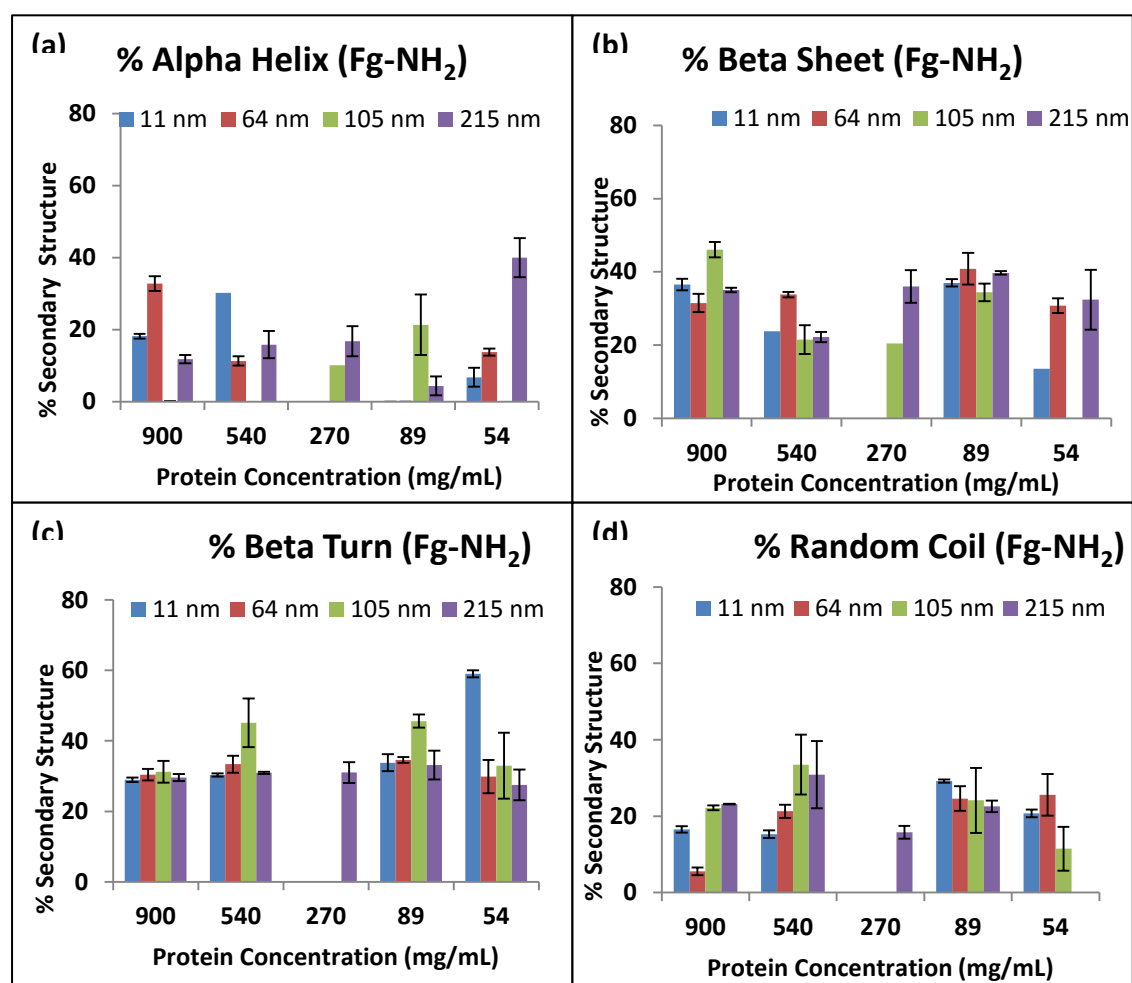
Appendix 1.1 Conformation assessment of BSA on carboxylic surface (COOH) of 11-215 nm (a) alpha helix, (b) beta sheet (c) beta turn and (d) random coil. Data shown are the mean \pm SD of three replicate samples, n=3.

The appendix shows the percentage of secondary structure of BSA on amine surface (NH₂) at surface curvature of 11-215 nm, shown in Appendix 1.2



Appendix 1.2 Conformation assessment of BSA on amine surface (NH₂) of 11-215 nm (a) alpha helix, (b) beta sheet (c) beta turn and (d) random coil. Data shown are the mean \pm SD of three replicate samples, n=3.

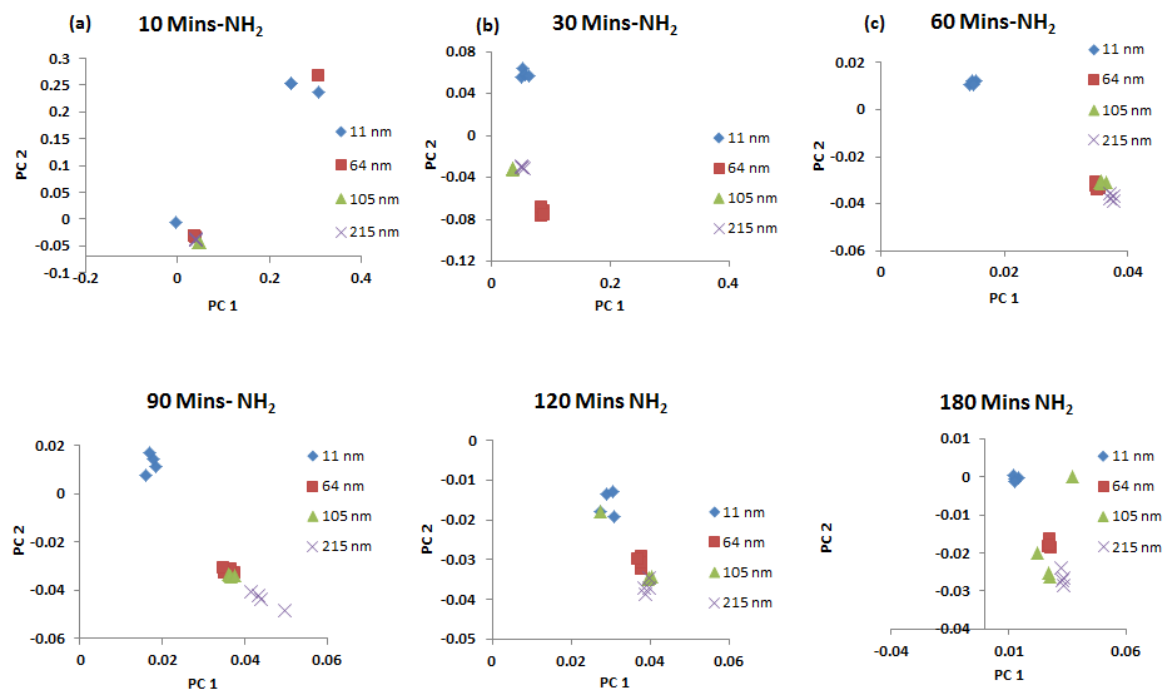
The appendix shows the percentage of secondary structure of Fg on carboxylic surface on amine surface (NH₂) at surface curvature of 11-215 nm, shown in Appendix 1.3.



Appendix 1.3 Conformation assessment of Fg on amine surface (NH₂) of 11-215 nm (a) alpha helix, (b) beta sheet (c) beta turn and (d) random coil. Data shown are the mean \pm SD of three replicate samples. Error bars correspond to parameters standard deviations

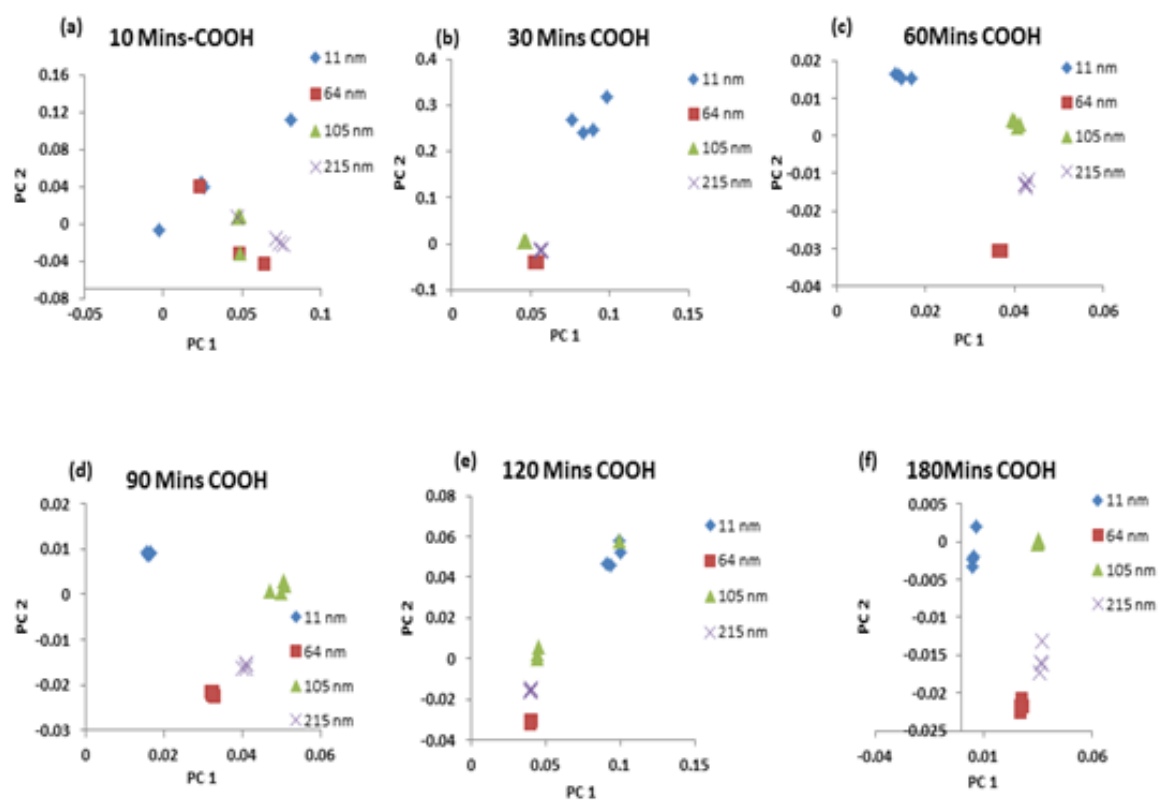
Appendix 2

PCA score dataset for Amine Surface (NH₂)



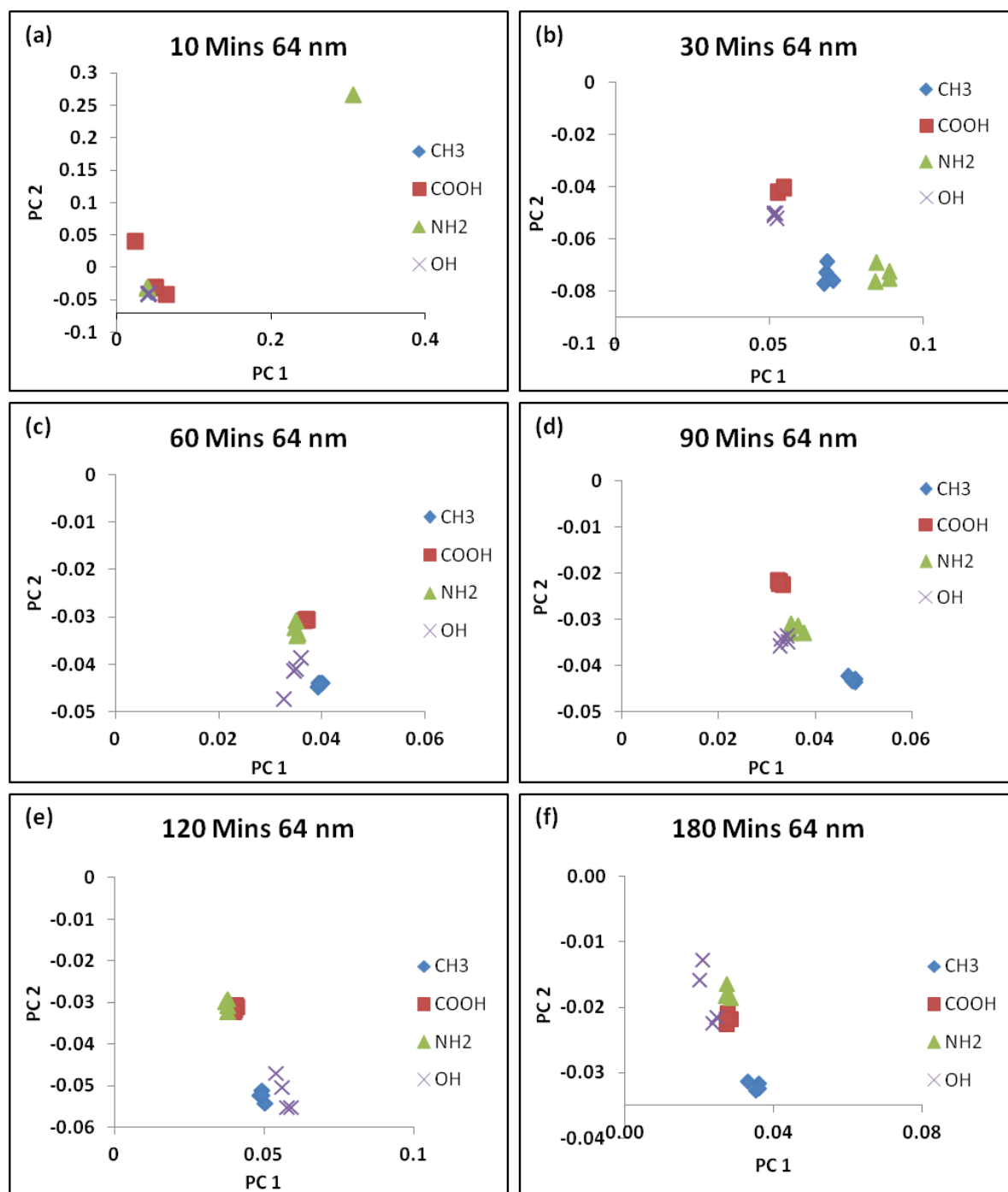
Appendix 1 PC 1 and PC 2 score plots of amide I of amine surface (NH₂) at different timepoints (10, 30, 60, 90,120 and 180 mins)

PCA score dataset for Amine Surface (COOH)



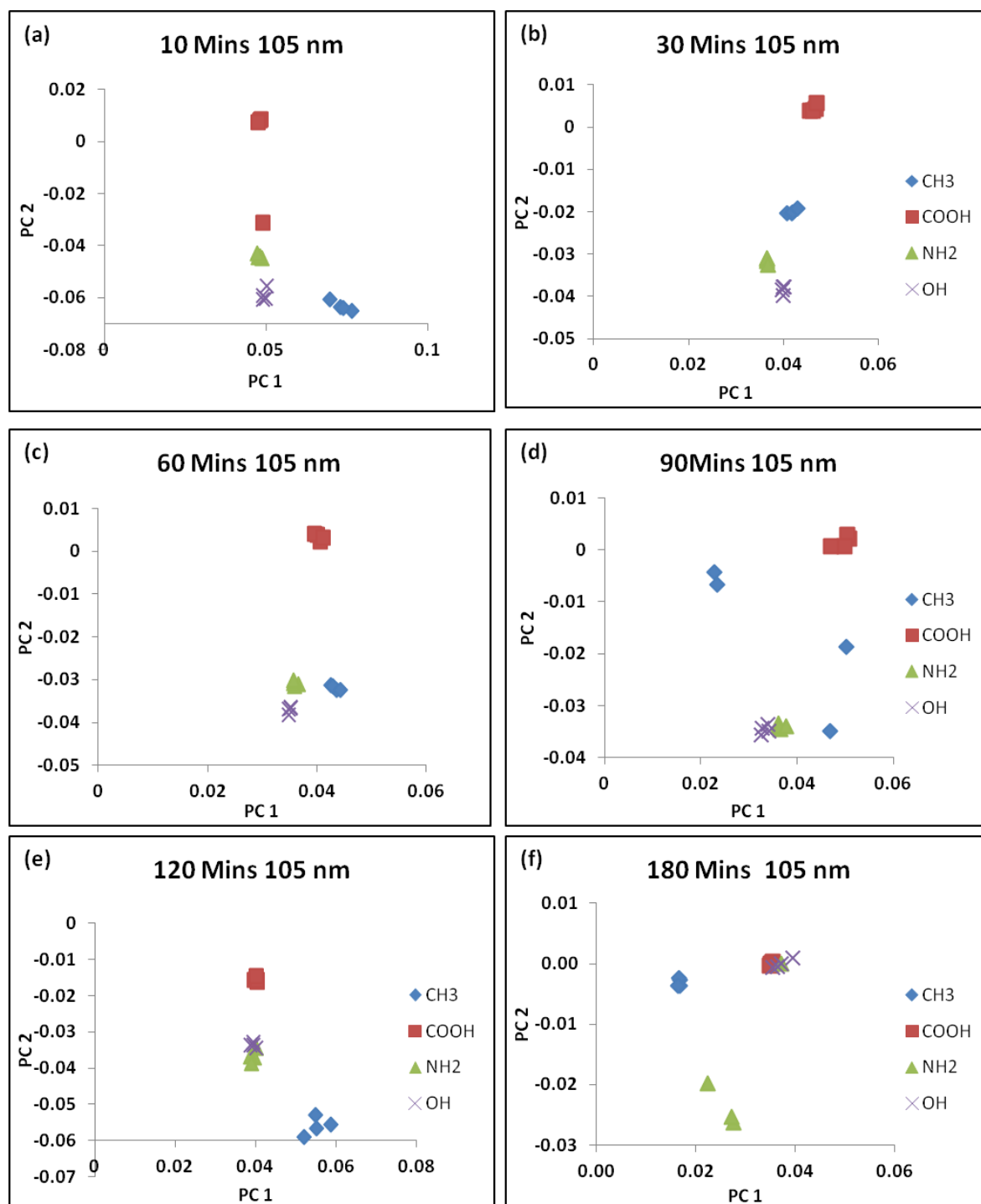
Appendix 2 PC 1 and PC 2 score plots of amide I of carboxylic surface (COOH) at different timepoints (10, 30, 60, 90,120 and 180 mins)

PCA score dataset for curvature size of 64 nm



Appendix 3 PC1 and PC2 loadings of 64 nm at different timepoints (10, 30, 60, 90, 120 and 180 mins)

PCA score dataset for curvature size of 215 nm



Appendix 4 PC1 and PC2 loadings of 215 nm at different timepoints (10, 30, 60, 90,120 and 180 mins)

